GFZ
Helmholtz Centre
POTSDAM

HELMHOLTZ CENTRE POTSDAM
GFZ GERMAN RESEARCH CENTRE
FOR GEOSCIENCES

Thai Chinh Nguyen

Use of the East Asia GPS receiving network to observe ionospheric VTEC variations, scintillation and EIA features during the Solar Cycle 24

Scientific Technical Report STR21/04

www.gfz-potsdam.de

HELMHOLTZ
RESEARCH FOR GRAND CHALLENGES

Recommended citation

Nguyen Thai, C. (2021): Use of the East Asia GPS receiving network to observe ionospheric VTEC variations, scintillation and EIA features during the Solar Cycle 24, PhD Thesis, (Scientific Technical Report STR; 21/04), Potsdam: GFZ German Research Centre for Geosciences.
https://doi.org/10.48440/GFZ.b103-21049

Originally published as

Nguyen Thai, C (2021): Use of the East Asia GPS receiving network to observe ionospheric VTEC variations, scintillation and EIA features during the Solar Cycle 24, Berlin: Technische Universität.
https://doi.org/10.14279/depositonce-11709

Imprint

Helmholtz Centre Potsdam
GFZ German Research Centre for Geosciences

Telegrafenberg
D-14473 Potsdam

Published in Potsdam, Germany
April 2021

DOI: https://doi.org/10.48440/GFZ.b103-21049
URN: urn:nbn:de:kobv:b103-21049

This work is published in the GFZ series
Scientific Technical Report (STR)
and electronically available at GFZ website
www.gfz-potsdam.de

Use of the East Asia GPS receiving network to observe ionospheric VTEC variations, scintillation and EIA features during the Solar Cycle 24

vorgelegt von
M. Sc.
Thai Chinh Nguyen

an der Fakultät VI - Planen Bauen Umwelt
der Technischen Universität Berlin
zur Erlangung des akademischen Grades

Doktor der Ingenieurwissenschaften
- Dr.-Ing. -

genehmigte Dissertation

Promotionsausschuss:

Vorsitzender:	Prof. Dr. Jürgen Oberst
Gutachter:	Prof. Dr. Harald Schuh
Gutachter:	Prof. Dr. Mahdi Alizadeh
Gutachter:	Prof. Dr. Lung-Chih Tsai

Tag der wissenschaftlichen Aussprache: 15. Dezember 2020

Berlin 2021

Preface

This thesis is the results of my work as a PhD student at Technische Universität Berlin and a scientific assistant at the German Research Centre For Geosciences (GFZ) from the end of 2015 to early 2020. For me, it was a challenging time but also lots of interesting scientific experiences at the A17 building on the Telegrafenberg hill in Potsdam.

First and foremost, I would like to formulate the most sincere thanks to my scientific supervisor Prof. Dr.-Ing. Harald Schuh, the Director of Department 1: Geodesy, GFZ. I am deeply grateful to him for accepting and bringing me to GFZ, one of the world's leading institutes in Earth science research. I feel very proud and excited to study and work in this outstanding institute together with nice colleagues who are very friendly and always ready to share their knowledge, ideas. During my studies, Prof. Schuh, with his profound scientific knowledge, provides me with a lot of valuable and useful scientific awareness not only about the ionosphere, which is my main research interest but also about the general space geodesy. His constructive comments always inspire me to work stronger. The devoted support and timely orientations from him are, definitely, the decisive factors for the completion of this thesis.

My gratitude, of course, also goes to Professor Mahdi Alizadeh, my second supervisor. He is such a smart scientist as all of his feedbacks and suggestions are deeply valuable and greatly help me improve the quality of the thesis. I highly appreciate his time and his working style. Besides, during my research fellowship at TU Berlin, I have received a lot of professional supports from Professor Wickert (GFZ), Professor Tsai (NCU), Professor Minh (VAST) and other colleagues at section Space Geodetic Techniques, GFZ. It is my great honour to work with them. On this occasion, I would like to send a lot of thanks to them, without their supports in both techniques and ideas, this thesis would not have been completed.

This PhD project is implemented with the financial supports from the International Cooperation Department, Ministry of Education and Training, Vietnam, as well as from the German Academic Exchange Service (DAAD) and GFZ. I would like to express my honest gratitude to these organizations for giving me the opportunity to live and study in Germany. Also, a special thanks to the Vietnam Academic of Science and Technology (VAST) for providing the ionospheric scintillation measurements, which is the main research data of the thesis.

After completing the dissertation, my first thoughts are with my daughter, my wife, my family, and my beloved ones, who have always been by my side, supporting me unconditionally under all circumstances. Thank you so much for their silent contributions and great sacrifices. Lastly, thank you to everyone who has made this thesis come true.

Abstract

The ionosphere is a complex and highly variable physical system with the F-layer, which occupies at the highest altitude, contains the greatest concentration of free electrons. Under the extreme circumstance of the ionosphere such as in the periods of high solar activity or magnetic storms or simply in the equinoctial months each year, this layer is very often disturbed. During the disturbances, the small-scale irregularities develop and disperse microwave radio signals, and thus generate rapid fluctuations in the amplitude and phase of satellite signals. This phenomenon causes the ionosphere to be scintillated and is called ionospheric scintillation. The impacts of scintillation cannot be mitigated by the multi-frequency technique that is very effective when dealing with ionospheric delay. Consequently, ionospheric scintillation is one of the most significant threats for space geodetic techniques, especially for stations operating in the polar regions or areas near the equator.

To study ionospheric scintillation, alternative methods have been proposed including the method of using high-rate receivers to directly output S_4 index over Vietnam region and the method of using standard GNSS dual-frequency to calculate ROTI index on a global scale.

Main results of this thesis are the temporal variations of total number electron (TEC) in Southeast Asia for eleven consecutive years and the appearance characteristics of scintillation over this area as well as globally during solar cycle 24 (SC24). For space geodesy, electromagnetic waves are most vulnerable in the equatorial ionization anomaly (EIA) as this region has many potential risks of errors for satellite signals. The research area (Southeast Asia) is also located entirely within the EIA. In this thesis, the temporal - latitudinal VTEC maps have been established to study the modifications of EIA's structure. Thereby, the featured occurrence of EIA crests in Southeast Asia is revealed. Also, the global morphology of anomaly crests averaged over 11-year period shows the worldwide distribution of EIA crests during SC24.

Throughout the thesis, the high consistency between the state of the ionosphere and the activity status of the Sun is evidenced by high correlations between VTEC and solar indices. In which, the radio flux index (F10.7 cm) is proved to be more agreeable to the VTEC development than the sunspot number (SSN). The behaviour of the ionosphere during intense magnetic storms is also investigated. The results show that the structure of EIA is often highly volatile during these severe ionospheric conditions.

Zusammenfassung

Die Ionosphäre ist ein komplexes und hochvariables physikalisches System, wobei die am höchsten gelegene F-Schicht die höchste Konzentration an freien Elektronen enthält. Unter den extremen Bedingungen der Ionosphäre, wie beispielsweise in den Perioden hoher Sonnenaktivität oder magnetischer Stürme oder einfach in den Äquinoktialmonaten eines jeden Jahres, ist diese Schicht der Ionosphäre häufig gestört. Während der Störungen propagieren und zerstreuen die kleinräumigen Unregelmäßigkeiten Mikrowellen-Radiosignale und erzeugen so schnelle Schwankungen in der Amplitude und in der Phase der Satellitensignale. Dieses Phänomen führt zu einer Szintillation der Ionosphäre und wird oft als ionosphärische Szintillation bezeichnet. Im Prinzip können die Auswirkungen der Szintillation nicht durch die Mehrfrequenztechnik verringert werden, die bei der Behandlung der ionosphärischen Verzögerung sehr effektiv ist. Aus diesen Gründen ist die ionosphärische Szintillation eine der größten Herausforderungen für geodätische Weltraumtechniken, insbesondere für Messstationen, die in den Polarregionen oder in äquatornahen Gebieten einschließlich Südostasiens arbeiten.

Zur Untersuchung der ionosphärischen Szintillation wurden alternative Methoden vorgeschlagen, darunter die Methode der Verwendung von Hochfrequenz-Empfängern zur direkten Ausgabe des S_4-Index über der Region Vietnam und die Methode der Verwendung der standardmäßigen GNSS Zweifrequenzmessungen zur Berechnung des ROTI-Index zur Untersuchung ionosphärischer Unregelmäßigkeiten im globalen Maßstab.

Die Hauptergebnisse der Arbeit beinhalten die zeitlichen Variationen des Gesamtelektroneninhalts (total electron content, TEC) in Südostasien für elf aufeinander folgende Jahre und die Erscheinungsmerkmale der Szintillation während des 24. Sonnenzyklus (SC24) sowohl über diesem Gebiet als auch auf globaler Ebene. Für die Weltraumgeodäsie sind elektromagnetische Wellen in der äquatorialen Anomalie der Ionosphäre (equatorial ionization anomaly, EIA) am anfälligsten, da diese Region viele potenzielle Fehlerrisiken für Satellitensignale aufweist, welche bei der Übertragung aus dem Weltraum die Ionosphäre durchqueren. Das Forschungsgebiet (Südostasien) befindet sich ebenfalls vollständig innerhalb der EIA. In dieser Arbeit wurden die zeit und breitenabhängigen Karten des VTEC erstellt, um die Veränderungen der Struktur der EIA zu untersuchen. Dabei wird das charakteristische Vorkommen von Kämmen der EIA-Anomalie in Südostasien offen gelegt. Außerdem zeigt die globale Morphologie der Anomalie-Kämme,

gemittelt über einen Zeitraum von elf Jahren, die weltweite Verteilung der EIA-Kämme während des SC24.

Der starke Zusammenhang zwischen dem Zustand der Ionosphäre und dem Aktivitätszustand der Sonne wird durch hohe Korrelationen zwischen dem VTEC und den Sonnenindizes einschließlich der Sonnenfleckenzahl (sunspot number, SSN) und dem Radioflussindex F10,7 cm belegt. Auch das Verhalten der Ionosphäre während intensiver magnetischer Stürme wird untersucht. Die Ergebnisse zeigen, dass die Struktur der EIA unter diesen extremen ionosphärischen Bedingungen häufig sehr volatil ist.

Table of contents

1. Introduction 1
1.1. Overview 1
1.1.1. Motivation and research objectives 1
1.1.2. Thesis outline 4
1.2. The ionosphere 6
1.2.1. The structure of the ionosphere 6
1.2.2. The variations of the ionosphere 7
1.2.3. Effects of the ionosphere on the propagation of electromagnetic waves 9
1.3. Ionospheric scintillation phenomena 13
1.3.1. Definition of ionospheric scintillation 14
1.3.2. Classification of ionospheric scintillation 14
1.3.3. Worldwide characteristics of ionospheric scintillation 15
1.3.4. Impacts of ionospheric scintillation 16
1.3.5. Ionospheric scintillation models 18
1.4. Other ionospheric disturbances 19
1.4.1. Travelling ionospheric disturbance 19
1.4.2. Sudden ionospheric disturbance 19
1.4.3. Ionospheric storm 19
1.4.4. Geomagnetic storm 20
1.4.5. Solar wind 20
1.4.6. Effect of the Moon 20

2. Calculation of ionospheric disturbances parameters from GNSS measurements 21
2.1 TEC estimation from dual-frequency GNSS observations 21
2.1.1. STEC from code pseudo-range 21
2.1.2. STEC from smooth pseudo-range 22
2.1.3. Converting STEC to VTEC using a mapping function 24
2.1.4. Calculating the coordinates of the ionospheric pierce point (IPP) 26
2.2. Alternative methods for detecting ionospheric scintillation 27
2.2.1. Computing S_4 index from high-rate GNSS observations 27
2.2.2. VTEC gradient 28
2.2.3. Rate of TEC index (ROTI) 29
2.3. Developing a software tool to calculate some ionosphere parameters 33

2.4. Some results and discussion 35
2.5. Chapter summary 38

3. TEC variations during SC24 over the South East Asia area 40
3.1. Data available in the research area during the period of 2007 - 2017 40
3.2. Diurnal variations 47
3.3. Seasonal variations 53
3.4. Annual variations 60
3.5. Correlation between VTEC and solar indices 66
3.6. Chapter summary 71

4. Occurrence characteristics of ionospheric scintillation over Vietnam region 76
4.1. Data and methodology 76
4.2. Eliminate sources of interference 80
4.3. Temporal distributions 84
4.3.1. Daily distributions 84
4.3.2. Seasonal distributions 88
4.4. Spatial distributions 92
4.5. Chapter summary 95

5. Ionospheric irregularity observations using ROT and ROTI indices 97
5.1. Using ROT and ROTI indices to study the disturbances in the ionosphere 97
5.2. Regional ionospheric irregularities maps 105
5.3. Global ionospheric irregularities maps 108
5.4. Chapter summary 113

6. Comparisons of EIA observations based on IONEX files 114
6.1. Temporal - latitudinal VTEC maps and methodology to study the characteristics of peak EIA crest 114
6.1.1. Global VTEC map derived from IONEX files 114
6.1.2. Methodology to study the occurrence characteristics of peak EIA crests 115
6.1.3. Establish temporal - latitudinal VTEC map from GNSS observations 117
6.1.4. Establish temporal - latitudinal VTEC map from GIM 119
6.2. A case study on the biggest geomagnetic storm of solar cycle 24 120
6.2.1. Magnetic field parameters, plasma activities and solar indices 121

6.2.2. TEC variations and the behaviour of the ionosphere 123
6.2.3. Ionospheric irregularities 127
6.3. Characteristics of peak EIA crest in the Southeast Asia area (105^0 meridian) during SC24 132
6.3.1. Occurrence time of peak EIA crests 134
6.3.2. Occurrence position of peak EIA crests 135
6.3.3. Occurrence amplitude of peak EIA crests 136
6.3.4. Annual variations of peak EIA crests 137
6.3.5. Remarkable conclusions on the characteristics of peak EIA crest 139
6.4. Chapter summary 141

7. Summary, conclusions, and outlook 144
7.1. Summary and conclusions 144
7.2. Outlook and further studies 148

Bibliography 152

List of Figures

Figure 1.1. Source and the division of layers in the ionosphere 7
Figure 1.2. Global distribution characteristics of ionospheric scintillation 16
Figure 1.3. The effect of ionospheric scintillation on GNSS signals 18
Figure 2.1. Single-layer mapping function model for the ionosphere 25
Figure 2.2. Projection of IPP on the horizontal plane 28
Figure 2.3. The footprint of satellite tracks at BAKO station in a single day 32
Figure 2.4. The flowing chat of the ionosphere software tool 33
Figure 2.5. The interface of the ionosphere software tool 33
Figure 2.6a. IS detected by PRN 7 at POTS station on 28.10.2003 36
Figure 2.6b. The ground track and sky-plot of PRN 7 from 10:00 to 14:00 UT 36
Figure 2.7a. IS detected by PRN 8 at BAHR station on 28.10.2003 37
Figure 2.7b. The ground track and sky-plot of PRN 8 from 6:00 to 12:00 UT 37
Figure 3.1. International sunspot number during SC24 40
Figure 3.2a. The radio flux index during SC24 41
Figure 3.2b. The Lyman-alpha index during SC24 41
Figure 3.3. Daily adjusted measurements of the solar flux density in SFU, from 1947 till the end of January 2018. 42
Figure 3.4a. Distribution (left) and satellite traces (right) of 16 GNSS stations over the research area 46
Figure 3.4b. Satellite traces of 16 GNSS stations over the research area 46
Figure 3.5. Daily variations of VTEC in October 2014 47
Figure 3.6. The daily averaged of Dst index during October 2014 48
Figure 3.7a. The averaged diurnal variations of VTEC at sta. CUSV in each month of 2009 49
Figure 3.7b. The averaged diurnal variations of VTEC at sta. CUSV in each month of 2014 49
Figure 3.8. Principle of the fountain effect in EIA region 51
Figure 3.9. Seasonal variations of the monthly maximum VTEC at station CUSV 53
Figure 3.10a. Seasonal variations of the monthly maximum VTEC in 2010 54
Figure 3.10b. Seasonal variations of the monthly maximum VTEC in 2014 54
Figure 3.11a. Daily mean VTEC during SC24 at station PIMO 55
Figure 3.11b. Daily mean VTEC during SC24 at station XMISs 55
Figure 3.11c. Daily mean VTEC during SC24 at station BAKO 55
Figure 3.11d. Daily mean VTEC during SC24 at station CUSV 56
Figure 3.11e. Daily mean VTEC during SC24 at station NTUS 56

Figure 3.11f. Daily mean VTEC during SC24 at station HKSL 56
Figure 3.11g. Daily mean VTEC during SC24 at station KUNM 57
Figure 3.12. The (monthly mean) temporal - latitudinal VTEC maps in 2012 (LT=UTC+7 h, TECU unit) 60
Figure 3.13a. Annual average variations of the monthly maximum VTEC 61
Figure 3.13b. Annual average variations of the monthly mean VTEC 61
Figure 3.14a. VTEC map at station PIMO during SC24 63
Figure 3.14b. VTEC map at station XMISs during SC24 63
Figure 3.14c. VTEC map at station BAKO during SC24 63
Figure 3.14d. VTEC map at station CUSV during SC24 64
Figure 3.14e. VTEC map at station NTUS during SC24 64
Figure 3.14f. VTEC map at station HKSL during SC24 64
Figure 3.14g. VTEC map at station KUNM during SC24 65
Figure 3.15. The actual variation trend of maximum monthly VTEC's annual average compared with the SSN of SC24 66
Figure 3.16a. Correlation between monthly max. VTEC and the SSN index at station CUSV 69
Figure 3.16b. Correlation between monthly max. VTEC and the F10.7 index at station CUSV 70
Figure 3.17a. The monthly mean VTEC of seven IGS stations and its correlation coefficient with the F10.7 index 71
Figure 3.17b. The monthly mean VTEC of seven IGS stations and its correlation coefficient with the SSN index 71
Figure 4.1. Raw S_4 index at HUE station during 22nd-29th March 2015 79
Figure 4.2. Filtering of S_4 index in the scintillation environment (left) and non-scintillation environment (right) 81
Figure 4.3. S_4 index filtering at HCM station during 4th-17th October, 2015 with different elevation cut-off (E): E=10^o (left), E=20^o (middle) and E=30^o (right) 82
Figure 4.4. S_4 index before (above) and after (below) filtering at HUE station on 22.10.2015 82
Figure 4.5. S_4 index before (above) and after (below) filtering at HCM station during 4th-17th October 2015 84
Figure 4.6a. Local time frequency of scintillation events appearance at HANOI in 2015 86
Figure 4.6b. Local time frequency of scintillation events appearance at HUE in 2015 86
Figure 4.6c. Local time frequency of scintillation events appearance at HCM in 2015 87

Figure 4.7a. Seasonal frequency of scintillation events appearance at HANOI in 2009 88
Figure 4.7b. Seasonal frequency of scintillation events appearance at HUE in 2009 89
Figure 4.7c. Seasonal frequency of scintillation events appearance at HCM in 2009 89
Figure 4.8a. Seasonal frequency of scintillation events appearance at HANOI in 2015 89
Figure 4.8b. Seasonal frequency of scintillation events appearance at HUE in 2015 89
Figure 4.8c. Seasonal frequency of scintillation events appearance at HCM in 2015 90
Figure 4.9. The trend of seasonal variations of scintillation activity 90
Figure 4.10. S_4 heat map over Vietnam region in 2009, 2015 (white area indicates no data) . 92
Figure 4.11. Directional distribution of scintillation events (elevation cut-off is 10^o)..... 93
Figure 5.1. ROT (top-left), ROTI (top-right) and S_4 (below) indices at HANOI station on October 24th 2015 98
Figure 5.2a. Comparison of scintillation events with different elevation threshold..... 99
Figure 5.2b. Comparison of scintillation events with different time span of ROTI calculation (top-left: 1 min, top-right: 10 mins, bottom-left: 15 mins, bottom-right: 20 mins) 101
Figure 5.3a. Ionospheric disturbances occur during the second half of October 2015 at HUE 102
Figure 5.3b. Ionospheric disturbances occur during the second half of October 2015 at CUSV 102
Figure 5.4. Ionospheric irregularities including ROTI index and VTEC gradient..... 104
Figure 5.5. Regional ROTI maps and the occurrence rates of ionospheric scintillation..... 106
Figure 5.6. Worldwide distribution of IGS stations 108
Figure 5.7. The footprint tracking of satellites at all 483 IGS stations on March 26th 2015 .. 109
Figure 5.8a. Spatial distribution of global ionospheric irregularities 109
Figure 5.8b. Temporal distribution of global ionospheric irregularities 110
Figure 5.8c. Distribution of ROTI by latitude (only ROTI≥0.5 tec/min are counted) 111
Figure 5.8d. Distribution of ROTI by longitude (above) and by time (below) at three different zones of the Earth (only ROTI≥0.5 tec/min are counted) 112
Figure 6.1. An example of GIM on January 31st 2020 shows the movement of peak EIA crests 116
Figure 6.2. The separation between the northern and southern crests of EIA (TECU unit) .. 116
Figure 6.3. Determine EIA's crests from temporal - latitudinal VTEC map (TECU unit) 117
Figure 6.4. The footstep of satellite traces expressed in two variables: time and latitude 117
Figure 6.5. The method of mean square sideslip for creating the gid data file 118
Figure 6.6a. Magnetic field indices during the middle of March 2015 121
Figure 6.6b. Plasma indices during the middle of March 2015..... 121

Figure 6.6c. Solar indices during the middle of March 2015 122
Figure 6.7. Mean daily of VTEC at some stations in the Southeast Asia area during the biggest geomagnetic storm of SC24..... 123
Figure 6.8. Temporal - latitudinal VTEC maps established at different longitudes: the top corresponds to 90^o longitude, the middle corresponds to 105^o longitude, and the bottom corresponds to 120^o longitude (TECU unit, LT=UTC+7 h). 125
Figure 6.9. The amplitude (a), appearance time (b), and geographic latitude (c) of the northern (blue square) and southern (red square) peak EIA crests during the period of 15^{th}-21^{st} of March 2015 126
Figure 6.10. The S_4 index at HANOI station on March 19^{th} 2015 127
Figure 6.11. The ROTI index at HUE station on 16^{th} (left) and 26^{th} (right) of March 2015 . 128
Figure 6.12a. S_4 and ROTI indices at HANOI during the last two weeks of March 2015 129
Figure 6.12b. S_4 and ROTI indices at HUE during the last two weeks of March 2015..... 130
Figure 6.12c. ROTI index at BAKO station during the last two weeks of March 2015 130
Figure 6.12d. ROTI index at CUSV station during the last two weeks of March 2015 131
Figure 6.12e. ROTI index at NTUS station during the last two weeks of March 2015..... 131
Figure 6.12f. ROTI index at XMISs station during the last two weeks of March 2015 131
Figure 6.13. Regional ROTI map on March 26^{th} 2015 indicates both temporal and spatial distributions of ionospheric irregularities. 132
Figure 6.14a. VTEC maps over the Southeast Asia area in 2007 132
Figure 6.14b. VTEC maps over the Southeast Asia area during the period of 2008 - 2014.. 133
Figure 6.14c. VTEC maps over the Southeast Asia area during the period of 2015 - 2017.. 134
Figure 6.15a. Occurrence time of peak EIA crests in each year. 134
Figure 6.15b. The difference in occurrence time of peak EIA crests in each year 135
Figure 6.16a. Geographic latitudes of peak EIA crests during 11-year period indicate that two anomaly crests are symmetric over the magnetic equator..... 135
Figure 6.16b. Geographic latitudes of peak EIA crests in each year 136
Figure 6.16c. The modification in distance between two peak EIA crests during 2007 - 2017 period..... 136
Figure 6.17. Amplitudes of peak EIA crests during 11-year period 137
Figure 6.18. Yearly variations of peak EIA crests. 138
Figure 6.19. The schemes of the combined theory of trans-equatorial neutral wind, subsolar point, and auroral equatorward wind in solstices 140
Figure 6.20. Developments of the geomagnetic storm occurred in March 2015 143

List of Tables

Table 1.1. Electron density of the main ionospheric layers 7
Table 2.1. List of IGS stations to study ionospheric scintillation 35
Table 3.1a. List of GNSS stations over the research area 43
Table 3.1b. List of GNSS stations over the research area 44
Table 3.2. Number of observed days during 11 years at seven IGS stations 45
Table 3.3. Annual average values of the monthly maximum and mean VTEC 52
Table 3.4. Percentage change of yearly averaged VTEC and F10.7 66
Table 3.5. Correlation coefficients between VTEC and solar indices 68
Table 4.1. List of stations used for ionospheric scintillation research in Vietnam region 76
Table 4.2. The output results of GSV4004B receiver 78
Table 4.3. Comparison of scintillation events with different elevation threshold 85
Table 5.1a. Comparison of scintillation events with different elevation threshold 100
Table 5.1b. Comparison of scintillation events with the different time span of ROTI calculation (elevation cut-off is 20^o) 100
Table 5.2. Statistics of S_4, ROTI indices and the ionospheric disturbances derived from the regional ROTI maps during the last two weeks of October 2015 103
Table 6.1. Abbreviations of used ionospheric products from IGS 115
Table 6.2. Top 20 biggest geomagnetic storms of SC24 120
Table 6.3. Statistics of S_4, ROTI indices and the ionospheric disturbances derived from the regional ROTI maps during the last two weeks of March 2015 128
Table 6.4. Occurrences of peak EIA crests in the Southeast Asia region during SC24 138

List of Abbreviations, Symbols and Nomenclature

ASCII	American Standard Code for Information Interchange
BEIDOU	Chinese Navigation Satellite System
CDDIS	Crustal Dynamics Data Information System
CME	Coronal Mass Ejection
CODE	Center for Orbit Determination in Europe
DCB	Differential Code Bias
DORIS	Doppler Orbitography and Radio-positioning Integrated by Satellite
DOY	Day Of Year
EIA	Equatorial Ionization Anomaly
EPF	Equatorial Plasma Fountain
ESOC	European Space Operations Centre
F10.7cm	Solar radio flux
GAIM	Global Assimilative Ionospheric Model
GALILEO	European Global Satellite Navigation System
GEO	Geostationary Earth Orbit
GIM	Global Ionospheric Maps
GISM	Global Ionospheric Scintillation Model
GISTM	GPS Ionospheric Scintillation and TEC Monitoring
GLONASS	GLObal NAvigation Satellite System
GNSS	Global Navigation Satellite System
GPS	Global Positioning System
GSV	GPS Silicon Valley
HCM	Ho Chi Minh
IGS	International GNSS Service
IONEX	IONosphere map Exchange
IPP	Ionospheric Pierce Point
IRI	International Reference Ionosphere
IS	Ionospheric Scintillation
ISMRB	Information Systems Management Review Board
JPL	Jet Propulsion Laboratory
LC	Linear Combination
LEO	Low Earth Orbit
LLR	Lunar Laser Ranging

LOS	Line Of Sight
LT	Local Time
Ly-α	Lyman alpha
ME	Magnetic Equator
MIDAS	Multi-Instrument Data Analysis System
MSLM	Modified Single Layer Mapping function
NASA	National Aeronautics and Space Administration
NOAA	National Oceanic and Atmospheric Administration
PRN	Pseudo-Random Noise
QZSS	Quasi-Zenith Satellite System
RINEX	Receiver INdependent EXchange format
RMS	Root Mean Square
ROT	Rate Of TEC
ROTI	Rate Of TEC Index
SBAS	Satellite Based Augmentation System
SC	Solar Cycle
SFU	Solar Flux Units
SID	Sudden Ionospheric Disturbance
SLM	Single Layer Model
SLR	Satellite Laser Ranging
SNR	Signal to Noise Ratio
SSN	SunSpot Number
STEC	Slant Total Electron Content
SWPC	Space Weather Prediction Center
TEC	Total Electron Content
TECU	Total Electron Content Unit
TID	Traveling Ionospheric Disturbance
UPC	Polytechnic University of Catalonia
UT	Universal Time
UTC	Universal Time Corrdinated
VAST	Vietnam Academic of Science and Technology
VLBI	Very Long Baseline Interferometry
VTEC	Vertical Total Electron Content
WBMOD	Wide Band Model
WDC-SILSO	World Data Center - Sunspot Index and Long-term Solar Observations

1. Introduction

1.1. Overview

1.1.1. Motivation and research objectives

For all space geodetic techniques that are currently in use, including GNSS (Global Navigation Satellite Systems), VLBI (Very Long Baseline Interferometry), SLR (Satellite Laser Ranging), and DORIS (Doppler Orbitography and Radio-positioning Integrated by Satellite), all measurements travel through the ionosphere. Therefore, their accuracy depends mainly on the very complex physical fluctuations of the ionosphere. The ionosphere is a dispersive medium for satellite signals operating in the microwave band with a basic principle: signals travelling through this medium are to the first approximation affected proportionally to the inverse of the square of their frequencies [Alizadeh et al., 2011]. As a consequence, the basic characteristic index of the ionosphere is the Total Electron Content (TEC) can be determined from the observations of these techniques. Research on TEC is a powerful way to help ionospheric scientists to grasp the rules of ionosphere variations, thereby improving the accuracy and also the efficiency of space geodetic techniques applications.

The ionosphere covers the region between approximately 50 and 1500 kilometres above the Earth's surface and is characterized by the presence of a significant number of free electrons and positively charged atoms and molecules called ions. The spatial and temporal dynamics of the ionospheric fluctuations depend on geophysical conditions e.g., solar and geomagnetic activities, season, time of day, geographical locations. The impact on the signals travelling from satellites through the ionosphere to receivers located on or near the Earth's surface is a function of the carrier frequency and the electron density along the signal path. Currently, each GNSS satellite transmits information for positioning on multi-frequency L1, L2, L5, or L6 bands. Among them, under most extreme ionospheric conditions, the ionospheric path delay at L1 may reach up to about 100 meters for low satellite elevation observations [El-naggar, 2011]. The basic GNSS observables are the so-called pseudo-range (or code) and the carrier phase. Both may be viewed as biased measurements of the slant range between a receiver and a satellite. Due to the dispersive nature of the ionosphere, ionospheric effect can be almost eliminated by forming the so-called ionosphere-free linear combination (LC) of simultaneous L1 and L2 measurements. By analyzing the so-called geometry-free LC, the difference between the L1 and L2 observable expressed in units of

length allows extracting information about the electron density from dual-frequency GNSS data. From the important role of TEC variations in applications of space geodetic techniques, in this thesis, we calculate TEC from GNSS data obtained at all available IGS stations located in the study area. This is the first research goal of the thesis.

From geodetic perspective, the ionosphere not only has the danger of TEC fluctuations, it can also cause many other sources of error such as ionospheric storms, Ionospheric Scintillation (IS), Sudden Ionospheric Disturbance (SID), Travelling Ionospheric Disturbance (TID),... Among them, ionospheric scintillation which is defined as the rapid modification of radio waves caused by small-scale structures in the ionosphere is one of the most unpredictable and ominous errors. While the errors due to TEC can be controlled and eliminated by the simple technique of using multi-frequency receivers, ionospheric scintillation has a more complex law of activity. In principle, the technique of using dual-frequency measurements cannot detect or remove this kind of error. Ionospheric scintillation can also be determined from TEC, but with the essence of the irregularities in the density and movement of free electrons in the ionosphere, its appearance and intensity also depend on other factors such as operating frequency of devices, geographic location, time (day or night, season, 11-year solar cycle), and the state of the Earth's magnetic. Ionospheric scintillation has been meticulously studied over the past several decades, but there are still research gaps due to the fact that in order to study it, special GNSS receivers which often work at a very high sampling rate are required. This kind of receiver is rather expensive and not as widely available as the standard dual-frequency receivers. In Vietnam, with the cooperation between the Institute of Geophysics, Vietnam Academic of Science and Technology (VAST) and Universities of Rennes1 and Telecom Bretagne in France, three scintillation receivers have been installed and located evenly in three parts (the northern part, the middle part, and the southern part) of the country. With the data provided by VAST in two years 2009 and 2015, we study the occurrence characteristics of scintillation activity over Vietnam area. That is the second goal of this research. However, in the absence of scintillation receivers, we can still use observations from standard dual-frequency GNSS receivers to detect scintillation error. These methods are becoming more and more widely used today as the global and dense availability of normal GNSS receivers. Therefore, propose alternative methods for detecting ionospheric scintillation is also one of the research goals.

Concerning ionospheric scintillation error, equatorial area is known as one of the most affected areas in the world. This is the region where the ionosphere often experiences the most extreme and abnormal variations. It is, hence, called the Equatorial Ionization Anomaly (EIA). It is well known that the EIA is characterized by an electron density trough at the magnetic equator, and two crests of enhanced electron density at about ±15° magnetic latitudes. The main driver of the EIA is the fountain effect. In the equatorial zone, there are different physical processes producing changes in the structure of EIA as field aligned plasma transport due to transequatorial neutral winds, photochemical processes produced by neutral composition effects,... For that reason, EIA research has become an interesting subject for space science, and so it is one of the next goals in my research.

Southeast Asia, with the almost areas located within the EIA region, is the main study area of this thesis. The main research data is all GNSS measurements collected at all available IGS stations (including 16 stations) in the research area plus the scintillation data over Vietnam region in two years 2009 and 2015. The study period is a full 11-year of solar cycle 24 (SC24) starting from the beginning of 2007 to the end of 2017. Such a sufficiently long study period can provide results that generalize the variations of TEC and ionospheric scintillation both in short and long term. In particular, the daily, monthly, seasonal, and annual variations of TEC and scintillation activity over the research area will be considered. Also from the results of TEC calculation for 11 consecutive years, we can present in details the progress of SC24.

On a global scale, the irregularities of the ionosphere will also be investigated by preparing the ionospheric irregularities maps using ROTI (Rate Of TEC Index) index. Meanwhile, the temporal - latitudinal TEC maps will be established from RINEX (Receiver INdependent EXchange format) or IONEX (IONosphere map Exchange) files to study the occurrence characteristics of EIA crests. These are the next two missions of my research. Besides, during severe conditions, the ionosphere can occur with abnormal and unpredictable states. The specific behaviour of the ionosphere during the intense geomagnetic storms of SC24 will be revealed from the exploitation of this map.

So far, two basic indicators that have been used primarily to study ionospheric scintillation are the S_4 index (obtained directly from the scintillation receivers) and the ROTI index (that can be calculated from the normal GNSS measurements). The correlation between these two indices is of great concern, therefore in this thesis, I will assess the compatibility between them by calculating the correlation coefficients at those stations having both types of data.

In overall, there are seven goals of this PhD project, they include:

- Analysis of TEC variations at seven IGS stations (KUNM, NTUS, BAKO, XMIS, HKSL, CUSV, PIMO) during the 11-year period of solar cycle 24.
- Propose alternative methods to detect scintillation error in the ionosphere from GNSS measurements.
- Study the occurrence characteristics of scintillation activity over the Vietnam area.
- Produce regional and global ionospheric irregularities maps.
- Study the correlation between ROTI and S_4 to show up the ionospheric disturbances during strong geomagnetic storms.
- Produce temporal - latitudinal VTEC maps from RINEX and/or IONEX files.
- Determine the characteristics of peak EIA crest (including time, position and amplitude) at the position of 105^{o}E longitude (Southeast Asia area).

1.1.2. Thesis outline

This thesis consists of 151 official pages excluding other sections, 110 figures, and 18 tables. The thesis is divided into seven chapters and from Chapter 2, at the end of each chapter, there is a section that summarizes the main contents of that chapter. The basic contents and main objectives of the chapters are identified as follows:

- Chapter 1 with 4 headings, 20 pages, 3 figures, and 1 table is the general introductions of the PhD project including the motivation and goals of the research (Section 1.1). After that is the introduction of the ionosphere as one of the layers of the atmosphere (Section 1.2). The main research object of this thesis is the ionospheric scintillation phenomenon will be presented in Section 1.3. And Section 1.4 will introduce other phenomena related to ionospheric turbulence that can affect the quality of electromagnetic wave propagation.

- Chapter 2 consists of 5 headings, 19 pages, 9 figures, and 1 table. The main target of this chapter is to develop a program that can calculate some ionospheric disturbances parameters from GNSS measurements. The content of this chapter is divided as follows: Section 2.1 will summarize the formulas and methods to calculate TEC from GNSS measurements; Section 2.2 will propose alternative methods for detecting ionospheric scintillation error in the GNSS observations; Section 2.3 will introduce and develop a software tool to calculate some basic parameters of the ionosphere like STEC, VTEC,

VTEC gradient, ROT, ROTI, S_4,… Section 2.4 will present some results calculated at two stations POTS and BAHR. Section 2.5 will be the summary of the chapter.

- The next chapter (Chapter 3) comprises 6 headings, 36 pages, 36 figures, and 6 tables. The main research content of this chapter is the temporal variations of TEC over the Southeast Asia region during the period of SC24. The first section of the chapter will give a short introduction of the solar cycle and also the research area, study period and usage data of the PhD project. Section 3.2 to Section 3.4 will respectively take into account the daily, monthly, and annual variations of TEC. Section 3.5 will study on the correlations between TEC results and the solar indices during the study period and the last section will be the summary as usual.

- Chapter 4, just as its name, will study the occurrence characteristics of ionospheric scintillation over Vietnam region. This chapter includes 5 headings, 21 pages, 17 figures, and 3 tables. In particular, the headings are divided as follows: Section 4.1 will introduce the type of equipment used in this chapter including three scintillation receivers (namely GSV4004B) located evenly through the Vietnam region. Section 4.2 will propose a filter formula that can detect and remove multipath error out of the observations obtained from the GSV4004B receiver. Sections 4.3 and 4.4 will, in turn, study the temporal and spatial distributions of ionospheric scintillation.

- Chapter 5 with the creation of regional and global ionospheric irregularities maps, the ROTI index will be primarily used to study the irregularities of the ionosphere over the Southeast Asia region and globally. It is composed of 4 headings, 16 pages, 13 figures, and 3 tables with the following basic contents: Section 5.1 will first put forward some advantages of ROTI index in studying ionospheric scintillation. The following section will establish ionospheric irregularities maps over the Southeast Asia area during the period that the ionosphere is highly disturbed. Meanwhile, in Section 5.3, the spatial and temporal distributions of ionospheric irregularities will be revealed on a global scale for the first time.

- Chapter 6 studies on the EIA covers 4 headings, 30 pages, 32 figures, and 4 tables. Its content is divided as follows: Section 6.1 will introduce the temporal - latitudinal TEC map and the method to study the EIA region. Section 6.2 will investigate the case of the strongest geomagnetic storm in SC24 happened on March 17th 2015. Section 6.3 will

present the temporal - latitudinal (mean monthly) TEC maps over the Southeast Asia region for the period of 2007 - 2017, from that, study the characteristics of seasonal and annual appearance, location and amplitude of EIA crests.

- The last chapter is the summary and conclusions which indicate the new findings and the most significant results of the thesis. Besides, the outlook and further open studies after this thesis are also outlined.

1.2. The ionosphere

1.2.1. The structure of the ionosphere

Concerning the propagation of electromagnetic waves in space, the atmosphere is divided into two main layers including the troposphere and the ionosphere. In which, the ionosphere is the region where the atmosphere is ionised by incoming solar radiation. This layer increases in thickness and moves closer to the Earth during daylight and rises at night allowing certain frequencies of radio communication over a greater range [Solomon et al., 2015]. For space geodetic techniques, the ionosphere has the most potential sources of error for electromagnetic waves travelling from space to receivers placed on the ground (ground-based measurements) or space near the surface of the Earth (space-based measurements). Therefore, it is the object of special interest in this field. The ionosphere is the upper part of Earth's atmosphere between approximately 50 km and 1500 km where sufficient electrons and ions are present to affect the propagation of radio waves. The source of the ionosphere is from the Sun and ionospheric activity is primarily associated with solar activity such as solar wind, solar flares, Coronal Maşs Ejection (CME), coronal holes,... When these solar disturbances are more frequent, it could lead to geomagnetic storms, and then the disturbances in the ionosphere are more frequent. The electron density correlates with several physical properties of the Earth and the Sun, resulting in a strong variability in space and time. The essential characteristic of the ionosphere is the number of Total Electron Content (TEC) which is defined as the integral of the electron density along the ray path between satellite and receiver. By this definition, TEC provides the number of electrons per square meter and it is strongly affected by solar activity. TEC has the unit of TECU with 1 TECU = $1x10^{16}$ electrons/m^2. TEC is significant in determining the scintillation, group and phase delays of a radio wave through a medium. For the propagation of microwave signal, the greater the total number of electrons on the signal path, the greater the time delay [Space Weather Services, Bureau of Meteorology, Australia Government]. According to altitude, the ionosphere is

divided by different layers including D, E, F_1, and F_2 as indicated in Figure 1.1 with each layer has a different number of electron density (as can be seen in Table 1.1). Among them, the F_1-layer located directly below the F_2-layer shows large variations that correlate with the relative Sunspot number [Seeber, 2003].

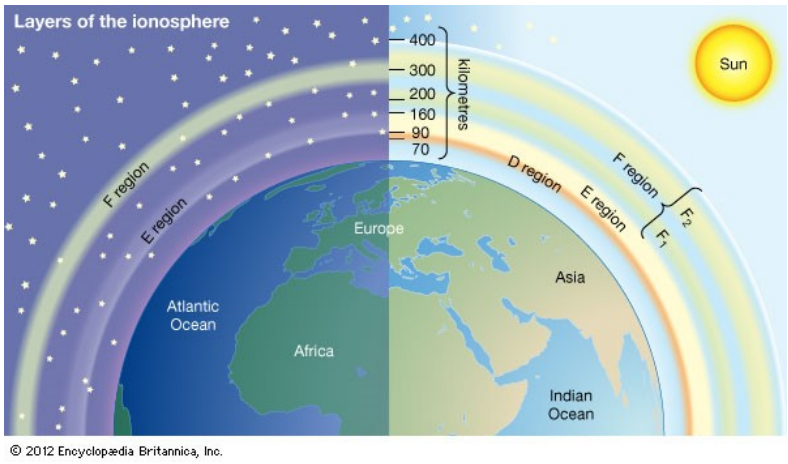

Figure 1.1. Source and the division of layers in the ionosphere

As shown in Figure 1.1, at night the ionosphere consists of only two layers of E and F, while during the daytime, the D layer appears and the F layer divided into two layers of F_1 and F_2. At night, the F layer is the only layer of significant ionization present, while the ionization in the E and D layers is extremely low. During the daytime, the D and E layers become much more heavily ionized, as does the F layer, which develops an additional, weaker region of ionisation known as the F_1 layer. The F_2 layer persists by day and night and is the main region responsible for the refraction and reflection of radio waves [Wikipedia].

Table 1.1. Electron density of the main ionospheric layers [Thomas Hobiger, 2006]

Layer	Extent	Electron density (electrons / m^3)
D	60 - 95 km	10^8 - 10^{10}
E	55 - 150 km	several 10^{11}
F_1	160 - 180 km	several 10^{11} - 10^{12}
F_2	max. around 300 km	up to several 10^{12}

1.2.2. The variations of the ionosphere

Since the ionosphere is ionized by solar radiation, its modifications are somewhat similar to the temperature and indeed, on a global scale, the electron density of the ionosphere is the greatest in summer, at noon and over the equator. Nonetheless, the variability of the ionosphere is not only that, due to the EUV radiation, that follows the solar cycle, the

ionosphere varies much more than this. The variation of the ionosphere depends on geographic location, time, Earth's magnetic field and is driven by the 11-year solar cycle (including solar activities, solar rotation, solar wind, and ionospheric storm). For the signal propagation point of view, the characteristics of the ionosphere also depend on the operating frequency. The variations of the ionosphere can be divided by temporal and spatial variations. The temporal variations of the ionosphere can be classified by diurnal, seasonal, and annual variations. Meanwhile, the spatial variations comprise vertical structure and latitudinal variations. Vertical structure including different layers such as D, E, F_1, and F_2 as presented earlier. Latitudinal variations are due to the effect of the solar zenith angle (as with the seasonal variations) and its influence is often divided by different latitude regions including equatorial region, mid-latitude region, and high-latitude region. Basic characteristics of the variations of the ionosphere can be briefly summarized as follows:

Diurnal variation: as the air temperature varies following the 24-hour cycle, this variation occurs throughout the day, following the apparent movement of the Sun. It affects the D, E and F_1 layers depending on the solar activity, and the solar zenith angle over the location. As the E layer is often considered to vanish at night, it has little effect on radio transmission. Meanwhile, the F_2-layer variation is the most complex, because of its day and night survival characteristics as well as its highest electron density compared to the other layers of the ionosphere.

Seasonal variation: in winter, the Sun is always lower over the horizon than in summer. This affects the critical frequencies of the D, E and F_1-layers, that is greater in summer than in winter. But this is the opposite for the F_2-layer at mid-latitudes, which shows a greater variation in winter. This difference is known as the "mid-latitude seasonal anomaly" [Rishbeth, 2000].

Annual variation: depends heavily on the solar cycle. The ionosphere is often highly volatile during years of high solar activity and less during years of weak solar activity. Its long-term behaviours are highly consistent with the solar indices such as the sunspot number (SSN index) or the radio flux index F10.7 cm. From geodetic viewpoint, the variations of the ionosphere can be investigated by the variations of TEC. This issue will be specifically studied in Chapter 3 when considering the temporal variations of TEC over the South East Asia region.

For latitudinal variations, the size and variability of electron density are largest in equatorial and polar regions. In mid-latitudes, the ionosphere is the least variable and electron density only fluctuates rapidly during geomagnetic storms. Usually, equatorial region can be characterized by the highest values of TEC and the peak electron density with the most pronounced amplitude and phase scintillation effects. One of the basic physical characteristics of this region is the fountain effect which is the combined effect of the high radiation level from the Sun, the electric and the magnetic fields of the Earth. These effects cause the electrons rising and moving along the horizontal lines of the magnetic field. The electrons travel as far as the geomagnetic latitudes of about 10^o to 20^o causing the high concentration of electrons, thus this region is often called equatorial anomalies. In this area, scintillation effect often has its greatest amplitude.

1.2.3. Effects of the ionosphere on the propagation of electromagnetic waves

As introduced in the previous sections, the ionosphere is an electromagnetic wave dispersion medium leading to signals being transmitted through this medium are delayed in both group and phase observations. The error due to the effect of the ionosphere on electromagnetic wave transmission is one of the most fundamental and significant sources of error and this error needs to be considered carefully when applying space geodetic techniques. In this section, background knowledge of microwave signal propagation is presented in order to comprehend the problem of ionospheric delay in space geodesy.

1.2.3.1. Phase and group velocity

Consider a single electromagnetic wave propagating in space with wavelength λ and frequency *f*. The velocity of its phase is then [Wells, 1974]:

$$v_{ph} = \lambda x f \tag{1.1}$$

with v_{ph} is denoted as phase velocity. For GNSS, the carrier waves *L1* and *L2* are propagating with this velocity. For a group of waves with slightly different frequencies, the propagation of the resultant energy is defined by the group velocity [Hofman-Wellenhof et al., 2000]:

$$v_{gr} = -\frac{df}{d\lambda} x \lambda^2 \tag{1.2}$$

This velocity has to be considered for GNSSS code measurement. The relation between phase and group velocity [Alizadeh et al., 2013] is:

$$v_{gr} = v_{ph} - \lambda \frac{dv_{ph}}{d\lambda} \tag{1.3}$$

Note that phase and group velocity are equal in non-dispersive media and correspond to the speed of light in vacuum (c). The wave propagation in a medium depends on the refractive index (n). Generally, the propagation velocity is obtained from:

$$v = \frac{c}{n} \tag{1.4}$$

Applying this expression to the phase and group velocity, we get appropriate formulas for the corresponding refractive indices n_{ph} and n_{gr}:

$$v_{ph} = \frac{c}{n_{ph}} \qquad v_{gr} = \frac{c}{n_{gr}} \tag{1.5}$$

From that, we find out the modified Rayleigh equation as follows:

$$n_{gr} = n_{ph} - \lambda \frac{dn_{ph}}{d\lambda} \tag{1.6}$$

A slightly different form is obtained by differentiating the relation $c=\lambda.f$ with respect to λ and f, that is:

$$\frac{d\lambda}{\lambda} = -\frac{df}{f} \tag{1.7}$$

By substituting the result into (1.6) we have:

$$n_{gr} = n_{ph} + f \frac{dn_{ph}}{df} \tag{1.8}$$

To the effect due to the ionosphere, when N_e increases, the group velocity slows down and the phase velocity speeds up to keep their product a constant.

1.2.3.2. Ionospheric refraction

Following [Seeber, 1993] the refractive index n_{ph} can be described as a series as follows:

$$n_{ph} = 1 + \frac{c_2}{f^2} + \frac{c_3}{f^3} + \frac{c_4}{f^4} + \cdots \tag{1.9}$$

Therein, the coefficients c_2, c_3, c_4,… do not depend on frequency but the quantity N_e denoting electron density or the number of electrons per cubic meters along the propagation path. We use an approximation by cutting off the series expansion after the quadratic term:

$$n_{ph} = 1 + \frac{c_2}{f^2} \tag{1.10}$$

differentiating this equation:

$$dn_{ph} = -\frac{2c_2}{f^3} df \tag{1.11}$$

By substituting equations (1.10) and (1.11) into equation (1.8) we obtain:

$$n_{gr} = 1 - \frac{c_2}{f^2} \tag{1.12}$$

It can be seen that from equations (1.10) and (1.12), the group and phase refractive indices deviate from unity with opposite sign. With an estimation of c_2 [Seeber, 1993] as:

$$c_2 = -40.3 \times N_e \ [Hz^2] \tag{1.13}$$

From that, we gain the group refractive index:

$$n_{gr}^{ion} = 1 + 40.3\frac{N_e}{f^2} \tag{1.14}$$

and phase refractive index:

$$n_{ph}^{ion} = 1 - 40.3\frac{N_e}{f^2} \tag{1.15}$$

The relation $n_{gr} > n_{ph}$ and thus $v_{gr} < v_{ph}$ follows because the electron density N_e is always a positive number. As a consequence of the different velocities, a group delay and a phase advance occur. In other words, GNSS code measurements are delayed and the carrier phases are advanced. Therefore, the code pseudo-ranges measured are longer and the carrier phase pseudo-ranges measured are shorter compared to the geometric distance between the satellite and the receiver. However, the amount of the difference is the same in both cases [Holfmann-Wellenhof et al., 1993].

The first order refractive index only accounts for the electron density within the ionosphere, while the effect of the Earth's magnetic field and its interactions with the ionosphere are considered in higher-order terms. For precise satellite positioning, these terms have to be considered as they may produce an ionospheric delay error of up to a few centimetres [Brunner and Gu, 1991; Bassiri and Hajj, 1993].

1.2.3.3. Ionospheric time delay and phase lead

According to Fermat's principle [Born and Wolf, 1964], the measured range s is defined by:

$$s = \int n ds \tag{1.16}$$

where the integration is performed along the path of the signal. The geometric distance s_0 between the satellite and the receiver may be obtained analogously by setting n=1:

$$s_0 = \int ds_0 \tag{1.17}$$

The delay (or advance) experienced by signals travelling through the ionosphere is the difference between the measured and geometric range. This is called the ionosphere delay or ionospheric refraction:

$$\Delta\rho^{ion} = \int n ds - \int ds_0 \tag{1.18}$$

In the first-order approximation, the ionospheric delay for phase measurements is:

$$\Delta\rho_{ph}^{ion1} = -\frac{40.3}{f^2}\int N_e ds_0 \tag{1.19}$$

and the group delay is:

$$\Delta\rho_{gr}^{ion1} = \frac{40.3}{f^2}\int N_e ds_0 \tag{1.20}$$

Actuality, ionospheric delay still contains the second and the third-order delays but they are not mentioned here. As an essential, the first, second and third orders of ionospheric delays require the distribution of the electron density (N_e) along the ray path. The integral of the electron density along the ray path is defined as TEC and it represents the total amount of free electrons in a cylinder with a cross-section of one square meter [Schaer, 1999]. TEC is measured in Total Electron Content Unit (TECU) with 1 TECU equivalents to 10^{16} electron/m^2. For an arbitrary ray path, the slant TEC (STEC) can be obtained from:

$$STEC = \int N_e(s)ds \tag{1.21}$$

where N_e is the electron density along with the light of sight (ds).

Using equation (1.21), the relation between the total electron content in TECU and ionospheric delay in meters can be obtained. Taking equation (1.19) into account for the carrier phase measurements we acquire:

$$\Delta\rho_{ph}^{ion} = -\frac{40.3}{f^2}STEC \quad [\text{m}] \tag{1.22}$$

in the case of group delay measurements, the result is the same, but with the opposite sign:

$$\Delta\rho_{gr}^{ion} = \frac{40.3}{f^2}STEC \quad [\text{m}] \tag{1.23}$$

The ionospheric path delay in meters per one TECU, related to a certain frequency (f) in HZ:

$$\vartheta = \frac{40.3.10^{16}}{f^2} \text{ [m/TECU]} \tag{1.24}$$

In actual use, TEC along the vertical at the given location should be taken into account. Since GNSS basically provides measurements of STEC, an elevation-dependent mapping function is required which describes the ratio between the STEC and the vertical TEC (VTEC). This mapping function is necessary to convert from STEC to the corresponding VTEC, its specific formula will be presented in Section 2.1.3.

1.2.3.4. Dealing with ionospheric delay

From the signal frequency dependence, the use of dual-frequency measurements can eliminate the effect of ionospheric delay by more than 99.9% [Navipedia]. In the case of using single-frequency receivers, this error can theoretically reach up to dozens of meters [Rovira-Garcia, 2020], so we have to apply an ionospheric prediction model. One of the most popular models is Klobuchar which can correct about 50% of ionospheric delay [Navipedia]. The most important parameter of the ionosphere affecting GNSS signal is TEC. It can be derived from equations (1.22) or (1.23). So far, there are different ways to handle ionosphere delays, they can be listed as follows from [Alizadeh et al., 2012]:

- Modelling TEC using physical and empirical models such as:

  - Klobuchar model
  - NeQuick model
  - IRI (International Reference Ionosphere) model
  - GAIM (Global Assimilative Ionospheric Model) model
  - MIDAS (Multi-Instrument Data Analysis System) model
- Eliminating the effect of TEC including:
  - Eliminating first order of ionospheric effects in GNSS measurements
  - Eliminating higher-order of ionospheric effects in GNSS measurements
  - Using multi-frequency observations
  - Using the VLBI technique
- Estimating TEC using different space geodetic techniques:
  - Determining TEC from GNSS observations
  - Obtaining TEC from satellite altimetry measurements
  - Estimating TEC from LEO satellite data
  - Determining ionospheric parameters from VLBI data
  - Acquiring ionospheric information from DORIS
  - Combination of different space geodetic techniques.

1.3. Ionospheric scintillation phenomena

The ionosphere is a complex and highly variable physical system, therein the F-layer contains the greatest concentration of free electrons. When this layer becomes disturbed and the small-scale irregularities develop, it will disperse radio waves and generate rapid fluctuations in the amplitude and phase of radio signals. Amplitude scintillation as a short-term fading can be so severe that signal levels drop below a GNSS receiver's lock threshold, meanwhile, phase scintillation which is characterized by rapid carrier-phase changes can produce cycle slips and sometimes challenge a receiver's ability to hold a lock on the signal. As mentioned in Section 1.1.1, unlike ionospheric delay, the impacts of scintillation cannot be mitigated by the dual-frequency technique. For these reasons, it is one of the most significant threats for space geodetic techniques, especially for stations operating in the areas near the equator or the polar regions.

To determine the impacts of ionospheric scintillation on space geodetic techniques, it is important to clearly understand the location, magnitude and frequency of occurrence of scintillation effects. Scintillation activity is most severe and frequent in and around the

equatorial regions, particularly in the hours just after sunset. In high latitude regions, scintillation is frequent but less severe in magnitude than that of the equatorial regions. Scintillation is rarely experienced in the mid-latitude regions, nonetheless, during the intense geomagnetic storms, ionospheric scintillation can occur suddenly at any time of the day and lead to the risk of declining accuracy for all applications of space geodetic techniques [SBAS Ionospheric Working Group]. In this section, some basic features of ionospheric scintillation such as definition, classification, global appearance characteristics, level of influence on electromagnetic waves, and ionospheric scintillation models will be presented in turn. Methods to detect ionospheric scintillation errors will be introduced in Chapter 2.

1.3.1. Definition of ionospheric scintillation

Ionospheric scintillation is defined as a relatively rapid fluctuation of the amplitude-phase of the radio signal and is mostly caused by irregularities in the ionosphere electron density along the path that the signal propagates [Space Weather Services, Bureau of Meteorology, Australia Government]. The irregularities cause small-scale fluctuations in refractive index and as the signal propagation continues after passing through the region of irregularities, phase and amplitude scintillation develops through the interference of multiple scattered signals. So far, ionospheric scintillation is a well-known phenomenon that has been studied extensively for many decades, major research on ionospheric scintillation can be found in the references, typical studies can be mentioned here include [Aarons, 1982, 1993, 1995; Basu et al., 1988; Pi et al., 1997;…].

The main cause of ionospheric scintillation is the turbulences in the F-region of the ionosphere. With the highest concentration of free electrons in this region and also being the layer that most directly and strongly affected by solar radiation, free electrons in this layer are easily disturbed under severe ionospheric conditions such as magnetic storms, high solar activity,…. When these free electrons got disturbed, it creates small-scale irregularities resulting in the rapid fluctuations of TEC. In fact, E-layer irregularities such as sporadic-E and auroral E can also produce scintillation, but their effect is minimal, especially on L-band GNSS signals [Space Weather Services, Bureau of Meteorology, Australia Government].

1.3.2. Classification of ionospheric scintillation

Conventionally, ionospheric scintillation is classified by three types: amplitude scintillation, denoted by S_4 index; phase scintillation, denoted by σ_φ index; and polarization scintillation.

Amplitude scintillation is the standard deviation of the signal intensity divided by the average of the signal intensity for a given period of time [Luo et al., 2020]:

$$S_4 = \frac{\sqrt{<I^2> - <I>^2}}{<I>} \quad (1.25)$$

where I is the signal intensity and $<I>$ represents the average of the signal intensity for a given interval of time. S_4 is a dimensionless number with a theoretical upper limit of 1.0, commonly estimated over an interval of 60 seconds for high-rate GNSS data. For lower sampling rate data, it can be calculated with a larger interval (5 minutes for instance).

Amplitude scintillation is classified by intensity as follows: $S_4 = 0$: nonexistent; $S_4 < 0.3$: weak scintillation (does not affect the signal); $0.3 \leq S_4 \leq 0.6$: moderate scintillation (affect the signal); and $S_4 > 0.6$: strong scintillation (strongly affect the signal).

Meanwhile, phase scintillation is quantified by σ_φ index which is defined as the standard deviation of the signal phase over a given time interval. This index is computed empirically and measured either in radians or degrees. A σ_φ greater than 1° is considered to be strong scintillation. At mid-latitudes, σ_φ rarely exceeds 1° for more than 1% of the time [Space Weather Services, Bureau of Meteorology, Australia Government].

1.3.3. Worldwide characteristics of ionospheric scintillation

1.3.3.1. Equatorial and low-latitude scintillations

Figure 1.2 shows a map indicating how scintillation behaviour varies by geographic location. The regions located around 15° north and south of the magnetic equator (the red areas) are referred to as the equatorial anomaly. Since the ionosphere is the densest and the thickest in two bands surrounding the magnetic equator, these regions experience the most significant activity including deep signal fades that can cause GNSS receivers to lose track of satellite signals [Kintner et al., 2009]. The yellow areas in the middle (including the area between the two red bands and the areas immediately adjacent to the anomaly lines) have a less intense of scintillation. Although the Sun shines above the equator, ionization still achieves its maximum density away from the equator. This is because of the combination of electric and magnetic fields. During this combination process, the free electrons to be lifted vertically and then diffuse northward and southward leading to reduce the ionization directly over the magnetic equator and increase the ionization over the anomaly regions [Balan et al., 2018]. This explains why scintillation is more intense in the anomaly regions than at the magnetic

equator. In these regions, ionospheric scintillation can occur abruptly after sunset, with rapid and deep fading lasting up to several hours until local midnight. After midnight, the level of ionization in the ionosphere is too low to support scintillation at GNSS frequencies.

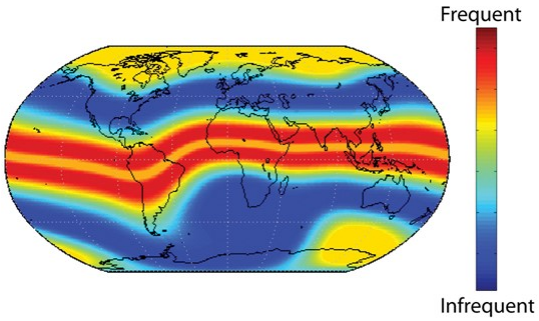

Figure 1.2. Global distribution characteristics of ionospheric scintillation [Kintner et al., 2009]

1.3.3.2. Mid-latitude scintillations

In the mid-latitude regions (shown in blue), scintillation activity is rare even during periods of high solar activity. It occurs only in response to extreme levels of ionospheric storms. During intense geomagnetic storms, the mid-latitude ionosphere can be strongly disturbed. Also in this time, the auroral oval extends towards the equator and the anomaly regions may extend towards the poles [Grodent et al., 2008]. These phenomena can cause ionospheric scintillation to be extended and increase the influences in these areas.

1.3.3.3. High-latitude scintillations

The occurrence of scintillation at auroral latitudes (the yellow areas in the north and south poles) is strongly dependent on geomagnetic activity levels, but can occur in all seasons and is not limited to local nighttime hours as the equatorial anomaly (refer to as of Figure 5.8b). In the high-latitude regions, the ionization density is less than that in the equatorial regions but the irregularities move at speeds up to ten times larger [(1.1)]. This means that larger sized structures in the polar ionosphere can create phase scintillation and that the magnitude of the phase scintillation can be much stronger. Large and rapid phase variations at high latitudes will cause a doppler shift in the GNSS signals which may exceed the phase lock loop bandwidth, resulting in a loss of lock and an outage in GNSS receivers [Kintner et al., 2007]. This is the reason why phase signal is more common in high-latitude regions than equatorial regions.

1.3.4. Impacts of ionospheric scintillation

The impacts of ionospheric scintillation can be divided into effects by amplitude and phase effects. Specifically as follows:

Amplitude scintillation directly affects the signal to noise ratio (C/No) of satellite radio signals, as well as the noise levels in code and phase measurements. During scintillation activity, the ionosphere does not absorb the microwave signal. Instead, the irregularities in the index of refraction scatter the signal in random directions. As the signal continues to propagate down to the Earth's surface, small changes in the distance of propagation along the scattered ray-paths cause the signal to interfere with itself, alternately attenuating or reinforcing the signal measured by the receiver. For space geodetic techniques, amplitude scintillation can be sufficiently severe that can make the signal strength drop below the level of the receiver needs and hence the need to re-acquire the signals. This will also cause a loss clock or even cycle slips in the signal and then degrade the quantity of positioning or reduced accuracy navigation solutions. The nominal C/No for the L1 signal is about 45dB-Hz, and tracking may be lost when the signal drops below ~25dB-Hz, but it is also dependent on the ability of the tracking loop of the receiver. Since the signal power on the GNSS L2 frequency is significantly less than that of L1 (~6dB lower), ionospheric scintillation is much more likely to impact the L2 signal than the L1 signal [Space Weather Services, Bureau of Meteorology, Australia Government].

Meanwhile for phase scintillation, if sufficiently severe, may stress phase-lock loops in GNSS receivers resulting in a loss of lock. Phase scintillation describes rapid fluctuations in the observed carrier phase obtained from the receiver’s phase lock loop. These same irregularities can cause increased phase noise, cycle slips, and even loss of lock if the phase fluctuations are too rapid for the receiver to track.

In the severely ionospheric conditions, scintillation errors can be as large as hundred meters [Kintner et al., 2007]. In principle, the lower signal frequencies, the more significant ionospheric scintillation effects [Guo et al., 2019]. Therefore, the effects of ionospheric scintillation on VLBI technique are usually smaller than that of GNSS technique because VLBI data are measured at higher frequencies (8.4 and 2.3 GHz) compared to GNSS measurements (1.2 - 1.6 GHz).

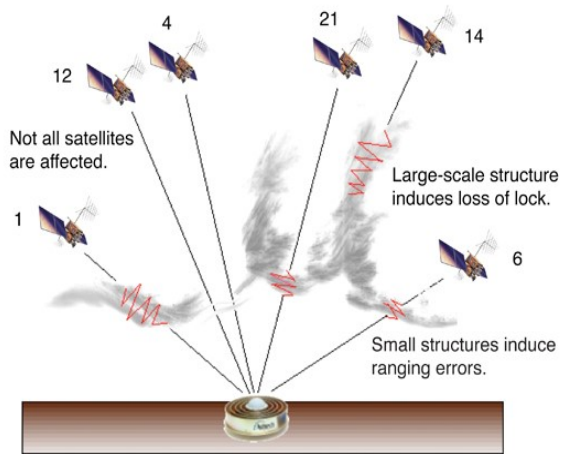

Figure 1.3. The effect of ionospheric scintillation on GNSS signals. Due to the patchy nature of irregularity structures, not all satellites (PRN 12 and 4 in this case) are affected simultaneously at the moment ionospheric scintillation occurs. Large-scale structures cause significant variation in ionospheric delay and loss of lock on the signal (PRN 14). Small-scale structures are less likely to cause loss of the signal but still can affect the integrity of the signal by producing ranging errors (PRN 1, 21, 6).

1.3.5. Ionospheric scintillation models

In the previous sections, some basic characteristics of ionospheric scintillation have been introduced. As its key sources are plasma instabilities, the variations of scintillation depend on the complex physical properties of the ionosphere. Thus, it is not easy to model scintillation activity on a large scale. In principle, ionospheric scintillation models represent the ionosphere fluctuations and scintillation activity under different geophysical conditions and they can be established from theoretical or empirical models. Currently, a couple of ionospheric scintillation models are widely used as follows:

- The Wide Band Model (WBMOD, USA, 2005): using experimental data to describe a worldwide climate of ionosphere plasma density irregularities. This model predicts both amplitude and phase scintillation.
- The Global Ionospheric Scintillation Model (GISM, France, 2007): provides the statistical characteristics of the transmitted signals. This model also predicts both amplitude and phase scintillation.
- The Ionospheric Scintillation (IONSCINT – G, USA): provides dynamic scenarios to simulate scintillation impacts. This model predicts only amplitude scintillation.

[1.1] https://www.gpsworld.com/gnss-systemsignal-processinginnovation-ionospheric-scintillations-12809/

1.4. Other ionospheric disturbances

1.4.1. Travelling ionospheric disturbance

Besides the influence of the Earth and the Sun, the variation of the ionosphere also has another factor which called Traveling Ionospheric Disturbance (TID). TID is among the Earth's ionosphere irregularities and it represents wave-like electron density structures propagating in the ionosphere. The motion of TID modulates the electron density distribution in space. It leads to a modification of plasma parameters, namely the refractive index, and affects the propagation of radio waves [Koval and Cesra, 2019]. This disturbance is one of the most common ionospheric phenomena that contribute to the disturbances in the ionosphere. Based on the characteristics of the period, velocity, source and spatial distribution, TID can be classified into two main categories: medium scale and large scale. Medium-scale TID has periods of less than one hour and large-scale TID has periods of over one hour and its main source are the geomagnetic disturbances. Usually, large-scale TID starts at high latitude areas but during geomagnetic storms, it can spread to lower latitudes.

1.4.2. Sudden ionospheric disturbance

Sudden Ionospheric Disturbance (SID) is a kind of disturbance in the ionospheric electron density, resulting from abnormally high ionization or plasma density and caused by a solar flare and/or solar particle event. SID can last from a few minutes to several hours and it is mainly due to the increased level of ionization in the D layer of the ionosphere [Moral et al., 2013]. The SID results in a sudden increase in radio-wave absorption that is most severe in the upper medium-frequency and lower high-frequency ranges, and as a result, often interrupts or interferes with telecommunications systems.

1.4.3. Ionospheric storm

Ionospheric storms are triggered by the enhanced flux of energetic electrons that are emitted at a large level by the Sun. Solar activity such as solar flares and coronal mass ejections (CME) often produce large variations in the particle and electromagnetic radiation incident upon the Earth. Such variations can lead to disturbances in the ionosphere. These disturbances, when affecting the ionosphere are known as ionospheric storms. They tend to generate large disturbances in ionospheric density distribution, total electron content, and the ionospheric current system [1.2]. Ionospheric storms can be caused by intense solar eruptions hurling out energetic particles also known as solar flares. It can endanger astronauts and

destroy satellite electronics. Ionospheric storms have important terrestrial consequences such as disrupting satellite communications and interrupting the flow of electrical energy over power grids.

1.4.4. Geomagnetic storm

Geomagnetic storm also called magnetic storm or solar storm is a major disturbance of Earth's magnetosphere that occurs when there is a very efficient exchange of energy from the solar wind into the space environment surrounding Earth. It usually occurs in conjunction with ionospheric storms and can be caused by solar flares and high-speed solar wind stream (coronal holes). The storms are usually associated with increased electron densities in the lower ionosphere and a simultaneous increase in absorption of radio waves. A geomagnetic storm usually starts with an increase in the earth's geomagnetic field intensity called the initial phase followed by a large decrease termed the main phase. In principle, it is impossible to predict precisely when a geomagnetic storm will occur, but scientists can predict when a CME or high-speed solar wind stream will sweep past Earth's magnetic field which creates the conditions that cause geomagnetic storms. Conventionally, there are five categories of geomagnetic storms including minor (G1), moderate (G2), strong (G3), severe (G4), and extreme (G5) levels. For space geodesy, during a geomagnetic storm, satellite signals can be scintillated, this results in a loss of observations or reduce the accuracy of the final results.

1.4.5. Solar wind

The solar wind is a stream of charged particles released from the upper atmosphere of the Sun. This also causing variability in electron density when continuous ejection of high energetic particles from the Sun penetrates the Earth's atmosphere and interferes with its magnetic field. The ejection of energetic particles from the Sun is enormously increasing due to solar flares and CME called ionospheric storms. This could lead to disturbances in the ionosphere and the electron density very quickly changes.

1.4.6. Effect of the Moon

Another factor that can affect the perturbation of the ionosphere is the revolution of the Moon. During the period that the Moon circles around the Earth (approximately 14.77 days), the atmospheric pressure of the Earth varies causing ionospheric disruptions. This phenomenon is normally called lunar gravitational tides.

[1.2] https://iono.jpl.nasa.gov/storm.html

2. Calculation of ionospheric disturbances parameters from GNSS measurements

2.1. TEC estimation from dual-frequency GNSS observations

Ionospheric delay, which is proportional to the Total Electron Content (TEC) along the propagation path, is one of the largest error in signal propagation. As discussed in Chapter 1, TEC is a key parameter in the mitigation of ionospheric effects and it can be derived from satellite geodetic measurements. So far, it is one of the most essential methods of investigating the Earth's ionosphere. TEC measurements are the total amount of free electrons along the line of sight (LOS) from satellites to receivers located on or near the Earth surface. In general, there are three techniques for measuring TEC including ionospheric soundings, radar technique, and using space geodetic techniques. Hitherto, there are two main approaches commonly used: [Smith, 1987] with the single-frequency method and [Warrant, 1996] with the dual-frequency method. Among them, the two-frequency method is the most efficient to determine TEC [Taoufiq et al., 2018]. GNSS satellites transmit electromagnetic waves on multiple frequencies allowing receivers equipped with a dual-frequency operation to be used. This enables us to extract the ionosphere TEC from GNSS observations. For decades, the method of TEC calculation from GNSS data has been extensively studied in many publications [Hofman-Wellenhof et al., 2000; Jakowski et al., 2011; Alizadeh et al., 2011; Adewale et al., 2012; Le Huy Minh et al., 2013;…].

2.1.1. STEC from code pseudo-range

For the calculation of TEC from GNSS observation files, I start with the pseudo-range measurements on the L1 and L2 frequencies. The pseudo-range is the geometric distance from the receiver's antenna to the satellite, plus other errors, such as clock offsets and atmospheric delays. To extract TEC, the pseudo-range can be divided into five components: the real range, the error due to the ionosphere, the error due to the satellite and receiver hardware delays, the error due to the troposphere and the error due to other factors. Following [Schaer, 1999], taking the fundamental equation for code pseudo-range at each frequency into account:

$$P_i^k(L1) = \rho_i^k + \Delta\rho_{i,ion}^k(L1) + c(\Delta t_i - \Delta t^k) + c(b^k + b_i)_{L1} + \Delta\rho_{i,trop}^k + \varepsilon_{L1} \quad (2.1a)$$

$$P_i^k(L2) = \rho_i^k + \Delta\rho_{i,ion}^k(L2) + c(\Delta t_i - \Delta t^k) + c(b^k + b_i)_{L2} + \Delta\rho_{i,trop}^k + \varepsilon_{L2} \quad (2.1b)$$

where $P_i^k(L1)$ and $P_i^k(L2)$ are the code pseudo-range; ρ_i^k is the geometric distance between the receiver *(i)* and the respective satellite *(k)*; c is the speed of light in the vacuum environment (c=299792458 m/s); $\Delta t_i, \Delta t^k$ are the receiver and satellite clock offsets concerning GPS time; $\Delta\rho_{i,trop}^k$ and $\rho_{i,ion}^k$ are the delay due to the troposphere and the ionosphere respectively; b^k and b_i are the satellite and receiver hardware delays expressed in units of time; and finally ε_{L1}, ε_{L2} indicate the random errors in the L1 and L2 frequencies.

By subtracting observations in equation (2.1) at simultaneous epochs, all frequency-independent effects such as clock errors and tropospheric delays are removed and the new observable is obtained, which contains only the ionosphere refraction and the inter-frequency hardware biases Δb^k and Δb_i, denoted as differential code biases (DCBs). The new equation is called the geometry-free linear combination [Alizadeh, 2011]:

$$P_{i,4}^k = P_{i,L1}^k - P_{i,L2}^k = \xi_4 \mathrm{x} \xi_E \mathrm{x} STEC_i^k + c(\Delta b^k - \Delta b_i) \qquad (2.2)$$

where STEC is the Slant Total Electron Content (unit TECU, 1 TECU = 10^{16} electron/m^2) along the ray-path from satellite to receiver. Note that STEC is not computed exactly at the receiver but at the so-called Ionospheric Pierce Point (IPP, see Figure 2.1). $\Delta b^k, \Delta b_i$ are the satellite and receiver DCBs respectively. $\xi_4 \approx -0.647$ and $\xi_E \approx 0.162$ m/TECU are factors that convert the ionospheric delay in L_4 to L_1.

From equation (2.2), it can be seen, that STEC is linearly proportional to the pseudo-range difference and DCBs. DCBs are the systematic errors between two GNSS code observations at the same or different frequencies, its values are described in nanoseconds and can be obtained from the IONEX (IONosphere map EXchange) file [(2.1)] or the website of GNSS Calendar And Utility [(2.2)]. Typically, a value of DCB represents one receiver or one satellite in one day. STEC can be calculated from GNSS measurements after correcting the effect of DCBs. In RINEX (Receiver INdependent EXchange format) files, in case there is no P1 and P2 observations, the C1 and C2 observations can be used instead.

2.1.2. STEC from smooth pseudo-range

Fundamentally, STEC can be calculated from the pseudo-range difference by code (code-derived STEC) or phase (carrier phase-derived TEC) observables. Usually, the code pseudo-range has the problem of being noisy and less accurate compared to the phase pseudo-range, meanwhile, the phase pseudo-range has the problem of resolving the ambiguity term. Using

code pseudo-range to directly derive absolute STEC estimate with an accuracy of about 1 - 5 TECU [Liu et al., 2005]. Hence, to take possession of the advantages of each fundamental observables, the phase-smoothed code pseudo-range should be used, this combination will reduce the noise of the code pseudo-range and eliminate the ambiguity of phase measurements. However, the key problem of this combination is to address the existence of integer phase ambiguity in carrier phase measurements. So far, the method of using carrier phase to smooth code-derived STEC has been carried out in two main approaches: the first approach is to perform the smoothing on raw GNSS measurements and then use the smoothed data to estimate STEC [Hatch, 1982; Lachapelle et al., 1986; Liu and Gao, 2001)]. The second approach extracts STEC directly from raw GNSS measurements and then smooth the derived TEC data [Skone, 1998; Liu, 2004]. Compared to un-smoothed STEC data (i.e. derived directly from GNSS code pseudo-range), the smoothed TEC data have an improvement of a few TECU in precision. [Liu et al., 2005] suggested the second smoothing approach should be used to derive the smoothed STEC from dual-frequency GNSS measurements, particularly when only a short period of data are available for smoothing. The STEC obtained from the smoothed pseudo-range is usually called levelled STEC. It is considered to be more pertinent than STEC computed from only code measurements. The algorithms for smoothing code pseudo-range can be found in [Hofmann-Wellenhof et al., 2000] or [Alizadeh, 2013]. [Hatch, 1982] provided a simple algorithm (also known as the Hatch filter) as follows:

Suppose R(s;n) and Φ(s;n) are the code and carrier measurement of a given satellite s at the time n. Then, the smoothed code $\hat{R}$(s;n) can be computed as:

$$\hat{R}(s;k) = \frac{1}{n}R(s;k) + \frac{n-1}{n}\left[\hat{R}(s;k-1) + (\Phi(\mathrm{s;k}) - \Phi(\mathrm{s;k-1}))\right] \qquad (2.2a)$$

therein, the algorithm is initialized with: $\hat{R}(s;1) = R(s;1)$ where n=k when k<N and n=N when k≥N. It should be noted that, this algorithm must be initialised every time that a carrier phase cycle-slip occurs. This algorithm can be interpreted as a real-time alignment of the carrier phase to the code measurement. That is:

[2.1] ftp://cddis.gsfc.nasa.gov/pub/gps/products/ionex/

[2.2] http://www.gnsscalendar.com/

$$\hat{R}(k) = \frac{1}{n}R(k) + \frac{n-1}{n}\left[\hat{R}(k-1) + \left(\Phi(\mathrm{k}) - \Phi(\mathrm{k}-1)\right)\right]$$

$$= \Phi(\mathrm{k}) + \frac{n-1}{n}\left[\hat{R}(k-1) - \Phi(\mathrm{k}-1)\right] + \frac{1}{n}[R(k) - \Phi(\mathrm{k})]$$

$$= \Phi(\mathrm{k}) + \frac{n-1}{n}\langle R - \Phi\rangle_{(k-1)} + \frac{1}{n}[R(k) - \Phi(\mathrm{k})]$$

$$= \Phi(\mathrm{k}) + \langle R - \Phi\rangle_{(k)} \qquad (2.2b)$$

where the mean bias $\langle R - \Phi\rangle$ between the code and carrier phase is estimated in real-time and used to align the carrier phase with the code.

2.1.3. Converting STEC to VTEC using a mapping function

For decades, many studies have developed techniques to derive absolute ray-path TEC by the processes of detecting and correcting cycle slip, levelling carrier-phase to pseudo-range observations, reducing multipath effect and estimating DCB [Blewitt, 1990; Sardo´n et al., 1994; Mannucci et al., 1998; Schaer, 1999; Syndergaard, 2002; Yue et al., 2011, …]. By simplifying electron density distribution into a geometric model, an obliquity factor called mapping function is often adopted to convert slant TEC (STEC) to equivalent vertical TEC (VTEC), which is more convenient for describing the overall ionization of the ionosphere [Klobuchar, 1987; Zhong et al., 2015]. The STEC values can be approximated into the equivalent vertical TEC by assuming a thin-shell ionosphere at a height from 350 to 500 km. To do so, an elevation-dependent mapping function is required. This function describes the ratio between STEC and VTEC:

$$F(z) = \frac{STEC}{VTEC} \qquad (2.3)$$

To obtain an approximation, a single-layer model (SLM) is usually adopted. In SLM, it is assumed that all free electrons are concentrated in an infinitesimally thin layer above the Earth's surface [Schaer, 1999]. The height (H) of that shell is slightly above the height where the highest electron density is expected (approximately above the height of the F_2-layer). Figure 2.1 depicts the basic geometry of the SLM in the Sun-fixed coordinate system. The signal transmitted from the satellite to the receiver crosses the ionospheric shell in the so-called Ionospheric Pierce Point (IPP). The zenith angle at the IPP is *z'* and the signal arrives at the ground station with zenith angle *z*. The relation between *z* and *z'*:

$$\sin(z') = \frac{R}{R+H}\sin(z) \tag{2.4}$$

where R is the mean Earth radius (usually accepted by 6371 km), and H is the mean height of the SLM or the ionosphere shell expressed in km.

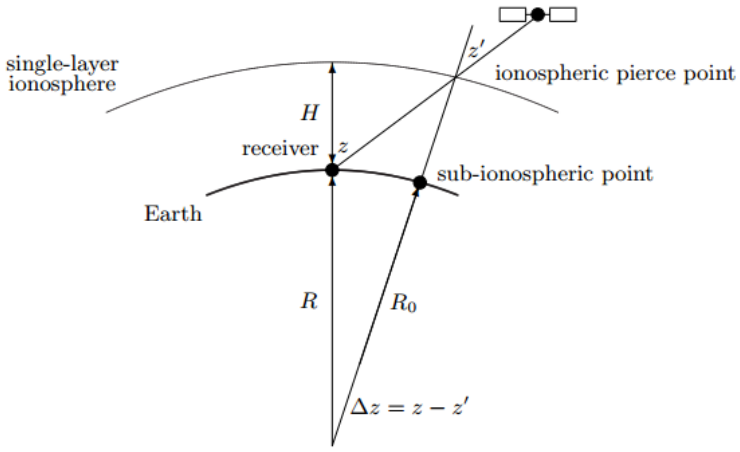

Figure 2.1. Single-layer mapping function model for the ionosphere

The mapping function depends on the elevation and the ionospheric effective height of SLM. In investigating the role of the effective height of SLM plays in mapping function, [Lanyi and Roth, 1988] proposed that this height has to be established between 350 and 400 km, at an average altitude of maximum electron density. [Hernández-Pajares et al., 2005] derived the height from worldwide distributed GNSS data, ranging from 350 to 650 km. [Brunini et al., 2011] investigated how the single-layer height between 300 and 550 km affected VTEC and DCB estimates. They concluded that a unique height did not achieve zero conversion errors and that solar activities, time of year, and latitude affected the errors. [Wang et al., 2016] demonstrated that every 100 km of height increase resulted in a difference of about 1.8 TECU in VTEC. Generally, for the convenience of the ionospheric modelling, the effective height is commonly fixed. For example, 350 km is applied to the wide-area augmentation system [Birch et al., 2002], and 450 km is applied to global ionospheric maps (GIMs) [Hernandez-Pajares et al., 2009]. Since the ionosphere is not homogeneous, the effective height varies as a function of location, time, and the levels of solar activity [Xiang et al., 2019].

The mapping function is the ratio between the vertical thickness of the ionosphere and the slant thickness of the ionosphere for the elevation E (E=90°-z). The influence of the ionosphere on GNSS signals is proportional to the length of the signal path through the

ionosphere. This length depends on satellite elevation, being greater at lower elevations. The *F(z)* coefficient in equation (2.3) can be calculated as follows [Dach et al., 2007]:

$$F(z) \approx \frac{1}{\sqrt{1-(\frac{R}{R+H}\sin(z))^2}} \tag{2.5}$$

where *H*=506.7 km, *R* is the mean Earth radius.

2.1.4. Calculating the coordinates of the ionospheric pierce point (IPP)

The point of interest for which a VTEC value has to be estimated is not the location of the receiver but the location of IPP (Figure 2.1). IPP is the intersection between the line of sight (LOS) and the SLM. Its perpendicular projection onto the Earth's surface is called the sub-ionospheric point.

The geocentric spherical coordinates (ϑ, λ) of the IPP can be computed from the receiver geodetic coordinates (B, L), the azimuth (A) and zenith distance (z) of the satellite as follows [Wienia, 2008]:

$$\vartheta = \arcsin(sinB.\cos(\Delta z) + cosB.\sin(\Delta z).cosA) \tag{2.6a}$$

$$\lambda = L + \arcsin(\frac{\sin(\Delta z).sinA}{sin\vartheta}) \tag{2.6b}$$

where $\Delta z = z - z'$ is the difference between the zenith distance at the receiver and the IPP.

Following equations (2.5) and (2.6a-b), to compute the IPP's coordinates and to convert from STEC to VTEC, the elevations (or zenith distances) of satellite need to be determined. For this task, we have two solutions. The first solution, we can download the precise coordinates of satellites from the website of IGS products [(2.3)]. Since the satellite coordinates are provided in every 15 minutes, to match up the satellite data with observation data, the satellite positions data must be interpolated into the same interval with the GPS measurements (30 seconds). The second solution is to calculate the coordinates of the satellite from the navigation file [(2.4)]. The detailed algorithms for calculating satellite's orbit can be found in [Seeber, 2003] or [Gouchang Xu, 2007].

2.2. Alternative methods for detecting ionospheric scintillation

2.2.1. Computing S_4 index from high-rate GNSS observations

Ionospheric scintillation occurs frequently after the sunset until the midnight in the equatorial areas, but it can appear at anywhere in the world and at any time when there is an ionospheric storm or during the high operation of the sun-cycle period. For space geodetic techniques, ionospheric scintillation can make the signal strength drops below the level of the receiver needs, this will cause loss of lock or even cycle slips in the signal and of course, this will degrade the quality of positioning. Ionospheric scintillation is classified by amplitude scintillation which occurs mostly at lower latitudes (about 15^o) and phase scintillation which occurs mostly at higher latitudes. The amplitude scintillation index (S_4) is the ratio of the standard deviation of the normalized signal intensity divided by the average of the signal intensity [Humphreys, 2008]:

$$S_4 = \sqrt{\frac{\langle I^2 \rangle - \langle I \rangle^2}{\langle I \rangle^2}} \tag{2.7}$$

where I stands for the signal intensity and $<I>$ is denoted by the mean value of I in a period. The computed time depends on the sampling rate of the data or interval between epochs of observations. Conventionally, S_4 is computed in every one minute for the 50 HZ rate observations.

One way of measuring completely scintillation characteristics is to use GNSS measurements of signal amplitude (the power) and phase at a very high sampling rate, such as 50 Hz. To be able to detect the amplitude scintillation, we need to use special receivers (for example Septentrio PolaRxS or Javad receiver) that can provide direct measurements of the scintillation indices. These are in-phase (I) and the quadrature (Q), which can be obtained from receiver correlators [Cokrlic et al., 2012]. From I and Q we calculate:

$$a(t) = \sqrt{s_I^2(t) + s_Q^2(t)} \tag{2.8}$$

and the signal power I:

$$I = \frac{a(t)^2}{2} \tag{2.9}$$

S_4 obtained from equations (2.7) to (2.9) is still affected by ambient (thermal) noise, which has to be estimated over the same time span for which the signal power is averaged. Therefore, in this case, S_4 index must be calibrated to eliminate the thermal noise [Cokrlic et al., 2013]. The problem of removing thermal noise out of S_4 index will be introduced in Section 4.2.

2.2.2. VTEC gradient

Another solution for detecting the appearance of ionospheric scintillation is to check whether there is a rapid fluctuation in the VTEC results as GNSS signal scintillations are highly correlated with the rapid changes in TEC along the signal path. The movement of GNSS satellites can be used to measure VTEC spatial variations. To identify spatial gradients, [Jiyun et al., 2006] proposed a "Time step method". By considering the distance between the IPP at two successive epochs, the vertical ionospheric gradient ($VTEC_{gradient}$) can be estimated. To compute the horizontal displacement of IPP after each epoch, there have been different solutions: solve the inverse geodetic problem from the geodetic coordinates of IPPs or project these IPPs onto a plane by using a map projection. In this study, I introduce a simple way to calculate IPP horizontal displacement as follows:

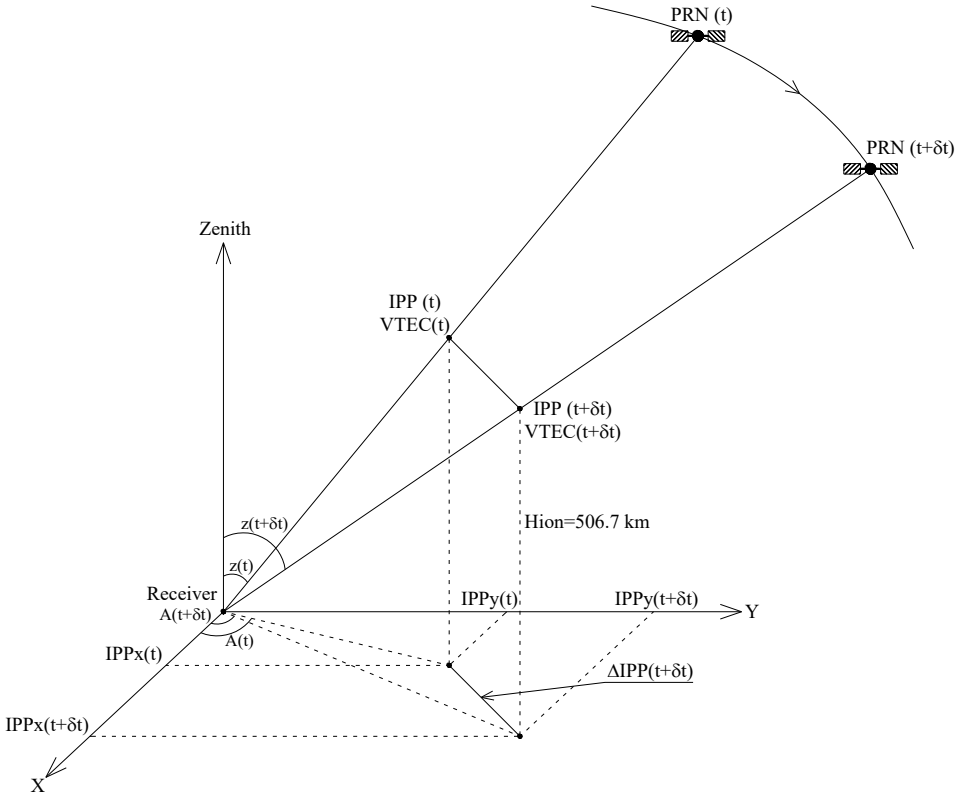

Figure 2.2. Projection of IPP on the horizontal plane

Assuming a flat Earth (which is a sufficient assumption for satellites at a very high elevation) with the IPP altitude H_{ion} = 506.7 km (the same as the height H used in mapping function, see Figure 2.2). The projection of the IPP vector onto the ground plane is:

$$IPP_x = H_{ion}.\frac{cosA}{tanz} \quad (2.10a)$$

$$IPP_y = H_{ion}.\frac{sinA}{tanz} \quad (2.10b)$$

where A and z is the azimuth and zenith distance of the satellite at the epoch of observation.

At each epoch of observations, we have one VTEC value and the rectangular coordinates of IPP (computed follow equation (2.6)) projected on the plane correspond to the respective satellite. When the satellite moves, the IPP and VTEC change respectively. We can compute the IPP horizontal displacements after each epoch as:

$$\Delta_{IPP}(t+\delta t) = \sqrt{[IPP_x(t+\delta t) - IPP_x(t)]^2 + [IPP_y(t+\delta t) - IPP_y(t)]^2} \quad (2.11)$$

where δt is the interval of the observables (30 seconds for daily data of IGS stations). Then we determine the VTEC gradient at the epoch ($t+\delta t$):

$$VTEC_{gradient}(t+\delta t) = \frac{VTEC(t+\delta t) - VTEC(t)}{\Delta_{IPP}(t+\delta t)} \quad (2.12)$$

As the delays due to different epoch are considered and divided by the corresponding separation, the estimated $VTEC_{gradient}$ is a combination of both temporal and spatial gradients. The VTEC gradient, has the unit of TECU/km, can be used to determine the spatial variations of VTEC and from this information, we can determine whether scintillation activity exists at the moment of observation. Some examples will be introduced in Section 2.4.

2.2.3. Rate of TEC index (ROTI)

The low-frequency phase fluctuation can be directly estimated by TEC changes along the ray path for a dual-frequency receiver. For these purposes, the Rate Of Tec (ROT) and the Rate Of Tec Index (ROTI) are calculated from RINEX data using the method proposed by [Pi et al., 1997]. Both S_4 and ROTI are important indices in monitoring ionospheric irregularities since these parameters describe the dynamic changes in the electron density. Based on the results reported by [Pi et al., 1997; Basu et al., 1999; Beach and Kintner, 1999], it was

concluded that ROTI could be used as a proxy for assessing the presence of ionospheric scintillation.

ROT index is to trace ionospheric irregularities and to provide spatial variation of electron density. The rate of change of ionospheric delay due to satellite signals received at a receiver is given from phase measurements as [Knut Stanley, 2014]:

$$ROT(i) = \frac{L_{GF}(i) - L_{GF}(i-1)}{\Delta t.10^{16}.40{,}3.(\frac{1}{f_1^2} - \frac{1}{f_2^2})} \quad (2.13)$$

with $L_{GF}(i)$ is the geometry-free phase combination at the time i:

$$L_{GF}(i) = L1(i).\lambda_1 - L2(i).\lambda_2 \quad (2.14)$$

where Δt is the time difference between the epochs, in minutes; f_1, f_2 are frequencies (Hz); L1, L2 are phase measurements in cycles and λ_1, λ_2 are the wavelengths in meter (λ_1=0.19029 m, λ_2=0.24421 m). ROT has the unit of TECU/min and it indicates the disturbances of the ionosphere.

From the ROT value computed at each interval, we can calculate the Rate Of Tec Index (ROTI). ROTI is defined as the standard deviation of the rate of TEC over some time interval, it characterizes small-scale and/or rapid variation of TEC and is strongly related to scintillation [Basu et al., 1999]. The expression of ROTI is as follow:

$$ROTI(k) = \sqrt{\frac{1}{N}\sum_{j=k-N}^{k}(ROT(j) - \overline{ROT})^2} \quad (2.15)$$

where N is the number of epochs;

$\overline{ROT}$ is the average of ROT for the interval k: $\overline{ROT} = \frac{1}{N}\sum_{j=k-N}^{k} ROT(j)$.

When computing ROTI, the time interval over which a value of ROTI is calculated must be taken into account. The choice of sample rate is critical for studies of small-scale irregularities, but in the case of large-scale irregularities, the sample rate is less important. [Jacobsen et al., 2014] indicates the impact of different sampling rates and calculation time intervals on ROTI values. They found that ROTI values calculated using different parameter choices are strongly positively correlated but ROTI values are quite different. The effect of a lower sample rate is to lower the ROTI value, due to the loss of high-frequency parts of the

ROT spectrum, while the effect of a longer calculation time interval is to remove or reduce short-lived peaks due to the inherent smoothing effect. In this study, ROTI is calculated for a time span of 5 minutes, as it gives a reasonably good temporal resolution while still having a good number of samples in each interval.

Usually, ROTI>0.5 TECU/min (1 TECU refers to 10^{16} electrons/m^2) indicates the presence of ionospheric irregularities at scale lengths of a few kilometres [Ma and Maruyama, 2006]. Considering the coexistence of large and small scale irregularities in equatorial irregularity structures during the early evening hour, [Basu et al.,1999] pointed out that ROTI measurements can be used to predict the presence of scintillation causing irregularities. Several studies have also indicated that large and small scale irregularities at scale size of a few kilometres and several hundred meters can be investigated simultaneously with ROTI and scintillation indices [Zou and Wang, 2009; Alfonsi et al., 2011; Seif et al., 2012].

Like VTEC gradient, the main advantage of ROTI over standard scintillation index (S_4) is that it is calculated based on measurements from normal dual-frequency GNSS receivers, which have a huge data available with global coverage. The algorithm to calculate ROTI is quite easily implemented and very straightforward. The main disadvantage is that this index does not contain information about the frequency of the irregularities, only that irregularities exist within the range limited by the sample rate (5 minutes) and measurement interval. Furthermore, the calculation of ROTI requires data from a dual-frequency receiver, whereas scintillation indices are calculated just using a single frequency (commonly the L1 frequency). Nevertheless, normal dual-frequency GNSS receivers are still far more common and much cheaper than scintillation receivers.

In this section, I propose four alternative methods for detecting ionospheric scintillation from GNSS data. Each method has its advantages and disadvantages and can be applied in different cases. For sure, the most reliable and appropriate index is S_4 directly obtained from high-rate GNSS receivers. This index reflects most truthfully and accurately about the amplitude of ionospheric scintillation at all levels. However, in case there are only normal dual-frequency GNSS receivers available, we are still able to detect the occurrences of ionospheric scintillation by using ROTI or VTEC gradient (the benchmark comparison for both indices are 0.5). Lastly, using the signal intensity S_1 and/or S_2 in the RINEX files to compute S_4 index is another possible solution, but this tactic only shows the presence of scintillation for each specific satellite at a particular time.

For a specific area, especially near the equator, the best way to monitor ionospheric scintillation activity is to set up a network of scintillation receivers surrounding the research area. Basically, one receiver can monitor an area of about 13^{o}x13^{o} (~225x10^{4} km^{2}) when accepting satellite elevation cut-off at 20^{o} as indicated in Figure 2.3. This method has been applied in the Vietnam area and the results will be discussed in Chapter 4. To study globally, using ROTI is the most convenient way because of the worldwide coverage of the standard dual-frequency GNSS receivers currently. Results on the global distribution of ionospheric irregularities by using ROTI index will be presented in Section 5.3.

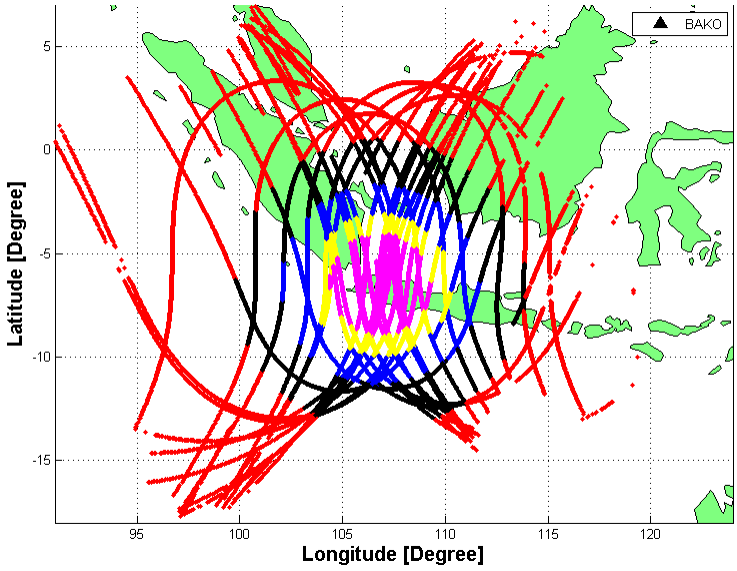

Figure 2.3. The footprint of satellite tracks at BAKO station in a single day. Different colors correspond to different satellite elevations: [0:20^{o}]: red, [20^{o}-30^{o}]: black, [30^{o}-40^{o}]: blue, [40^{o}-50^{o}]: yellow and [50^{o}-90^{o}]: magenta.

2.3. Developing a software tool to calculate some ionosphere parameters

From the above formulas and algorithms, I program a MATLAB software tool to study the ionosphere from RINEX files. The purposes of this software are to compute some parameters of the ionosphere like VTEC, VTEC gradient, ROT, ROTI, S_4,… and then estimate the ability of the occurrences of scintillation activity. The input data of the program are the observation (*.obs) and navigation (*.nav) files. This program is available with daily data (interval 30 seconds) or high-rate data (1 Hz, 10 Hz, 50 HZ, …). Figure 2.4 depicts the flowing chart of the software tool and Figure 2.5 shows the interface of the software tool.

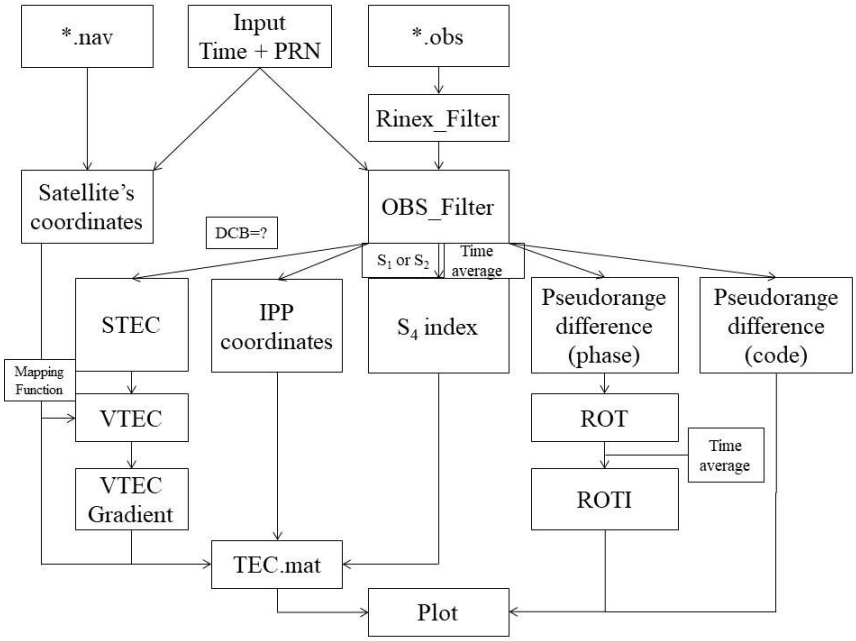

Figure 2.4. The flowing chat of the ionosphere software tool

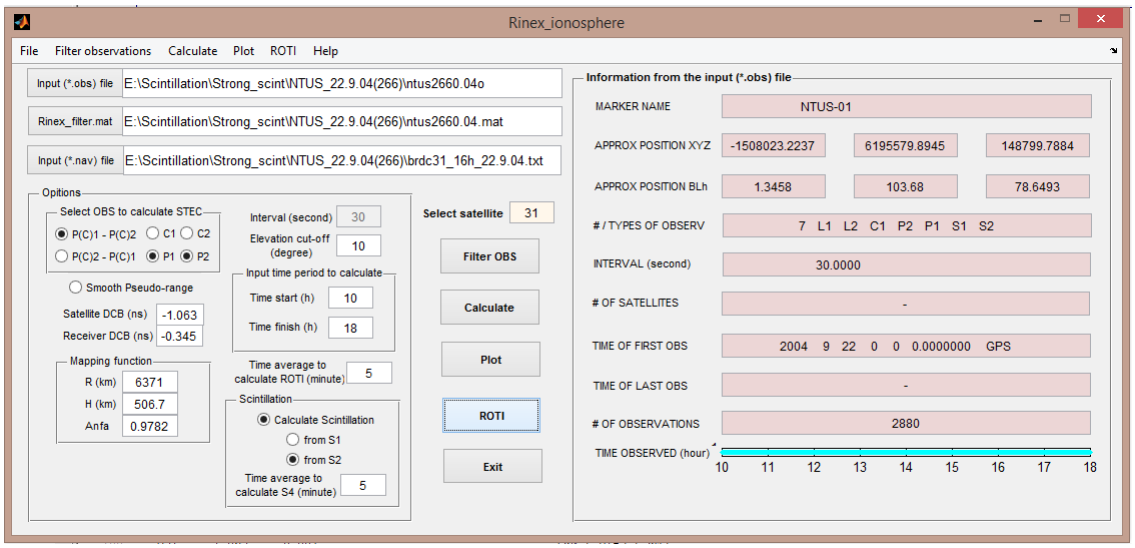

Figure 2.5. The interface of the ionosphere software tool

The specific calculation sequences of the software tool are described as follows:

- The first step of the program is to filter the observations from the RINEX files (Rinex_Filter). Since in the RINEX files, all observations are arranged at different epochs, thus the observations need to be rearranged following its observed satellite and epoch.
- In the second step, the measurements are filtered again. This second filter step will collect the data of the selected satellite in the selected time. The difference between the two filter steps is that the first one dealing with all satellites and all epochs, but the second one allocates only the selected satellite and epoch.
- At the same time with the filtering observations, the program also calculates the coordinates of the selected satellite during the selected time from the navigation file. These coordinates (only elevations component) are necessary to convert STEC to VTEC by using a mapping function.
- After the filtering, STEC is first computed. In this step, the user can choose whether to smooth the pseudo-range or not. Simultaneously, the user is requested to input the DCBs of satellite and receiver. User can also choose which observations will be used to calculate STEC (P1, P2, or C1, C2). In our study, the code pseudo-range is selected instead of smooth pseudo-range to compute STEC.
- Then STEC is converted to VTEC using the satellite elevations obtained in the previous steps. After that, the VTEC gradient is calculated for checking the possible rapid fluctuations in VTEC results.
- The coordinates of IPP are also computed and stored in the final products (TEC.mat). All of these results can be leveraged later for other purposes.
- The amplitude scintillation (S_4 index) is calculated following equation (2.7) with I is either S_1 or S_2 observations, user can choose S_1 or S_2 alternatively for this task. In this step, the average time to calculate S_4 must be inputted. In our results, which will be shown in the next section, the S_4 index is computed from both S_1 and S_2 in every 5 minutes.
- Before determining ROT and ROTI, the program calculates and compares the difference in pseudo-range derived from code and phase measurements. This information can be used to detect the incidental cycle slip error in the phase measurements.

- The last computation is to determine ROT and ROTI following equations (2.13), (2.14), and (2.15). For ROTI computation, the calculation time interval must be set up. In our research, this value is chosen by 5 minutes as discussed before.
- All the results will be stored in *.MAT files (TEC.mat and ROTI.mat) and can be used later for other purposes. The file TEC.mat contains the most important information about the ionosphere such as epoch (in hours and Julian day), STEC computed from code and phase smooths code pseudo-range, the azimuths and elevations of the satellite, VTEC, VTEC gradient, the geodetic coordinates of IPP and S_4 index. To evaluate the intensity of scintillation activity, all these results are plotted and examined. As mentioned before, based on the variations of VTEC gradient, S_4, ROT and ROTI, the levels of scintillation activity can be estimated and also the correlations between ionospheric scintillation and the changes of VTEC can be explored.

2.4. Some results and discussion

In order to show example presentations of data analysis performance using the ionosphere software tool established above, I investigate ionospheric scintillation (IS) error may appear in GNSS observations. In this study, I compute several ionosphere parameters at two stations: BAHR in Bahrain and POTS in Germany on October 28th 2003. Geographic coordinates of these stations are given in Table 2.1.

Table 2.1. List of IGS stations to study ionospheric scintillation

No	Station	Geographic coordinates		Country	Latitude region
		Latitude (^{o})	Longitude (^{o})		
1	BAHR	26.21	50.61	Bahrain	Mid
2	POTS	52.38	13.07	Germany	High

On October 28th 2003, there was a so-called Halloween storm. Figures 2.6 and 2.7 illustrate the presence of ionospheric scintillation at POTS and BAHR stations. Since there were no S_1 and S_2 observations in the RINEX files of these stations, the S_4 index could not be calculated in this case, but instead, I analyze the occurrence of ionospheric irregularities based on VTEC gradient and ROTI indices. In these figures, the top-left panel is VTEC and elevations of the satellite, the top-right panel is VTEC gradient, the bottom-left describes ROT, and the bottom-right shows ROTI. The horizontal axis expresses GNSS time in hours.

The elevation-cut off is 10^{o} aims to eliminate TEC measurements from low-elevation satellites.

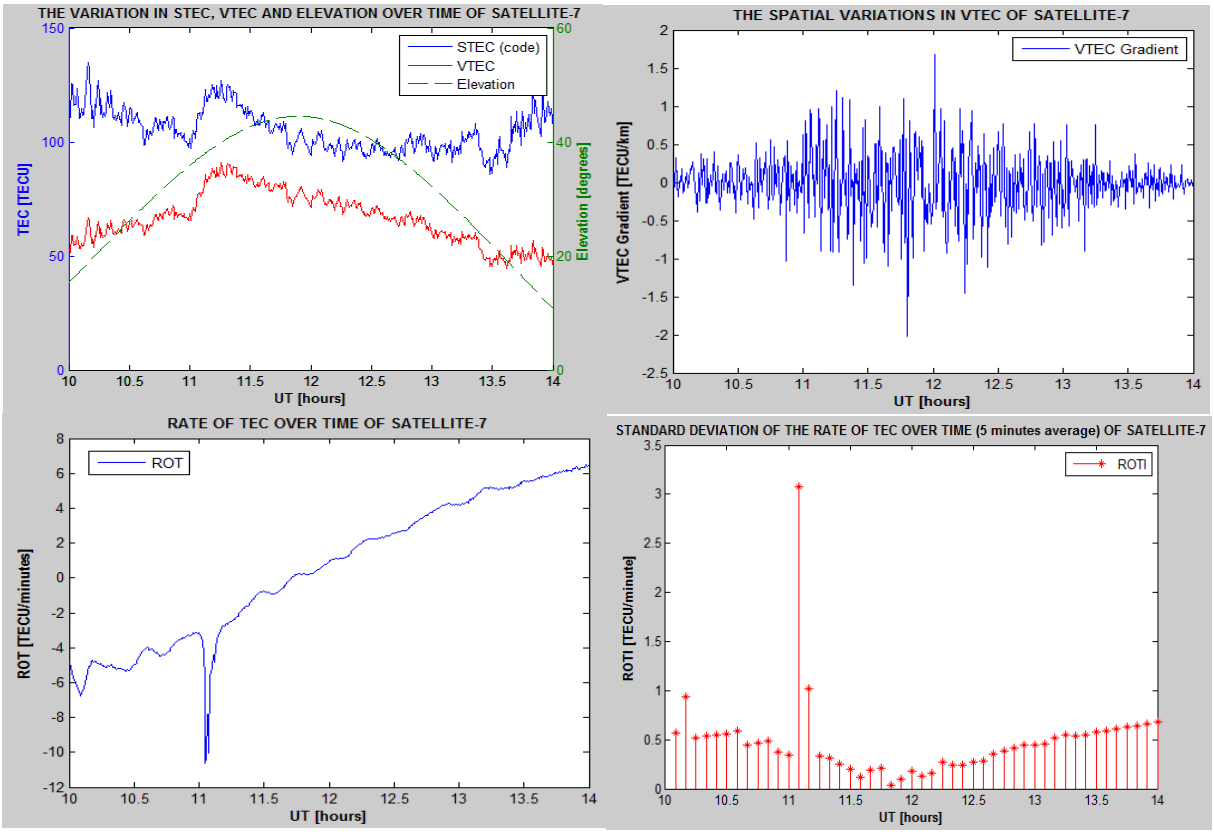

Figure 2.6a. IS detected by PRN 7 at POTS station on 28.10.2003

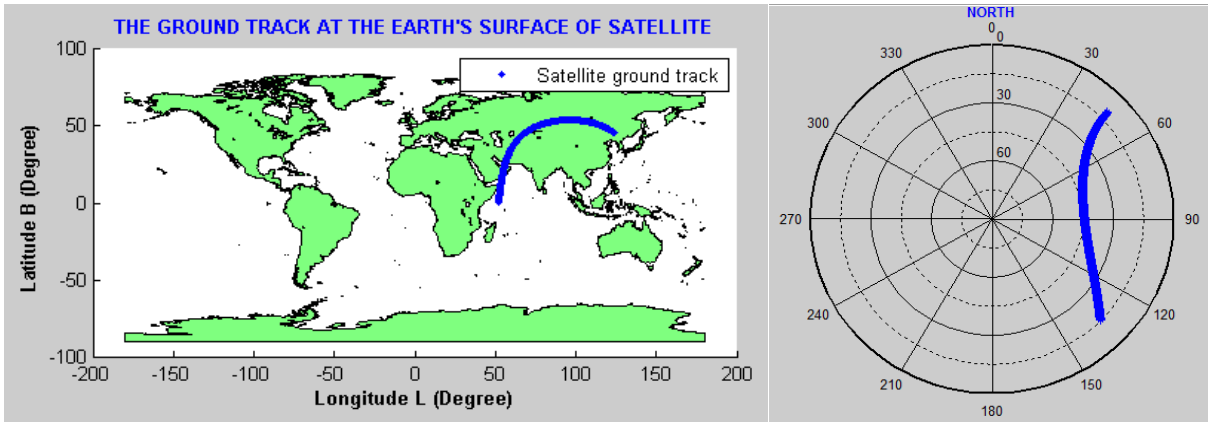

Figure 2.6b. The ground track and sky-plot of PRN 7 from 10:00 to 14:00 UT

On this day, there was a remarkable scintillation error affecting all visible satellites at more than 11 UT. It is characterized by sudden, rapid changes in VTEC level or fluctuations of VTEC gradient. In these figures, it is seen that ROTI increased suddenly at the moment scintillation occurred. ROTI values were from 2 to 3 TECU/min for all satellites at two

stations, this means the intensity of ionospheric scintillation was quite similar at both stations. Due to the ionospheric storm on this day, VTEC mean value was generally quite high.

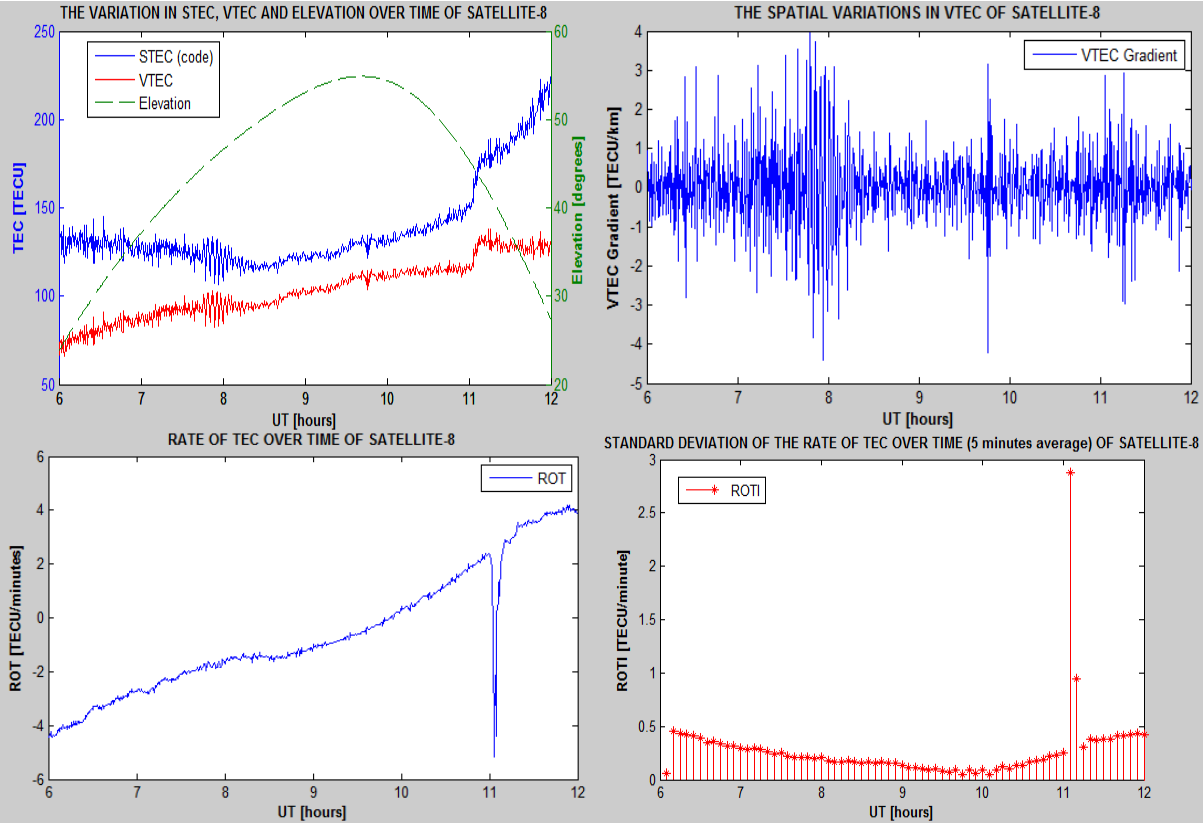

Figure 2.7a. IS detected by PRN 8 at BAHR station on 28.10.2003

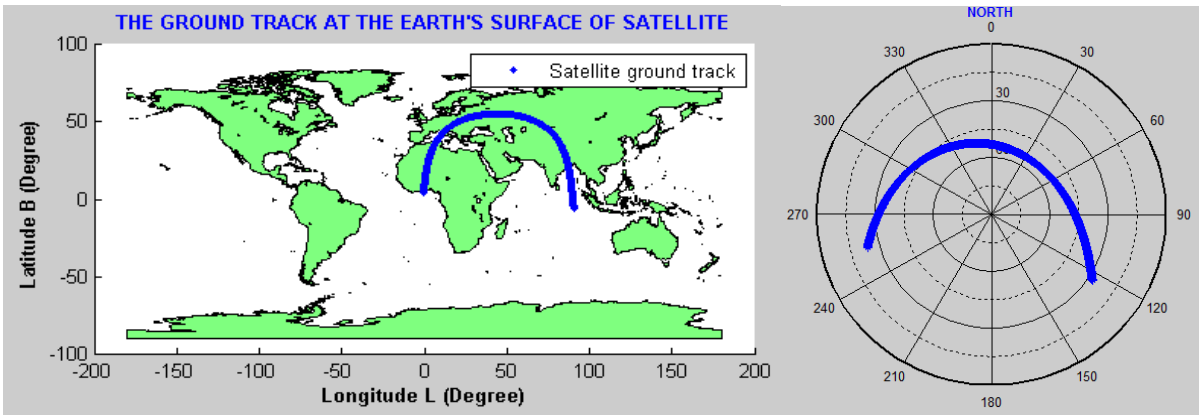

Figure 2.7b. The ground track and sky-plot of PRN 8 from 6:00 to 12:00 UT

[2.3] https://www.igs.org/products
[2.4] ftp://cddis.gsfc.nasa.gov/gps/data/daily/
[2.5] ftp://cddis.gsfc.nasa.gov/gps/data/daily/

2.5. Chapter summary

From this chapter onwards, at the end of each chapter, a summary of the main contents of the chapter will be given. Also, new findings and significant results will be synthesized. For this chapter, the main contents can be reviewed and summarized as some points below:

- Section 2.1 summarizes the formulas and methods to calculate TEC from GNSS measurements. A mapping function is also presented for converting from STEC (multi-value) to VTEC which is a unique value representing the state of the ionosphere (concerning the radio propagation) at a given point.

- Section 2.2 proposes alternative methods to detect ionospheric scintillation in GNSS observations. Characteristics and scope of application of each method are also discussed. Followings are the basic features and advantages, disadvantages of each method:

    - Using S_4 index only derived from the high-rate GNSS receivers which are quite expensive and far from being widely used as conventional GNSS receivers. But its main advantage is the accurate reflection of the presence and intensity of ionospheric irregularities. It is, so far, still the most used and common indicator for studying ionospheric scintillation. Fundamentally, this method is the best in case of studying a moderate area of the Earth.

    - VTEC gradient is also an index can be directly calculated from the standard dual-frequency receivers. The idea of this method is to check for potential rapid fluctuations in VTEC results. This index is used to determine both temporal and spatial gradients of the ionosphere.

    - ROTI index: together with S_4, this index is commonly used in study ionospheric disturbances, especially during geomagnetic storms when the ionosphere is highly volatile. More importantly, this index can be derived from conventional dual-frequency receivers with enormous data available worldwide. This method combines the advantages of the other three methods: as accurate and efficient as S_4 index, can be easily and universally calculated on a global scale like VTEC gradients. Fundamentally, this method is the best in case of global study.

- Section 2.3 develops a software tool to calculate some basic parameters of the ionosphere like STEC, VTEC, VTEC gradient, ROT, ROTI, S_4,… This program will also be used for the calculations in Chapter 3 and Chapter 5.

- Section 2.4 presents some results calculated at two stations BAHR and POTS. Calculation results perspicuously show ionospheric scintillation errors detected in the measurements at these stations. Concurrently, it demonstrates the effectiveness of the proposed methods.

Thus, there are two basic indicators to study ionospheric disturbances including the S_4 index and the ROTI index. In Chapter 4, S_4 index will be mainly used to study the characteristics of ionospheric scintillation over Vietnam region. ROTI index, meanwhile, will be used to study both temporal and spatial distributions of ionospheric irregularities over Southeast Asia area and on a global scale, this matter will be explored in Chapter 5.

3. TEC variations during SC24 over the South East Asia area

3.1. Data available in the research area during the period of 2007 - 2017

The Sun has its own seasons with an average duration of about 11 years. During this cycle, the Sun enters a period of increased activity called solar maximum and a period of decreased activity called solar minimum. Cycles span from one minimum to the next. The solar cycle or sunspot cycle is the result of a solar dynamo, in which electric currents and magnetic fields are built up in the outer layer of the Sun and then ruined in energetic outbursts. Solar cycle 24 (SC24) was the most recent solar cycle, which began on January 4th, 2008 and was confirmed to be ended at the end of 2019. In fact, it had declined more quickly than scientists forecasted. To describe the intensity of Sun activity, so far, different solar indices have been used like sunspot number (SSN), solar radio flux (F10.7cm), solar flares, solar corona, total solar irradiance**, s**olar ultraviolet emissions, AP index, KP index, Dst index, AE, index, AL index, AU index, Polar Cap (PCN) index, Lyman-alpha (Ly-α) index, … Most of these indices can be obtained from the official website of OMNIWeb of NASA [(3.1)]. Among them, the first two indices (SSN and F10.7cm) are most common and especially, they are widely applied in the field of radio propagation.

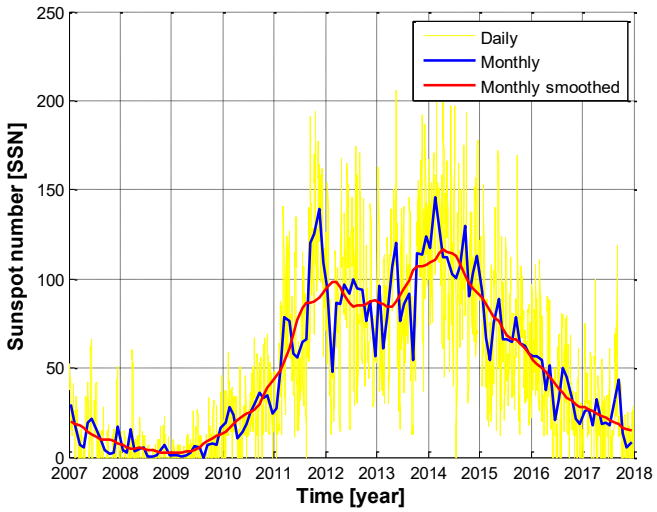

Figure 3.1. International sunspot number during SC24 [(3.3)]

The official daily and monthly sunspot numbers are determined by the World Data Center - Sunspot Index and Long-term Solar Observations (WDC-SILSO) at the Royal Observatory of Belgium [(3.2)]. Figure 3.1 shows the SSN obtained during SC24. Data are downloaded from the official website of SILSO. We can see that, during this period, Sun activity was minimal until

early 2010, it reached its maximum in April 2014 with 23 months smoothed sunspot number of 81.8. More examples of Sun activity using other indicators during SC24 are also illustrated in the Figures 3.2a and 3.2b. All these figures clearly indicate the activity trends of SC24: got minimum in the years 2008, 2009, then from 2010 to 2012 was the increasing phase, reached the maximum in both years 2013, 2014, and followed by decreasing phase during 2015 - 2018 period.

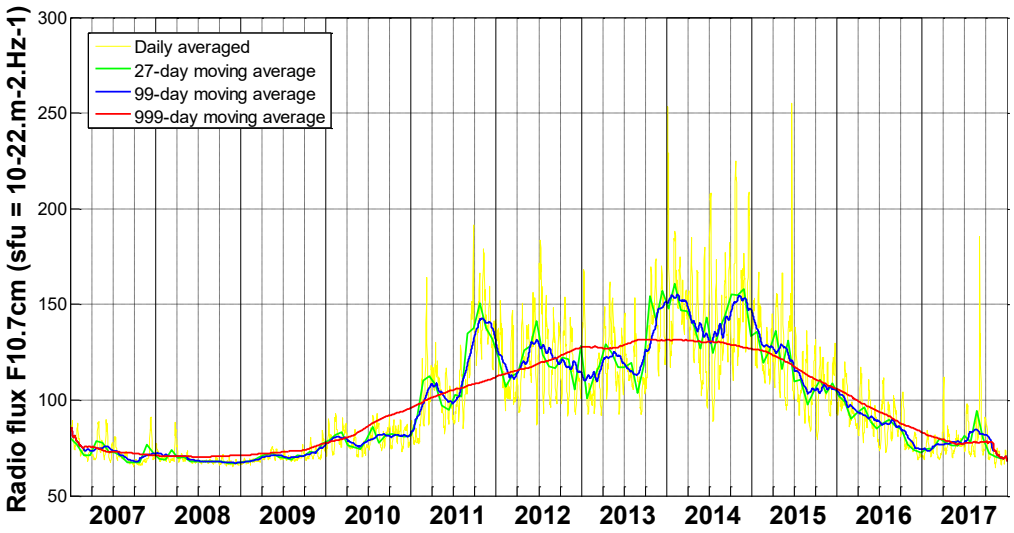

Figure 3.2a. The radio flux index during SC24 [3.1]

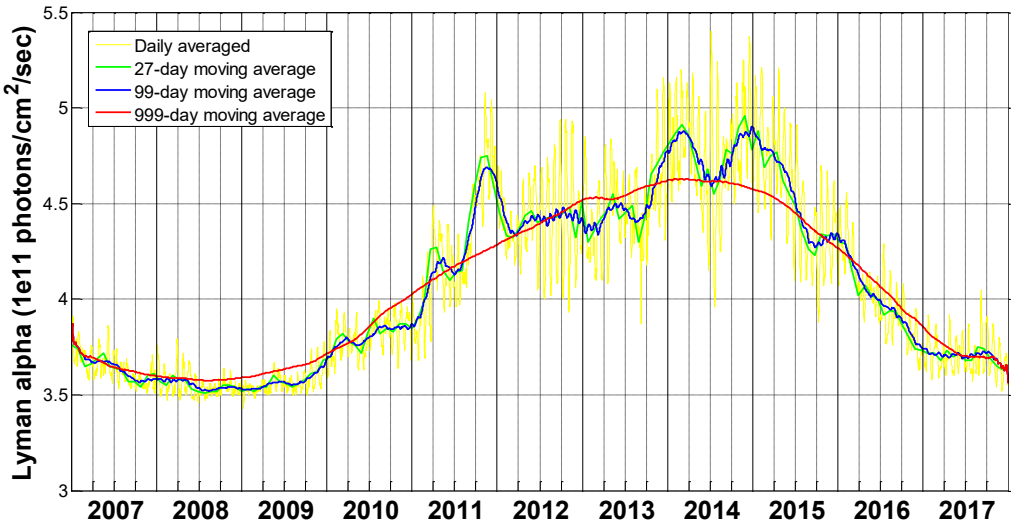

Figure 3.2b. The Lyman-alpha index during SC24 [3.1]

The solar flux, meanwhile, has a major impact on radio communications propagation conditions. It indicates the level of radiation that is being received from the Sun. This solar index is measured by detecting the level of radio noise emitted at a frequency of 2800 MHz (wavelength: 10.7 cm). The index is quoted in terms of Solar Flux Units (SFU) with 1 SFU is equivalent to 10^{-22} W m^{-2} Hz^{-1}. Figure 3.3 depicts different solar cycles for over 70 years and compares the intensity of SC24 to others in SFU.

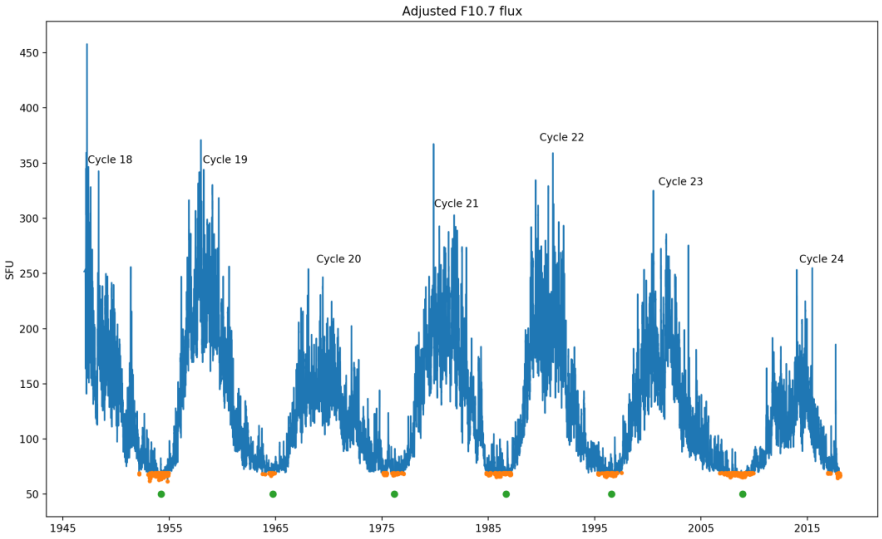

Figure 3.3. Daily adjusted measurements of the solar flux density in SFU, from 1947 till the end of January 2018.

The green dots mark the time of the official minima of the different sunspot cycles. The orange dots highlight the period when the flux drops below or is equal to 70 SFU [3.4]

During the 11-year of a solar cycle, the ionosphere changes both its thickness and characteristics. The changes are most complicated and unpredictable at the equatorial latitudes in a band around 15° northward and southward from the equator. The Southeast Asia region with latitude is from 15°S to 30°N and longitude is from 95°E to 130°E is located in this area. Thus, it is very often affected by the volatility of the ionosphere. This region covers eleven countries: Brunei, Myanmar, Cambodia, Timor-Leste, Indonesia, Laos, Malaysia, Philippines, Singapore, Thailand and Vietnam. The study period is one full solar cycle, from the beginning of 2007 to the end of 2017. To study the variations of the ionosphere, I use the most basic indicator of the ionosphere is VTEC index. VTEC are calculated by using the software tool introduced in Chapter 2. VTEC is computed over the entire 11-year period at all available IGS stations located in the research area. Table 3.1 provides detailed information of all stations used in this study including 13 IGS stations and 3 scintillation receivers located in Vietnam.

Table 3.1a. List of GNSS stations over the research area

No	Station	Geographic coordinates		Geomagnetic coordinates (reference year 2017)		Elevation (m)	Data available	Site name
		Latitude (deg)	Longtitude (deg)	Latitude (deg)	Longitude (deg)			
1	HANOI	21.03	105.96	11.33	178.86	36.56	2009, 2015	Phuthuy
2	HUE	16.46	107.59	6.78	-179.58	33.19	2009, 2015	Hue
3	HCM	10.85	106.56	1.20	179.41	14.32	2009, 2015	Baclieu
4	KUNM	25.03	102.80	15.33	175.90	2023.00	2007 - 2013	Kunming
5	CUSV	13.74	100.53	4.14	173.54	76.06	2008 - 2017	Chulalongkorn
6	NTUS	1.35	103.68	-8.22	176.49	79.00	2007 - 2017	Nanyang Technological Uni
7	BAKO	-6.49	106.85	-16.03	179.68	158.18	2007 - 2017	BAKOSURTANAL
8	XMIS	-10.45	105.69	-19.96	178.46	261.60	2007 - 2017	Christmas Island
9	HKSL	22.37	113.93	12.72	-173.58	95.30	2010 - 2017	Siu Lang Shui
10	PIMO	14.64	121.08	5.24	-166.48	95.53	2007 - 2017	Manila Observatory
11	JOG2	-7.76	110.37	-17.27	-176.67	174.40	2015, 2017	YogYakarta
12	TWTF	24.95	121.16	15.49	-166.83	203.12	2017	Taoyuan
13	KMNM	24.46	118.39	14.91	-169.42	49.10	2017	Kinmen
14	CKSV	23.00	120.22	13.52	-167.63	59.60	2017	Tainan
15	PPPC	9.77	118.74	0.32	-168.59	66.54	2017	NAMRIA
16	PGEN	6.06	125.13	-3.10	-162.10	121.12	2017	NAMRIA

Table 3.1b. List of GNSS stations over the research area

No	Station	Province	Country	Current receiver type	Current satellite system
1	HANOI	Hanoi	Vietnam	GSV4004B	GPS ionospheric scintillation and TEC monitoring
2	HUE	Hue	Vietnam	GSV4004B	GPS ionospheric scintillation and TEC monitoring
3	HCM	Ho Chi Minh	Vietnam	GSV4004B	GPS ionospheric scintillation and TEC monitoring
4	KUNM	Kunming	China		No longer working
5	CUSV	Bangkok	Thailand	JAVAD TRE_3 DELTA	GPS+GLONASSNASS+GALILEO+BEIDOU+QZSS
6	NTUS	Singapore	Singapore	LEICA GR50	GPS+GLONASS+GALILEO+BEIDOU+QZSS
7	BAKO	West Java	Indonesia	LEICA GR50	GPS+GLONASS+GALILEO+BEIDOU+QZSS+SBAS
8	XMIS	Western Australia	Australia	TRIMBLE NETR9	QZSS+GPS+GLONASS+GALILEO+BEIDOU
9	HKSL	Hong Kong	China	LEICA GR50	GPS+GLONASS+GALILEO+BEIDOU+QZSS+SBAS
10	PIMO	Metro Manila	Philippines	JAVAD TRE_G3TH DELTA	GPS+GLONASS+GALILEO+BEIDOU+QZSS
11	JOG2	Daerah Instimewa Yogyakarta	Indonesia	JAVAD TRE_G3TH DELTA	GPS+GLONASS+GALILEO+QZSS
12	TWTF	Taiwan	Taiwan	SEPT POLARX4	GPS+GLONASS+QZSS+SBAS
13	KMNM	Kinmen	Taiwan	TRIMBLE NETR9	GPS+GLONASS+GALILEO+BEIDOU+QZSS+SBAS
14	CKSV	Tainan	Tainan	TRIMBLE NETR9	GPS+GLONASS+GALILEO+BEIDOU+QZSS+SBAS
15	PPPC	Palawan	Philippines	LEICA GR50	GPS+GLONASS+GALILEO+BEIDOU+QZSS+SBAS
16	PGEN	South Cotabato	Philippines	LEICA GR50	GPS+GLONASS+GALILEO+BEIDOU+QZSS+SBAS

Figures 3.4a and 3.4b show the stations distribution and the traces of the visible satellites at 400 km altitudes in a single day over the research area. In these figures, different colour corresponds to different satellite elevation as indicated in the captions. As the results at all stations are almost similar, I only select the outcomes at seven IGS stations: KUNM, NTUS, BAKO, XMIS, HKSL, CUSV, and PIMO to present in this chapter. Table 3.2 shows the total number of days with GNSS measurements at these stations. The sign "-" indicates no data obtained. From this datasheet, it can be seen that data at three stations PIMO, XMIS, and BAKO are quite stable and complete (reach over 90% of total days of 11 years). Only four stations: PIMO, XMIS, BAKO, and NTUS were able to obtain full data for 11 years. Data at two stations HKSL and KUNM are less than 60%, due to the lack at the beginning years (2007 - 2009) at HKSL station and in the last few years (2014 - 2017) at KUNM station. Nevertheless, with such a number of measurements, we can study the temporal variations of VTEC over this area both in short-term and long-term variations. In the next sections, daily, seasonally, and annually variations of VTEC at these seven stations will be revealed and discussed.

Table 3.2. Number of observed days during 11 years at seven IGS stations

Year	Stations						
	PIMO	XMIS	BAKO	CUSV	NTUS	HKSL	KUNM
2007	364	350	294	-	178	-	354
2008	341	298	354	72	347	-	360
2009	316	359	330	364	279	-	364
2010	365	356	321	363	356	188	363
2011	363	340	358	346	345	193	358
2012	366	364	358	365	366	268	347
2013	365	365	360	363	365	361	31
2014	356	362	344	289	219	340	-
2015	349	365	329	264	95	349	-
2016	366	343	322	364	43	346	-
2017	365	346	310	338	252	361	-
Σ =	3916 (97.5%)	3848 (95.8%)	3680 (91.7%)	3128 (77.9%)	2845 (70.9%)	2406 (59.9%)	2177 (54.2%)

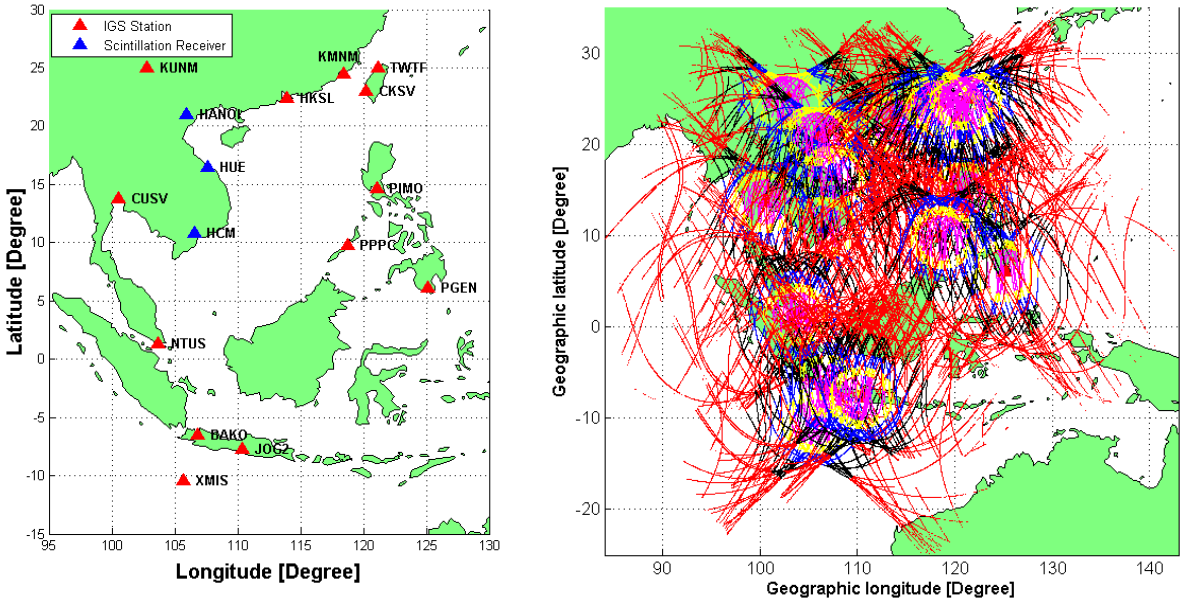

Figure 3.4a. Distribution (left) and satellite traces (right) of 16 GNSS stations over the research area (Different color refers to different satellite elevation: red: <20°, black: [20°,30°], blue: [30°,40°], yellow: [40°,50°], magenta: >50°)

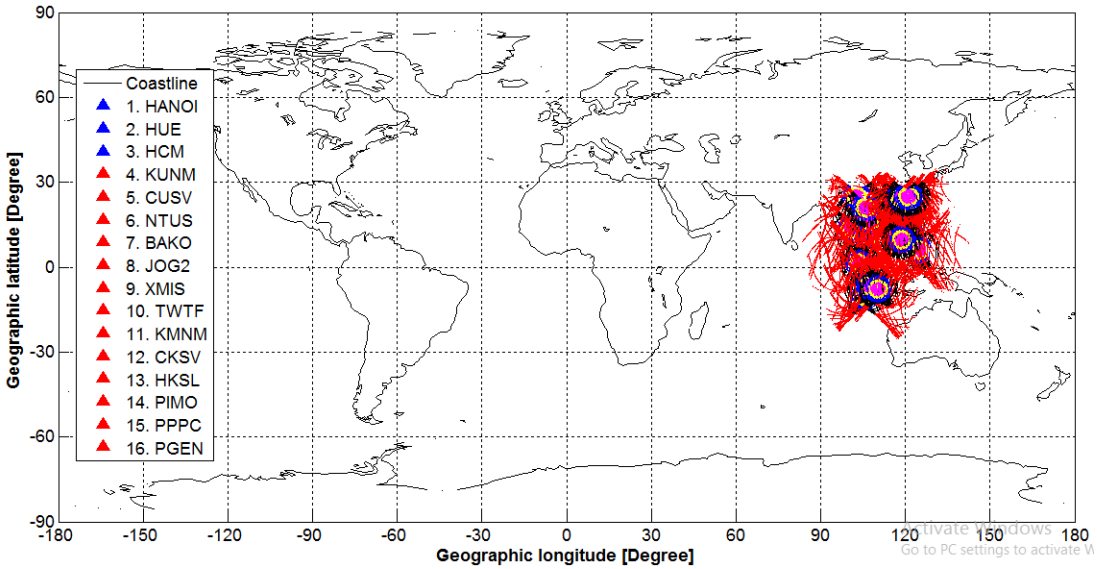

Figure 3.4b. Satellite traces of 16 GNSS stations over the research area (Different color refers to different satellite elevation: red: <20°, black: [20°,30°], blue: [30°,40°], yellow: [40°,50°], magenta: >50°)

3.1 https://omniweb.gsfc.nasa.gov/form/dx1.html
3.2 http://sidc.oma.be/silso/
3.3 http://www.sidc.be/silso/datafiles
3.4 http://www.stce.be/news/417/welcome.html

3.2. Diurnal variations

The diurnal variation of TEC is attributed to the daily rotation of the Earth. To determine the diurnal variation of the ionosphere, VTEC at seven IGS stations (KUNM, NTUS, BAKO, XMIS, HKSL, CUSV, and PIMO) have been calculated for the 11-year period from 2007 to 2017. Measurements of the above stations are the RINEX files version 3.00 were downloaded from the official website of The Crustal Dynamics Data Information System (CDDIS) [3.5]. VTEC is calculated by using the combination of phase and pseudo-range measurements which is more reliable than those by using only the pseudo-range measurements as indicated in some publications [Liu et al., 1996, Carrano & Groves, 2009]. In our preliminary results, there were a few VTECs that had negative values, mainly due to the multipath error. All these values had been removed before moving to the next steps. Also, I put the satellite elevations cut-off at 20^{o} for all calculations to constrain the incidental errors at observations with low satellite angle.

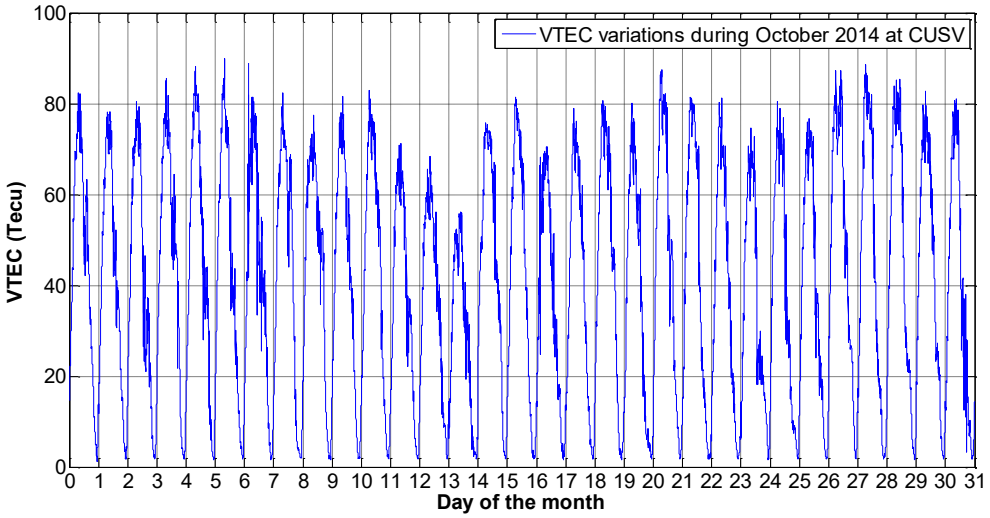

Figure 3.5. Daily variations of VTEC in October 2014

It is also necessary to mention that, each observed day corresponds to one file. Therefore, in total, I have exactly 22000 files (this corresponds to approximately 78.3% of the total number of measurements for seven stations in 11 years). These 22000 files were processed and calculated to give VTEC values at every half of a minute (signal recording interval of the IGS receivers). The sampling rate of RINEX observation in 30 seconds will allow giving more precision in the calculation of VTEC than using GIM model which only provides VTEC every 2 hours.

Figure 3.5 describes diurnal variations of VTEC. The example chosen is one of the peak months of solar activity, i.e. October 2014. There are no large magnetic disturbances in this month, the Dst index varies from -36 nT to 3 nT as shown in Figure 3.6 (source: OMNIWeb [3.6]). However, the diurnal amplitude of VTEC varies significantly and repeatedly from day to day indicating that, there is no direct relation between Dst index and diurnal amplitude of VTEC.

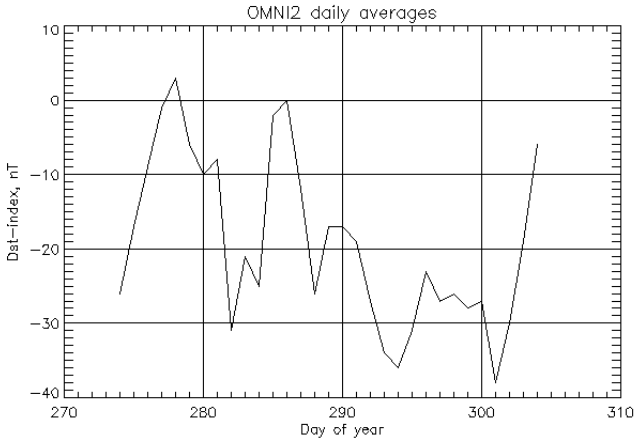

Figure 3.6. The daily averaged of Dst index during October 2014

To have a more clear view of daily variations of VTEC in different months, the monthly mean VTEC have been calculated. Figures 3.7a-b show two examples of the diurnal variations of VTEC at station CUSV in two years (2009 and 2014) having a very different intensity of solar activity. In these figures, the horizontal axis represents 24 hours in local time, the vertical axis represents the value of VTEC in TECU. Different colours and lines style correspond to different months of the year.

[3.5] ftp://cddis.nasa.gov/gnss/data/daily/
[3.6] https://omniweb.gsfc.nasa.gov/form/dx1.html

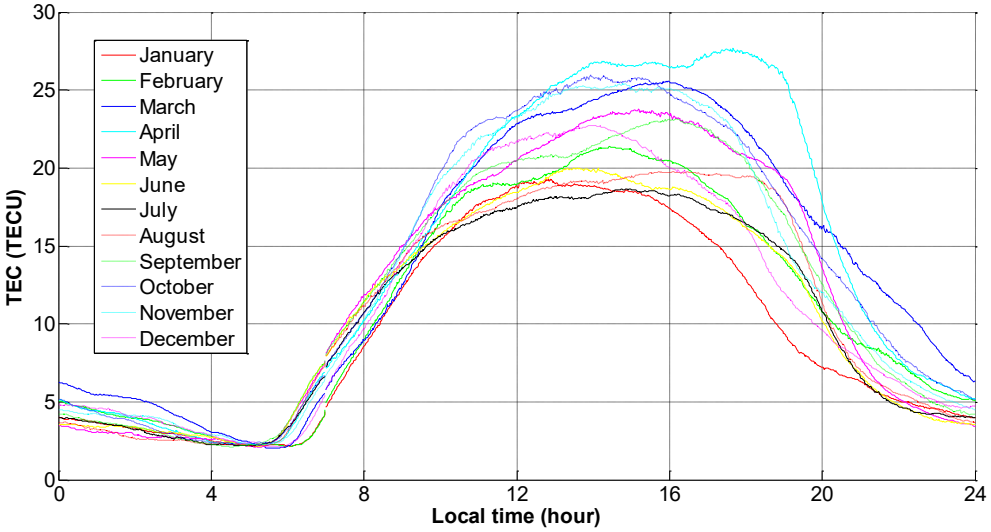

Figure 3.7a. The averaged diurnal variations of VTEC at sta. CUSV in each month of 2009

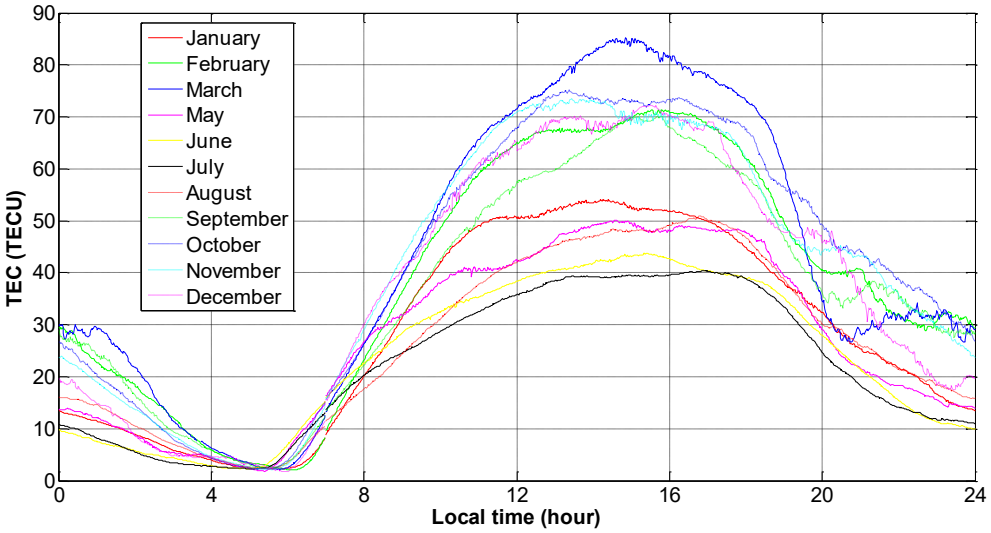

Figure 3.7b. The averaged diurnal variations of VTEC at sta. CUSV in each month of 2014

According to local time, starting at the lowest value in the early morning, VTEC gradually increases to its maximum at afternoon. Shortly thereafter, VTEC begins its downward process for a circuit until the early morning of the next day and repeats this process as indicated in Figure 3.5. Thus, the diurnal variation of VTEC reaches a maximum in the daytime at about 13h-16h (LT) and a minimum at nighttime, about 04h-05h (LT). The diurnal amplitude of monthly mean VTEC changes from minimum at night of about 3 TECU to a maximum of about 80 TECU right after the afternoon. These values are also dependent on the month of the year and the solar cycle. After 22h local time, VTEC does not fluctuate much and maintains low values for all night. This maximum amplitude of VTEC may have a delay of about 13 m to the range for the L1 frequency.

The fact that VTEC reaches its maximum at daytime and minimum at nighttime is completely understandable and can be explained by the formation and existence of the ionosphere under the effect of solar radiation. Besides, this phenomenon also mainly depends on the ion photochemical process. During the daytime, this process happens vigorously with high ion and electron generation rates causing the total number of the electron in the ionosphere to increase and reach its maximum. We know that at the moment of exactly noon (12h LT), the position of the Sun is at the zenith of the station, the rate of ion generation and the electron reach a maximum. But the maximum level of VTEC hardly happens at midday local time but is reached in the early afternoon. This shows that in addition to ionizing solar radiation, VTEC also depends on other dynamic processes such as wind in the ionosphere, electric field, magnetic field,... By the time the Sun goes down, the total number of electron gradually decreases due to the absence of ion photochemical process, which is dominated by the process of collision and recombination. However, the electronic concentration is still maintained during the night hours due to the neutral wind in the meridian plane facing the equator. This raises the plasma along the magnetic field line to a higher height, at which the electron attenuation coefficients are small enough to maintain the existence of the total number of electron throughout the night.

From the results of VTEC calculation, I also collect the maximum and calculate the mean of VTEC at every month during 11 years for all seven stations and then compute the average of these values in each year. The results are shown in Table 3.3 ("-" means no data obtained) and this table is graphed in Figures 3.13a and 3.13b. In this table, the last row is the average of the maximum and monthly mean VTEC during 11 years, the last column is yearly averaged of radio flux F10.7 index (source: OMNIWeb). The third row is the correlation coefficient between the corresponding column and the F10.7 index. All these coefficients are approximately 1, which indicates a high correlation between VTEC calculated with the solar index. At this point, we only consider the maximum monthly VTEC. Calculation results show that the value of VTEC at 3 stations BAKO, XMIS, HKSL is much higher than the remaining stations. The reason for this phenomenon is because of its position. Looking back at Figure 3.4a, stations BAKO and XMIS are located close to the southern crest of EIA and station HKSL is located right over the northern EIA's crest. Meanwhile, stations CUSV, NTUS, and PIMO are located closer to the magnetic equator, hence, mean VTEC at these three stations are considerably smaller than the two above stations. Station KUNM is located a little north of the equatorial anomaly line, but still closer to the EIA northern crest than the stations CUSV, NTUS, PIMO, so its average VTEC is a little bit higher.

The difference in VTEC at different latitudes is due to the influence of the equatorial plasma fountain (EPF). Accordingly, ions are ejected from the equator to form an increase in ionic density to the north and south of equator. Figure 3.8 describes the process of the plasma fountain in the equatorial anomaly area. The equatorial plasma fountain and equatorial anomaly arise from the vertical upward drift of plasma across the geomagnetic field lines at equatorial latitudes due to (ExB) forces and the subsequent downward diffusion of plasma along the field lines to higher latitudes under the influence of gravity and pressure gradient forces [Hanson and Moffett, 1966]. The plasma fountain and the anomaly exhibit north-south asymmetries about the geomagnetic equator mainly due to field-aligned plasma flows caused by neutral winds [Rishbeth, 1972 and Titheridge, 1995]. The result of this phenomenon leads to the F region electrodynamic (ExB) drift generates the plasma fountain and the anomaly symmetrically to the magnetic equator. The anomaly crests at both hemispheres occur under the impact of the neutral wind with larger plasma flow. During the daytime, when the drift is upward, the fountain rises to about 800 km altitude at the equator and covers about ±30° magnetic latitude. Outside the reach of the fountain, plasma flows toward the equator from both hemispheres. This convergence of plasma leads to the formation of an additional layer (called the G layer) within ±10° of the magnetic equator during the prenoon hours when the drift is large. At the magnetic equator, the maximum plasma concentration of the G layer can be greater than that of the F layer for a short time just before noon and when the drift starts to decrease. In the evening, soon after the drift turns downward, the fountain becomes a reverse fountain with a supply of ionization from both hemispheres from regions outside the fountain. The reverse fountain acts as the main source for the nighttime increase in ionization at equatorial anomaly latitudes, with some contribution from the prereversal strengthening of the forward fountain [Balan et al., 1995].

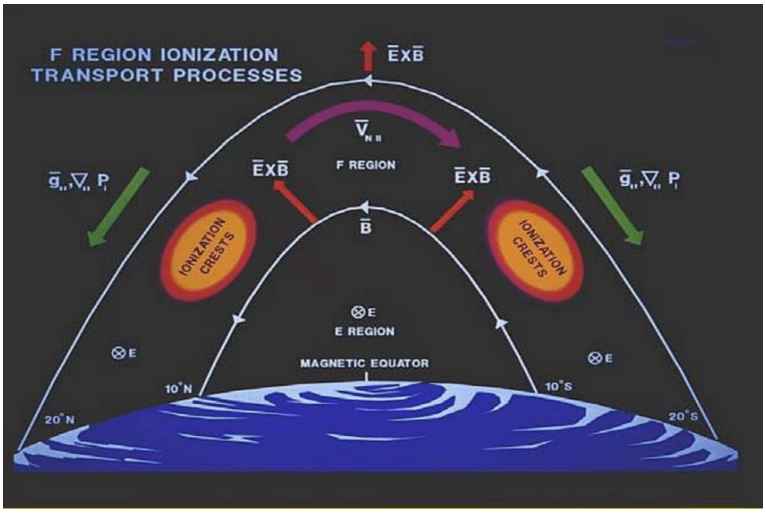

Figure 3.8. Principle of the fountain effect in EIA region [3.7]

[3.7] https://www.slideserve.com/ula/ionosphere-climate-studied-by-f3-cosmic-constellation

Table 3.3. Annual average values of the monthly maximum and mean VTEC

Year	CUSV		KUNM		NTUS		BAKO		XMIS		HKSL		PIMO		F10.7cm
	max	mean	max	mean	max	mean	max	mean	max	mean	max	mean	max	mean	
	0.99	1.00	0.95	0.99	0.99	0.98	1.00	0.98	0.99	0.95	0.97	0.93	0.92	1.00	
2007	-	-	53.2	12.5	39.7	12.9	63.2	13.5	48.8	10.7	-	-	37.0	13.5	73.1
2008	29.8	11.7	46.7	12.0	35.2	12.9	58.4	13.1	56.3	11.2	-	-	32.5	12.4	69.0
2009	30.1	12.0	46.1	12.1	31.4	12.3	53.3	12.9	48.5	11.6	-	-	31.8	12.5	70.5
2010	40.5	16.4	64.3	15.6	42.7	16.6	63.7	17.9	55.1	13.3	53.8	14.4	43.6	16.6	80.0
2011	62.2	25.3	88.8	23.1	74.4	24.0	93.4	26.6	92.3	20.9	72.7	21.2	65.7	26.1	113.3
2012	69.0	28.2	97.6	25.8	78.9	26.9	99.8	30.3	104.4	24.2	93.6	28.1	70.4	28.5	120.0
2013	69.7	29.1	-	-	70.7	28.0	94.6	31.9	105.6	24.9	96.5	29.4	73.1	29.8	122.7
2014	77.5	33.4	-	-	95.9	32.0	121.8	36.6	113.5	29.2	115.2	35.2	93.5	35.5	145.9
2015	69.8	29.7	-	-	96.1	32.8	113.2	31.0	97.8	23.4	109.0	27.4	72.6	29.1	117.7
2016	50.0	20.1	-	-	50.3	21.1	68.8	20.3	94.4	16.0	70.7	17.1	50.8	19.4	88.7
2017	41.2	15.9	-	-	37.9	14.5	55.2	16.5	67.2	12.6	56.0	12.9	42.6	15.2	77.3
Average	54.0	22.2	66.1	16.8	59.4	21.3	80.5	22.8	80.4	18.0	83.4	23.2	55.8	21.7	

Comparing the average value of VTEC among the months, we also see VTEC obtained in the equinoctial months like March (Mar), April (Apr) or September (Sep), October (Oct) has a much higher value than the rest of the year. This is a manifestation of the seasonal distribution of VTEC and will be analyzed in detail in Section 3.3. Besides, the maximum amplitude of VTEC in 2014 is approximately three times than that in 2009. Concerning this difference between the most active (2014) and weakest (2009) solar years in the 24th cycle of the Sun, we can realize the impact of solar activity on the amplitude of VTEC. This matter will be investigated in Sections 3.4 and 3.5.

3.3. Seasonal variations

Figure 3.9 shows seasonal variations of monthly maximum VTEC at station CUSV. The horizontal axis represents months and the vertical axis is VTEC in TECU. VTEC's monthly variations are shown for 11 years corresponding to different line types and colours. Such performance also facilitates the monitoring and comparison of VTEC between years, which will be discussed in the next section.

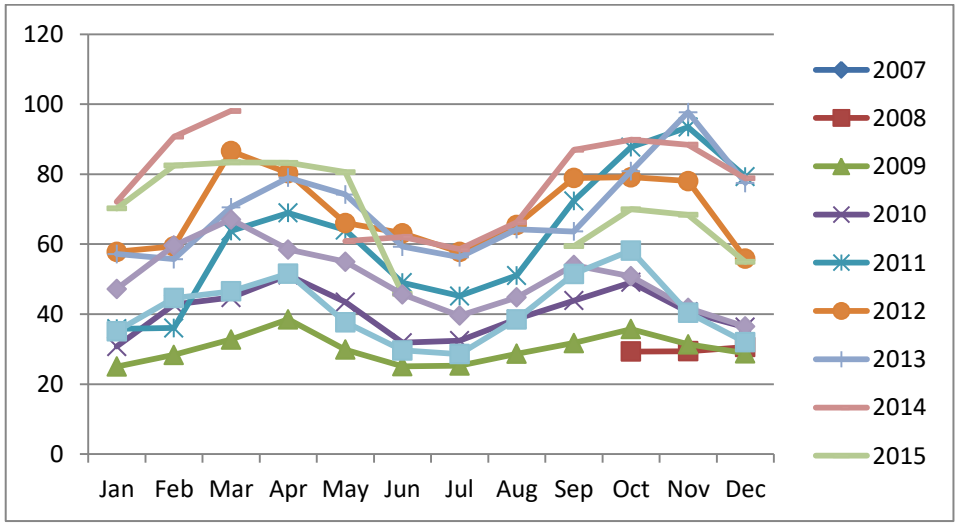

Figure 3.9. Seasonal variations of the monthly maximum VTEC at station CUSV

Whilst Figure 3.9 depicts the seasonal variation of VTEC at one station for all 11 years, Figures 3.10a-b show the monthly variation of VTEC for all stations in a year. Figures 3.10a and 3.10b correspond to 2010 and 2014 respectively. Note that the data in 2014 at station KUNM is missing. From these figures, it can be recognized the seasonal changing trend of VTEC as follows: reaching its maximum in the equinoctial months, which are the vernal equinox (March - April), and the autumnal equinox (September - October) and minimum in winter and summer months. Generally, the seasonal variation depicts a semi-annual distribution. This changing trend is completely similar to that of ionospheric scintillation, which will be discussed in Chapter 4 (Figure 4.9).

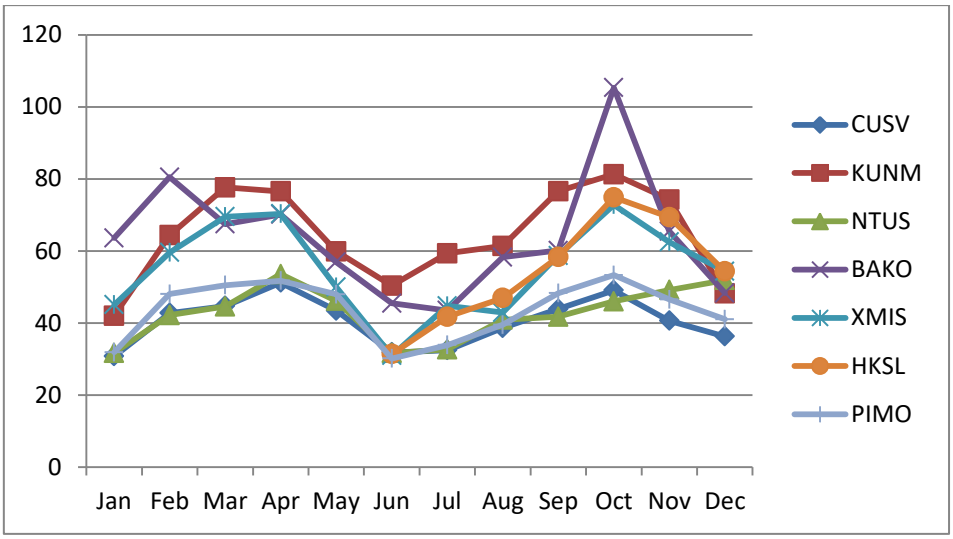

Figure 3.10a. Seasonal variations of the monthly maximum VTEC in 2010

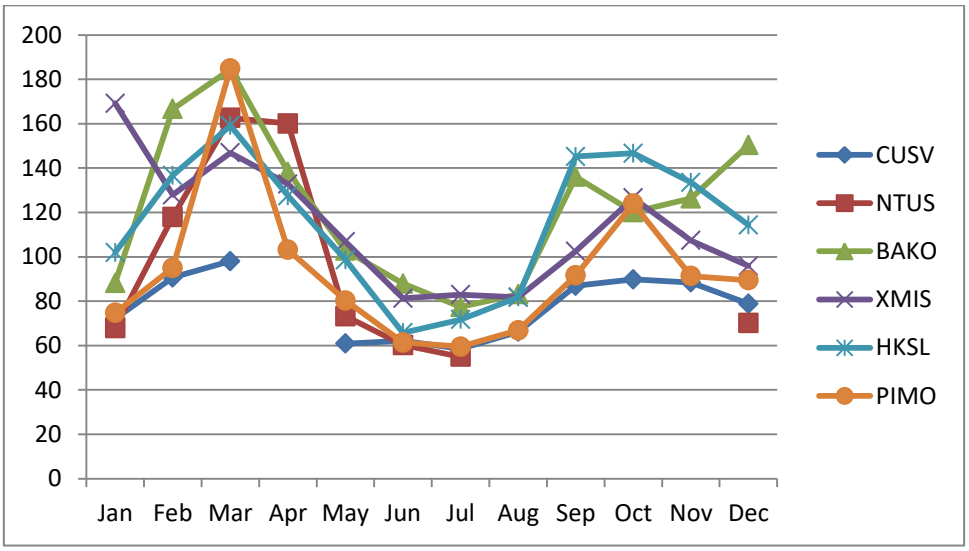

Figure 3.10b. Seasonal variations of the monthly maximum VTEC in 2014

As mentioned in Section 3.1, VTEC has been computed at the sampling rate of GNSS observations i.e. 30 seconds. Thus, there are 2880 VTEC values calculated per day in case the RINEX file provides full data of 24 hours. To study the VTEC variations in long-term, I calculate the mean value of VTEC for each day based on 2880 VTEC results. The results are then illustrated in 11 years (4018 days) as shown in Figures 3.11a-g.

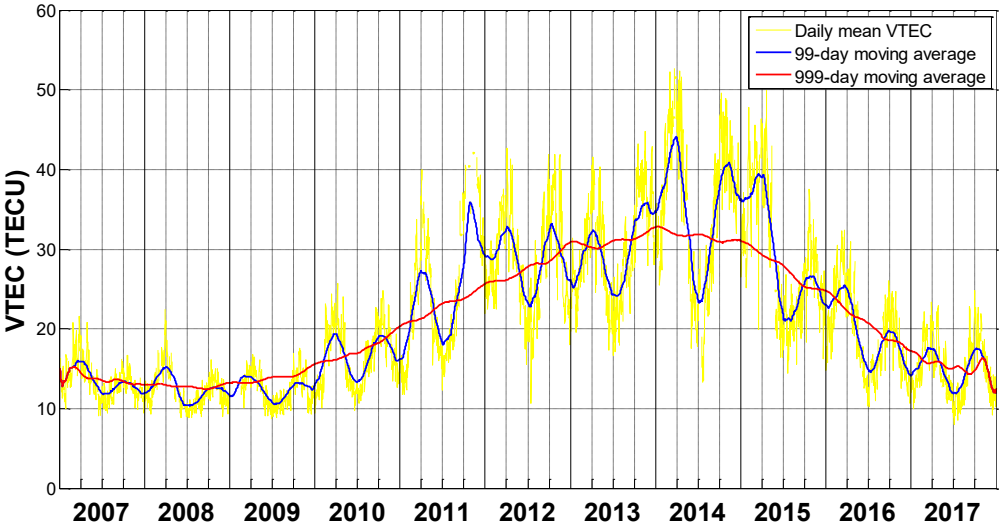

Figure 3.11a. Daily mean VTEC during SC24 at station PIMO

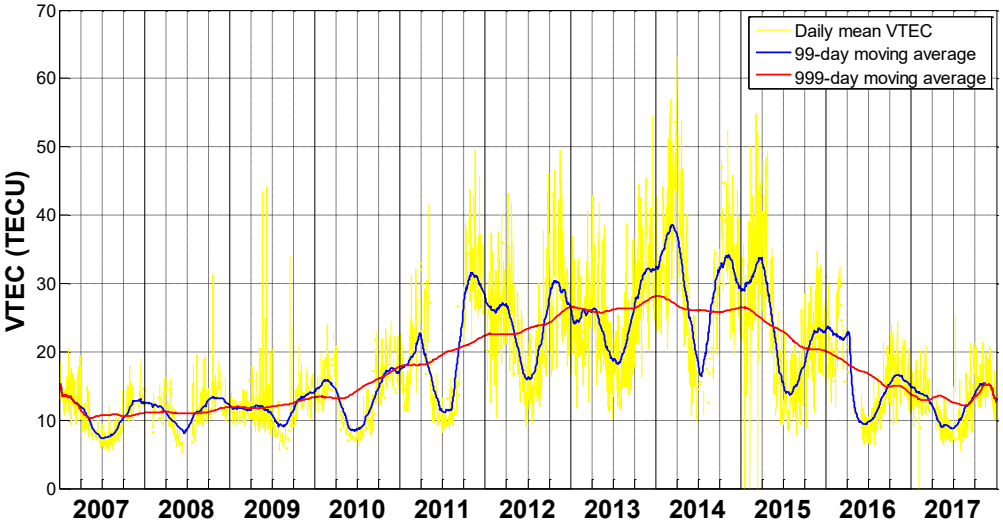

Figure 3.11b. Daily mean VTEC during SC24 at station XMIS

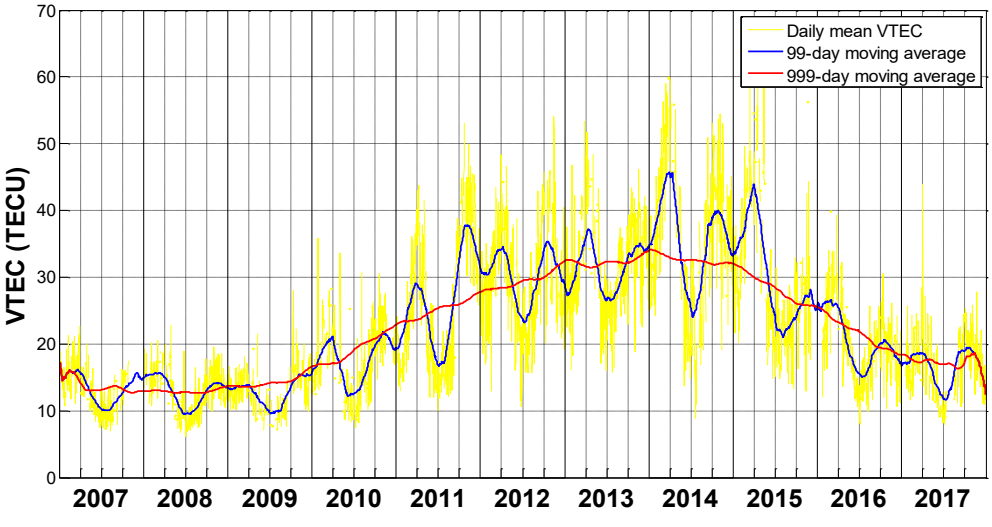

Figure 3.11c. Daily mean VTEC during SC24 at station BAKO

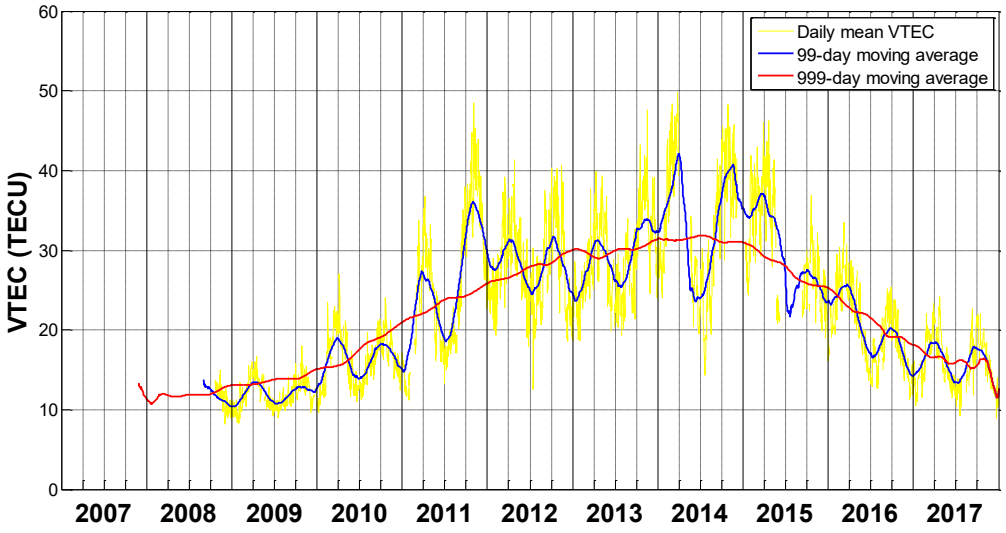

Figure 3.11d. Daily mean VTEC during SC24 at station CUSV

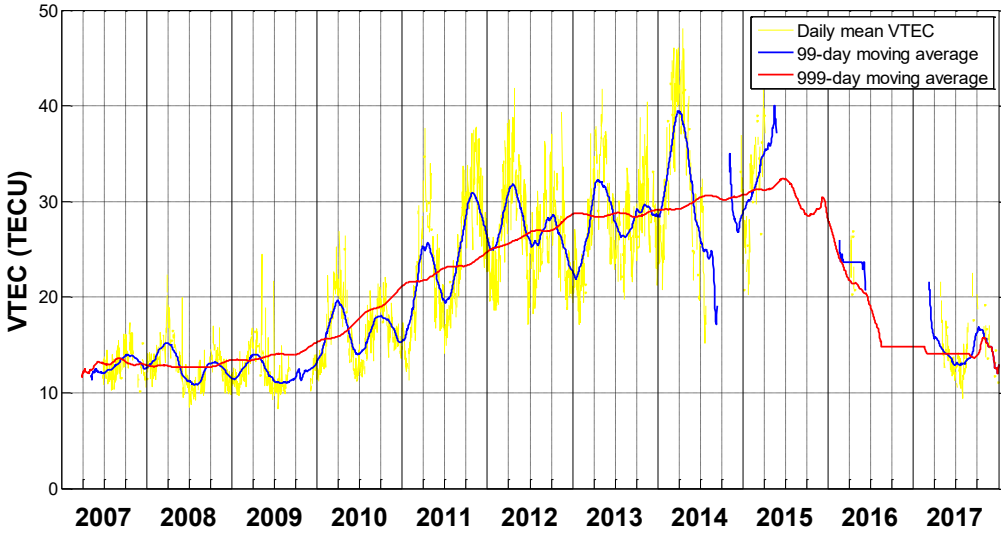

Figure 3.11e. Daily mean VTEC during SC24 at station NTUS

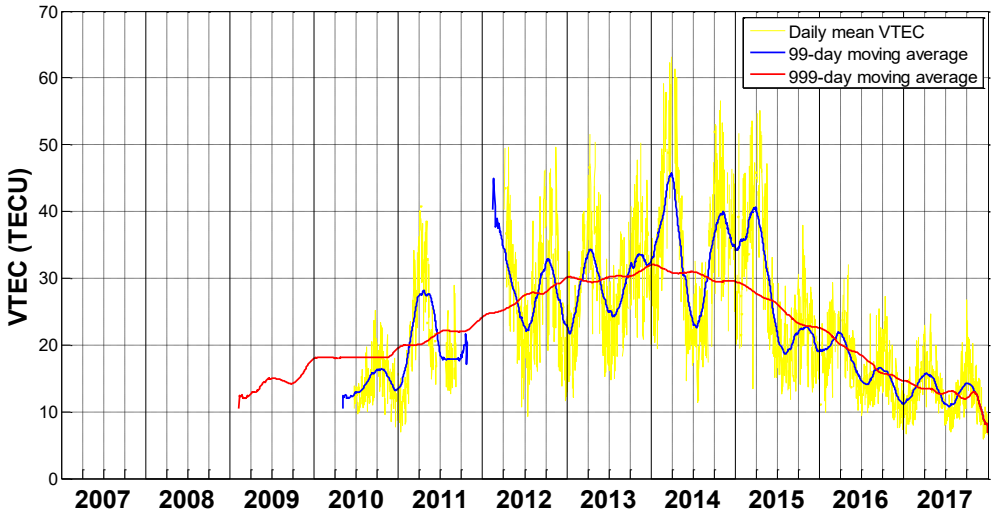

Figure 3.11f. Daily mean VTEC during SC24 at station HKSL

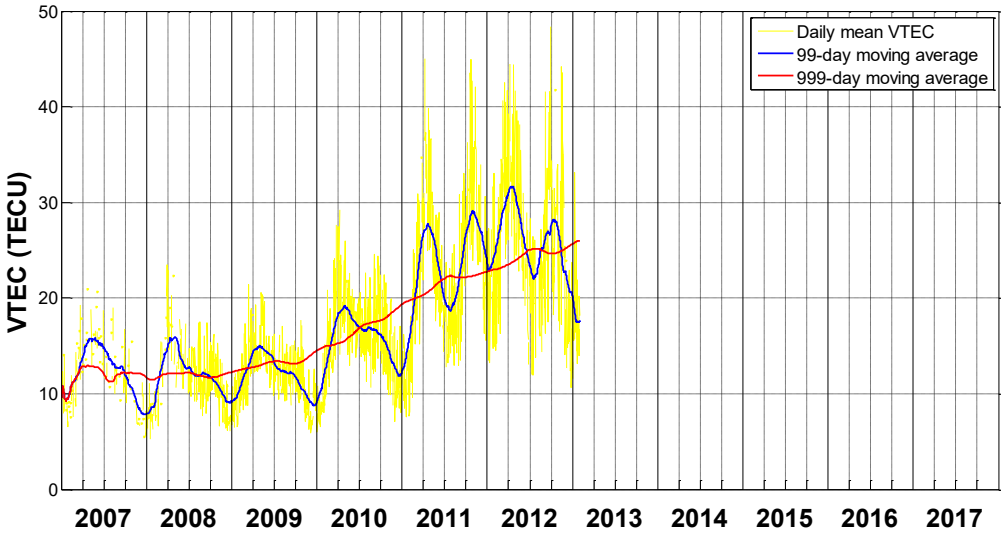

Figure 3.11g. Daily mean VTEC during SC24 at station KUNM

In these figures, I also use the moving average smooth function, which is commonly used in time series analysis, to smooth out short-term fluctuations and highlight longer-term trends of VTEC. In Figures 3.11a-g, the yellow line is daily VTEC mean, blue and red lines are the moving average smooth functions with spans are 99 days and 999 days, respectively. The semi-annual variations of the ionosphere can also be observed in these figures with two ups and downs each year. This trend reflects a seasonal asymmetry in the solstices and equinoxes or in other words, the seasonal variation of the ionosphere shows a semi-annual pattern.

Suppose we need to smooth the vector y to obtain the result yy = smooth(y). This function smooths the data in the column vector y using a moving average filter. Results are returned in the column vector yy. Assume the span for the moving average is 5, then the first few elements of yy are given by:

yy(1) = y(1)
yy(2) = (y(1) + y(2) + y(3))/3
yy(3) = (y(1) + y(2) + y(3) + y(4) + y(5))/5
yy(4) = (y(2) + y(3) + y(4) + y(5) + y(6))/5
...

For the moving average method, span must be odd. With 4018 days in 11 years, the chosen spans are approximately 100 days and 1000 days in order to properly describe the essence of the long-term variations of VTEC.

The temporal variability characteristics of TEC in the Southeast Asia region are similar to the research results for the Indian region as [Rama Rao et al., 2006] concluded. So far, seasonal variability of the ionosphere has been carefully studied and explained in many papers. The explanation for this phenomenon can be summarized in several approaches as follows: because of the seasonal changes in atmospheric composition [Wu et al., 2004 and Rama Rao et al., 2006]; due to the combined effect of the solar zenith angle and magnetic field geometry [Wu et al., 2004 and Bagiya et al., 2009]; the daytime E×B drift velocities are larger in the equinoctial months and winter months than in the summer months resulting in semi-annual variation [Olatunji, 1967, Scherliess and Fejer, 1999, Bailey et al., 2000, and Liu et al., 2006, 2009]; owing to the variation in the noon solar zenith angle, which is an important factor for the production of ionization [Olatunji, 1967, Bailey et al., 2000, and Liu et al., 2006, 2009].

In the context of this research, the seasonal variations of TEC can be explained based on the physical mechanism of the ionosphere. Theoretically, the Sun's intensity of radiation hitting the Earth is highest in the summer, and then the rate of ionization due to radiation is also the highest. In other words, the ion generation rate in the ionosphere in summer is the largest of the year. According to this theory, TEC can reach a peak in the summer. But the actual results show that TEC's seasonal variability can be considered as opposed to the increase in the rate of ionization. Such results are thought to be related to the equilibrium between the production process and the disappearance of ions in the ionosphere. As already known, the main neutral gas components in the atmosphere are O, N_2 and O_2. Thus, the main ions generated by ion photochemical and the interaction in the atmosphere are O^+, NO^+ and O_2^+ according to photochemical reaction equations. In the F region of the ionosphere, the ion generation rate is directly proportional to the concentration of atomic oxygen (O) and the ion recombination increases mainly with the increase of molecular nitrogen density (N_2). According to the global electron model, atomic oxygen density declines sharply in the summer and increases in the equinox seasons, the N_2 component increases in the summer and dominates the atomic oxygen. Thus, in the summer, the rate of plasma generation decreases with the rate of recombination increased significantly. As a result, the density of electrons in the ionosphere decreases and in the equinox months, the ion generation rate increases leading to electronic density increases and reaches its maximum.

Diurnal and seasonal variations of the ionosphere can also be identified in the temporal - latitudinal VTEC maps in Figure 3.12. This kind of map is produced from the observations (RINEX file) at all IGS stations in the research area during the study period (2007 - 2017) and it indicates time and latitude distribution of VTEC. Methods of establishing this type of map will be introduced in Chapter 6, data used is monthly mean VTEC. In this section, I only show the illustrations for 2012. Similar to other maps used to determine the variation of VTEC over time, in this figure, the horizontal axis represents UTC. As the longitude of the research area is 105^{o}, so the LT is equal to UTC plus 7 hours. The vertical axis, instead of showing the intensity of VTEC as usual, is used to indicate geographic latitude. The intensity of VTEC can be estimated by colour based on the colour bar scale on the right side of the images, its unit is TECU. It can be seen that this type of map not only provides information about the temporal variations but also the spatial variations of the ionosphere. With all available data in the research area, the ionosphere can be investigated in the latitude area range from about 10^{o}S to 30^{o}N at the position of 105^{o}E longitude. At first glance, we can recognize the two crests of equatorial anomaly exist symmetrically to the magnetic equator. Therefore, using this map would be very convenient for the study of EIA. This issue will be extensively studied in Chapter 6.

From Figure 3.12, it can be seen that activity intensity of the ionosphere is strongest in March, April and September, October, November (equinox months) and gets weakest in June, July and December (solstice months). Daily variations are also evidently recognizable when VTEC reaches its highest value just after lunch, and then maintains low values throughout the evening and night until early morning the next day. However, its value and variability also greatly depend on the latitude, the amplitude gets stronger in places close to the crests of the anomaly. For further study the northern and southern hemispheres, additional GNSS stations need to be added in these areas. Or a simpler way is to take advantage of the global VTEC data (GIM) from the IONEX file (this will be presented in Chapter 6).

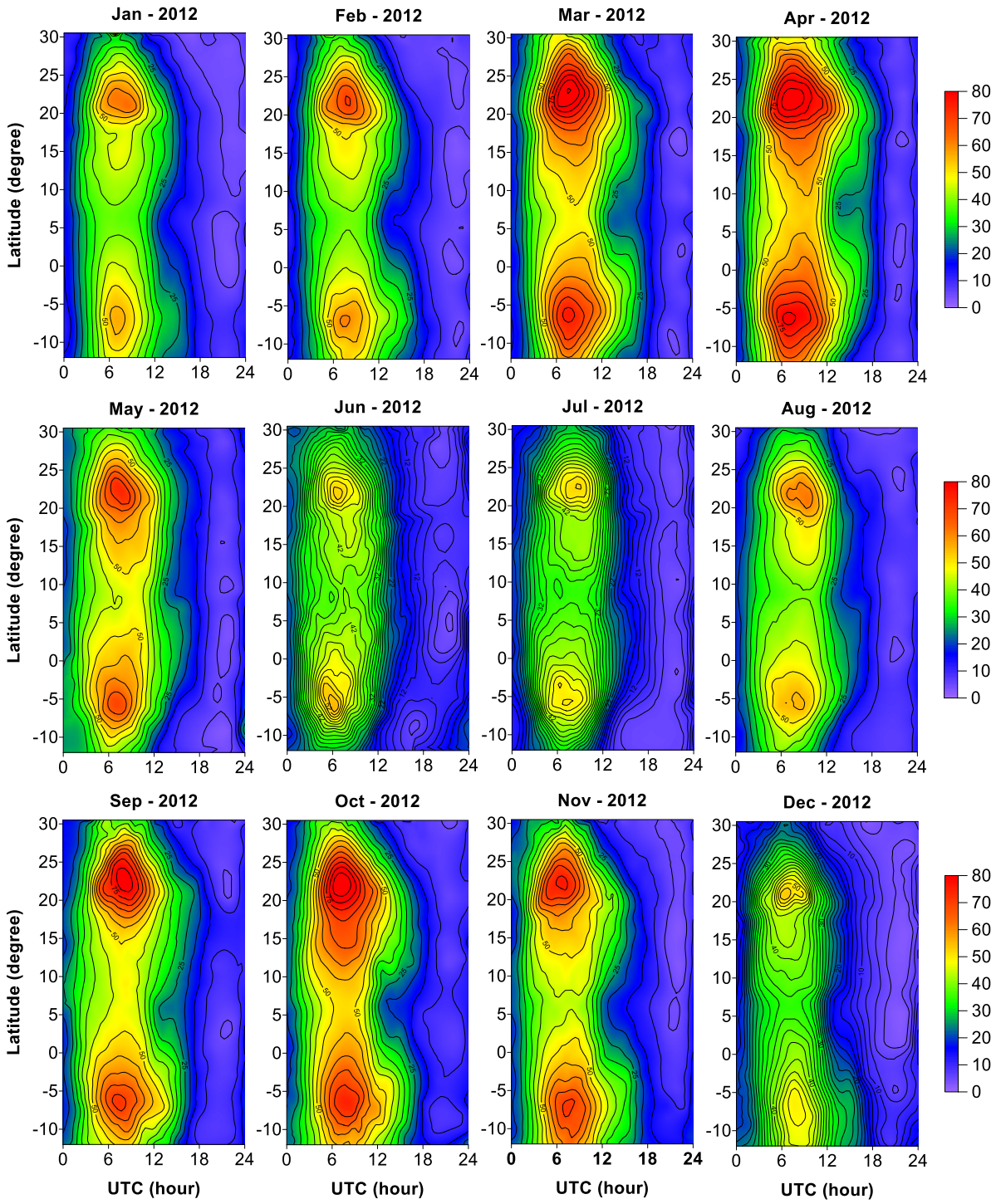

Figure 3.12. The (monthly mean) temporal - latitudinal VTEC maps in 2012 (LT=UTC+7 h, TECU unit)

3.4. Annual variations

The purpose of the 11-year VTEC calculation is to have enough databases for the analysis of the annual changes of the ionosphere, as well as to consider its interaction concerning the phase of solar activity. Figures 3.13a-b (horizontal axis is 11 years starting from 2007,

vertical axis is TECU) graph the data given in Table 3.3 with the data illustrating the annual average of the largest VTEC (Figure 3.13a) and the mean VTEC (Figure 3.13b) in each month. The plots best illustrate the similarity between the variability of the ionosphere and the intensity of the Sun's activity, that is VTEC reached the lowest values in the period of 2008 - 2009, then increased steadily in the following years from 2010 to 2013 and peaked in 2014 before entering the period of decline from 2015 to 2017.

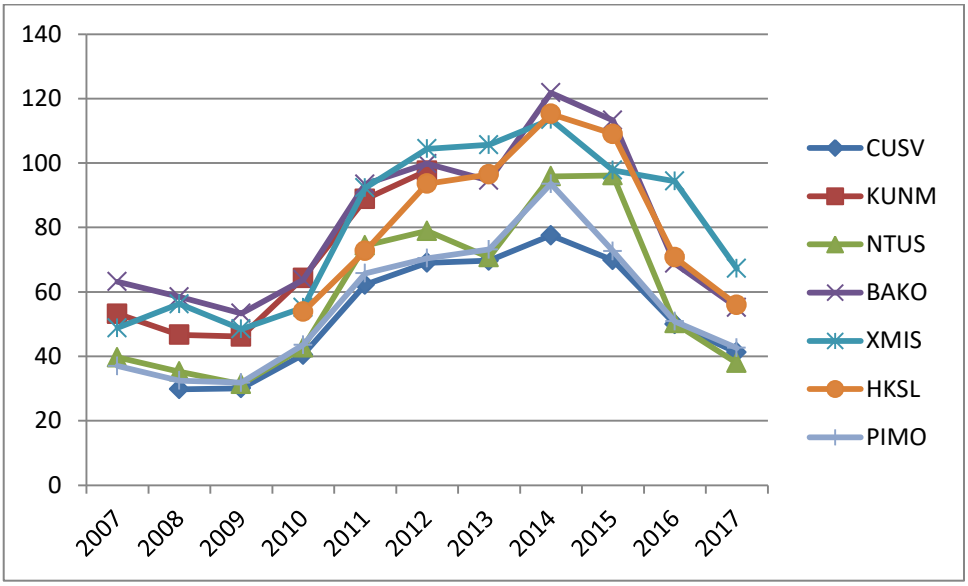

Figure 3.13a. Annual average variations of the monthly maximum VTEC

Figure 3.13b. Annual average variations of the monthly mean VTEC

Figures 3.14a-g show the VTEC maps of seven stations which have been established for the whole year during 11-year of SC24, the white areas indicate no data. As the receiving stations are at different latitudes, time is converted into local time aims to be more physical and clear to show diurnal variation of VTEC. In these figures, the horizontal axis represents local time, the vertical axis is symbolized in months to point out seasonal variations of VTEC. Bar colour scale is the benchmark for evaluating VTEC amplitude, it is the same for all maps to facilitate VTEC comparison between years. This type of map shows all kind of temporal variations of the ionosphere including daily, seasonally, and yearly. The trend of quarterly variation of VTEC is straightforward in each year, nevertheless, this trend also depends on the phase of the Sun's cycle. Indeed, in both Figures 3.11 and 3.14, the amplitude of VTEC at each station is greater in autumn than in spring for 2009 - 2013 periods (increasing phase of SC24), whereas for 2014 - 2016 (decreasing phase of SC24), the amplitude of VTEC is greater in spring than in autumn. Thereby, in addition to the seasonal changes that occur regularly every year, the ionosphere also varies according to the phase of solar cycle with the following rule: VTEC in two equinox months changes uniformly along with the uptrend or downtrend of solar phase. This feature is not shown clearly from 2007 to 2009, which is the transitional period between the 23^{rd} and 24^{th} of solar cycle.

In Figures 3.14a-g, with more than 90% data collected, the annual variability comparisons at PIMO, XMIS and BAKO stations are more clearly identifiable than the rest. It can be seen in all figures, the map for 2014 always reflects the remarkable value of VTEC compared to the remaining years, followed by the adjacent years of 2013, 2015 and somewhat of 2012. Meanwhile, the heat map for the years from 2007 to 2010 and 2016, 2017 is rather quiet as the solar radiation operates at a relatively low intensity during these years. In general, the annual variation trend of the ionosphere exhibited in these figures is completely similar to the trend shown in Figure 3.13 and have a good agreement with the 11-year period of the Sun. This agreement is entirely understandable since the state of the ionosphere (concerning the radio propagation) primarily depends on solar radiation. Other noise factors such as solar wind, solar flares, CME and coronal holes may also have a partial impact on the ionosphere but it can only affect in a short term, while in the long term the solar radiation is, of course, still a crucial factor. To find out more about this conformity, I calculate the correlation coefficients between VTEC and the solar indices. This issue will be considered in the next section.

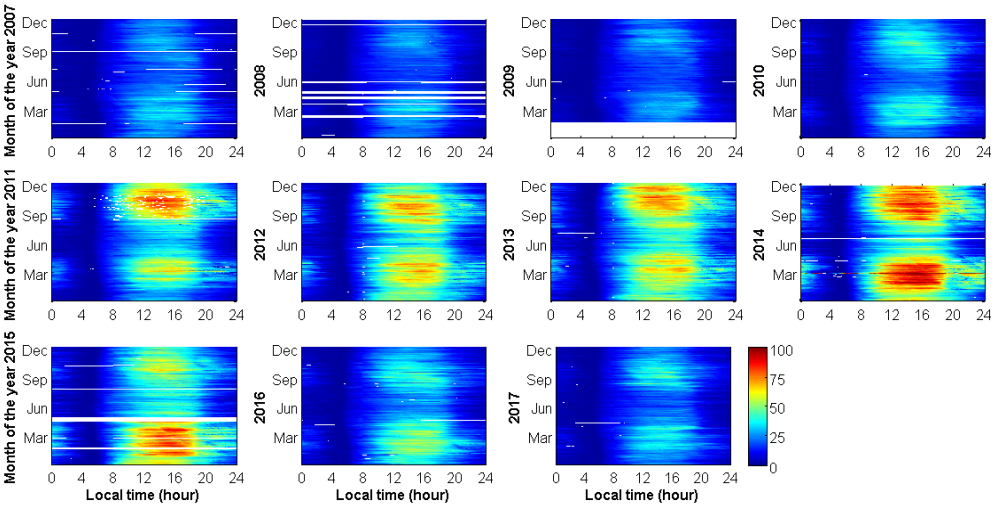

Figure 3.14a. VTEC map at station PIMO during SC24

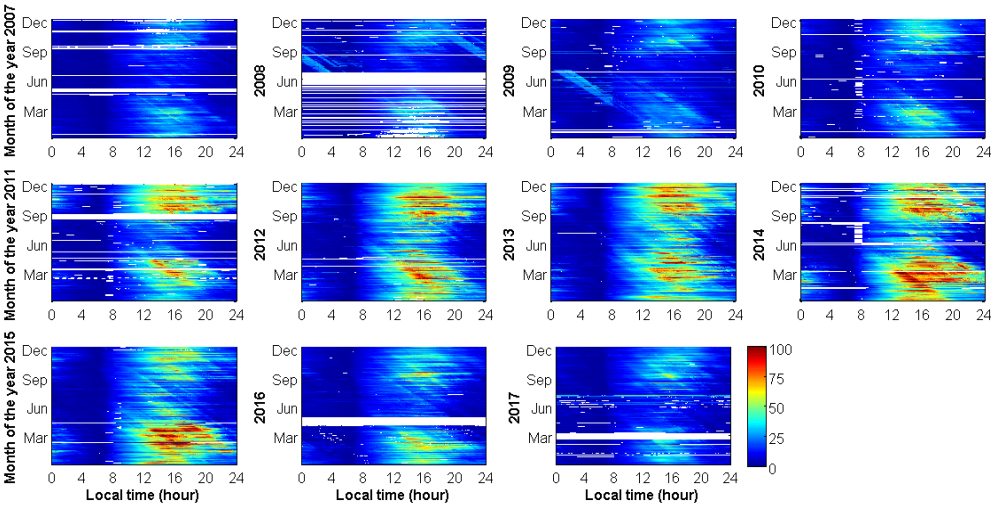

Figure 3.14b. VTEC map at station XMIS during SC24

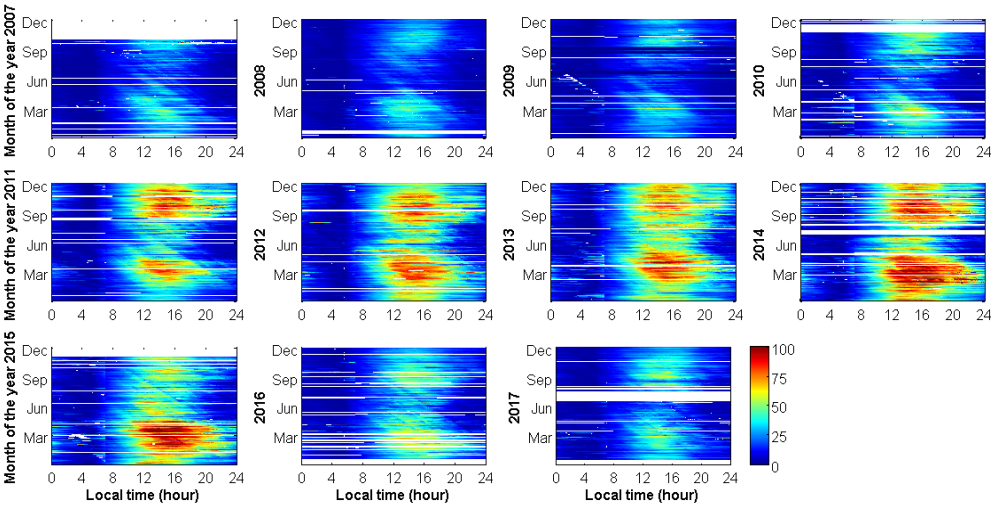

Figure 3.14c. VTEC map at station BAKO during SC24

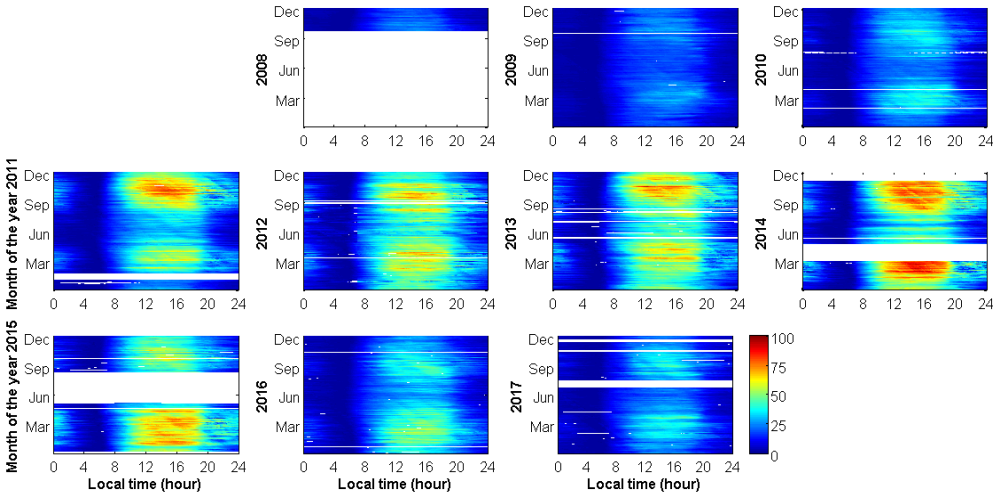

Figure 3.14d. VTEC map at station CUSV during SC24

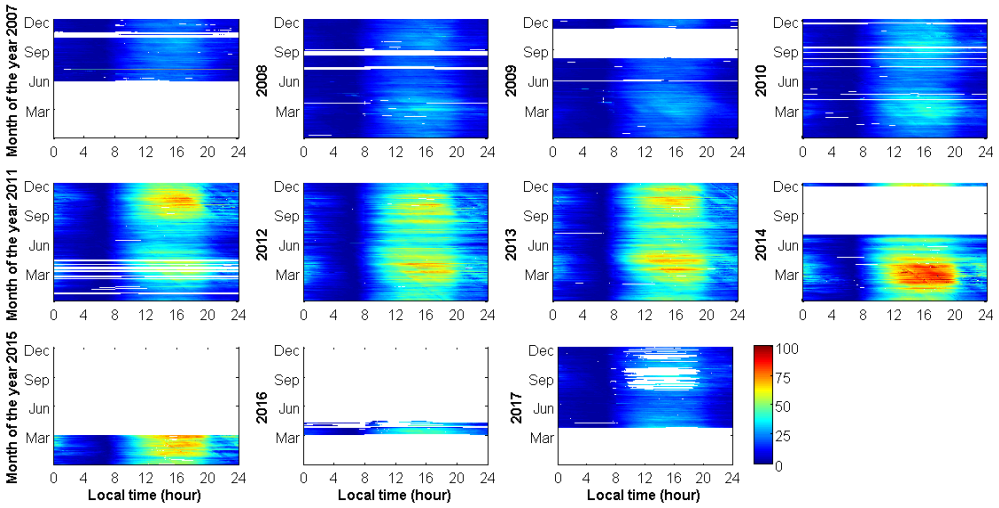

Figure 3.14e. VTEC map at station NTUS during SC24

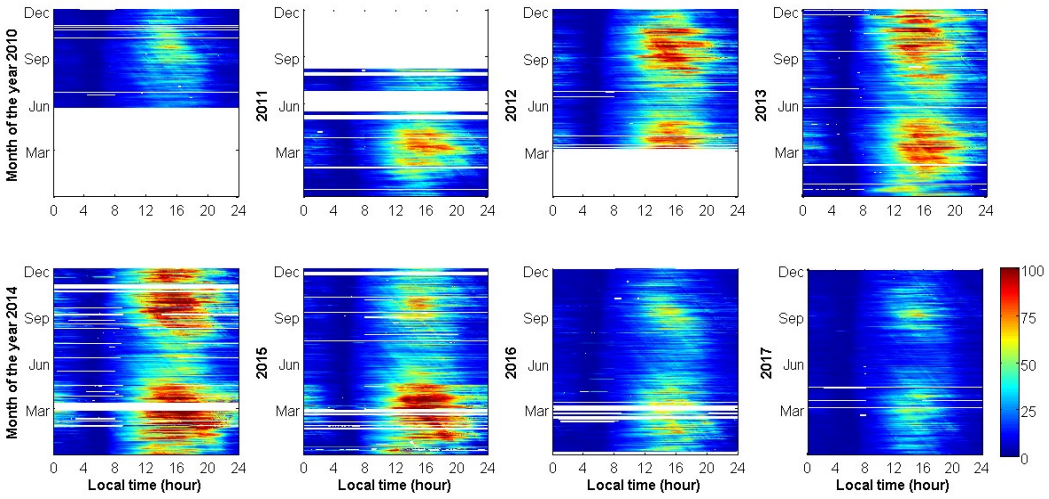

Figure 3.14f. VTEC map at station HKSL during SC24

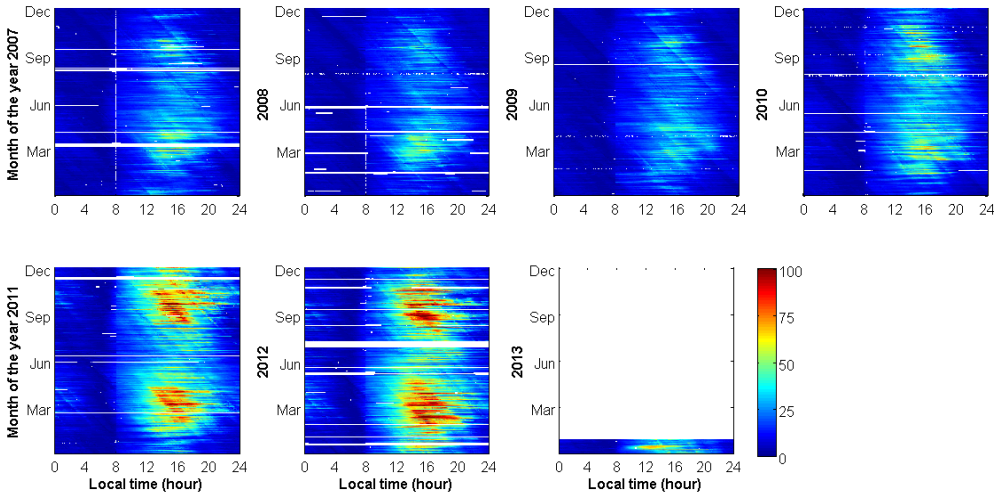

Figure 3.14g. VTEC map at station KUNM during SC24

Overall, the annual trend of the ionosphere has been inspected in this section. Nonetheless, if paying close attention to the period 2010 - 2014, although this is an upward phase of the solar cycle, VTEC has made a slight change in the amplitude of fluctuations at the end of 2012 and early 2013. This modest but abnormal change is also visible in Figures 3.13a-b. Specific calculation results of the change of the mean value of VTEC (including monthly mean and monthly maximum) and solar activity index (F10.7) in different stages of SC24 are displayed in Table 3.4, therein VTEC calculation results are averaged from seven stations according to the data given in Table 3.3. Specifically, while in the period 2010 - 2014, the average annual growth rate of monthly mean VTEC was 28.3%, this index was 4.0% from 2012 to 2013. Therefore, only in the period of 2012 - 2013, the growth rate of monthly mean VTEC reduced from 36.9% previously to 4.0%, even the average (of seven stations) of maximum monthly VTEC not only does not increase but also decreases by 1.1% (compared to the previous 34.9% increase) during this stage. Also in this table, the correlation coefficients between yearly averaged of monthly mean VTEC and yearly averaged of monthly maximum VTEC with the F10.7 index are very high, respectively 0.98 and 0.99. This demonstrates a high degree of consistency between the calculated results and the official published solar indices. Based on the background of Figure 3.1, I describe in detail (percentage of increase or decrease) the variation in amplitude of fluctuation of monthly maximum VTEC in 11 years of research as shown in the Figure 3.15. Of course, these results are only based on data obtained at a few IGS stations in the Southeast Asia region.

Table 3.4. Percentage change of yearly averaged VTEC and F10.7

Period	Monthly mean VTEC (%)	Monthly maximum VTEC (%)	F10.7cm (%)
2010 - 2012	+36.9	+34.9	+25.0
2012 - 2013	+4.0	-1.1	+2.3
2013 - 2014	+16.8	+21.7	+18.9
2010 - 2014	+28.3	+26.7	+20.6
2014 - 2017	-18.9	-17.1	-15.7

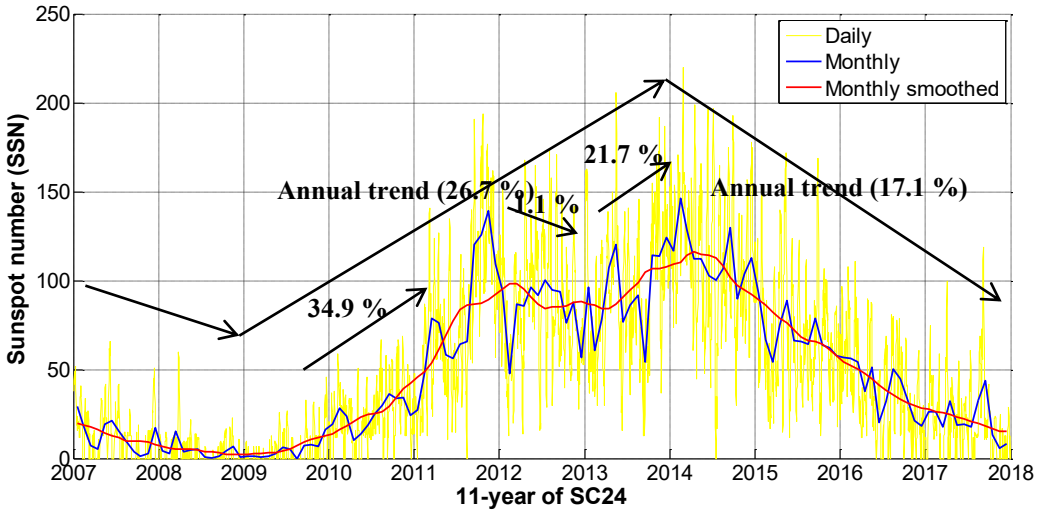

Figure 3.15. The actual variation trend of monthly maximum VTEC's annual average compared with the SSN of SC24

3.5. Correlation between VTEC and solar indices

As mentioned in Section 3.1, the solar radio flux at 10.7cm (2800 MHz), called F10.7 index, is an excellent indicator of solar activity. It is one of the longest-running records of solar activity. Among the solar indices, this index correlates well with the sunspot number and is commonly used in space weather research. In the field of geodesy, it can be used to study radio propagation which is a key point of all space geodetic techniques. The F10.7 index has been measured consistently in Canada since 1947 and can be made reliably and accurately from the ground in all weather conditions. It has the unit of SFU. Usually, this index can vary from below 50 SFU to above 300 SFU mainly depends on the active state of the Sun. Actual observation results in the period of 2007 - 2017 showed that this index reached the maximum value of 255.0 SFU on June 22nd 2015 (DOY 173) and reached the minimum value of 64.6 SFU on November 9th 2017 (DOY 313).

Meanwhile, the index most commonly used to characterize the intensity of solar activity in all areas of research is generally the sunspot number (SSN). It is determined by counting sunspots areas on the Sun. With such a principle, this index is somehow not so straightforward and sometimes the final result from different research centres is not identical. There are two official SSN indices in common use: the Boulder Sunspot Number and the International Sunspot Number. Therein, the first one is computed by the NOAA Space Environment Center using a formula devised by Rudolph Wolf in 1848 [3.8]:

$$R=k\,(10g+s) \tag{3.1}$$

where R is the sunspot number; g is the number of sunspot groups on the solar disk; s is the total number of individual spots in all the groups; and k is a variable scaling factor (usually <1) that accounts for observing conditions and the type of telescope (binoculars, space telescopes,…). Each observatory provides their own k factor and the final result expresses in daily value is obtained by combining the data. The second one, meanwhile, has been being produced by the Solar Influences Data Center in Brussels, Belgium. Both the Boulder and the International numbers are calculated from the same basic formula, but they incorporate data from different observatories resulting in the Boulder number is usually about 25% higher than the International Sunspot Number. The SSN index can range from 0 to over 200. During the last 11 years, the largest SSN index recorded is 220 occurring on 27.02.2014 (DOY 58).

In this section, I rely on the two above solar indices to evaluate our VTEC results and also to examine the correlation between the ionosphere alteration (which is characterized by TEC) and the solar cycle. Only for the daily mean VTEC, I add the Lyman alpha (Ly-α) index which is mainly used in physics, aims to compare with these two widespread solar indices. To measure the strength of the relationship between VTEC and solar indices, an equation of correlation coefficient has been used. The express of this equation is as follows:

$$Correl(X,Y) = \frac{\sum(x-\bar{x})(y-\bar{y})}{\sqrt{\sum(x-\bar{x})^2 \sum(y-\bar{y})^2}} \tag{3.2}$$

where: x is VTEC with different calculation options; y is the solar index (Radio flux F10.7cm or SSN); and $\bar{x}$ and $\bar{y}$ are the average value of x and y. This is the “Pearson product-moment” correlation which is one of the most commonly used correlation coefficients. It measures the strength and direction of the linear relationship between two variables. Its value can range from −1 to +1, where ±1 indicates the strongest possible agreement and 0 the strongest

possible disagreement. The strength of the relationship varies in degree based on the value of the correlation coefficient. Usually, a correlation coefficient with an absolute value not less than 0.8 would represent a strong relationship. In case formula (3.2) gives a result of 0.9 or greater, it can be considered that x and y vary completely uniformly.

VTEC has been calculated to compare with the solar indices including the monthly maximum, the monthly mean and the daily mean. In a single day, I have 24x60x2=2880 results, in a single month I have about 2880x30=86400 results, the results in one year is around 2880x365=1051200, and in total 11 years, I have about11563200 results. With different consideration periods such as daily, monthly or yearly, the highest VTEC value is collected and the average VTEC value is computed. Then apply formula (3.2) to calculate the correlation coefficients that produce the results shown in Table 3.5.

Table 3.5. Correlation coefficients between VTEC and solar indices

Stations	Monthly maximum (1)		Monthly mean (2)		Daily mean (3)			Average
	SSN	F10.7	SSN	F10.7	SSN	F10.7	Ly-α	
BAKO	0.66	0.72	0.83	0.87	0.72	0.76	0.81	0.80
CUSV	0.87	0.89	0.87	0.90	0.77	0.83	0.87	0.85
KUNM	0.86	0.85	0.82	0.80	0.70	0.72	0.76	0.76
NTUS	0.72	0.74	0.89	0.89	0.82	0.85	0.89	0.87
HKSL	0.64	0.73	0.77	0.83	0.63	0.70	0.76	0.74
XMIS	0.64	0.65	0.78	0.85	0.64	0.71	0.74	0.75
PIMO	0.83	0.86	0.86	0.90	0.76	0.82	0.86	0.84

In Table 3.5, the last column is the mean correlation coefficient of all corresponding coefficients. From this table, some points can be drawn as follows:

- The correlation coefficients between the monthly mean VTEC (group 2) and the solar indices are better than the monthly maximum (group 1) and the daily mean (group 3) as all these factors corresponding to it reach around 0.85. In which, three stations CUSV, NTUS, and PIMO all have a correlation coefficient of approximately 0.9.
- In group 1 the results at CUSV station (average 0.88) are most similar to the solar indices.
- As the average of the three solar indices at all stations in group 3 does not exceed 0.8, the correlation coefficient calculated by day (group 3) seems to give lower value than the correlation coefficient calculated by month (groups 1 and 2). According to the basic principle of time series analysis, this is completely understandable since the monthly data series often gives more generalization than the daily data series.

- Among the three solar indices used, the F10.7 and Lyman alpha indices are considered to be more consistent with the VTEC results since the average correlation coefficient calculated is approximately 0.80, the corresponding number for SSN index is about 0.77.
- The result of VTEC at CUSV station (average correlation coefficient is 0.85) is closest to the trend of solar cycle in the research period. The best correlation index is also found at this station, which is the correlation coefficient between monthly mean VTEC and the F10.7 index. Meanwhile, the results at KUNM, HKSL, and XMIS stations showed little similarity (less than 0.80) to the solar indicators, this properly partly due to the lack of data at these stations. In addition, HKSL station also noted the lowest correlation factor of 0.63 between the daily mean VTEC and the SSN index.

Figures 3.16a-b illustrate an example of the correlation between monthly maximum VTEC and the solar indices at CUSV station (F10.7 index corresponds to Figure 3.16a, SSN index corresponds to Figure 3.16b). The horizontal axis is time representing the study period, the left vertical axis is the TEC value in TECU, and the right vertical axis is the solar indices. Note that some empty columns are due to lack of data in the corresponding months at CUSV station. These plots give a visual view of the interaction between (monthly maximum) VTEC and solar indicators. The seasonal variations of VTEC and its dependence on the solar cycle phase can be also somewhat realized.

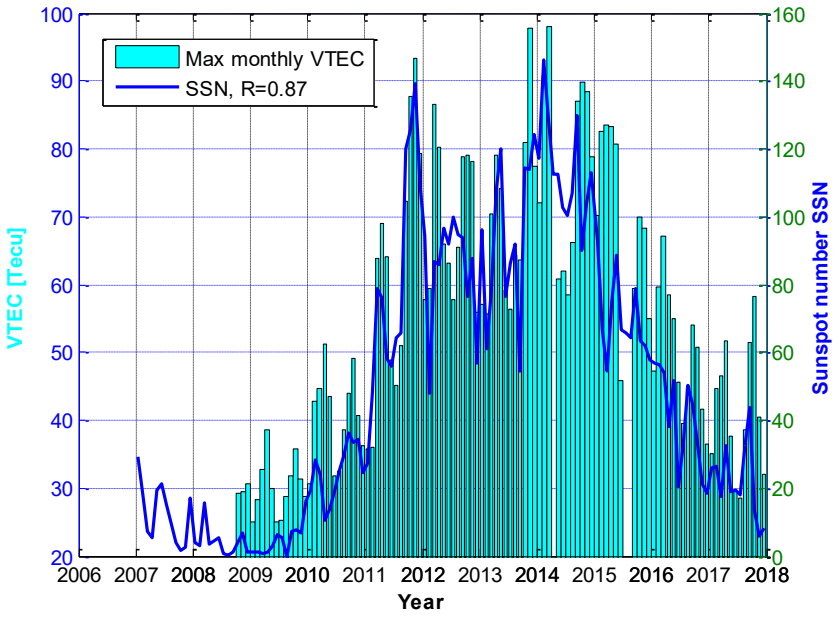

Figure 3.16a. Correlation between monthly max. VTEC and the SSN index at station CUSV

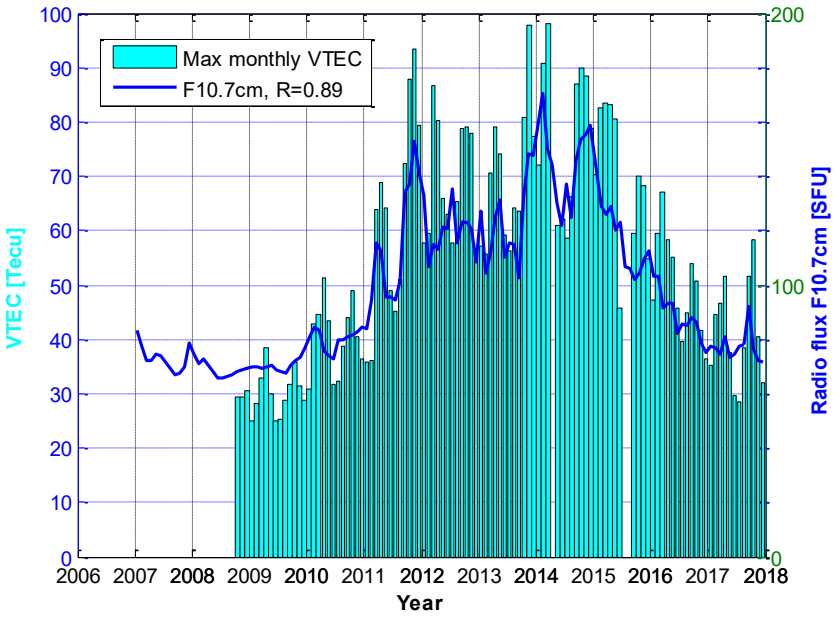

Figure 3.16b. Correlation between monthly max. VTEC and the F10.7 index at station CUSV

Figures 3.17a-b describe the monthly mean VTEC of seven stations and their correlation factors with the solar indices. The description of the coordinate axis notation is similar to the Figures 3.16a-b. Stations are distinguished by its colour. The dashed blue line represents for mean VTEC, but this is not the mean VTEC calculated from seven stations but the mean VTEC for the whole Southeast Asia region attained from the IONEX data of GIM (this result is obtained by the calculations in Chapter 6). It can be realized that VTEC obtained from IONEX file in the Southeast Asia region has a better level of compliance with the F10.7 index (Corr. factor 0.89) than that of SSN index (Corr. factor 0.87). These figures visually depict the similarities between monthly mean VTEC and the indications of solar cycle. Once again, the annual variation of the ionosphere as indicated in Figure 3.15 is reproduced in these plots, which is that during the 2010 - 2014 growth period, VTEC showed signs of slowing down a bit in early 2013 before returning to the usual cycle. Besides, the seasonal and annual variability of the ionosphere can also be exhibited in these figures.

[3.8] https://spaceweather.com/glossary/sunspotnumber.html

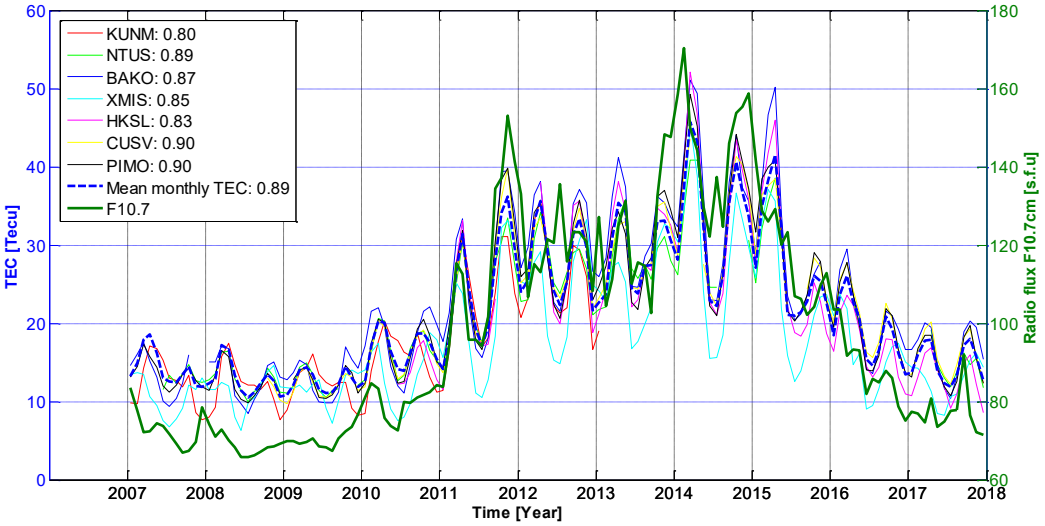

Figure 3.17a. The monthly mean VTEC of seven IGS stations and its correlation coefficient with the F10.7 index

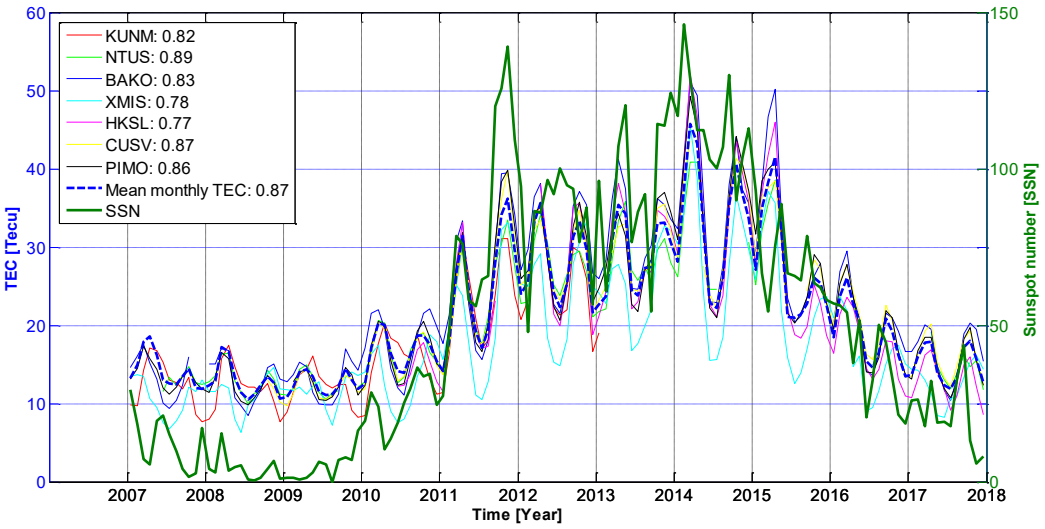

Figure 3.17b. The monthly mean VTEC of seven IGS stations and its correlation coefficient with the SSN index

3.6. Chapter summary

In this section, I summarize the main contents and some significant results obtained in this chapter. These include:

- Section 3.1 provides a brief introduction to the solar cycle, which highlights the important impact of the Sun on the ionosphere. Introducing the solar indices currently in use and emphasizing on the two solar indices: radio flux F10.7cm and the International Sunspot

Number (SSN), which are befitting and widely applied in the research of radio propagation.

- Also in this section, the research area, study period and usage data are introduced. Specifically as follows: the research region is Southeast Asia stretches from 15^{o}S to 30^{o}N latitude and from 95^{o}E to 130^{o}E longitude; study period is a full solar cycle with 11 years starting from the beginning of 2007 until the end of 2017; data is all available IGS stations over the research area during the study period. They are KUNM, HKSL, PIMO, CUSV, NTUS, BAKO, and XMIS stations located from the north to the south. Nearly 80% of GNSS measurements were collected at seven stations during 11 years (in which three stations reached over 90%). This amount of data is estimated to be sufficient to study the variations of the ionosphere (characterized by TEC) both in short-term and long-term. All these data are then calculated and processed by the ionosphere software tool introduced in Chapter 2 to give VTEC results for the entire study period at all stations (with an interval of 30 seconds).

- Starting from Section 3.2, the temporal variations of the ionosphere are gradually clarified. The first is the diurnal variation with some main conclusions are as follows:

    - Daily variation happens even in the very quiet days (as evidenced by the Dst index).
    - Specifically, the daily variation of TEC takes place as follows (in local time): reaches its highest value after lunch (peaks at about 2-3 pm), then steadily reduces and remains stable at low value during the nighttime (reaches the lowest value at about 4-5 am), and then gradually increases again in the morning before reaching the peak of the next day. This cycle is notorious and confirmed by numerous publications so far.
    - The explanation for this process has been given, it can be summarized that the reason mainly due to the formation and existence of the ionosphere under the effect of solar radiation.
    - A table of annual average values of the monthly maximum and mean VTEC has been presented. Data given in this table shows a high correlation between VTEC results and the F10.7cm index as all correlation coefficients are greater than 0.9.

  - Explain the equatorial plasma fountain (EPF) effect to clarify the relationship between EIA and the ionosphere, which is the cause of VTEC differences between stations: VTEC usually reaches a larger value at stations near the equatorial anomaly (specifically at three stations BAKO, XMIS, and HKSL in our case study).

- Seasonal variations of the ionosphere are considered in Section 3.3, which providing some main results as follows:

  - TEC reaches its maximum in the equinoctial months two times per year, these are in vernal equinox and autumnal equinox and gets minimum in winter and summer seasons. This rule has also been announced in many reference articles.
  - The cause of the seasonal variations of TEC is explained by the physical mechanism of the ionosphere.
  - The results of VTEC calculation for 11 years at seven stations are graphed by charts of daily mean VTEC. This type of map clearly illustrates the daily, monthly, and annual changes of the ionosphere.
  - The next invention of this section is the dependence of seasonal variation of VTEC on solar phase: VTEC computed (in the research area) in months of equinox varies uniformly with the trend of the solar phase.
  - The temporal - latitudinal VTEC map has been introduced to show both temporal and spatial distribution of VTEC. Besides, this map can provide information such as location, time of occurrence, and intensity of the crests of EIA, thereby clarifying the important role of EIA in the study of the ionosphere (in terms of VTEC's amplitude: depends on the reciprocal position of the observed station compared to the anomaly lines). This issue will be further investigated in Chapter 6.

- Section 3.4 presents the annual variation of the ionosphere with the following basics:

  - There has been a good agreement between the calculated VTEC results with the officially published solar indices.
  - The VTEC maps at seven stations during 11 years of research has been established. Similar to the plots of daily mean VTEC, this kind of map is an

aggregate representation of VTEC's time variation in all time frames: daily, monthly, and yearly.

- The annual variation of VTEC is explained based on the impact of the Sun's activity on the ionosphere since this layer of the atmosphere is ionized by the solar radiation.
- The solar cycle is a well-known definition and during the period of 2007 - 2017, it is widely accepted that the period of 2010 - 2014 was the increasing phase and the period of 2014 - 2019 was the decreasing phase of SC24, in which 2014 was the year with the most active solar radiation and 2008, 2009 were quite quiet years. However, from my research, it was found that during the rising solar phase of 2010 - 2014, there was a slight fluctuation in VTEC amplitude in early 2013 resulting in the maximum amplitude of VTEC in 2014 being slightly reduced. Specifically, VTEC value increased by 34.9% from 2010 to 2012, then unexpectedly decreased slightly by 1.1% in the following year, after that returned to increase by 21.7% in the period of 2013 - 2014. Overall, VTEC increased by 26.7% from 2010 to 2014. These numbers are highly similar to the F10.7 index as exposed in Table 3.4 and Figure 3.15.

- The last mission of this chapter (Section 3.5) is to find out the correlation between calculated VTEC results and the solar indices during the study period. Specific content as follows:
  - The first is to reintroduce the two basic solar indices: F10.7cm and SSN and give an explanation of why choosing these two indices to study the correlation between the Sun's activity and the variations of the ionosphere.
  - Then, a formula for calculating correlation coefficient was introduced, it's the Pearson formula which is commonly used in probability statistics research.
  - Applying this formula, correlation coefficients between VTEC and solar indices have been calculated with different VTEC options: monthly maximum, monthly mean, daily mean. From the results given in Table 3.5, some noticeable remarks are indicated as:
    - The best type of VTEC corresponds to the solar indices is the monthly mean;

- Daily correlation is less relevant to solar indices than monthly correlation;
- For the research area and study period, the F10.7 index shows more consistency with the calculated VTEC than the SSN index;
- Among the stations used, the variations of VTEC at CUSV station are considered to be the most similar to the solar indices. Conversely, the correlation between VTEC at HKSL station and the solar indices is lowest.

- The plots illustrate the monthly mean VTEC at seven IGS stations have been also put on view, which indicate:
  - Again, the F10.7 index proved to be more appropriate than the SSN index in describing the correlation with the calculated VTEC.
  - For the first time, monthly VTEC has averaged calculation (from GIM data) for the entire Southeast Asia region. This is a unique VTEC value specific to the whole Southeast Asia area, not represents for a single point as the VTEC results calculated earlier.
  - Seasonal and annual variations (including the modest but abnormal change at the beginning of 2013) of VTEC are also clearly seen in these plots.

4. Occurrence characteristics of ionospheric scintillation over Vietnam region

4.1. Data and methodology

To study the occurrence characteristic of the ionospheric scintillation over the region of Vietnam, data from three continuously operating GPS receivers located through this area has been used: HANOI (at Phuthuy, the northern part of Vietnam), HUE (the middle part of Vietnam), and HCM (at Hocmon - Baclieu in Ho Chi Minh city, the southern part of Vietnam). These three stations are the result of the framework of the co-operation between the Institute of Geophysics, Vietnam Academic of Science and Technology (VAST) and Universities of Rennes1 and Telecom Bretagne in France. The main aim of this project is to monitor the Total Electron Content (TEC) and ionospheric scintillation over Vietnam region. The dual frequencies receiver used is GSV4004B (GPS Silicon Valley) produced by NovAtel company, it operates at a sample rate of 50 Hz and is therefore suitable for monitoring local and regional ionospheric activity. The primary purpose of the GSV4004B GISTM (GPS Ionospheric Scintillation and TEC Monitoring) is to collect ionospheric scintillation and TEC data for all visible GPS satellites (currently up to 12 satellites), and one to three SBAS GEO (Satellite-Based Augmentation System for Geostationary Earth Orbit) satellite, and output data logs, called ISMRB (Information Systems Management Review Board), to a serial port in either binary or ASCII format [GSV4004B, User's manual]. Table 4.1 lists basic information of the stations used in this study and Table 4.2 shows the main results derived from this receiver.

Table 4.1. List of stations used for ionospheric scintillation research in Vietnam region

No	Station	Geographic coordinate		Receiver	Type of station
		Latitude	Longitude		
1	HANOI	21.02938^o	105.95871^o	GSV4004B	GISTM
2	HUE	16.45881^o	107.59347^o	GSV4004B	GISTM
3	HCM	9.29903^o	105.71102^o	GSV4004B	GISTM

As already introduced in Chapter 1, there are three types of scintillations: amplitude scintillation (described by S_4 index); phase scintillation (described by σ_φ index); and polarization scintillation. Many studies [Alfonsi et al., 2006; Li et al., 2007; Jacobsen and Daehnn, 2014; Hlubek et al., 2014] have indicated that amplitude scintillation is more

appropriate for the low-latitude areas and phase scintillation is more common in the high-latitude areas. This is because in the high-latitude regions, the ionization density is less than that in the equatorial regions, but the irregularities move at a speed ten times faster [(4.1)]. Moreover, phase scintillation is very often influenced by multipath propagation error, the noise of the receiver's phase, the drift of Doppler's phase, … Therefore, in general phase scintillation index have not been widely using for the study of scintillation in the EIA region [Guo et al., 2019]. In this chapter, to indicate the appearance of scintillation activity, S_4 index obtained at three GISTM stations located through Vietnam area has been used. The method of computing S_4 index is already introduced in Section 2.2.

At three GISTM stations, the GSV4004B receiver can provide information about ionospheric scintillation such as S_4 index, the standard deviation of the code/carrier phase (σ_{CCD}), and the specific parameters of the amplitude scintillation of GPS signals when travelling through the ionosphere. The receiver GSV4004B consists of three major components: an L1/L2 GPS antenna, a GPS receiver (NovAtel's EuroPak-3M) and a power supply with various inter-connecting cables. Among them, the Euro-3M GPS receiver, with modified software (firmware), can track up to maximum 11 GPS signals at the L1 frequency (1575.42 MHz) and the L2 frequency (1227.6 MHz). It measures phase and amplitude at 50 Hz rate and code/carrier divergence at 1 Hz rate for each satellite being tracked on L1 and computes TEC from combined L1, L2 pseudo-range and carrier phase measurements. The 12^{th} channel aims to measure a noise floor for C/N0 and S_4 correction computations. The S_4 index is calculated from the normalized standard deviation of raw signal intensity (S_{4T}) in every one minute [Aarons, 1982]:

$$S_{4T} = \sqrt{\frac{<SI^2> - <SI>^2}{<SI>^2}} \tag{4.1}$$

with SI is the signal intensity; <SI> is the average of signal intensity in 60 seconds. The S_{4T} index derived from equation (4.1) including the amplitude scintillation and the ambient noise which is defined as:

$$S_{4No} = \sqrt{\frac{100}{C/No}\left[1 - \frac{500}{19C/No}\right]} \tag{4.2}$$

with C/No is the ratio of signal to noise. The corrected S_4 index at frequency f_1 is then computed by removing the effects of ambient noise (S_{4No}) as follow:

$$S_4 = \sqrt{S_{4T}^2 - S_{4No}^2} \quad (4.3)$$

The raw amplitude measurements are detrended (by normalization), either with a 6th-order Butterworth low-pass filter output (with a user-specified cut-off frequency) or with the measurement average over the 60-second interval (if the user-specified cut-off frequency is zero). The total S_4 index includes S_4 due to the effects of ambient noise (and multipath noise as well) is computed over the same 60-second interval as the phase parameters. The receiver also computes the correction to the total S_4 index (effect of ambient noise), based upon the average of the raw 1-Hz C/N0 values over the same 60-second intervals. Simultaneously with the calculation process of total S_4 index, the receiver also collects raw code/carrier divergence (the difference between code and carrier pseudo-range) at every second. The average and standard deviation of the code/carrier divergence are then computed every minute. These values are indicative of multipath (and other noises) activity and can be used to distinguish between S_4 due to multipath and S_4 due to scintillation effect since there is no code/carrier divergence affected by scintillation.

Table 4.2. The output results of GSV4004B receiver

No	Data	Unit
1	Week Number (WN)	N/A
2	Time of Week (TOW)	Seconds
3	PRN	N/A
4	Receiver status	N/A
5	SV Azimuth angle	degrees
6	SV Elevation angle	degrees
7	C/No	dB-Hz
8	Total S_4	dimensionless
9	Correction to total S_4	dimensionless
10	1-second phase sigma	Radians
11	3-second phase sigma	Radians
12	10-second phase sigma	Radians
13	30-second phase sigma	Radians
14	60-second phase sigma	Radians
15	Average of Code/Carrier divergence	Meters
16	Sigma of Code/Carrier divergence	Meters

17	TEC at TOW-45	TECU
18	ΔTEC from TOW-60 to TOW-45	TECU
19	TEC at TOW-30	TECU
20	ΔTEC from TOW-45 to TOW-30	TECU
21	TEC at TOW-15	TECU
22	ΔTEC from TOW-30 to TOW-15	TECU
23	TEC at TOW	TECU
24	ΔTEC from TOW-15 to TOW	TECU
25	L1 Lock time	Seconds
26	Chanel status	N/A
27	L2 Lock time	seconds
28	L2 C/No	dB-Hz

Source: GSV4000B (GISTM), User's manual

In this research, I use data from GSV4000B receivers in two years 2009 and 2015 to study the diurnal and seasonal variations of ionospheric scintillation. Because of the technical problems during the process of data collection, the derived data for the whole year was not full. In the particular case of 2009, only 308 days were observed at HANOI station, 279 days at HUE station, and 357 days at HCM station. The corresponding number for 2015 was 341, 324 and 221 days, respectively. Specific information about the non-data days is realizable in Figures 4.7, 4.8 and 4.10.

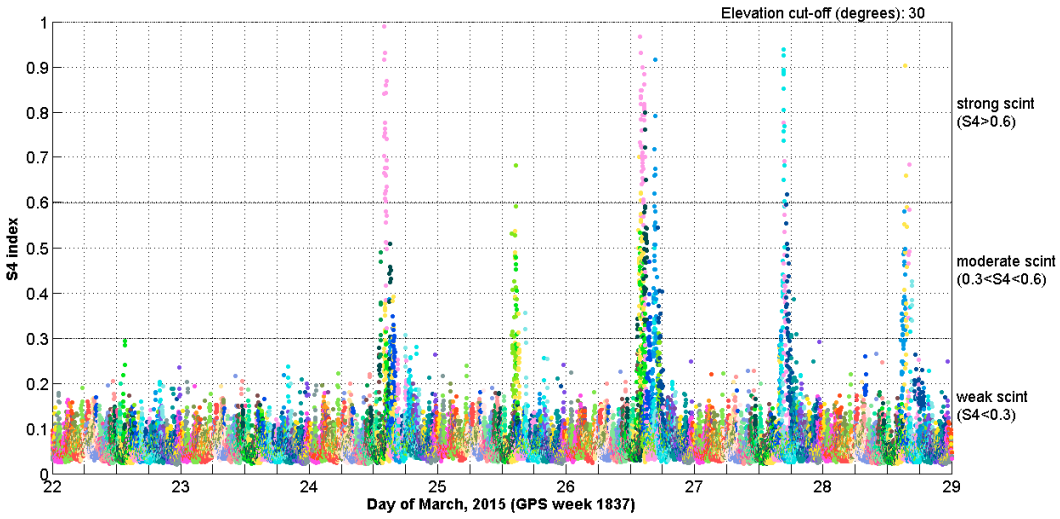

Figure 4.1. Raw S_4 index at HUE station during 22nd-29th March 2015

Figure 4.1 shows an example of the pure (not yet filtered) S_4 index received from the receiver GSV4000B at HUE station in one week of March 2015. The elevation cut-off is 30^o aims to constrain the unexpected errors for the observations close to the horizon. In this figure, different colours correspond to different observed satellites. The value of S_4 index varies between 0 and 1, is divided into three intensity levels: weak or slight level with S_4<0.3, medium level with S_4 between 0.3 and 0.6, and the rest is strong level. The result from Figure 4.1 indicates several disturbed days in the last week of March 2015. Scintillation activities can be observed from day 24th until the end of the month, while days 22nd and 23rd are rather quiet. Nevertheless, there is still a certain amount of noise left in the result, which is not necessarily caused by the scintillation. These noises must be detected and removed from the observations.

4.2. Eliminate sources of interference

Sources of error such as atmosphere layer, the scattering of water vapour and especially multipath error may interfere with the accurate determination of amplitude of scintillation. These influence factors often increase at low satellite elevation, for this reason, we have to limit the satellite elevation cut-off. This value is often set at 20^o, meaning that all visible satellite with an elevation angle less than 20^o will be ignored. Limiting this vision may reduce the number of satellites observed but allow us to significantly eliminate the effects not caused by the ionosphere. There are various sources of error that influence the determination of amplitude scintillation in GNSS measurements and multipath error is among them. The multipath error itself is a complex research problem and limiting the satellite threshold cannot prevent this error at all. This error is very much dependent on the surrounding environment where the receiver is located. When using GSV4004B receiver to study ionospheric scintillation, an additional filter limit must be used as follows [Wilson et al.,1992; GSV4004B User's manual]:

$$\sigma_{min} = 0.652.S_4 - 0.125 \quad (4.4)$$

with S_4 is amplitude scintillation derived directly from the receiver; σ_{min} is separation limit between ionospheric scintillation and multipath scintillation. The value of σ_{min} computed by equation (4.4) will be compared with the standard deviation of the code/carrier phase (σ_{CCD}). This index is also received directly from the receiver as indicated in Table 4.2. Since in a scintillation environment, there is very little code/carrier divergence due to scintillation. So, if $\sigma_{CCD} \leq \sigma_{min}$ then the observation is considered to be affected by scintillation errors, otherwise

it refers to other errors and have to be eliminated. It is also needed to emphasize that, using equation (4.4) not only eliminates errors caused by multipath signals but it is also used to remove all small S_4 observations (<0.191), most of which are not multipath errors. Examples of using this filter limit to separate scintillation events and other noises are shown in Figures from 4.2 to 4.5.

Figure 4.2 compares two cases when using the above algorithm with the red line is the limitation to filter S_4 index. All the S_4 values below the red line (blue dots) are acceptable and believed to be scintillation events, meanwhile, the red dots (above the red line) are reckoned to be multipath fading plus noises and will be eliminated. On March 19th 2015 (scintillation day), there are 256 observations (2.71%) are maintained and 9183 observations (97.29%) are ignored. It should be noted that the ignored observations here include the observations with S_4 less than 0.2. For the purpose of studying the effects of ionospheric scintillation on GNSS measurements, a scintillation index below 0.2 is unlikely to have any effect on the result of positioning. Therefore, this filtering algorithm is acceptable for the statistics of scintillation occurrences. In the next sections, all S_4 index is supposed to be filtered by this filtering algorithm.

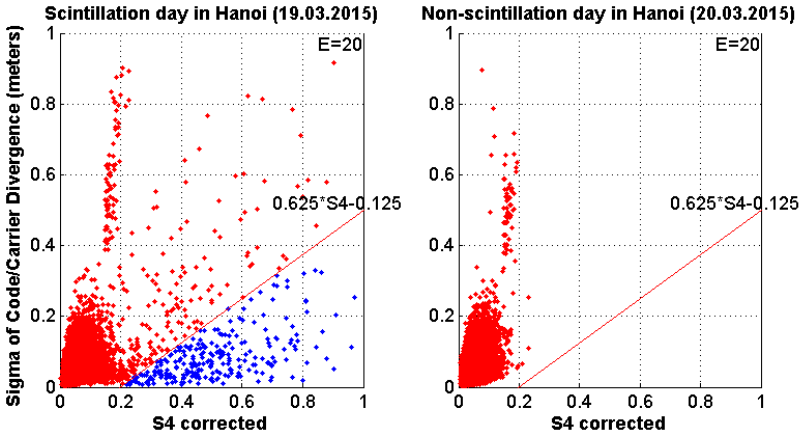

Figure 4.2. Filtering of S_4 index in the scintillation environment (left) and non-scintillation environment (right)

Figure 4.3 compares the number of ignored observations when using different satellite elevation threshold (E). In the case E=10^o: there are 367 observations (0.21%) are maintained and 174545 observations (99.79%) are ignored; If we use E=20^o, then 230 observations (0.17%) are maintained and 133200 observations (99.83%) are ignored; When choose E=30^o only 140 observations (0.14%) are maintained and 101014 observations (99.86%) are ignored. Thus, it is seen that the lower satellite elevation cut-off used, the bigger noises are detected.

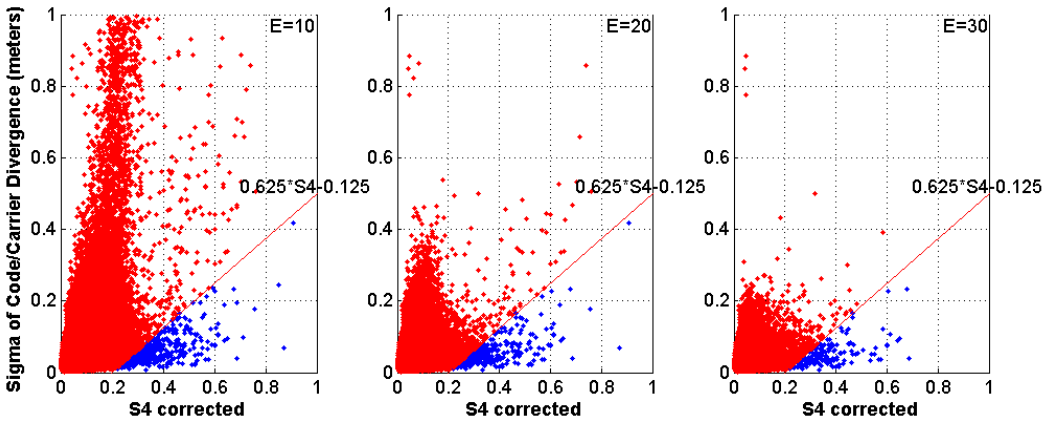

Figure 4.3. S_4 index filtering at HCM station during 4th-17th October, 2015 with different elevation cut-off (E): E=10° (left), E=20° (middle) and E=30° (right)

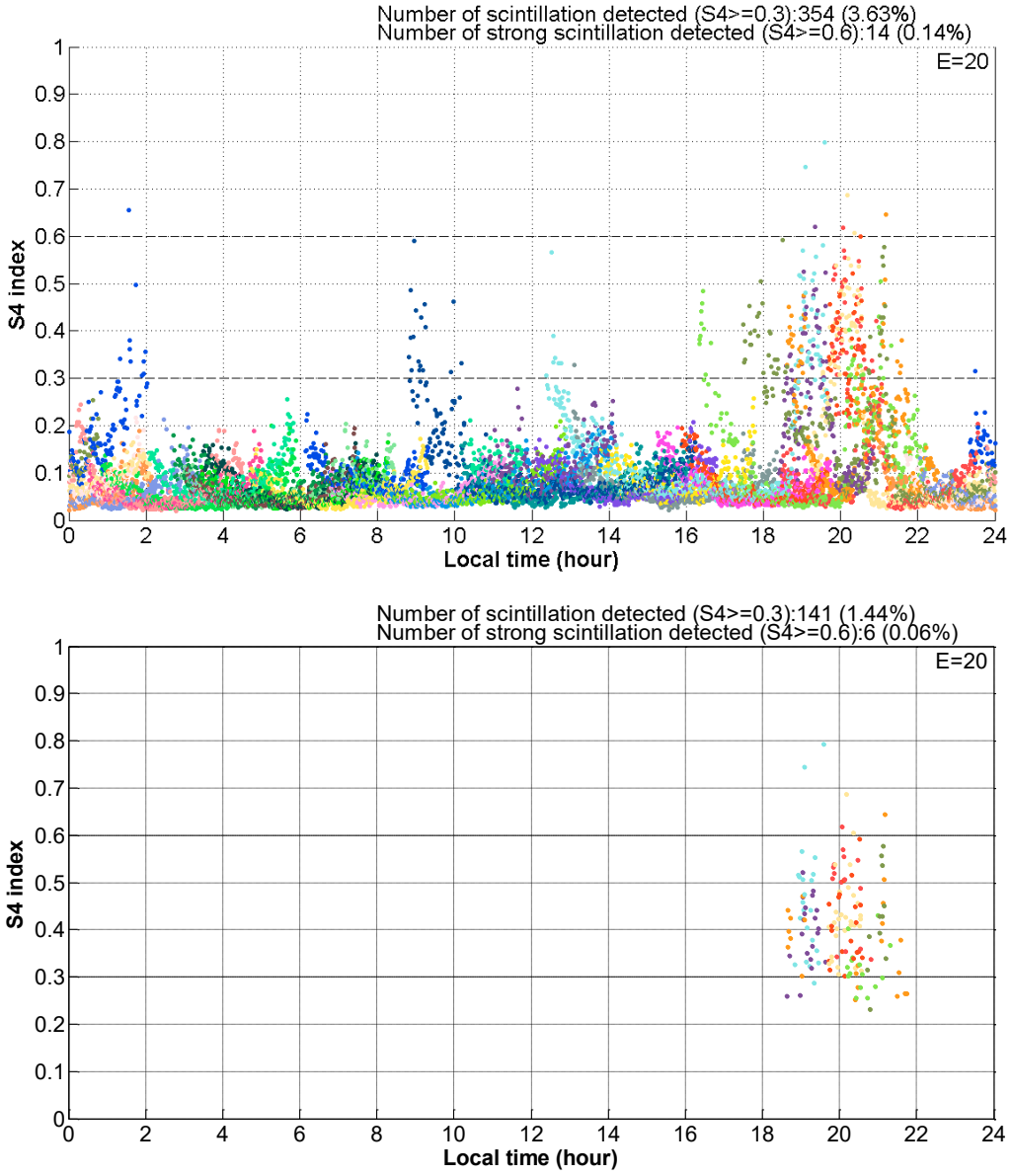

Figure 4.4. S_4 index before (above) and after (below) filtering at HUE station on 22.10.2015

Figure 4.4 shows S_4 index of all observed satellites at HUE station on October, 22nd 2015, a disturbed day to the ionosphere concern. It can be seen that, after filtering, the number of scintillation events dropped down from 3.63% to 1.44%. The significant S_4 index (greater than 0.3) detected at around 0 - 2 am and 8 - 10 am local time is certainly not caused by scintillation error, but some other noises (mainly multipath errors). Therefore, by using this filtering method, the multipath errors can be detected and removed from the raw GNSS observations.

Another example of using a filter to separate S_4 index not caused by scintillation signal is exhibited in Figure 4.5. The data was observed in Ho Chi Minh City in two weeks, starting from October 04th to October 17th 2015. From the plot of unfiltered S_4, it can be seen that there were a lot of noises appear sporadically during the observed time. After filtering, most of these noises disappeared and the scintillation signals could be easy to be detected in some particular days. Before filtering, there were 431 observations affected by noises including scintillation noise and multipath noise (S_4 index was greater than 0.3). But after the filtering process, there were only 178 observations left. Thus, 253 (about 0.19%) observations had been considered to be multipath error and were eliminated. The number of scintillation events, in this case, was around 0.13% of all observations.

[4.1] https://www.gpsworld.com/gnss-systemsignal-processinginnovation-ionospheric-scintillations-12809/

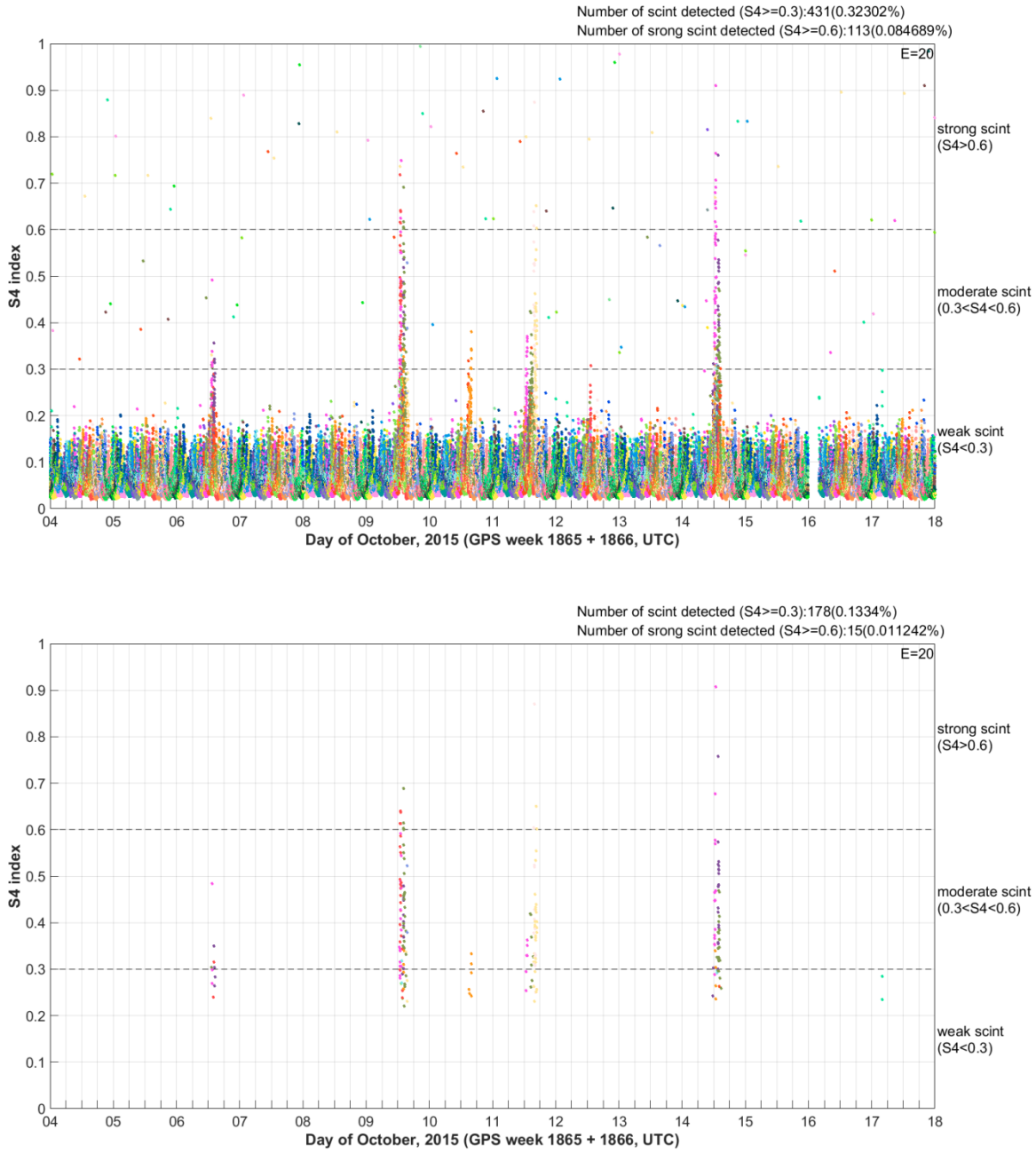

Figure 4.5. S_4 index before (above) and after (below) filtering at HCM station during 4th-17th October 2015

4.3. Temporal distributions

4.3.1. Diurnal distributions

Using the results obtained from the GSV4000B receivers and applying the above filter algorithm, a statistic of the occurrence of scintillation activity in a single day for the whole data in 2015 at three stations: HANOI, HUE and Ho Chi Minh (HCM) was calculated. Since the Sun's activity was not significant in 2009, the diurnal distribution was somehow unclear,

thus the results of 2009 are not displayed here, only the results of 2015 is shown to indicate the daily variation of scintillation activity.

But first, to study the effect of choosing satellite elevation threshold on the total number of scintillation events, the detected scintillation events at HANOI station in 2015 with different elevations cut-off was counted. The total days observed at HANOI station in 2015 was 341.

Table 4.3. Comparison of scintillation events with different elevation threshold

No	Elevation cut-off	Number of observations	Number of scintillation event detected ($S_4 \geq 0.3$)	Number of strong scintillation event detected ($S_4 \geq 0.6$)
1	0^o	4249229	11539 (0.27%)	2747 (0.06%)
2	10^o	3875417	10619 (0.27%)	2733 (0.07%)
3	20^o	3091002	9042 (0.29%)	2566 (0.08%)
4	30^o	2394135	6860 (0.29%)	2106 (0.09%)
5	40^o	1735296	4631 (0.27%)	1417 (0.08%)

In Table 4.3, it can be seen that the number of scintillation events detected reduces very quickly when the elevation cut-off increases, however, the percentage almost stays the same. This is understandable because when we increase the satellite elevation cut-off, the number of observations is also significantly reduced. As discussed before, to restrict the effects of multipath and other potential errors, we limit the satellite elevation threshold to 20^o in our calculations. Figures 4.6a, 4.6b, and 4.6c show the diurnal distribution of scintillation activity at three stations located from the north to the south of Vietnam in 2015. The frequency of scintillation occurrences is represented by the number of times and its percentage during 24 hours. Intense scintillation ($S_4 \geq 0.6$) is distinguished by a different colour bar.

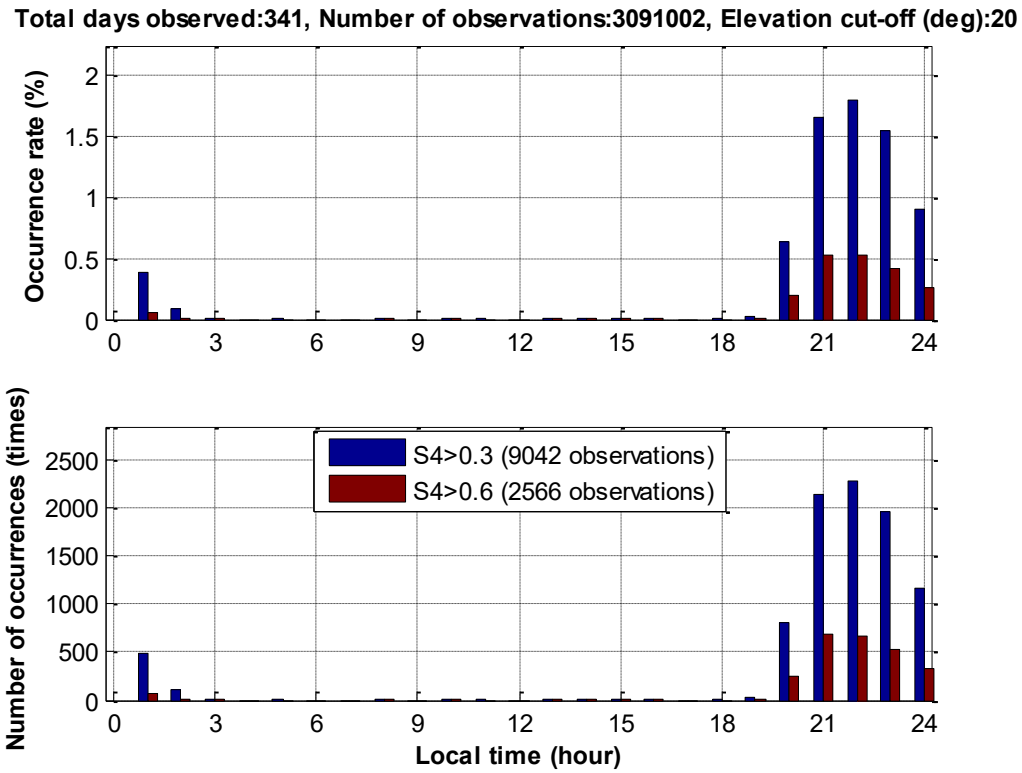

Figure 4.6a. Local time frequency of scintillation events appearance at HANOI in 2015

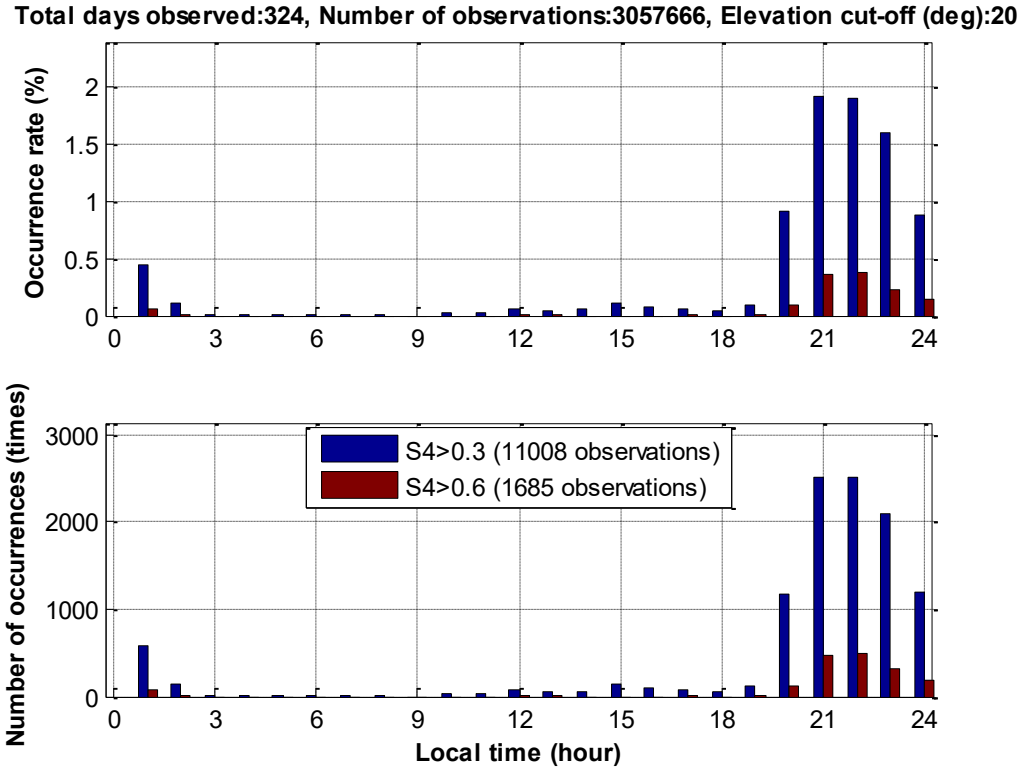

Figure 4.6b. Local time frequency of scintillation events appearance at HUE in 2015

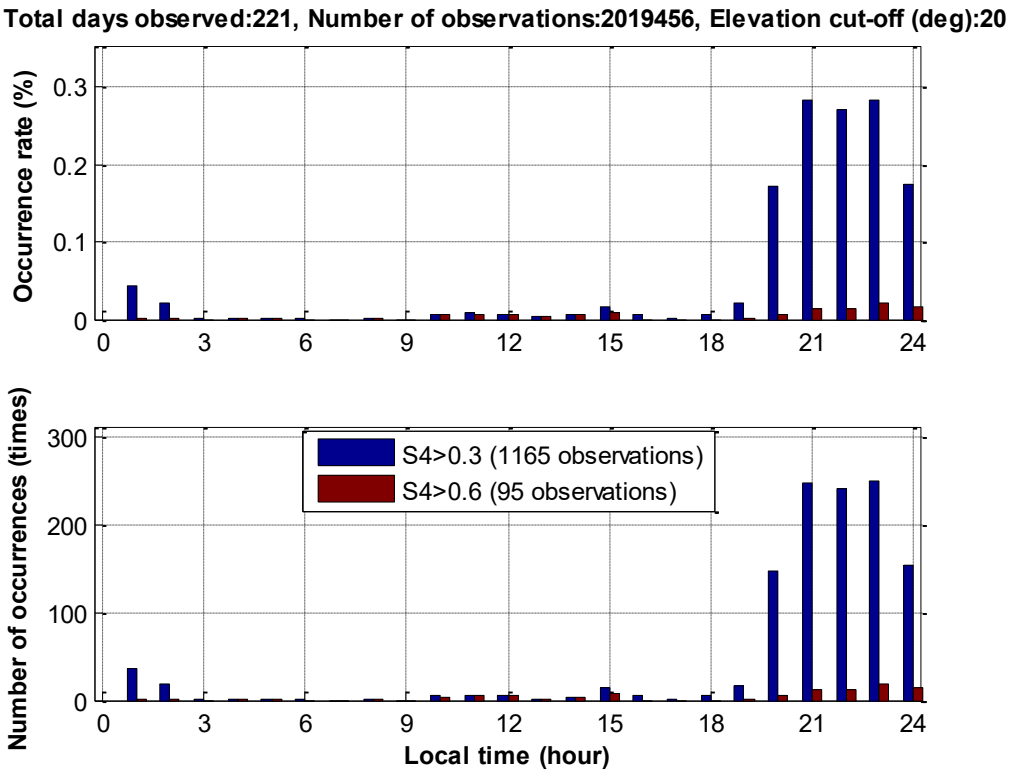

Figure 4.6c. Local time frequency of scintillation events appearance at HCM in 2015

The results clearly show that ionospheric scintillation generally peaks several hours after dusk, exists until around midnight and then gradually disappears. It rarely occurs in the daytime. The time that scintillation activity is most active is around 10 pm local time.

Since HANOI and HUE stations are located close to the equatorial anomaly area, the number of scintillation events at these two stations is almost ten times more than at HCM station, that is approximately 2000 times (nearly 2%) compared to only about 200 times (nearly 0.3%) during the active hours of scintillation activity. For the whole day, the number of scintillation events detected at HANOI and HUE stations is also much higher than at HCM station (stations HANOI, HUE, HCM have 9042, 11008, 1165 scintillation events respectively). Strong ionospheric scintillation (S_4>0.6) is also detected predominantly at HANOI station with over 28% of all scintillation events. This percentage at HUE station is approximately 15% and at HCM station is only around 8%. This is completely understandable as HANOI station (~ 21^o north latitude) is located almost over the equatorial anomaly and HCM station (with around 9.3^o north latitude) is the furthest station from the northern crest of the equatorial anomaly.

The above phenomenon can be explained by the physical process that generates ionospheric scintillation in the equatorial region as follows: At the time after sunset, plasma density and kinetic electric field in region E decreases, the peak of the equatorial anomaly disappears as well, while at this time the kinetic electric field starts to develop in the F region. Under the effect of the eastward electric field component, the total number of the electron density increases abnormally before reversing to the west, layer F in the equatorial region is raised to a higher height, where has a low plasma density and the plasma collisions are rare to happen. The positive total electron content gradient of the bottom of the F layer rapidly increases, causing the electron to become unstable and disturbed leading to plasma proliferation. This state is called Rayleigh - Taylor instability and is the cause of density anomalies in the equatorial ionosphere [Rama Rao et al., 2006]. The non-linear development of these instabilities leads to the formation of large regions of electrolytic depletion, a phenomenon often observed in the equatorial anomaly area and called the plasma bubble [Amory-Mazaudier et al., 2006; Beniguel, 2011; Otsuka et al., 2002]. By various techniques, it is observed that the size of the disturbance can range from tens of centimetres to hundreds of kilometres. The gradients on the edges of the density attenuation give rise to small scale disturbances, which is the cause of the amplitude scintillation on the satellite signal transmitted in the equator area at nighttime and can be recorded on GPS receiver.

4.3.2. Seasonal distributions

To study the seasonal variations of ionospheric scintillation phenomenon, the frequency of their occurrences at HANOI, HUE, HCM stations in two years 2009 and 2015 are presented in Figures 4.7a-c and Figures 4.8a-c. The left panel shows the intensity of all scintillation activity in different months and the right panel shows only the scintillation events (S_4>0.3) with the bracket indicates total observed days in the corresponding month.

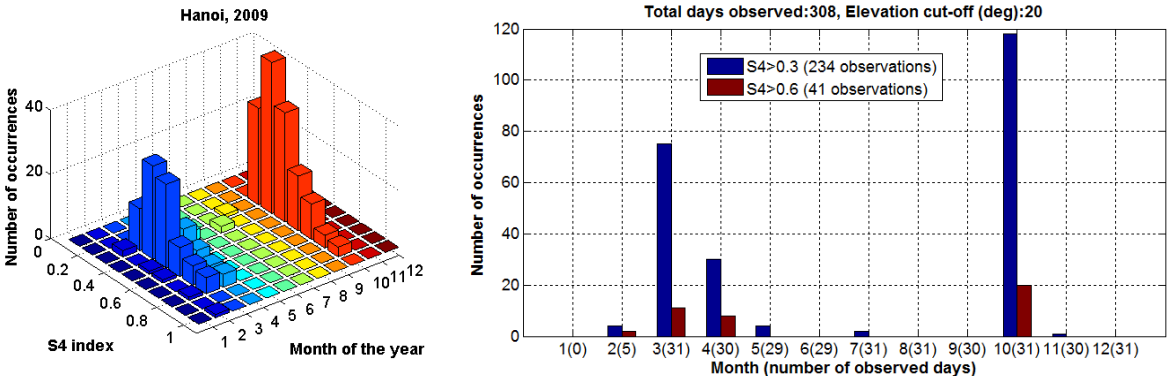

Figure 4.7a. Seasonal frequency of scintillation events appearance at HANOI in 2009

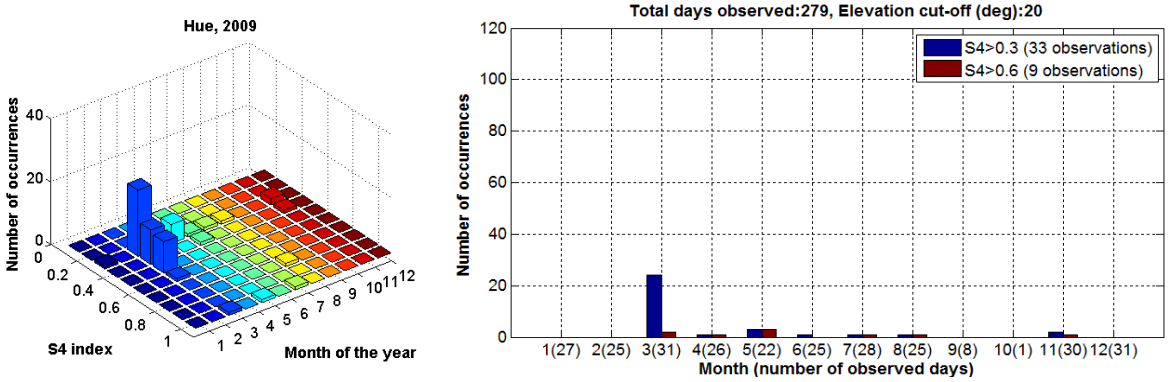

Figure 4.7b. Seasonal frequency of scintillation events appearance at HUE in 2009

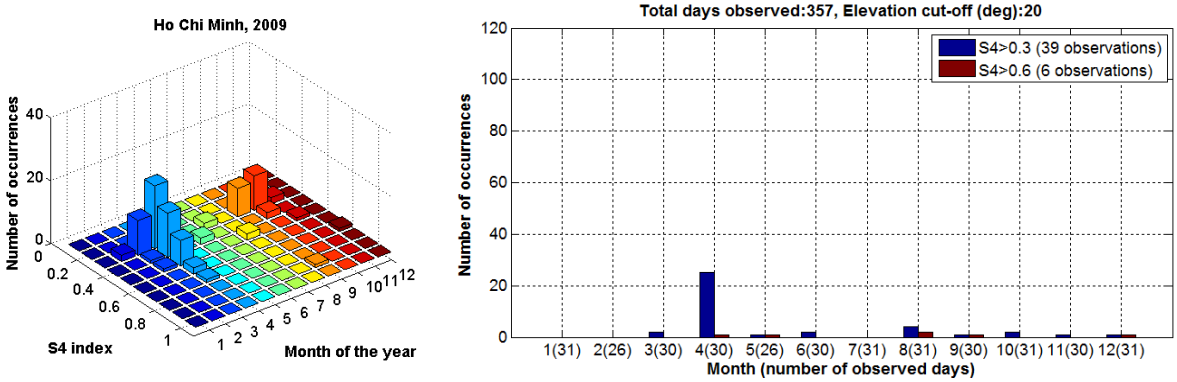

Figure 4.7c. Seasonal frequency of scintillation events appearance at HCM in 2009

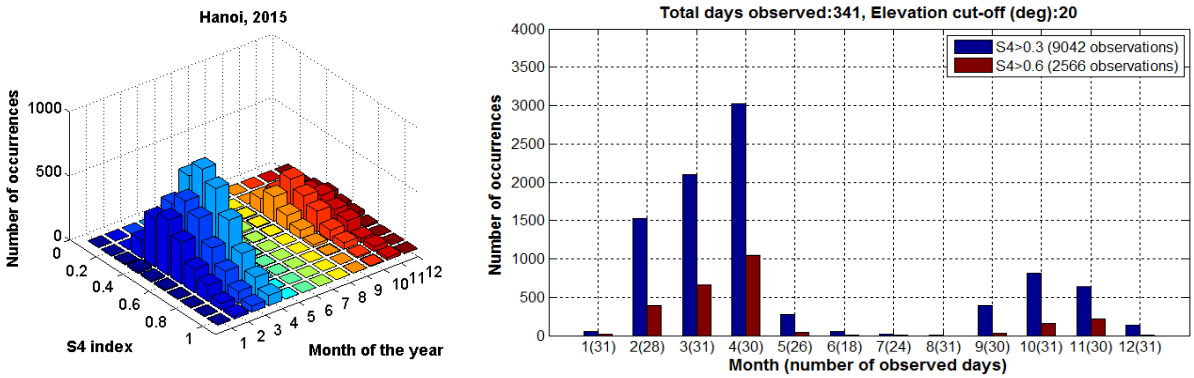

Figure 4.8a. Seasonal frequency of scintillation events appearance at HANOI in 2015

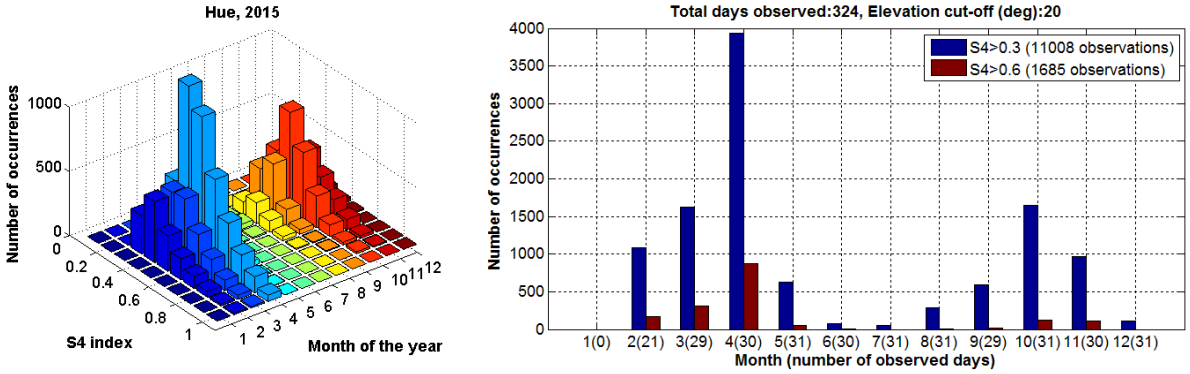

Figure 4.8b. Seasonal frequency of scintillation events appearance at HUE in 2015

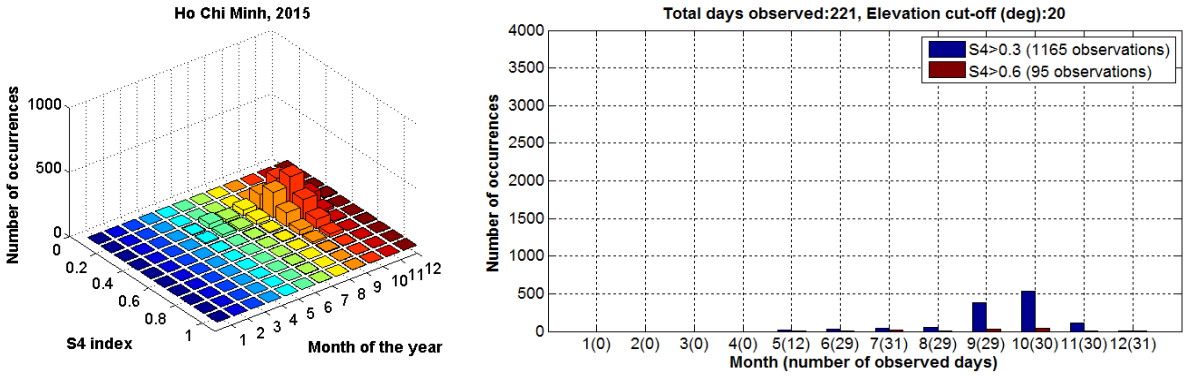

Figure 4.8c. Seasonal frequency of scintillation events appearance at HCM in 2015

The results indicate that in each year the occurrence of ionospheric scintillation shows a very clear seasonal variation: occurs mainly in the equinoctial months (March, April and September, October) and is very seldom appears during the summer and winter months. The seasonal appearance of ionospheric scintillation in Vietnam is consistent with previous scientific publications when investigating other stations in the same area [Aarons, 1982; Cervera et al., 2006; Rama Rao et al.,2006; Abadi et al., 2014]. The seasonal occurrence of scintillation activity is also almost similar to the seasonal variation of TEC investigated in Chapter 3. In general, the seasonal variation of ionospheric scintillation can be described as in Figure 4.9. In one year, the number of scintillation events gets minimum in solstitial months, it goes up gradually from January to March, then goes down slowly from April to June, July and later goes up again in the next three months to reach the second peak of the year in September and October. The final phase of the year sees the decline of scintillation events from October to December.

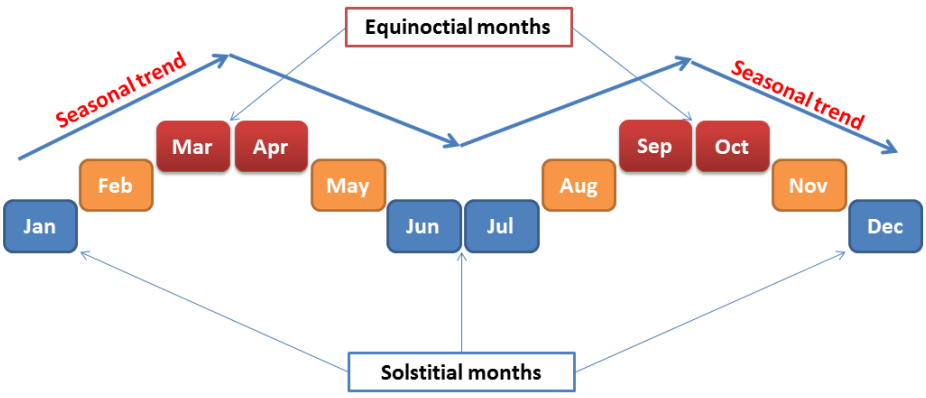

Figure 4.9. The trend of seasonal variations of scintillation activity

As discussed in Chapter 3, TEC variation is dependent on solar cycle's phase. In this case, the difference of scintillation events between two peaks of the year (Mar, Apr and Sep, Oct) at HANOI and HUE stations in 2015 also shows the same rule. That is scintillation events in the vernal equinox are higher than that in the autumnal equinox as 2015 is in the decreasing phase of the solar cycle. The result at HCM station can not be displayed because data from January to almost the end of May 2015 is missing. Again, the intensity of scintillation activity at HANOI and HUE stations is much higher than in HCM station because of the different distance to the crest of the equatorial anomaly. In 2015, the highest number of scintillation events at HANOI and HUE stations is discovered in April, having around 3000 events and nearly 4000 events respectively.

As 2009 is the weakest year of SC24, not so many scintillation events were detected, strong scintillation (S_4>0.6) appeared only a few times (6, 9, 41 events detected at HCM, HUE, and HANOI stations respectively). The seasonal distribution is only straightforward at HANOI station because of the lack of the data at HUE station (only 279 days were observed) and the very low in intensity of ionospheric scintillation in HCM city this year. In total, there were only 39 observations had been determined to be affected by scintillation error at HCM station, this number at HANOI and HUE stations was 234 and 33 events respectively, but the actual number could be much higher as the big lack of data. The significant difference in intensity of scintillation between 2009 and 2015 also exposes the dependence of ionospheric scintillation on solar activity. Because of the lack of data in other years of SC24 (only the data in two years 2009 and 2015 were provided), the correlation between ionospheric scintillation activity and the solar cycle cannot be conducted in detail. But with the results of two years gained, we have a very clear seasonal distribution of scintillation activity and somewhat its variation in the different active years of the Sun. The dependence of ionospheric scintillation on solar cycle has been extensively studied by many excellent ionospheric researchers over the last decades at different areas in the equatorial region, such as Basu et al., 1999 studied in the America region; Rama Rao et al., 2006 studied for India region; Alfonsi et al., 2010 studied in South East Asia, …

Figure 4.10 compares the heat map of scintillation activity at three stations in two years 2009 and 2015. White areas indicate no data collected or the data is corrupted. A particular S_4 index represents for a visible satellite at a certain epoch, so at one epoch there could be several S_4 indices. The S_4 index shown in Figure 4.10 is the maximum at a particular epoch

and it is described in 24 hours for all days of the year. While images for 2009 are quite insipid as a result of a quiet year, images for the year 2015 clearly shows both diurnal and seasonal variations of ionospheric scintillation in different parts of Vietnam. The northern part of Vietnam (represented by HANOI station) is the most affected area by scintillation phenomenon, then the middle part (represented by HUE station). The southern part (represented by HCM station) is the less affected region.

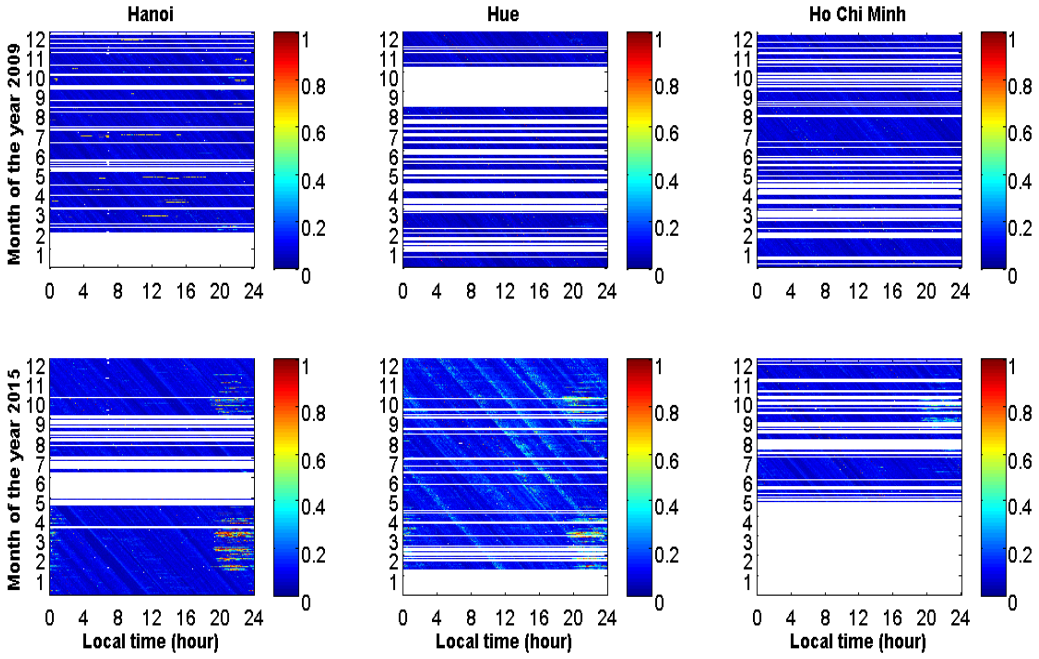

Figure 4.10. S_4 heat map over Vietnam region in 2009, 2015 (white area indicates no data)

4.4. Spatial distributions

In the previous sections, the temporal distribution of scintillation activity in both short-term and long-term has been discussed. Nonetheless, when studying about ionospheric scintillation error, we take into account not only the temporal distribution but also spatial distribution. Especially in the application of satellite navigation, it is important to determine the spacial allocation of the occurrence of ionospheric scintillation to estimate the effect of scintillation error on positioning measurements. Therefore, in this section, I analyze the appearance of ionospheric scintillation according to the satellite's elevation and azimuth at each station.

Figure 4.11 discloses the directional distribution of scintillation events at three stations in two years 2009 and 2015. All detected scintillation events in the whole year are shown in the polar horizontal coordinate system by its satellite elevation and azimuth with different colours: green is slight scintillation (S_4<0.4), yellow represents for average scintillation (S_4

between 0.4 and 0.6), red stands for strong scintillation (S_4 between 0.6 and 0.8) and black indicates very intense scintillation (S_4>0.8). The elevation cut-off used in this case is 10^o aims to study the impact of satellite's elevation on the occurrence of scintillation error.

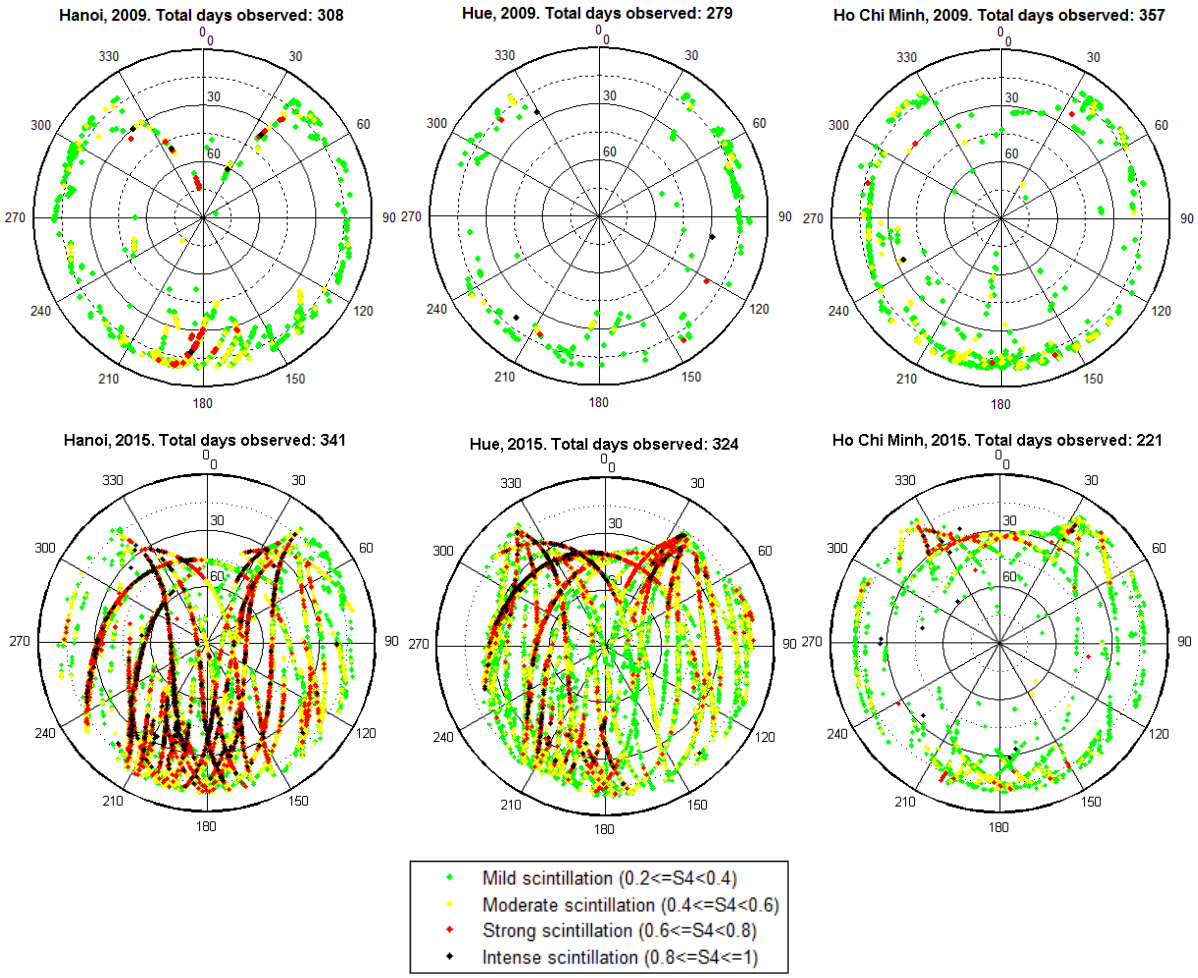

Figure 4.11. Directional distribution of scintillation events (elevation cut-off is 10^o)

At first glance, we can see that not so many scintillation events are detected in 2009 as this year is the lowest active year of the Sun in SC24. Scintillation with intensity from weak to strong appears scattered from low to high satellite elevations on the observation area of HANOI station, with the appearance focuses in the south of the station. From the results of this year, we can realize the dependence of occurrence of scintillation activity on the satellite's elevation. Most of scintillation events appear at low (less than about 40^o) satellite elevation observations. This means ionospheric scintillation effect is more sensitive with low satellite elevation observations than the near zenithal observations. This is an important conclusion on the spatial distribution of ionospheric scintillation concerning satellite's elevation of observations. This fact is likewise conformity with the case at HCM station in

2015 when ionospheric scintillation seems to be less frequent and intense in this area than in HUE and HANOI. Also here, scintillation occurs mainly in areas with low satellite elevations, it rarely appears in areas with satellite views larger than 40^o. Besides, strong amplitude scintillation is also rarely observed at this station during this year.

Now I consider the direction of ionospheric scintillation. From the image of HCM station in 2015, we can see almost strong and intense scintillations toward the north. As in the case study, the latitude of HCM station is around 9.3^o in the northern hemisphere, while the EIA in Vietnam area (105^o East Longitude) is about 19^o north latitude (determination of EIA will be introduced in Chapter 6). This means that scintillation activity tends to appear toward the EIA. This experience is also in accordance with the situation at HANOI and HUE stations in 2015. HANOI with approximately 21^o north latitude, lies above and very close to the EIA, and of course, endures more intense scintillation events than the rest two stations with the spatial distribution of scintillation surrounded evenly. Nonetheless, we still observe that the intense scintillations gather a little bit more in the south than in other areas. The trending of towards EIA of ionospheric scintillation is more clearly at HUE station since its latitude is around 16.5^oN and the majority of strong scintillation events lies in the upper half of the polar horizontal coordinate system.

In summary, the distribution of ionospheric scintillation is concentrated to the south of HANOI station and the north at HUE and HCM stations. It is considered to be towards the crest of the northern equatorial anomaly. This anomaly region is located south of HANOI and north of HUE and Ho Chi Minh city. The results at HUE and HCM stations both show that there are significant scintillation events focus at the azimuth angles of 150^o - 210^o in the satellite viewing area less than 30^o. This shows the presence of a focusing area of active ionospheric scintillation on the other side of the equator (the southern equatorial anomaly crest).

It is also needed to add that, in 2015 scintillations with strong amplitude at HUE station appear less than at HANOI station. Since both HANOI and HUE stations are located quite close to EIA, the spatial distribution of scintillation concerning satellite's elevation does not make sense in this case.

4.5. Chapter summary

- Section 4.1 introduces the instruments used in this study, these include three scintillation receivers (namely GSV4004B) located through Vietnam region (one in the north part, one in the middle part, and one in the south part). These receivers operate at a sample rate of 50 Hz and therefore can provide S_4 index with appropriate frequency. The formula calculation of S_4 and the receiver's outputs are also provided in this section. Note that the data received is only available in 2 years: 2009 (underactive solar year) and 2015 (active solar year).

- Section 4.2 introduces a filter formula that can detect and filter multipath error from the raw data of GSV4004B receiver. Also in this section, some illustrative examples during different periods are represented to show the actual effect of using this filtering algorithm.

- The temporal distributions of ionospheric scintillation in Vietnam region are revealed in Section 4.3 with some main contents as follows:
    - Daily contributions:
        - The first content of this section is to explore the effect of different satellite elevation on the number of scintillation events detected. It is concluded that using satellite elevation threshold of 20^o is the most well-suited, balancing the elimination of observations with low satellite elevation and still ensuring the total number of observations obtained.
        - Daily frequency of scintillation events appearance at three stations (HANOI, HUE and HCM) in 2015 have been put on view. These plots give the results of daily variations.
        - The diurnal variations of ionospheric scintillation are explained by the physical process produces ionization scattering at the equator.
    - Seasonal distributions:
        - Seasonal frequency of scintillation events appearance at three stations in 2009 and 2015 have been displayed to indicate the quarterly variations of scintillation activity (Figure 4.9).

  - The S_4 heat maps over Vietnam region are also presented, which perspicuously exhibit the diurnal and seasonal variations of ionospheric scintillation in different parts of Vietnam.

- The last Section (4.4) studies on the spatial distributions of scintillation activity by providing a plot of its directional allocation over the Vietnam region. This figure shows where ionospheric scintillation is predominantly concentrated and at which satellite elevation, the GNSS observations are vulnerable to scintillation error. The results also indicate the level of scintillation activity in different parts of Vietnam regarding its reciprocal positions to the EIA.

5. Ionospheric irregularity observations using ROT and ROTI indices

5.1. Using ROT and ROTI indices to study the disturbances in the ionosphere

As stated in the previous chapters, for the measurement of ionospheric scintillation, two widely used parameters are the amplitude scintillation (S_4 index) and phase scintillation (σ_φ index). The derivation of these two parameters requires GNSS scintillation observation data sampled at very high frequency (usually 50Hz or higher). Nonetheless, most GNSS receivers do not provide scintillation data because of their low data rates. The International GNSS Service (IGS) is an example, they only provide the 30-second rate observations for normal users and especially 1-second rate observations for real-time positioning. Even in the case of Real-Time Kinematic (RTK) positioning, low rate GNSS receiver is enough for this kind of application. Numerous local and regional GNSS stations or networks have been installed in many campaigns for various applications, but they usually use receivers to collect data at a rate of at least 1 second. If GNSS data of low sampling rate can be utilized to study ionospheric scintillations, it will significantly augment the current scintillation observation facilities [Aquino et al., 2005; Beniguel et al., 2009; Sreeja et al., 2011; Morton et al., 2014]. Undoubtedly, the huge amount of low-rate GNSS data will provide invaluable information for researchers to observe ionospheric scintillation [Zhe Yang et al., 2015].

In my research, ionospheric disturbances are measured by ROTI index. As for the definition from [Aarons, 1971], ionospheric scintillation is the rapid fluctuation in the amplitude and phase of satellite signals due to the rapid and uneven variations of the electron density within the ionosphere when it passes through the ionosphere. [Pi et al., 1997] proposed an index called Rate Of Total electron content Index (ROTI) which is defined as the standard deviation of the Rate Of Tec (ROT) over a 5-minute period to statistically present ionospheric irregularities using a network-based GPS monitoring system. This method provides the availability of using data from normal GNSS receivers with global coverage (for instance IGS stations) to study ionospheric scintillation. Its main advantage over scintillation indices is that it is calculated based on measurements from the standard dual-frequency GNSS receivers sampling at 1 Hz, which have been and still are far more common than scintillation receivers. Detailed formulae for the ROT and ROTI calculations have been introduced in Section 2.2.4. In this chapter, I use these indices to investigate the ionospheric irregularities and consider the ROTI value greater than 0.5 TECU/min is the sign of the disturbances in the

ionosphere [Ma and Maruyama, 2006]. The data sampling rate is 30 seconds (as the IGS data standard) and the calculation time interval chosen is 5 minutes to get a reasonably fine time resolution as discussed in Section 2.2.4.

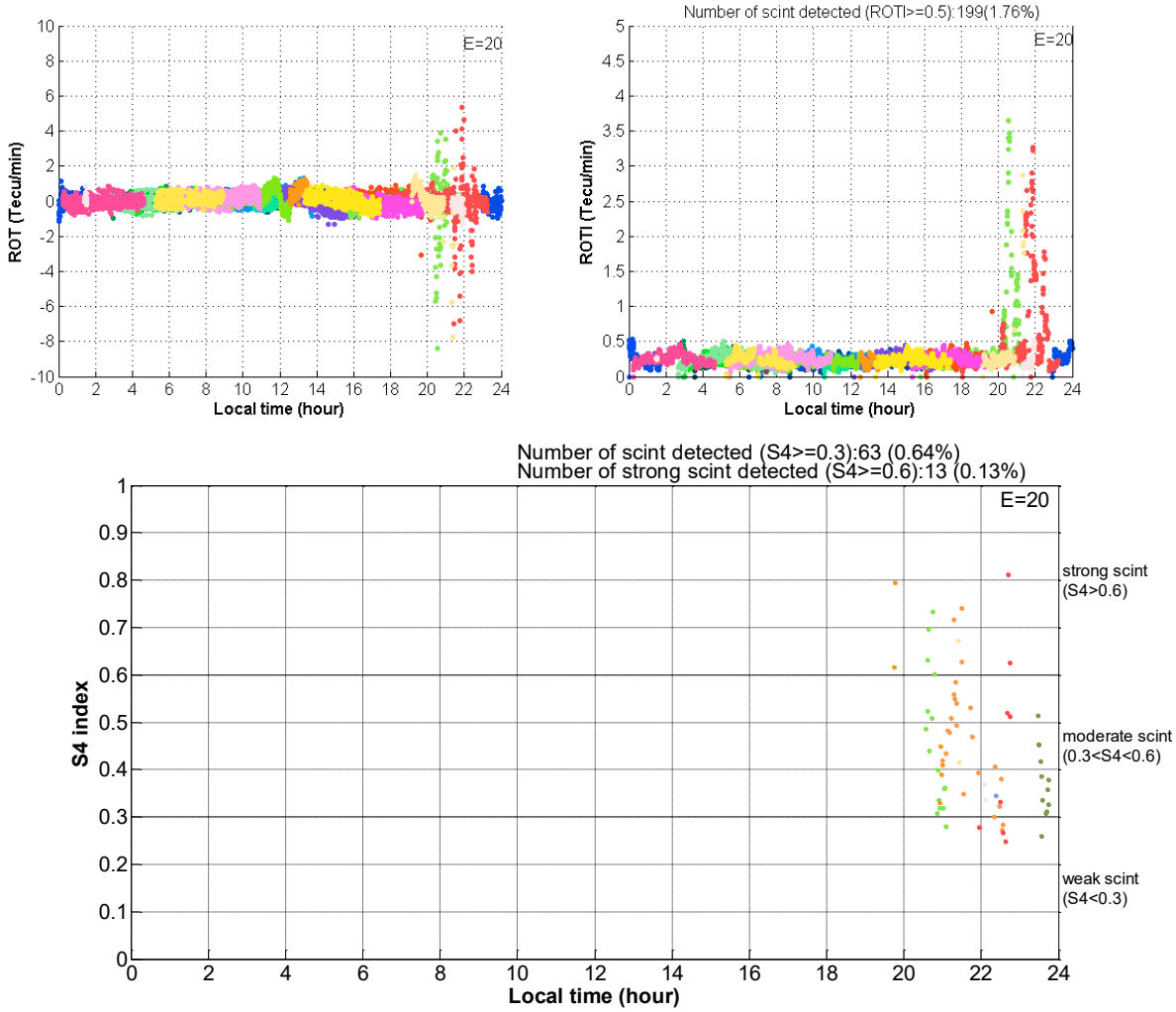

Figure 5.1. ROT (top-left), ROTI (top-right) and S_4 (below) indices at HANOI station on October 24th 2015

Figure 5.1 shows an example of ionospheric irregularities detected by ROT, ROTI, and S_4 indices on October 24th 2015. In this figure, different colours correspond to different satellites and the legend "E=20" at the upper right corner indicates the satellite elevation cut-off used is 20^{o}. A good similarity between S_4 index and ROT and ROTI indices can be found in this figure. As usual, ionospheric irregularities mostly appear during the period between 20h and 24h local time, this is following the results of previous chapters. On this day, the number of ionospheric irregularities (ROTI≥0.5) detected is 199 correspondings to 1.76% of the total observations. Meanwhile, the number of scintillation events (S_4≥0.3) is 63 correspondings to

0.64% of the total observations. Note that the total number of observations is different in each case since in the calculation of ROTI, standard observations with the interval of 30 seconds are used, meanwhile, to determine S_4 index, we need to use high rate data (50Hz) with the interval of 0.02 second. Nonetheless, the results obtained from Figure 5.1 still show some equivalences between S_4 and ROTI both in appearance time and intensity of ionospheric irregularities.

As is well known, measurements with low satellite elevation are often sensitive measurements that are susceptible to various sources of error, especially multi-path errors. It is no exception in the case of ionospheric scintillation detection. Therefore, to study the effect of satellite elevation used on the determination of ionospheric irregularities from GNSS measurements, I compare the number of ionospheric irregularities detected using different satellite elevation cut-off including 0^o, 10^o, 20^o, 30^o, and 40^o. In all these examinations, the time span of ROTI calculation is fixed for 5 minutes. The results are shown in Figures 5.1, 5.2a and listed in Table 5.1

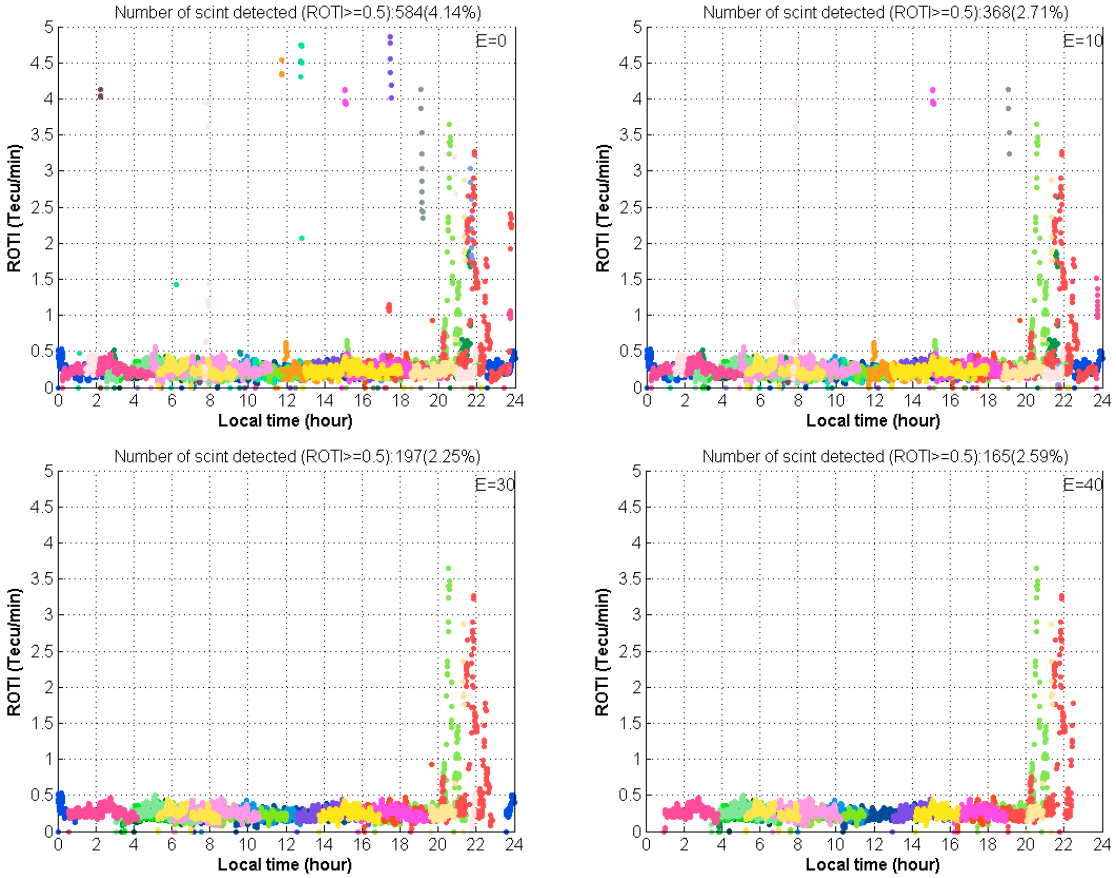

Figure 5.2a. Comparison of scintillation events with different elevation threshold

Table 5.1a. Comparison of scintillation events with different elevation threshold (time span calculation is 5 minutes)

No	Elevation cut-off	Number of scintillations (ROTI≥0.5) detected	Percentage of scintillations (ROTI≥0.5) detected
1	0^o	584	4.14 %
2	10^o	368	2.71 %
3	20^o	199	1.76 %
4	30^o	197	2.25 %
5	40^o	165	2.59 %

From Figure 5.2a, it can be seen that when using low satellite elevation (especially in the case E= 0^o), a lot of disturbances are detected scattered at different times of the day. Their causes are thought to originate from other sources than ionospheric scintillation errors. The case of E=20^o and E=30^o give almost the same numbers of ionospheric irregularities detected (199 and 197, respectively). However, if we choose E=30^o, the number of total observations received will be significantly reduced (this can be realized by the percentage calculated in the last column of Table 5.1). Therefore, the proposed equilibrium option is to choose E=20^o, which is also consistent with the conventional regulation when processing data in other GNSS applications.

Based on this result, I use the satellite elevation cut-off of 20^o to investigate the effect of choosing different time span of ROTI calculation on the number of ionospheric irregularities detected. The time intervals selected for the inspection are 1, 5, 10, 15, and 20 minutes respectively. Results can be found in Figures 5.1, 5.2b and Table 5.1b.

Table 5.1b. Comparison of scintillation events with the different time span of ROTI calculation (elevation cut-off is 20^o)

No	Time span calculation (min)	Number of scintillations (ROTI≥0.5) detected	Percentage of scintillations (ROTI≥0.5) detected
1	1	229	2.03 %
2	5	199	1.76 %
3	10	232	2.06 %
4	15	267	2.37 %
5	20	281	2.49 %

It can be seen that when choosing a time span of 5 minutes, the number of ionospheric irregularities detected is minimum (199), and when the time span is larger, this number also increases accordingly. With the case of selecting a time span equal to 1 minute, we can see from Figure 5.2b that there are quite a lot of ROTI values with large amplitude (approx. 0.5

TECU/min) appearing during the whole calculation period. This is because in each ROTI calculation, only two measurements are used as GNSS observations interval is 0.5 minute. Such measurements are not sufficient to ensure the detection of short-term fluctuations (if they exist) in the VTEC calculation results, therefore, the results obtained do not reflect the small-scale disturbances in the ionosphere. As discussed in Section 2.2.4, the time span of ROTI calculation should be chosen to ensure giving a reasonably temporal resolution and still having a good number of observations for each interval calculation. Also, note that in most articles use ROTI index, the authors often use a time span of 5 minutes as refers to [Pi et al., 1997]. From all these factors, in our subsequent calculations related to ROTI index, the selected time span calculation is fixed at 5 minutes. It comes with a commonly used satellite elevation threshold of 20^{o} (except in some special cases).

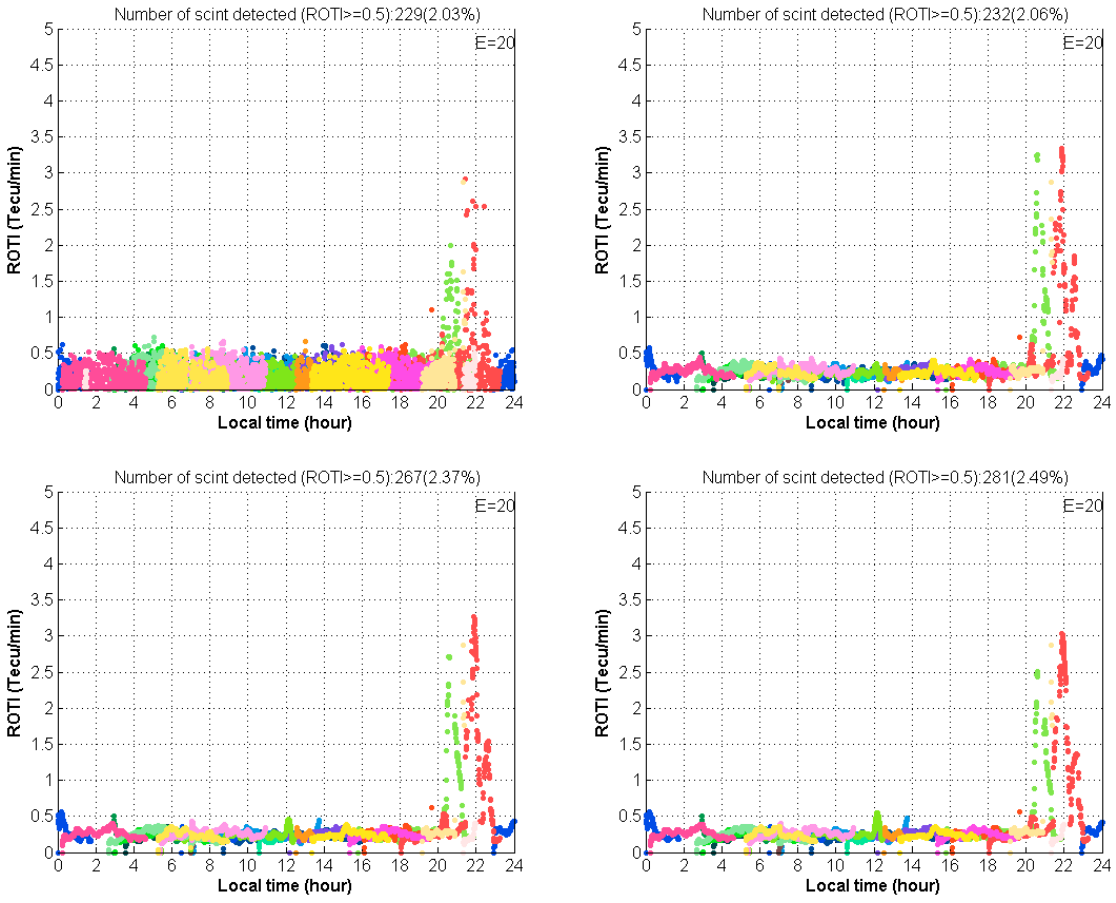

Figure 5.2b. Comparison of scintillation events with different time span of ROTI calculation (top-left: 1 min, top-right: 10 mins, bottom-left: 15 mins, bottom-right: 20 mins)

More examples of the similarity between ROTI and S_4 and their suitability for the study of irregularities in the ionosphere will be further discussed in Section 6.2.3 when studying the ionospheric disturbances that occur during strong magnetic storms.

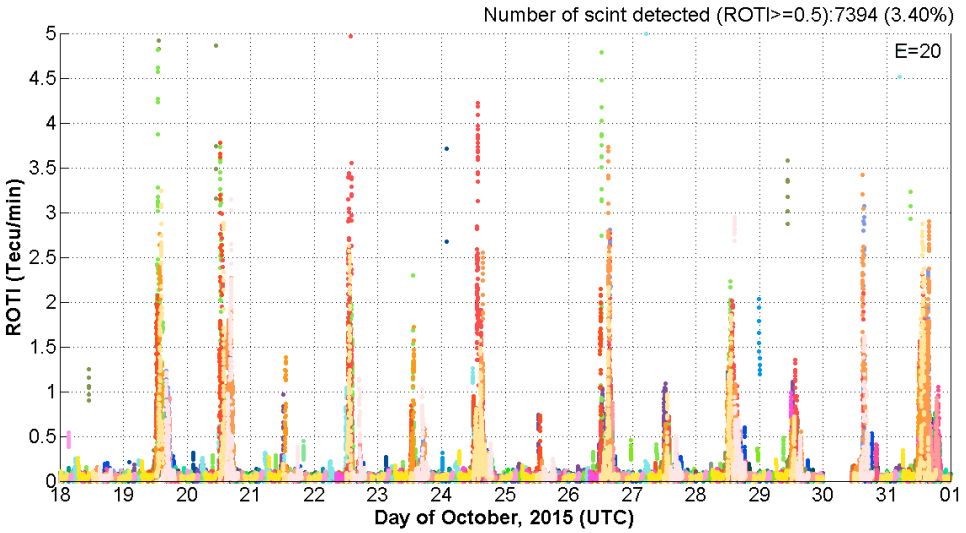

Figure 5.3a. Ionospheric disturbances occur during the second half of October 2015 at HUE

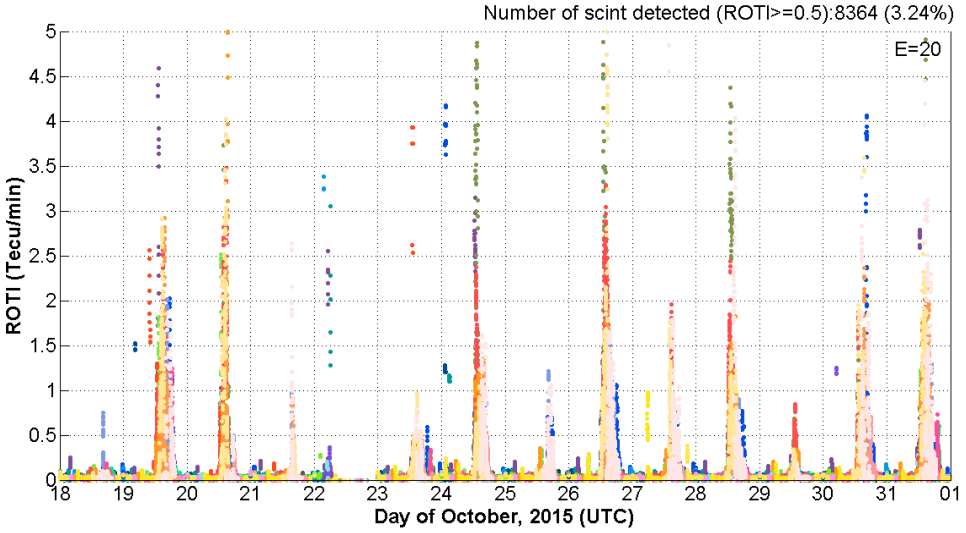

Figure 5.3b. Ionospheric disturbances occur during the second half of October 2015 at CUSV

Figures 5.3a-b show examples of the detection of ionospheric irregularities using ROTI index during the period of the last two weeks of October 2015 at two stations HUE and CUSV. The number of ionospheric irregularities detected at two stations is 7394 and 8364 respectively. As usual, they are usually observed in the evening and rarely occur during the daytime. Note that the percentage shown in these figures is the per cent rate of disturbed observations (with corresponding ROTI>=0.5) to all observed observations. It usually reaches a maximum of no more than 5% but it could much affect the quality of GNSS measurements. Basically, in GNSS positioning and most of the other GNSS applications, we expect this percentage to be zero and in case they persist, a reasonable method should be proposed to eliminate them before processing.

Similar results to Figures 5.3a-b are also obtained at other stations in the Southeast Asia area during this period. This proves that the ionosphere in this area was strongly disturbed during the second half of October 2015. Table 5.2 provides the number of ionospheric irregularities detected during this time. The indices used are the S_4 and ROTI, thresholds to assess the ionosphere turbulences are 0.3 and 0.5 (TECU/min) respectively. To facilitate the evaluation of the irregularities in the ionosphere, this table also provides the number of ionospheric scintillations detected from ROTI maps which are established from some IGS stations (indicated in the last column) in the Southeast Asia region (the issue of establishing ROTI maps will be addressed later). Similar table of results (Table 6.4) for the period of the second half of March 2015 will be presented in Section 6.2.3. This section also takes into account the correlation between the two indices.

Table 5.2. Statistics of S_4, ROTI indices and the ionospheric disturbances derived from the regional ROTI maps during the last two weeks of October 2015

Days of October	HANOI station				HUE station				Regional ROTI maps		
	S4 index		ROTI index		S4 index		ROTI index				
	Num	%	Num	%	Num	%	Num	%	Num	%	Num of stations used
18	0	0.0	0	0.0	0	0.0	10	0.1	54	0.0	8
19	172	1.8	224	2.2	154	1.6	1039	7.5	5552	4.3	8
20	143	1.5	44	0.4	108	1.1	980	6.1	4629	3.6	8
21	0	0.0	0	0.0	11	0.1	44	0.3	1211	0.9	8
22	59	0.6	16	0.2	141	1.4	666	4.5	2729	2.3	8
23	1	0.0	0	0.0	7	0.1	140	0.8	337	0.3	8
24	63	0.6	201	1.8	154	1.6	533	3.5	4196	3.5	7
25	0	0.0	no data		0	0.0	18	0.1	209	0.2	7
26	52	0.5	101	1.0	44	0.5	572	3.5	4838	3.6	8
27	2	0.0	1	0.0	44	0.4	163	0.9	968	0.7	8
28	98	1.0	11	0.1	229	2.3	1243	7.9	4221	3.2	8
29	35	0.4	15	0.2	45	0.5	251	1.5	1313	1.0	8
30	23	0.2	18	0.1	28	0.5	216	2.3	1406	1.2	8
31	0	0.0	0	0.0	217	2.2	1501	10.0	5434	4.5	8

From Table 5.2 and Table 6.4, we find that the number of ionospheric disturbances detected in the second half of March and the second half of October was 18349 and 37178, respectively, with the corresponding percentages are 12.5% and 29.2%. Comparing these numbers between two periods, it can be seen that although the storm Saint Patrick occurred in March 2015 is considered to be the strongest geomagnetic storm during SC24, but the turbulence level of the ionosphere during this period is not equal to that in October the same year. In particular, while in the second half of March, only in a few days (16^{th}, 19^{th}, and from

24th to 28th) the ionospheric disturbances were detected, this disorders occurred on most days during the last two weeks of October, even with greater intensity.

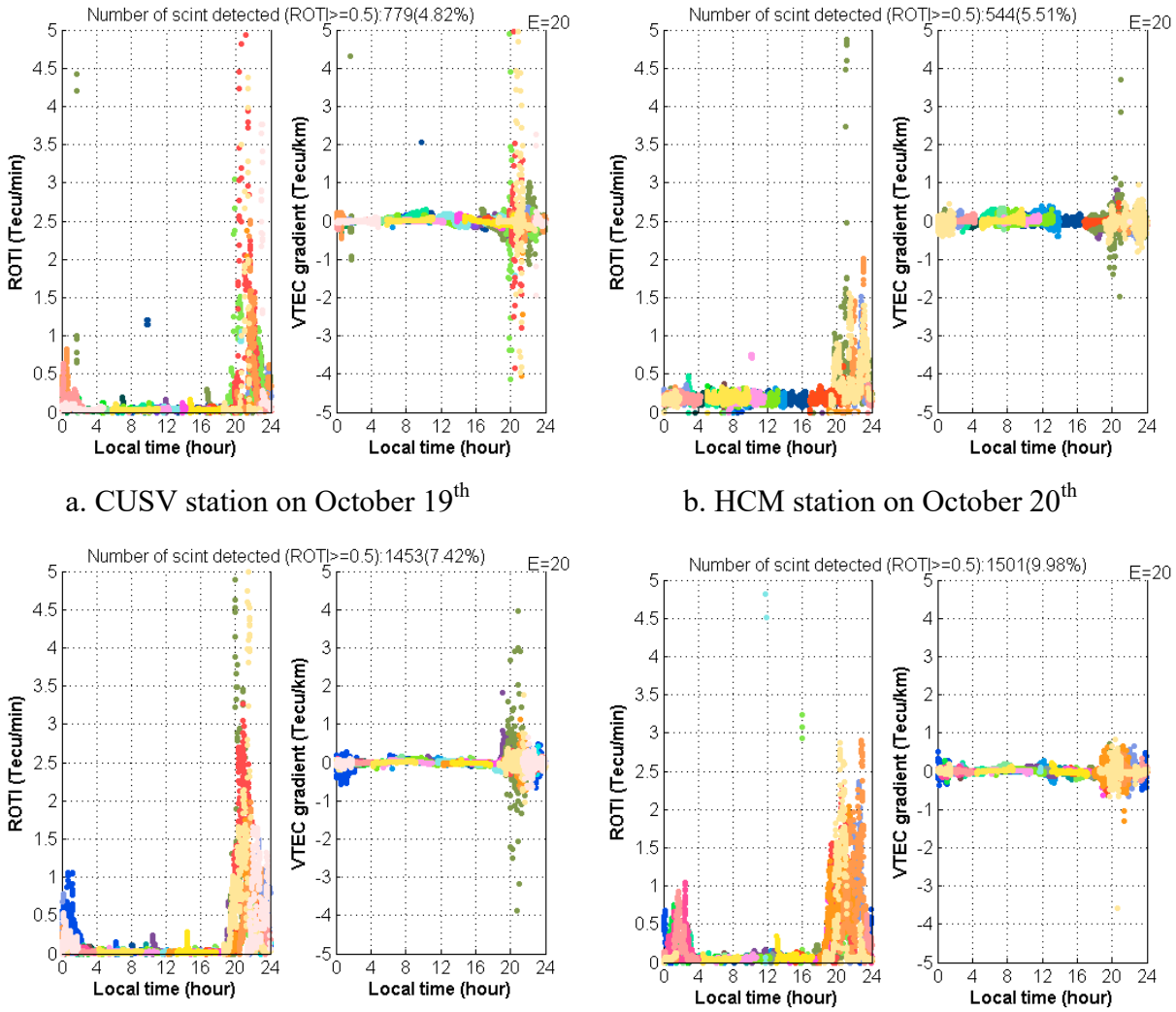

a. CUSV station on October 19th

b. HCM station on October 20th

c. CUSV station on October 26th

d. HUE station on October 31st

Figure 5.4. Ionospheric irregularities including ROTI index and VTEC gradient

Figure 5.4 illustrates some typical examples of ionospheric irregularities at some stations over several days during the last two weeks of October 2015. In these plots, I also include VTEC gradient along with ROTI index. While the ROTI index has a TECU/min unit, that is only capable of expressing fluctuations of ionospheric disturbances over time, VTEC gradient with the corresponding unit of TECU/km can express the level of irregularities in the ionosphere both in temporal and spatial status. Therefore, in Figure 5.4, they have the similarity in occurrence time of ionospheric scintillation (i.e. between 20 and 24 LT), but the intensity cannot be compared with each other because of the difference in the essence of the two indices: ROTI shows the fluctuations of TEC per minute, while VTEC gradient indicates TEC fluctuations per kilometre.

5.2. Regional ionospheric irregularities maps

Table 5.2 mentioned the ROTI maps, which are often used to assess the level of disturbances in the ionosphere both in temporal and spatial distributions. Figure 5.5 shows ROTI maps over the Southeast Asia region in four days (19th, 20th, 26th, and 31st) with the strongest disturbances in October 2015. The research area is in range of 15°S - 25°N latitude and 95°E - 115°E longitude, thus, this area covers the whole EIA region. As can be seen in these maps, the geographic latitude areas from 0° to 5° do not have many observations due to the lack of stations in these areas. The purpose of creating this type of map is to find out the features of ionospheric irregularities including its locations, characteristics and occurrence time. It can also show the exact number of observations (and the percentage to the total number of observations) affected by ionospheric scintillation error.

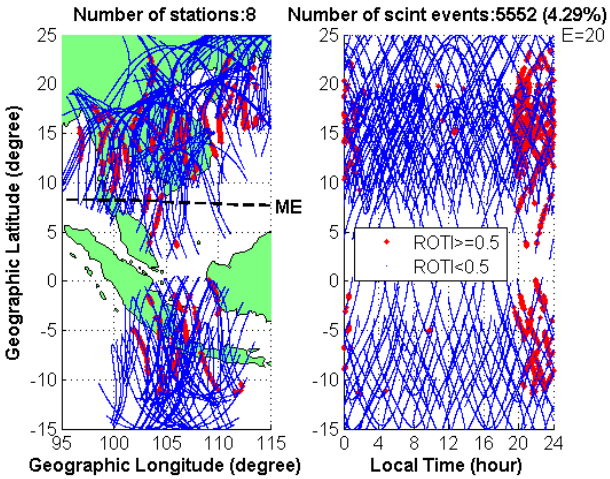

a1. Regional ROTI map on 19th

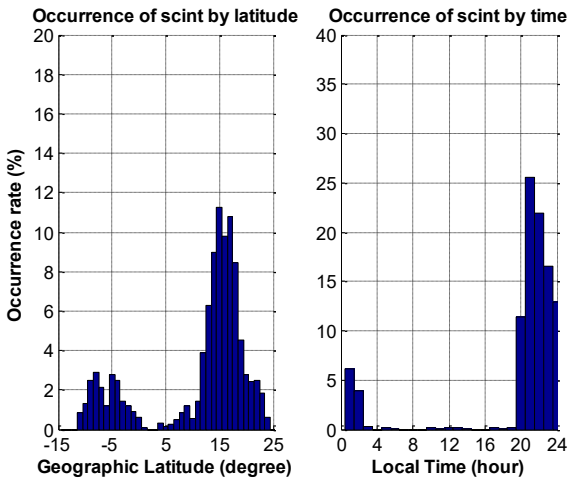

a2. The occurrence of scintillation on 19th

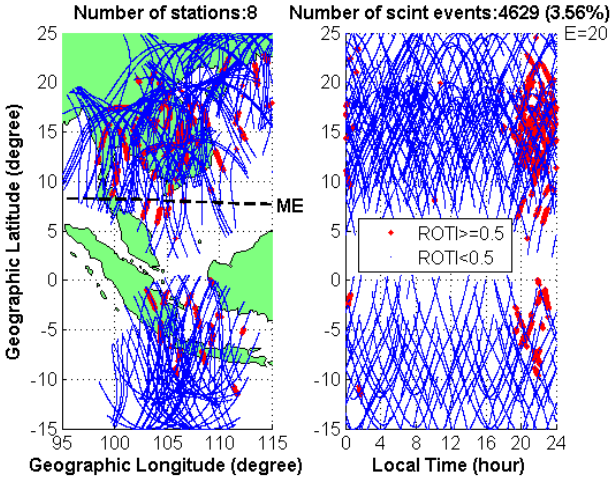

b1. Regional ROTI map on 20th

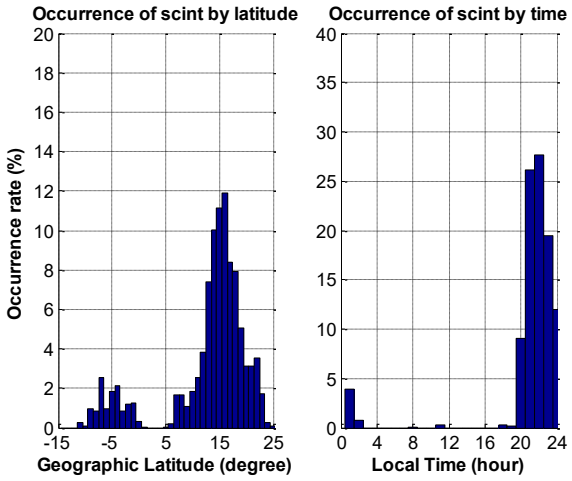

b2. The occurrence of scintillation on 20th

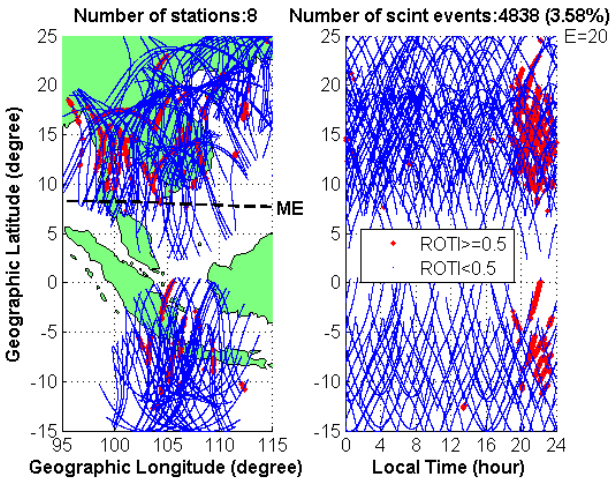

c1. Regional ROTI map on 26th

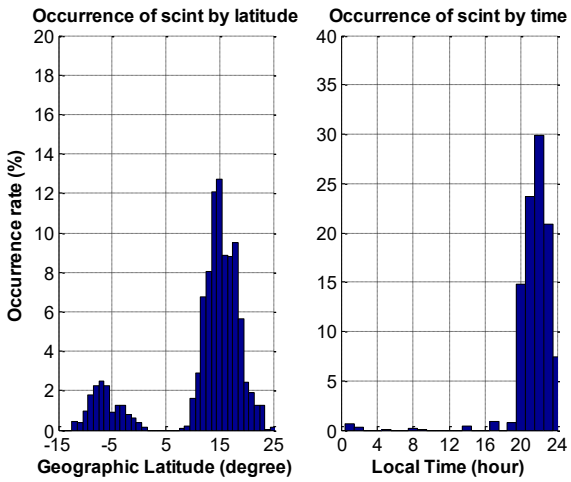

c2. The occurrence of scintillation on 26th

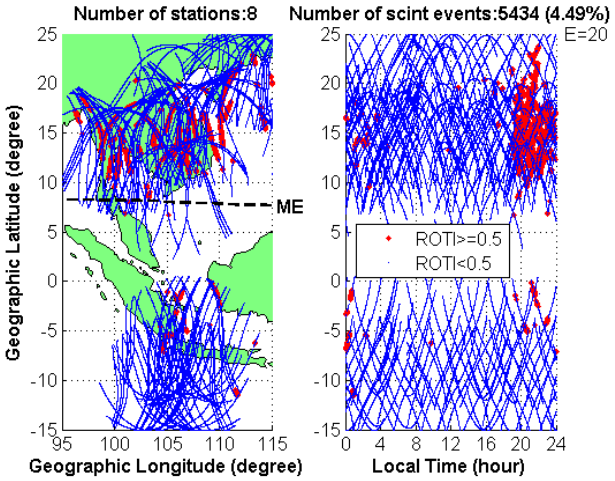

d1. Regional ROTI map on 31st

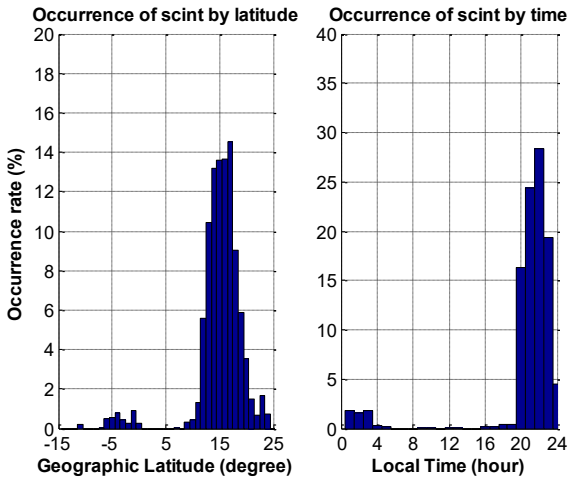

d2. The occurrence of scintillation on 31st

Figure 5.5. Regional ROTI maps and the occurrence rates of ionospheric scintillation

In the above figures, plots on the left side are the regional ROTI maps, plots on the right side show the percentages of the occurrence of ionospheric irregularities in both terms of latitude and time. ME stands for magnetic equator. The dots in ROTI maps are the satellite footprints tracking which are the intersections between the Line Of Sight (LOS) from satellites to receivers and the Singer Layer Model (SLM) of the ionosphere at the attitude of 450 km. The red dots indicate observations with ROTI index of not less than 0.5 TECU/min, which is the sign of ionospheric disturbances, and the blue ones show the quiet status of the ionosphere (ROTI<0.5 TECU/min). Data for these maps are the GNSS measurements from all available IGS stations in the research area (usually 8 stations). The location map and details of the stations can be found in Section 3.1. The total number of ionospheric irregularities detected and its percentage to all observed measurements are also given in the top of the ROTI maps and are listed in columns 10 and 11 of Table 5.2. Meanwhile, the plots of

ionospheric scintillation's occurrence on the right side show the appearance percentages in latitude (resolution of 1^{o}) and in time (resolution of 1 hour), they are the percentages to all detected ionospheric irregularities, but not to all observed measurements.

As noted above, these maps provide both spatial and temporal distributions of ionospheric scintillation, however, its main drawback is that it is not yet possible to give the perturbation intensity of the ionosphere at different locations. From Table 5.2 and Figure 5.5, some noteworthy remarks about ionospheric irregularities in the Southeast Asia region can be drawn as follows:

- During the second half of October 2015, ionospheric disturbances appeared quite a lot in most of the days including days 19^{th}, 20^{th}, 24^{th}, 26^{th}, 28^{th}, and 31^{st} with all reached over 3% of the total observations. In the remaining days (except on the 22^{nd} with ionospheric disturbances being moderate of 2.3%), the ionosphere remained in a relatively quiet state with the percentages of ionospheric irregularities being approximately or less than 1%. According to my research results, October has also recorded as the period that ionospheric irregularities with strong intensity occurred the most in 2015, even more than that in March when the super geomagnetic storm Saint Patrick happened.
- For spatial distribution: they usually appear concentrated in the areas near and around the two anomaly crests of EIA. Paying close attention, ionospheric irregularities often occur continuously in a certain period with a specific satellite, meaning that at the same location not all observations to all satellites are affected by the ionospheric scintillation error. Besides, ionospheric irregularities are found to occur more in the northern hemisphere than in the southern hemisphere. The main reason is due to the natural physical characteristics of the ionosphere during this period, however, this is maybe partly due to the lower number of stations used in the southern hemisphere than in the northern hemisphere.
- For temporal distribution: they occur mostly at night, between 20 and 24 local hours, of which, during the period of 21-22 LT alone accounted for about half of the total amount of ionospheric scintillation detected. In the remaining time of the day, ionospheric irregularities befall very little.

5.3. Global ionospheric irregularities maps

In the previous section, I use available data at all IGS stations located in Southeast Asia to study ionospheric irregularities in this region. Based on this idea, the intention to study ionospheric irregularities on a global scale using all existing IGS stations is formed. Currently, there are about 500 IGS stations located worldwide as can be seen in Figure 5.6. Normally, for the computation of ROT, ROTI indices with data from all of these stations in one day, calculation time can last for a couple of days. So, I tried to prepare this kind of map for a certain number of days. The chosen dates are those days when the ionosphere is thought to be strongly disturbed, for example, March 26th, and October 19th in 2015, or June 30th, September 8th, and December 31st in 2017 and some other days in 2013, 2014.

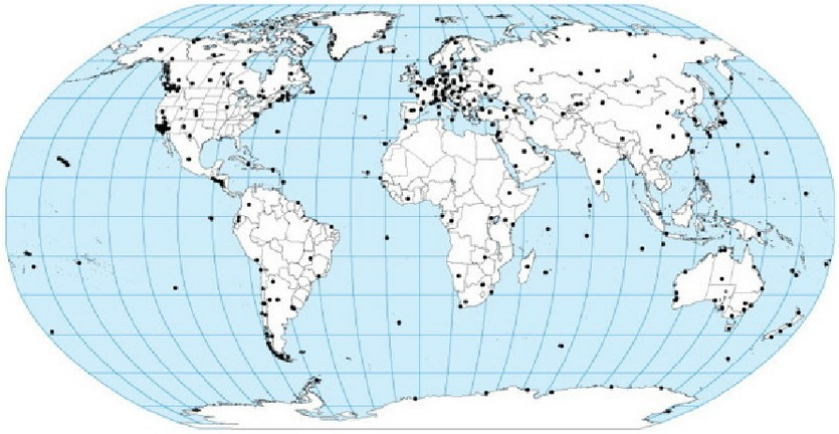

Figure 5.6. Worldwide distribution of IGS stations [5.1]

The obtained results show that on quiet days, the established maps are rather tedious and the distribution rule of ionospheric irregularities is not as clear as expected. Among the results obtained, I select the most typical example of the distribution of ionospheric irregularities on a global scale to show here. That is the global ROTI map established on March 26th 2015. The total number of IGS stations used is 483. Figure 5.7 shows the satellite footprint tracking of all these stations with the satellite elevation cut-off is 20^{o}.

[5.1] http://www.igs.org/network/netindex.html

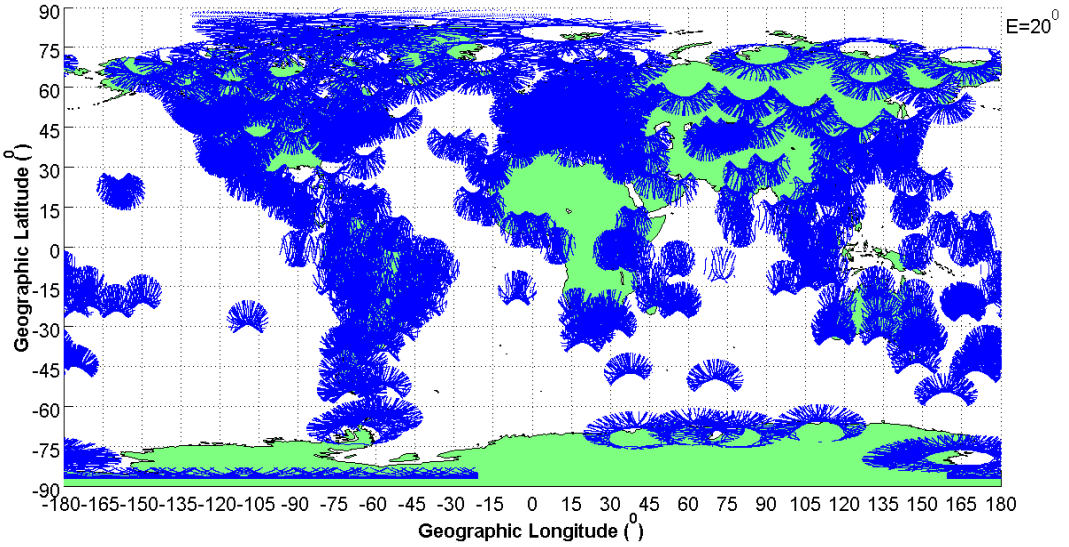

Figure 5.7. The footprint tracking of satellites at all 483 IGS stations on March 26th 2015

As can be foreseen, the density of IGS stations is not uniform globally. In addition to the ocean regions without any GNSS stations, in some land areas, the number of IGS stations is also very sparse, typically in most of North Africa area and part of South Africa area. Besides, in the territory of the Russian Federation and China, the density of GNSS stations does not cover the vast areas of these two countries. And as can be predicted, the density of IGS stations is most dense in the areas of western Europe, North America, South America and somewhat in the Pacific Islands, Australia and East Asia.

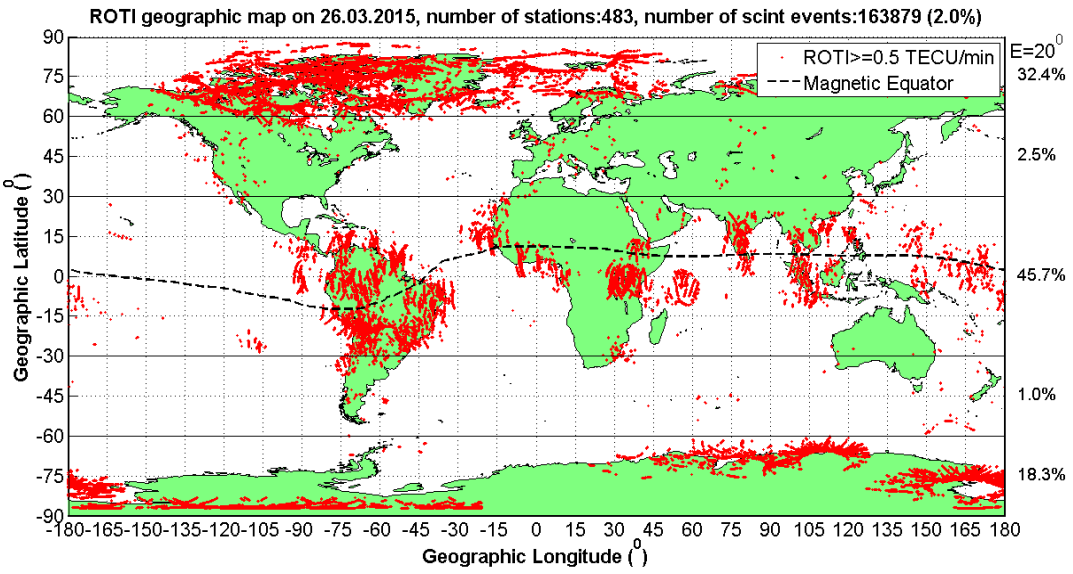

Figure 5.8a. Spatial distribution of global ionospheric irregularities (refers to as of Fig. 1.2) (only ROTI≥0.5 TECU/min are displayed)

The global ROTI map on March 26th 2015 is illustrated in Figure 5.8a. In this figure, to highlight the ionospheric disturbances, only ROTI not less than 0.5 TECU/min is flaunted. The total number of ionospheric irregularities detected is 163879 corresponds to approximately 2.0 % the total number of observations obtained on this day. The regions most likely to be affected by the ionospheric disturbances are South America, Southeast Asia, and the Arctic. This is following the published research results on the global spatial distribution of ionospheric scintillation [Basu et al., 1988, 2002; Kintner et al., 2009]. A comparison of the distribution of scintillation occurrence in different regions of the world can be found in [Tsai et al., 2016]. In this section, for the comparison of occurrence density of ionospheric irregularities at different latitudes of the Earth, the Earth is divided into five different latitudinal bands from the north to the south as follows: the northern high latitudes (latitudes>60°N), northern mid-latitudes (latitudes between 30°N and 60°N), low latitudes or equatorial regions (latitudes between 30°S and 30°N), southern mid-latitudes (latitudes between 30°S and 60°S), and southern high latitudes (latitudes<60°S). The result of occurrence density is given on the right side of the Figure 5.8a. This result indicates that ionospheric irregularities mainly occur in the low latitude areas when it accounts for nearly half (45.7 %) of the total ionospheric irregularities detected, followed by the two-pole areas with the superiority of the northern pole compared to the southern pole (32.4 % and 18.3 %, respectively). As expected, the high latitude areas are the least likely to experience ionospheric disturbances. Only about 3.5 % of the total number of ionospheric irregularities is detected in these areas, in which the northern high latitudes (with 2.5 %) accounting for the majority.

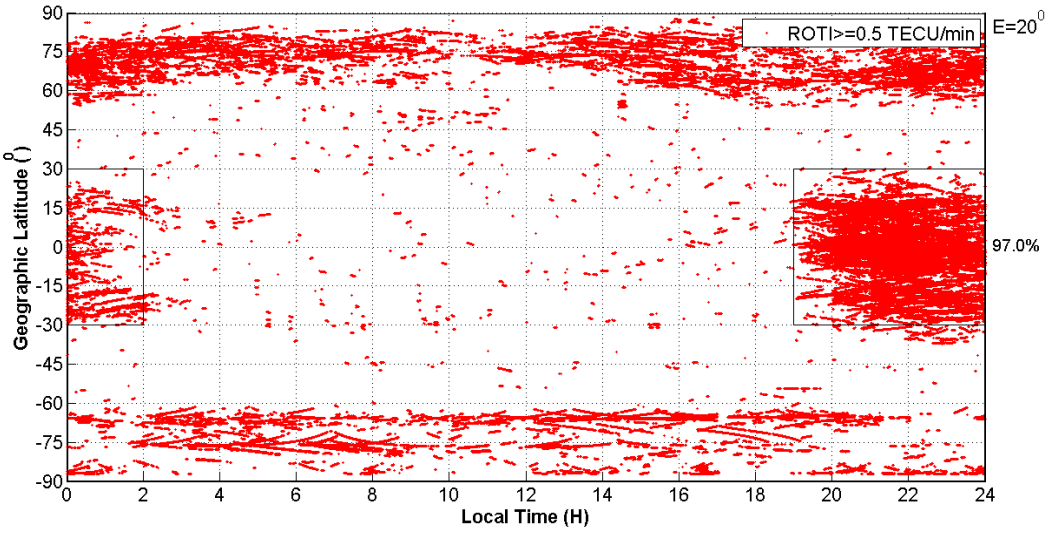

Figure 5.8b. Temporal distribution of global ionospheric irregularities

While Figure 5.8a describes the global spatial distribution of ionospheric irregularities, Figure 5.8b indicates its global temporal distribution. Similar to spatial distribution, the temporal distribution of ionospheric irregularities has a clear differentiation by latitude regions. In the low-latitude regions, about 97.0 % of ionospheric irregularities detected appears during the nighttime from 19 LT to 2 LT the next day. The remaining 3.0 % only occurs scattered at different times of the day. This rule is in accordance with the research results pointed out in Chapter 4. Thus, the occurrence rule of ionospheric scintillation at low-latitude areas is very transparent, that it only appears in the evening (this can be easily noticeable in Figure 5.8d for the low-latitude areas). This is in contrast to the high-latitude areas, where ionospheric scintillation can occur at any time of the day as can be seen in Figure 5.8b or Figure 5.8d. For the mid-latitude regions, due to the very limited number of ionospheric irregularities detected, the rule of temporal distribution cannot be formed.

By showing Figures 5.8c-d, I continue to analyse the distribution of ROTI by location including latitude (c) and longitude (d). The occurrences rate (%) given is the percentage corresponding to the total ionospheric irregularities detected on March 26th, not the percentage of the total number of observations.

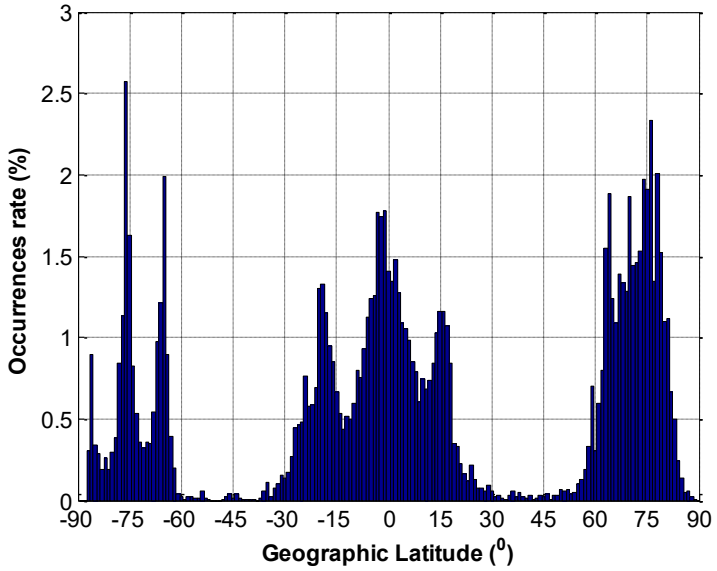

Figure 5.8c. Distribution of ROTI by latitude (only ROTI≥0.5 TECU/min are counted)

It can be seen that ionospheric irregularities are mainly concentrated in the equatorial and high-latitude regions, but rarely occur in the mid-latitudes areas. While in the low-latitude areas, ionospheric irregularities tend to appear symmetrically over the equator, in the high-latitude regions, the northern hemisphere noted a higher number of ionospheric irregularities compared to the southern hemisphere.

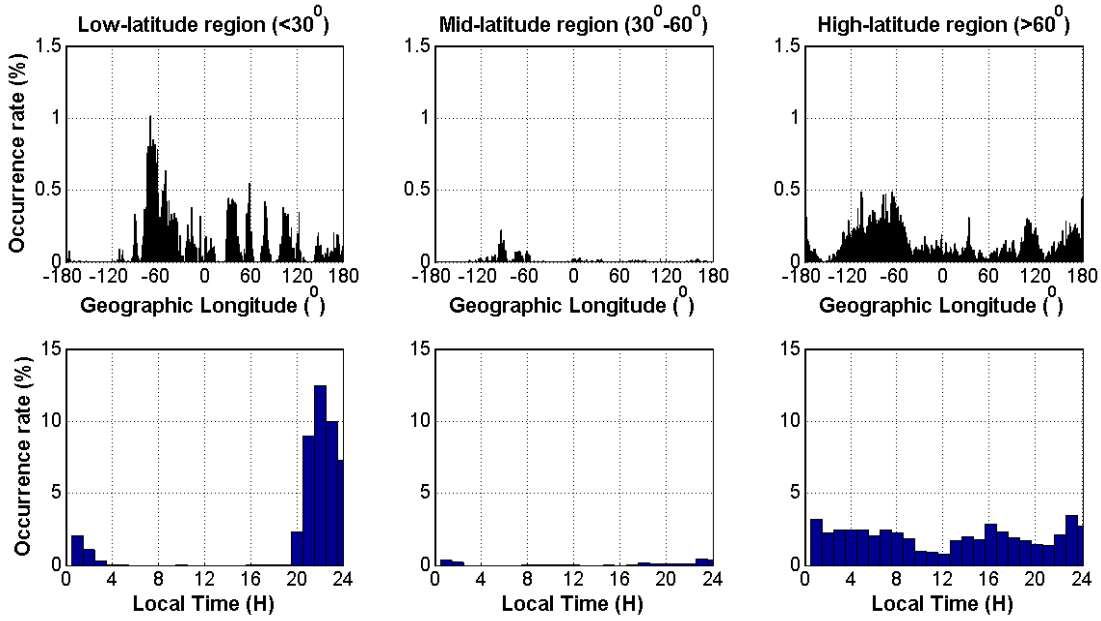

Figure 5.8d. Distribution of ROTI by longitude (above) and by time (below) at three different zones of the Earth (only ROTI≥0.5 TECU/min are counted). While the mid-latitude areas show almost nothing as can be predicted, the high-latitudes are the regions where ionospheric irregularities can occur randomly at any longitude and at any time of the day. The appearance rule is most straightforward in the low-latitude regions with the appearing time only at night and most concentrated in the area of 60°W longitude (the South America region).

5.4. Chapter summary

In this chapter, I primarily use the ROTI index to study the ionospheric irregularities in the Southeast Asia region and globally. The main contents can be summarized as follows:

- Section 5.1 first reintroduces the advantages of using ROTI index to study ionospheric scintillation which emphasizes the advantages of the huge amount of GNSS data currently available globally. Short examinations on the use of different elevation threshold and different time span of ROTI calculation have been conducted and concluded: using satellite elevation cut-off at 20^o and choosing ROTI time span calculation of 5 minutes are the most reasonable. Calculation results of ROTI and VTEC gradient in the second half of October 2015 indicate several days during this period, the ionosphere was strongly disturbed based on the abnormally high number of the ionospheric irregularities.

- Section 5.2 provides ionospheric irregularities maps over the Southeast Asia region during the last two weeks of October 2015, thereby showing the temporal and spatial characteristics of the occurrence of disturbances in the ionosphere.

- In Section 5.3, for the first time, both spatial and temporal distributions of ionospheric irregularities have been exposed on a global scale (Figures 5.8a-d), in which, the percentage of occurrences (both location and time) is calculated to give out specific numbers for different regions of the world. Research results of this chapter are consistent with the conclusions announced in the previous chapters as well as previously published papers on the characteristic distributions of ionospheric scintillation. One of the most significant results is that Southeast Asia (along with South America) is one of the two areas most affected by scintillation phenomenon of the ionosphere.

6. Comparisons of EIA observations based on IONEX files

6.1. Temporal - latitudinal VTEC maps and methodology to study the characteristics of peak EIA crest

6.1.1. Global VTEC map derived from IONEX files

The IONEX (IONosphere map EXchange) file is one of the products of the International GPS Service for Geodynamics (IGS). This file format is based on a first format proposal by [Schaer, 1996], which strongly follows the RINEX files. The main purpose of the IONEX files is to supports the exchange of two- and three-dimensional VTEC maps given in a geographic grid. Ionospheric VTEC maps (referred to GIM) in agreement with the IONEX format contain VTEC values at points arranged in a globally distributed grid of size 71×73 over latitude×longitude respectively. In latitude, grid points range from +87.5^{o} to -87.5^{o} with a spatial resolution of 2.5^{o}. In longitude, grid points are arranged from -180^{o} to +180^{o} with a resolution of 5^{o}. Conventionally, every two hours starting from 00:00 UT, a new VTEC map is prepared. In total, 13 VTEC maps are established every day with the last one is exactly at the same epoch with the first one of the next day. In short, VTEC maps are produced with a resolution of 2 hours, 2.5^{o} and 5^{o} in universal time, latitude and longitude respectively. Currently, the IONEX files can provide the VTEC maps with a higher time resolution, for instance at every 1 hour or even every quarter an hour. In most cases, attachment with the VTEC maps is the TEC RMS maps which indicate the accuracy of the corresponding VTEC maps. Presently, there are four ionosphere associate analysis centres including CODE (Center for Orbit Determination in Europe, Astronomical Institute, University of Berne, Switzerland), ESOC (European Space Operations Centre of ESA, Darmstadt, Germany), JPL (Jet Propulsion Laboratory, Pasadena, California, U.S.A), and UPC (Polytechnic University of Catalonia, Barcelona, Spain) are responsible for providing the final and rapid ionosphere products according to IONEX format. They include VTEC maps, RMS maps and daily-constant P1, P2, DCB values of satellites and all available IGS stations. The results of each analysis centre are then combined into the official IGS ionosphere product. The abbreviations used for the VTEC maps and latency of availability are given in Table 6.1.

With the IGS final VTEC map has the highest quality and internal consistency of all IGS products. It is made available every week, by each Friday, with a delay up to 13 days for the last day of the week and up to 20 days for the first day of the week. The accuracy of the final ionospheric TEC grid is about 2 - 8 TECU. Meanwhile, the IGS rapid VTEC map has a

quality nearly comparable to that of the final VTEC map. It is made available daily with a delay of about 17 hours after the end of the previous observation day (the IGS rapid VTEC map is released daily at about 17:00 UTC). The accuracy of the rapid ionospheric TEC grid is about 2 - 9 TECU. Like other IGS products, the VTEC maps (or GIM) can be downloaded at the IGS official website [6.1]. Besides, real-time ionospheric maps (updated every 5 minutes) are also available at the website of NASA [6.2]. These maps are used to monitor ionospheric weather, and to nowcast ionospheric storms that often occur responding to activities in solar wind and Earth's magnetosphere as well as the thermosphere.

Table 6.1. Abbreviations of used ionospheric products from IGS [Wienia, 2008]

Analysis Center	Final VTEC map	Latency (days)	Rapid VTEC map	Latency (hrs)	Time resolution (hrs)
CODE	CODG	5	CORG	<12	1
ESOC	ESAG	5	ESRG	<12	2
JPL	JPLG	4	JPRG	<12	2
UPC	UPCG	5	UPRG	<12	2
Combined	IGSG	11	IGRG	<24	2

6.1.2. Methodology to study the occurrence characteristics of peak EIA crests

Figure 6.1 shows an illustrative example of GIM (determined from CODE) extracted from the IONEX file on January 31st 2020. From these maps, it is seen that the EIA region (the red areas with large VTEC values) moves continuously from east to west. This movement is to ensure that the regions with the maximum VTEC (the crests of EIA) always occurs after the local noontime as conclusions about the VTEC's daily variations given in Chapter 3. The red regions have an extraordinary VTEC value and it runs along the equator, leading to its name being an equatorial anomaly. But if we look closely (as disclosed in Figure 6.2) at the anomaly regions, it can be seen that they are not one block but consists of two anomaly peaks with one located in the north and one located in the south, namely the northern crest and southern crest. As such, the morphology, movement footstep and appearance time of EIA are somewhat dimly revealed from GIM. Nonetheless, with the time resolution of only one or two hours, using GIM cannot be determined accurately the position, occurrence time and amplitude of the crests of EIA. For this task, I use the so-called temporal - latitudinal VTEC map instead. This kind of map can be prepared directly from GNSS measurements or IONEX files.

[6.1] https://kb.igs.org/hc/en-us/articles/115003935351
[6.2] https://iono.jpl.nasa.gov/latest_rti_global.html

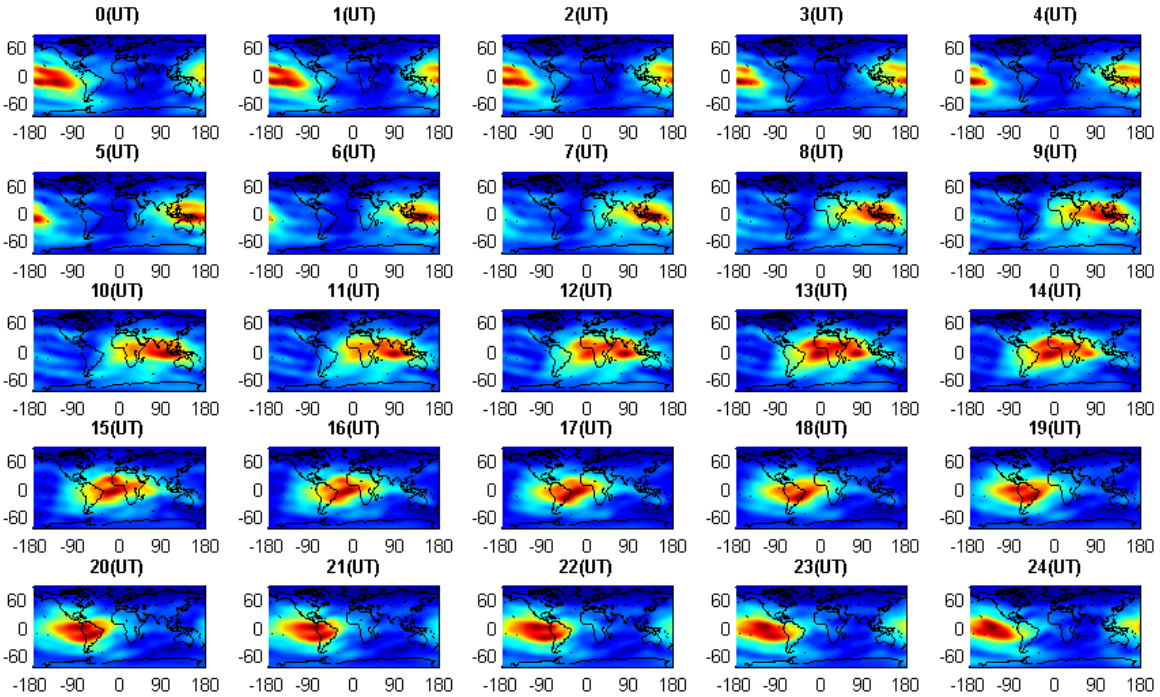

Figure 6.1. An example of GIM on January 31st 2020 shows the movement of peak EIA crests (The color bar can be seen in Figure 6.2 with the unit of TECU)

The temporal - latitudinal VTEC map is already displayed in Section 3.3. This is a two-dimensional map that is established at a certain longitude, its two dimensions are time and latitude. The amplitude of TEC can be estimated by comparing its tint with the bar colour scale attached. Thus, instead of using a geospatial map with two dimensions of longitude and latitude, this type of map is only created at a specific longitude. The purpose of this is to be able to determine the third component (i.e. time) to answer the question when the EIA's crests appear. This map can provide sufficient information about TEC such as occurrence time, position, amplitude and therefore, it can be used to determine EIA's crests as described in Figure 6.3.

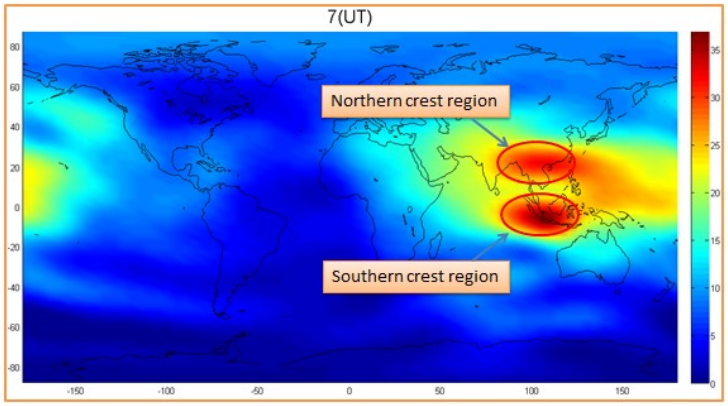

Figure 6.2. The separation between the northern and southern crests of EIA (TECU unit)

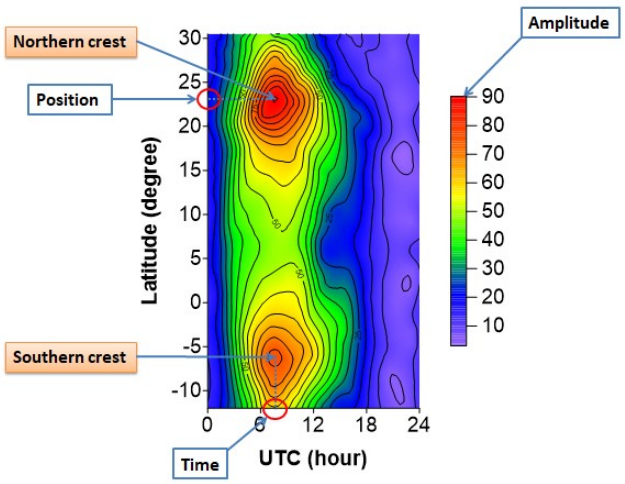

Figure 6.3. Determine EIA's crests from temporal - latitudinal VTEC map (TECU unit)

6.1.3. Establish temporal - latitudinal VTEC map from GNSS observations

In principle, the temporal - latitudinal VTEC map can be created from the GNSS observations (RINEX files) or GIM (derived from IONEX files) or the combination of them. The issue of using IONEX files to create VTEC map will be mentioned later, in this section I consider the case of establishing VTEC map from RINEX files. Figure 3.4a (Chapter 3) describes the satellite traces at IPP's height of some GNSS stations by its latitude and longitude. From this, we can prepare the VTEC map at each different epochs. However, the reliability of this map is very poor due to the limit of the number of stations (only a few) as well as the number of observed satellites (maximum 12). Also, it should be noted that Figure 3.4a depicts the satellite traces throughout the day. In our case, VTEC maps are created at each specific epoch, so the actual number of satellite traces available is very few, resulting in an established map will not guarantee the required accuracy. More importantly, if we use this type of map (which only uses spatial data), the time data (inherent in the calculation of TEC) cannot be taken advantage.

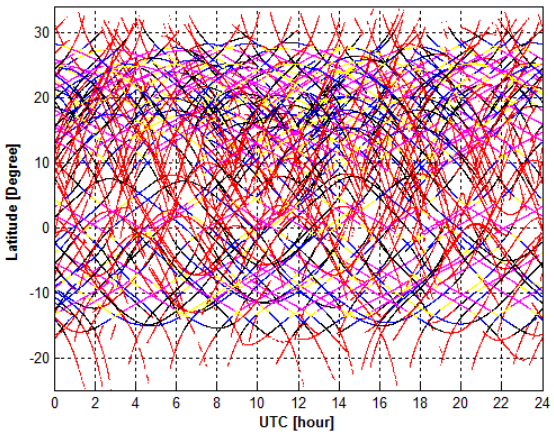

Figure 6.4. The footstep of satellite traces expressed in two variables: time and latitude

Figure 6.4 shows the footprint of the satellite traces by its time and latitude (different colours correspond to different satellite elevations as indicated in the caption of Figure 3.4a). Set side by side with Figure 3.4a, the superiority of satellite traces distribution can be seen. In this case, the satellite trace measurements are distributed more evenly and denser. Therefore, a map created by time and latitude certainly gives better resolution than a map created by longitude and latitude. Besides, this map can provide time parameters, which are the basis for determining the appearance time of EIA's crests. Thus, from the results of VTEC calculation, data of time, latitude, and VTEC are selected to establish the temporal - latitudinal VTEC map. All of these values are filtered at a certain longitude, for instance, 105°E for the Southeast Asia region.

In order to create a map from the discrete measurements as shown in Figure 6.4, the first step is to convert them into the format of grid data. In my study, the method of "mean square (window) sideslip" is used. The essence of this method is to use a moving square (size mxn, m is time and n is latitude) sliding from the left to the right (0h → 24h) and from below to above (Lat1 → Lat2) with the steps (x) and (y). In each time of moving, the value of time, latitude, and VTEC are average calculated from all the data inside the window. Each of these average values represents one mesh (of the grid data). After the square has slid all the data area, grid data with three elements: time, latitude, and VTEC is obtained. In essence, they are the average of all values inside the running square. The nature of this method is described in Figure 6.5. During the actual calculation, I investigate the reliability of this method with different sizes of the square and different steps of the sideslip, from which drawing a conclusion the size of the square is best at 2 (hrs) x 2°, the (x) step of 0.5 hours and (y) step of 0.5° are the best.

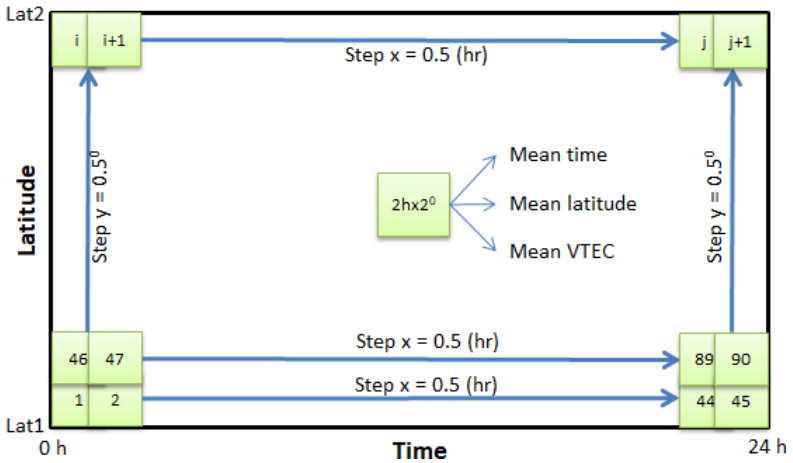

Figure 6.5. The method of mean square sideslip for creating the gid data file

6.1.4. Establish temporal - latitudinal VTEC map from GIM

The above steps are required when using RINEX files to establish the temporal - latitudinal VTEC map where values of time, latitude and VTEC are derived from the VTEC calculation results. In case we use IONEX files, all of these values are available. Nonetheless, the essence of the IONEX files is that TEC is arranged in different time intervals corresponding to different latitudes and longitudes. Thus, to create such gid data files, the IONEX files need to be rearranged with a subroutine program.

It is also needed to mention techniques for mapping interpolation. According to my study, from the grid data file, the methods that can be used for the mapping interpolation are kriging, radial basis function, and local polynomial, in which the first method gives the best interpolation results. Therefore, all maps created in this study use kriging interpolation. The maps are put on view by the rainbow image together with the contour (Figure 6.3).

Thus far, two methods of producing temporal - latitudinal VTEC map have been proposed. Among them, the first method using RINEX files takes more time to calculate and the scope of the established map is also limited following the limited number of GNSS stations. However, this method has the main advantage of having a higher TEC resolution since TEC are calculated at the same interval with the sampling rate of GNSS measurements (i.e. 30 seconds). For the second method, TEC resolution is customarily only one or two hours, which is indeed the biggest drawback of this method. Nevertheless, this solution does not take much time to calculate (no need to use the “mean square sideslip” method to create grid data file), and most importantly with the global VTEC data contained in the IONEX files, this method can be used to study the ionosphere in any part of the world without using GNSS receivers. The temporal - latitudinal VTEC map introduced in Figure 3.12 (Chapter 3) is prepared by using the first method. In this chapter, with the purpose of creating a large VTEC map, I mainly use the second method.

The method of using temporal - latitudinal VTEC map to study EIA is somewhat similar to the research of ionospheric scintillation indicated in Chapter 2. That is, if the study is conducted in a moderate area, it is best to use the network of available receivers that meet the requirements. If the scope of the research is immense or global, it is advisable to take advantage of published data (IGS products for instance). Both proposed methods have their own advantages and disadvantages. The best way to ensure a high accuracy of VTEC map is to combine them, it is taking advantage of the IONEX data and adding VTEC calculated from GNSS measurements available in the research area to increase VTEC resolution.

6.2. A case study on the biggest geomagnetic storm of solar cycle 24

In this section, I use the temporal - latitudinal VTEC map to investigate how the ionosphere reacts on the occasion of a very intense geomagnetic storm. Table 6.2 presents the top 20 strongest geomagnetic storms during SC24 based on their geomagnetic disturbance planetary index (ap).

Table 6.2. Top 20 biggest geomagnetic storms of SC24

No.	Date	ap index (nT)	No.	Date	ap idex (nT)
1	17.03.2015	108	11	11.09.2015	60
2	08.09.2017	106	12	09.09.2015	59
3	09.03.2012	87	13	02.10.2013	58
4	15.07.2012	78	14	01.06.2013	58
5	07.10.2005	74	15	22.06.2015	57
6	17.03.2013	72	16	25.10.2016	57
7	23.06.2015	72	17	05.04.2010	55
8	20.12.2013	70	18	27.08.2015	52
9	08.05.2016	70	19	28.09.2017	51
10	26.08.2018	67	20	29.06.2013	50

With the ap index of 108 (nT), the storm emerged in the middle of March 2015 is the biggest geomagnetic storm during SC24, its SYM/H index down to -223 nT. This storm reached the G4 level (severe) on the NOAA geomagnetic storm scale. The main phase of the storm happened on 17th March leading to its name the Saint Patrick's Day storm. According to the scientists of the Space Weather Prediction Center (SWPC), the storm can lead to the disruption of high-frequency radio transmission for hours in several large areas. During the storm, ionospheric electric field disturbances observed in the medium and low latitude regions have different timescales. They strongly influence the distribution of ionospheric plasma, originate from the direct penetration of the magnetospheric electric field into the ionosphere and the effects of ionospheric disturbance dynamo last longer [Gonzales et al., 1979; Spiro et al., 1988; Kelley et al., 2003; Richmond et al., 2003;…]. In the next sections, I investigate how the magnetic field of the Earth, the plasma, and the solar indices have changed before, during and after the storm. Ionospheric disturbances and the behaviour of the ionosphere will also be considered.

6.2.1. Magnetic field parameters, plasma activities and solar indices

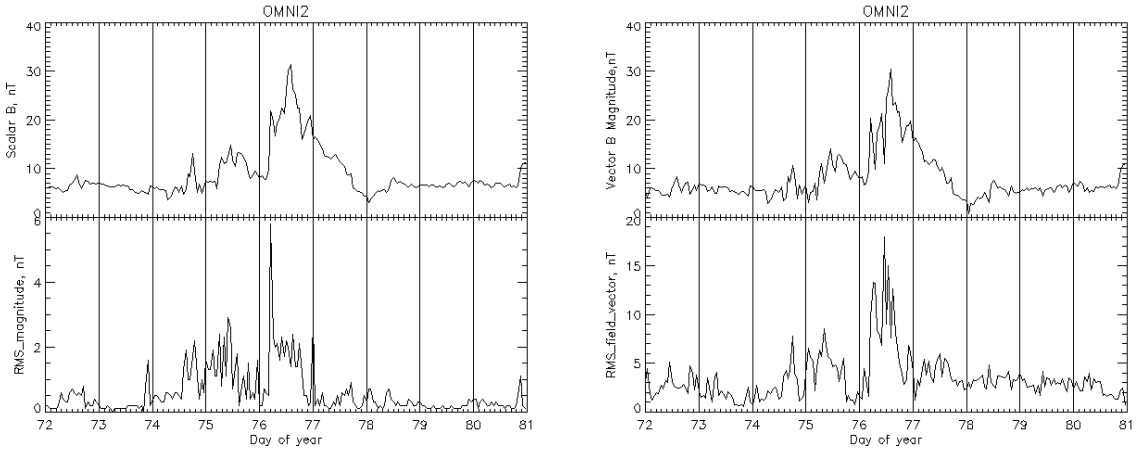

Figure 6.6a. Magnetic field indices during the middle of March 2015

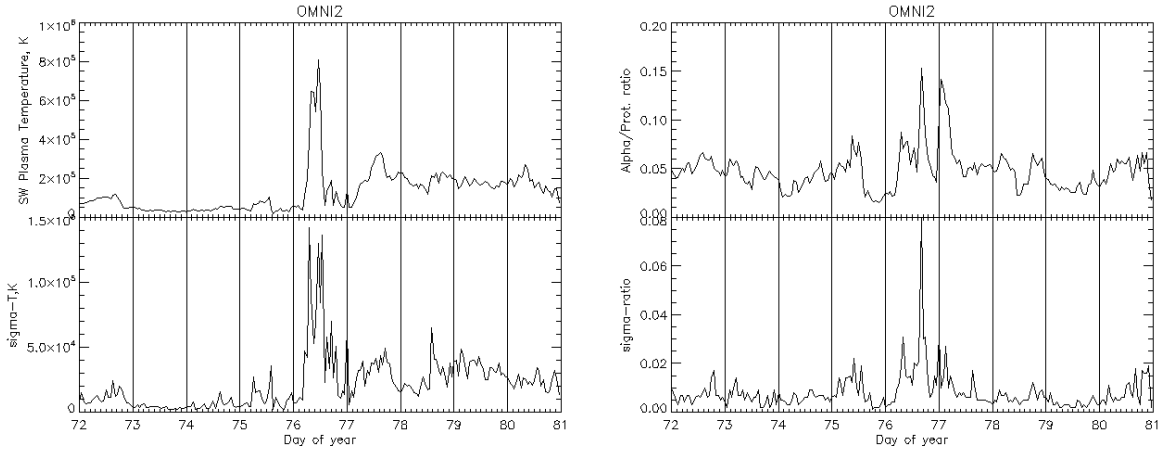

Figure 6.6b. Plasma indices during the middle of March 2015

As the main storm occurred on March 17th 2015 (DOY 76), I investigate the magnetic field indices, plasma activity indices, and solar indices four days before and after the storm. The corresponding DOYs are from 72 to 80 as indicated in the horizontal axis of Figures 6.6a-c. Data for all these figures are available at the official website of OMNIWeb [(6.3)]. Figure 6.6a describes the magnetic field of the Earth including IMF Magnitude Average (nT) and its corresponding error Sigma in IMF Magnitude Avg (nT) in the left panel; Average IMF Vector of Magnitude (nT) and its corresponding error Sigma in IMF Vector Avg (nT) in the right panel. Figure 6.6b depicts the plasma activities including Proton Temperature (Kelvin) and its corresponding error Sigma-T (Kelvin) in the left panel; Alpha/Proton Density Ratio and its corresponding error Sigma-Alpha/Proton Ratio in the right panel. Figure 6.6c, meanwhile, portrays the solar indices such as Kp*10, Dst (nT), ap (nT), AE (nT), AL (nT), AU (nT), and polar cap (pc) index from Thule.

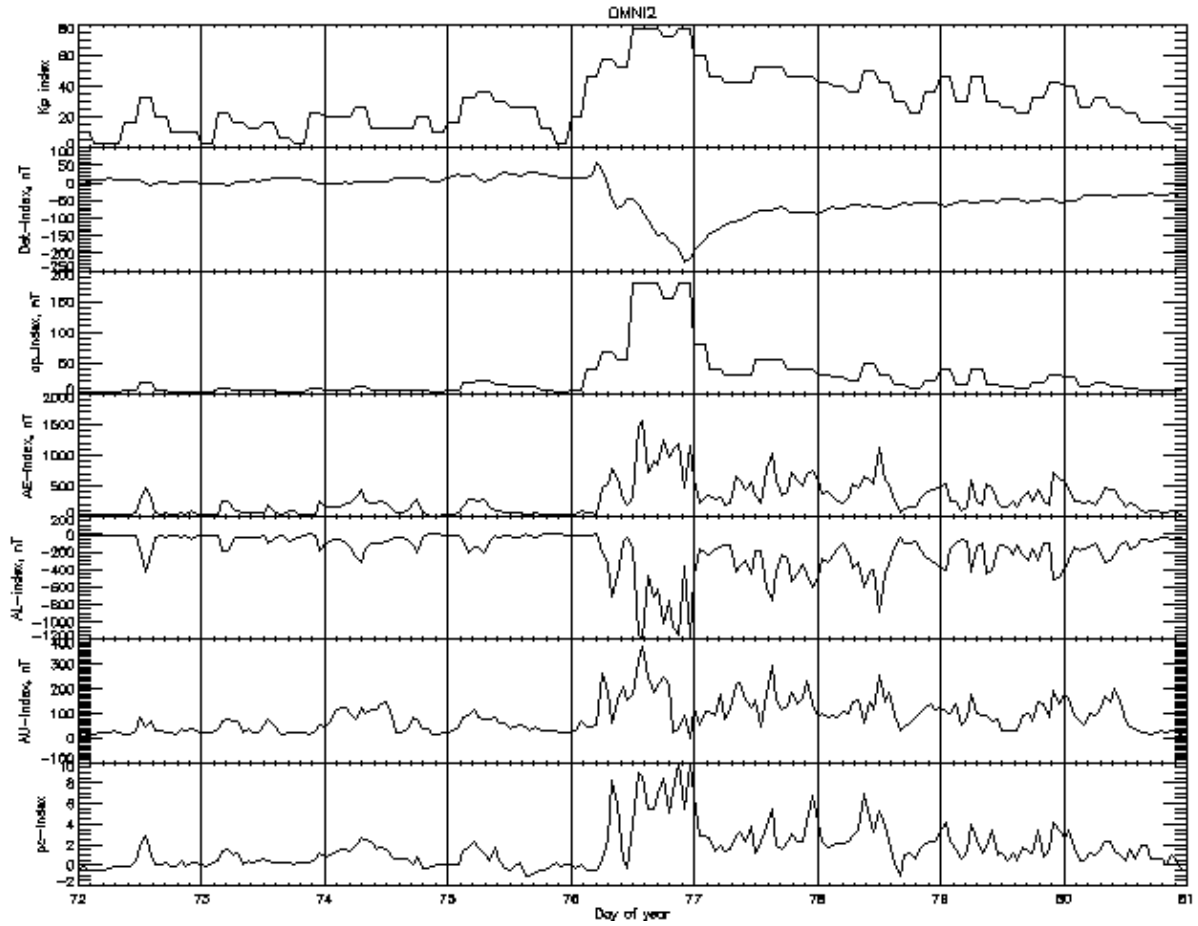

Figure 6.6c. Solar indices during the middle of March 2015

From Figures 6.6a-c, it is seen that all the basic indices related to the Earth's magnetic field abruptly changed their values on the day the storm started, i.e. March 17th. Also on this day, all the indicators given above recorded the strongest fluctuations during the study period. In general, before the storm, the indices remained stable at low levels. After the storm (from the day 18th to the day 21st) the indices were not as high as the day 17th but there were still certain fluctuations that occurred.

Specifically, the daily averaged value of the IMF magnitude Avg on the 17th was at a peak of 19.2 (nT), while two days before and after had the corresponding indices of 10.2 (nT) and 10.7 (nT). In the remaining days, this index was maintained at a low level of approximately 6-7 (nT). In case measured by hour, on the day 17th the hourly averaged value of the IMF magnitude Avg index began to grow sharply from 4 UT to 5 UT with the corresponding increase from 9.7 (nT) to 21.9 (nT). After that, the index remained at a high level until the end of the day and gradually decreased during the next day (18th) to maintain stability from the day 19th onwards. During the storm, its maximum value was around 31.5 (nT) at 14 UT on the

day 17th. In the course of the study period, Plasma indices were recognized to behave similarly to the magnetic field indices when comparing Figures 6.6a and 6.6b.

We now consider how the solar indices fluctuated during that period. All the daily averaged of solar indices reached their absolute highest values on 17th except the Dst index peaked on 18th. During the study period, the Kp index remained the highest value of 77 for the whole period from 12 UT to 23 UT on the day the storm arrived. Meanwhile, the Dst index remained almost positive values until 7 UT this day. After this moment, it kept maintaining the negative values until the end of 21st. Since the value of 56 (nT) at 5 UT, day 17th, the Dst index continuously decreased until around 22 - 23 UT the same day and was recorded its lowest values below -200 (nT) during this moment. Other solar indices such as ap, AE, AL, AU, and pc all recorded similar variations.

Thus, the indices of the magnetic field, plasma and Sun's activities have reflected the appearance with very strong intensity of the magnetic storm occurred on March 17th. In the following sections, I will explore how VTEC and the ionosphere in the Southeast Asia region had changed due to the effects of the storm.

6.2.2. TEC variations and the behaviour of the ionosphere

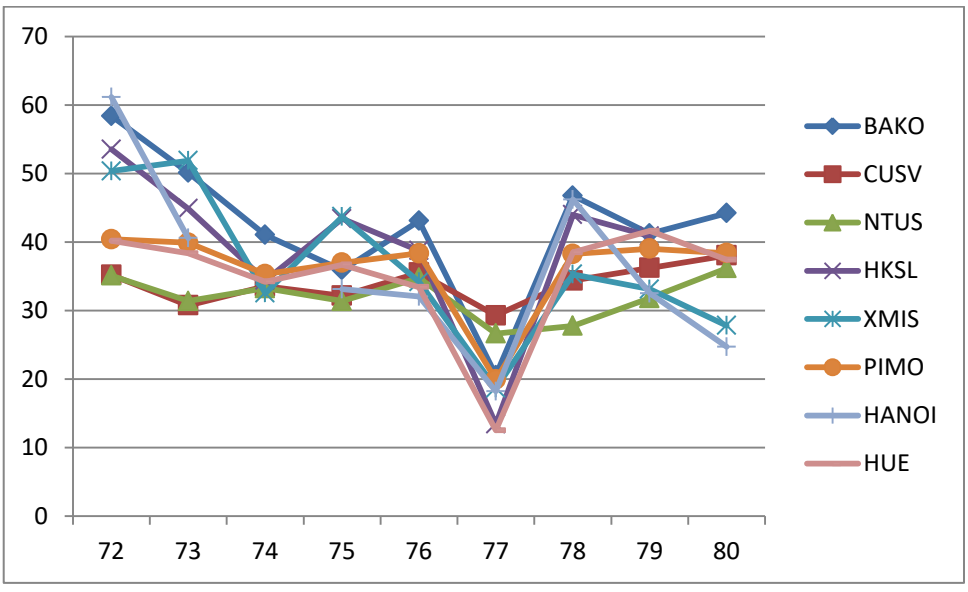

Figure 6.7. Mean daily of VTEC at some stations in the Southeast Asia area during the biggest geomagnetic storm of SC24

[6.3] https://omniweb.gsfc.nasa.gov/form/dx1.html

Figure 6.7 shows the variations of daily mean VTEC at some stations in the South East Asia region before, during, and after the storm with the horizontal axis is DOY (from 72 to 80 corresponds to 13th to 21st of March), the vertical axis is VTEC values in TECU. It can be seen that one day after the storm started, VTEC at all stations suddenly plummeted to approximately 20 TECU, of which, HKSL and HUE stations recorded the deepest decline, respectively 13.4 and 12.5 TECU. The average value of VTEC at all stations in the days 17th, 18th and 19th were 36.3, 19.9, and 38.9 TECU respectively. From there, it can be seen the average decrease in VTEC amplitude one day after the storm kicked off was about 45.1%, but it restored almost immediately since after 18th (DOY 77), VTEC values were recovered to be close to the previous values.

In order to investigate how the ionosphere behaved during the storm, the temporal - latitudinal VTEC maps (Figure 6.8) have been created from IONEX files for seven consecutive days starting from March 15th. These VTEC maps are established in three areas of longitude respectively 90^{o}, 105^{o}, and 120^{o} aims to compare the reaction of the ionosphere in different longitude areas. In Figure 6.8, the horizontal axis represents time of the day, the vertical axis indicates latitude. The maps correspond to the days from 15th to 21st are put from left to right respectively. The bar colour scale from 0 to 100 TECU is common for all maps in three longitude areas to facilitate comparison. Map groups from top to bottom are corresponding to longitude regions of 90^{o}, 105^{o}, and 120^{o}.

As introduced in Section 3.3, this type of map gives us a very clear view of the two equatorial anomaly crests and their symmetry across the magnetic equator. From Figure 6.8, it can be seen that the morphology of anomaly changed continuously day by day during the storm. The first and most noticeable thing in this plot is the disappearance of an anomaly on 18th, or in other words, just one day after the storm came into existence, two anomaly crests had merged into one. To examine more meticulously the behaviour of the ionosphere during the storm, I determine the occurrence time, position (in latitude) and intensity (amplitude of VTEC) of the two equatorial anomaly crests from 15th to 21st. The results, which shown in Figures 6.9a-c, are determined for the longitude region of 105^{o}. Comparing the three groups of maps (upper, middle, and lower) in Figure 6.8, it is seen that the variations of the ionosphere in the adjacent longitude areas of 90^{o} and 120^{o} almost have the same tendency as in the longitude area of 105^{o}.

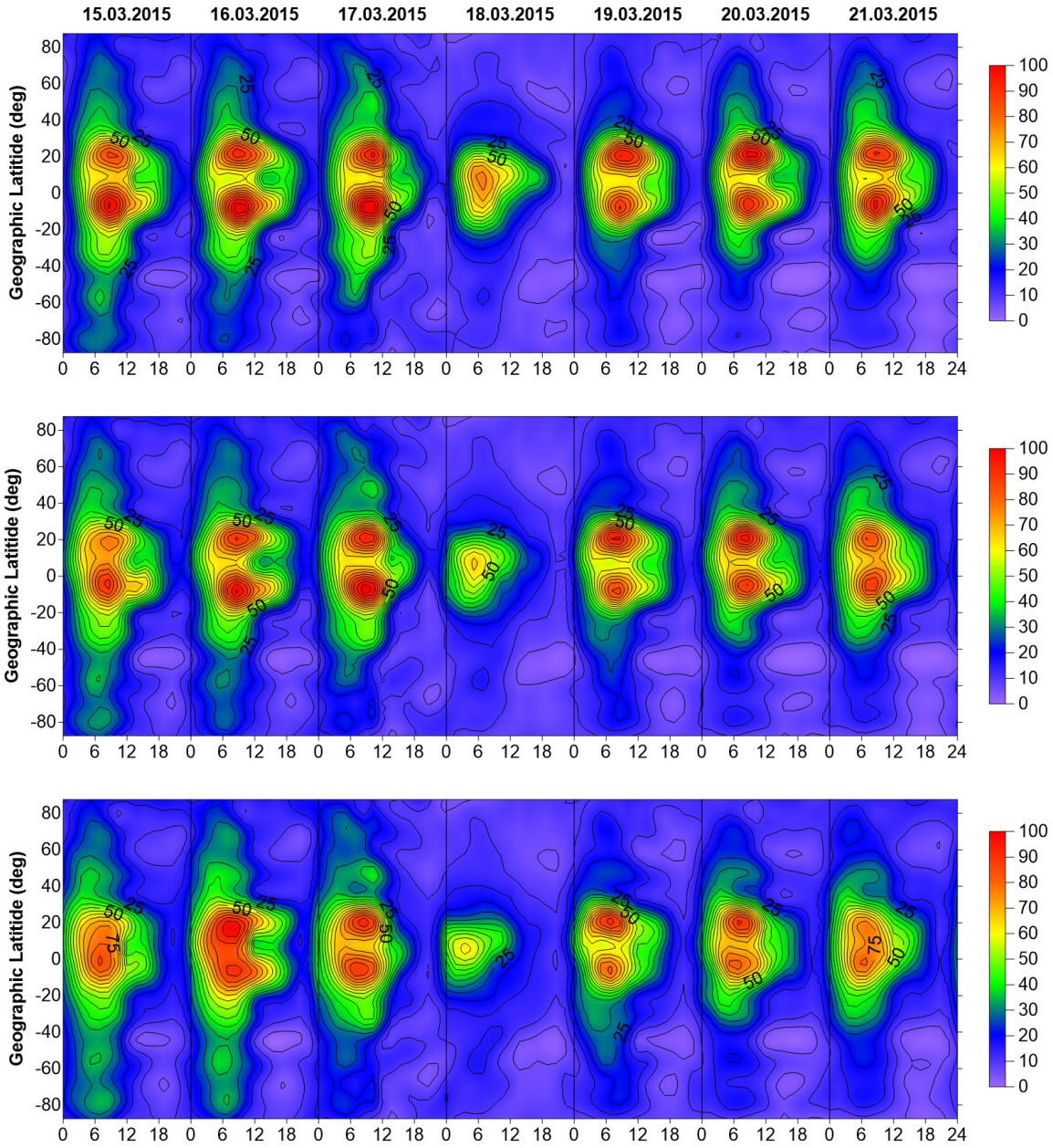

Figure 6.8. Temporal - latitudinal VTEC maps established at different longitudes: the top corresponds to 90° E longitude, the middle corresponds to 105° E longitude, and the bottom corresponds to 120° E longitude (TECU unit, LT=UTC+7 h).

On the day 18th, in addition to the disappearance of the southern crest as shown in Figure 6.9c, the sudden change in the occurrence time of this common anomaly crest is also an interesting reaction of the ionosphere. Whereas before that day, the occurrence time of two peak anomaly crests was about 15:30 LT, on this day the common anomaly crest occurred at more than 12 LT, which is about 3.5 hours earlier. Similar to the amplitude of VTEC, just in one day, the appearance time of anomaly crests returned to its previous state but somewhat earlier.

The average position of the two anomaly crests will be determined in the latter part of this thesis, which is about 19.0°N latitude and 3.3°S latitude for the northern and southern crests respectively (Table 6.4). But on the day two anomaly crests combined into one, its common latitude was about 7.1°N. In other words, on 18th, the southern anomaly crest completely disappeared while the northern anomaly crest moved approximately 12° towards the equator compared to its position the previous day.

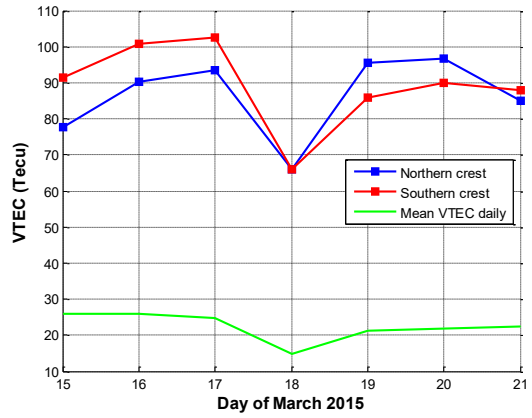

(a)

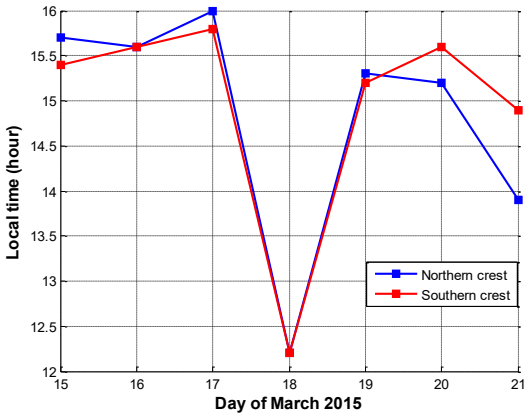

(b)

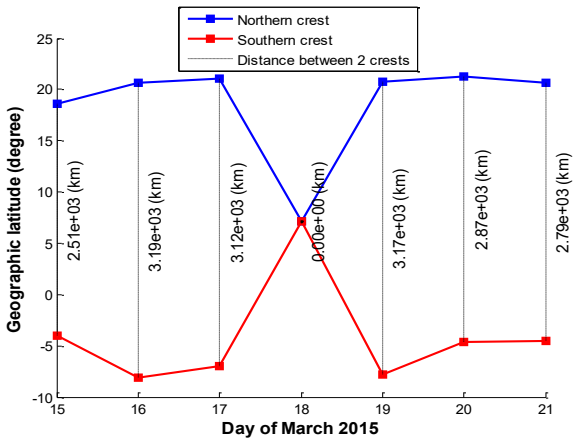

(c)

Figure 6.9. The amplitude (a), appearance time (b), and geographic latitude (c) of the northern (blue square) and southern (red square) peak EIA crests during the period of 15th-21st of March 2015

In summary, the behaviour of the ionosphere during the strongest geomagnetic storm of SC24 occurred on 17th of March 2015 can be summarized as follows: one day after the storm began, the development of ionospheric disturbance dynamo and the degeneration of EIA leading to the northern crest moved equatorward a distance of nearly 12°, the southern crest entirely vanished, and the average VTEC amplitude for the whole area of Southeast Asia decreased by about 40% (amplitude of northern and southern crests decreased by 29.2% and 35.4% respectively). Also on 18th, the occurrence time of the common anomaly crest was more than 12 LT, about 3.5 hours earlier than usual. Nonetheless, all these variations of the ionosphere happened only in one day after the storm emerged. From 19th onwards, the state of the ionosphere was almost returned to its origin.

The complete disappearance of the southern crest of EIA was also observed by [Lin et al., 2005] during another strong geomagnetic storm happened in September and October 2003. This phenomenon can be explained as follows: in the early stages of the geomagnetic storm, the interactions between the solar wind and the southward of interplanetary magnetic field provoke the eastern electric field to penetrate directly into the ionosphere [Kikuchi et al., 2000]. This eastward electric field enhances the fountain effect and also the amplitude of the anomaly crests and stimulates its expansion towards the pole. During the storm, when the high-energy particle flow of the solar wind deeply penetrates the polar atmosphere and heats it, there is an occurrence of the meridian neutral wind blowing equatorward. The complex interactions between the neutral wind and the Earth's magnetic field cause the phenomenon called the ionospheric disturbance dynamo [Blanc & Richmond, 1980]. In which, the electric field in the low latitude regions is in the westward direction, opposed to the eastward electric field under normal conditions. This westward parallel electric field emerges in the recovery phase, causing the downward plasma drift, the descent in the fountain effect and the degeneration of the structure of EIA.

6.2.3. Ionospheric irregularities

In this section, I inspect the ionospheric disturbances during the last two weeks of March 2015. Similar to Table 5.2, the indices to be considered are S_4 and ROTI indices. The number of ionospheric irregularities detection and its percentage of $S_4 \geq 0.3$ and ROTI$\geq$0.5 TECU/min are given in Table 6.3. This table also provides the number of ionospheric scintillation detected in ROTI maps which established from several IGS stations (indicated in the last column) in the Southeast Asia region (15^{o}S - 25^{o}N latitude and 95^{o}E - 115^{o}E longitude).

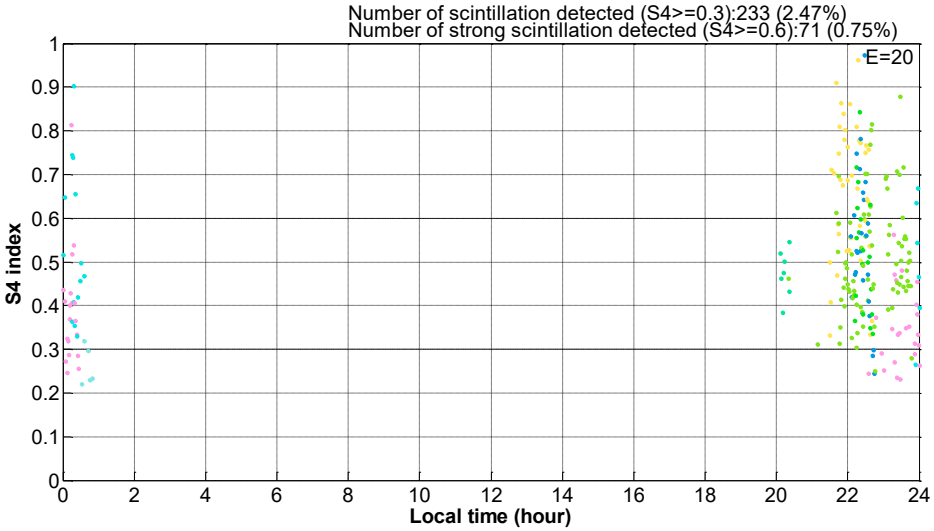

Figure 6.10. The S_4 index at HANOI station on March 19th 2015

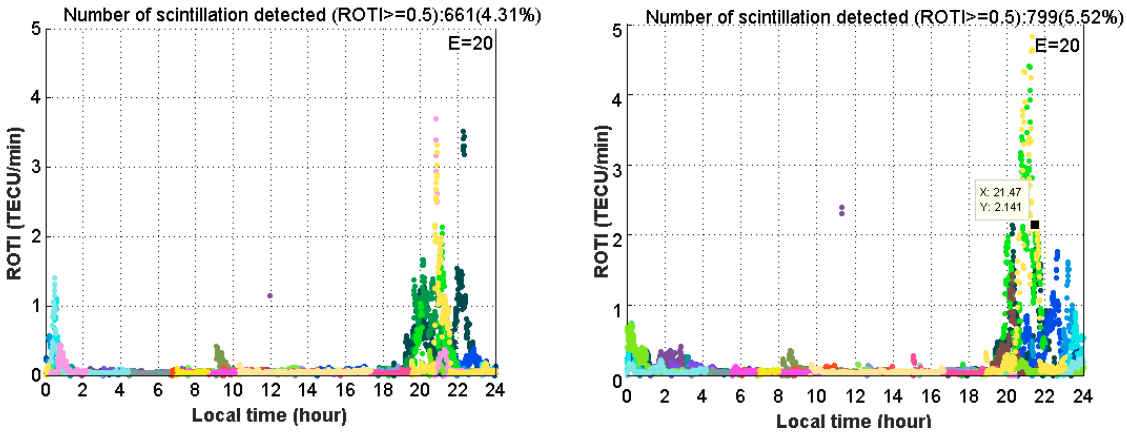

Figure 6.11. The ROTI index at HUE station on 16th (left) and 26th (right) of March 2015

Table 6.3. Statistics of S_4, ROTI indices and the ionospheric disturbances derived from the regional ROTI maps during the last two weeks of March 2015

Days of March	HANOI station				HUE station				Regional ROTI maps		
	S4 index		ROTI index		S4 index		ROTI index				
	Num	%	Num	%	Num	%	Num	%	Num	%	Num of stations used
15	0	0.0	no data		2	0.0	38	0.4	1383	1.0	8
16	189	2.0	196	1.8	130	1.4	661	4.3	4785	3.0	9
17	0	0.0	4	0.0	0	0.0	2	0.0	318	0.2	9
18	0	0.0	3	0.0	0	0.0	13	0.1	225	0.1	9
19	233	2.5	285	3.0	82	0.9	36	0.3	1197	0.8	9
20	0	0.0	11	0.1	1	0.0	0	0.0	129	0.1	9
21	0	0.0	0	0.0	0	0.0	0	0.0	97	0.1	8
22	0	0.0	0	0.0	0	0.0	53	0.4	163	0.1	8
23	1	0.0	0	0.0	0	0.0	7	0.1	38	0.0	9
24	28	0.3	92	0.9	46	0.5	428	3.3	1784	1.3	9
25	10	0.1	33	0.3	35	0.4	110	0.7	617	0.4	9
26	174	1.9	71	0.9	173	1.8	799	5.5	4884	3.2	9
27	32	0.3	58	0.5	99	1.0	183	1.5	1468	1.2	8
28	24	0.3	20	0.2	27	0.3	167	1.3	1261	1.1	7

We first consider the correlation between S_4 and ROTI at HANOI and HUE stations (note that S_4 data at HCM station was not collected during this period). The correlation coefficients between S_4 and ROTI (concerning the percentage of detection) at HANOI and HUE stations are 0.92 and 0.86, respectively. This proves a good agreement between these two indices during the study period. This agreement can also be visually seen in Figures 6.12a-b which show the ionospheric disturbances at these two stations during the second half of March 2015.

From Table 6.3 and Figures 6.12a-b, it can be seen on 16th, 19th, and 24th-28th of March, extremely strong ionospheric disturbances were observed at both HANOI and HUE stations.

Meanwhile, on the remain days 17th, 18th, and 20th-23th, very few ionospheric disturbances were detected. Similar results were also recognized at BAKO, CUSV, NTUS, and XMIS stations (Figures 6.12c-f). These results are also in accordance with the total number of ionospheric irregularities obtained from ROTI maps. At all six stations during the nights of March 17th and 18th, ionospheric disturbances hardly grew because of the development of ionospheric disturbance dynamo and the enhancement of westward electric field. These phenomena stimulated ionospheric F-layer to move downward and thus the ionospheric disturbances were prevented.

Figures 6.10 and 6.11 illustrate S_4 and ROTI indices for a specific day. In these figures, ionospheric disturbances can be seen at around 22 LT, this experience is consistent with the research results in Chapter 4. This can also be recognized in Figure 6.13 with the predominance of ROTI≥0.5 TECU/min appearing before midnight. Unlike Figures 6.10 - 6.12, which only provide time information, Figure 6.13 provides both temporal and spatial distribution of ionospheric irregularities occurred over the research area. As can be predicted, most ionospheric irregularities appeared in the areas around the equatorial anomaly crests.

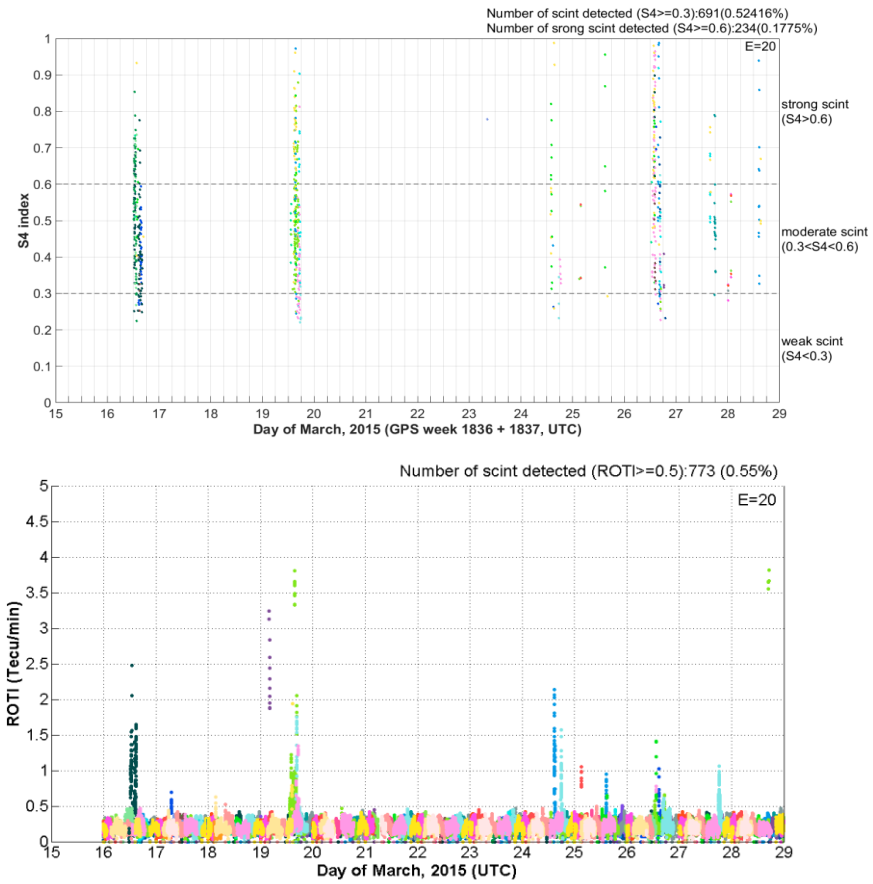

Figure 6.12a. S_4 and ROTI at HANOI station during the last two weeks of March 2015

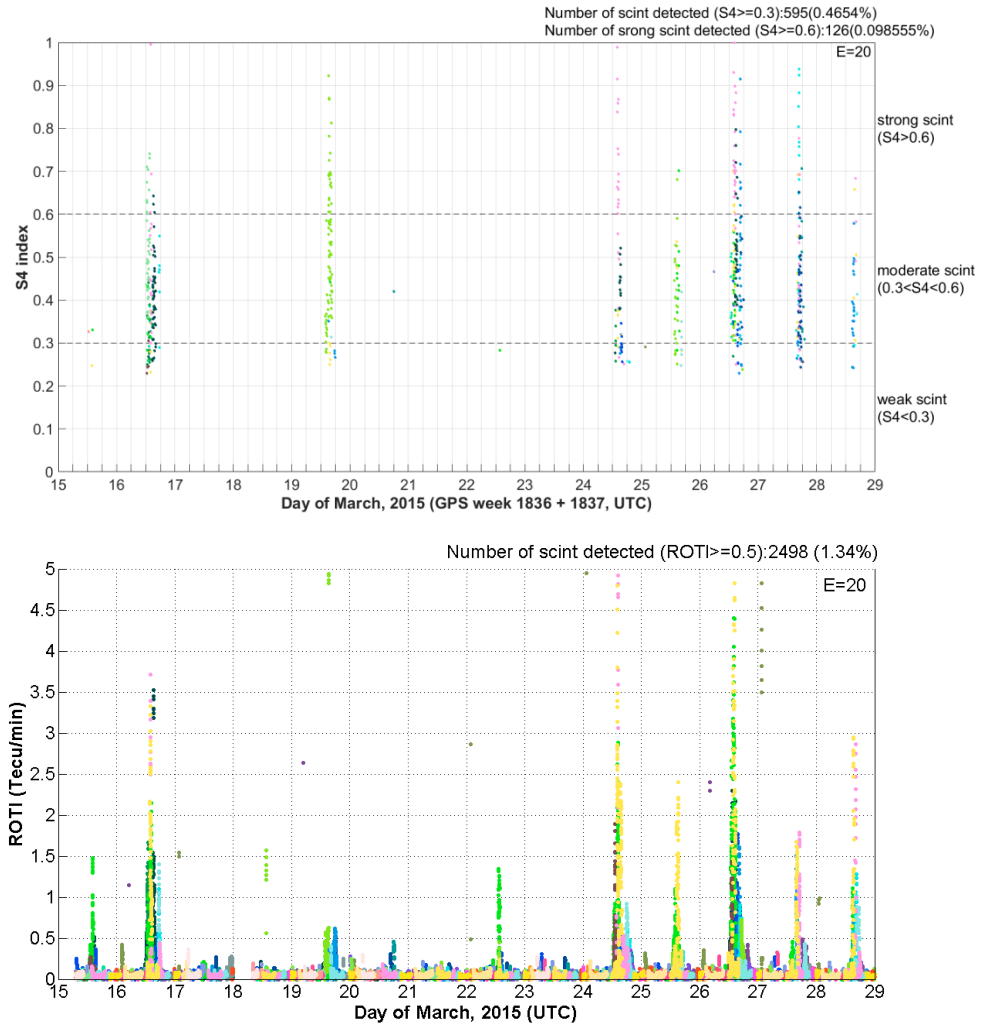

Figure 6.12b. S_4 and ROTI indices at HUE station during the last two weeks of March 2015

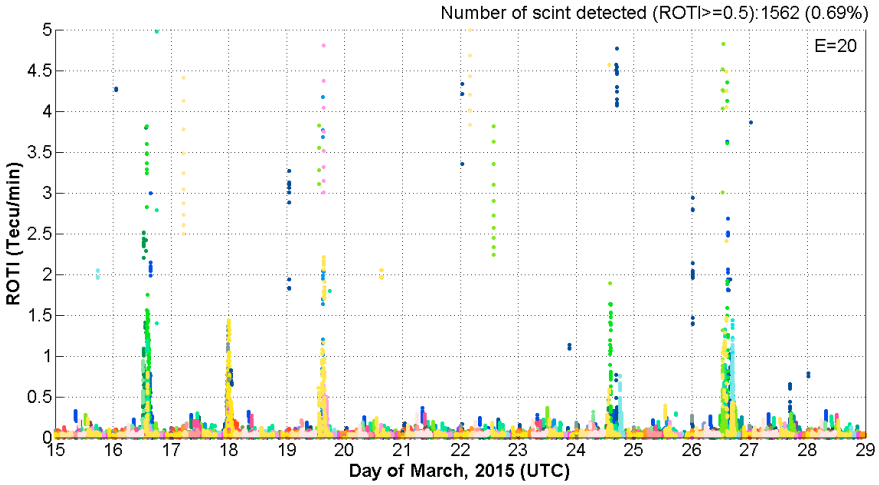

Figure 6.12c. ROTI index at BAKO station during the last two weeks of March 2015

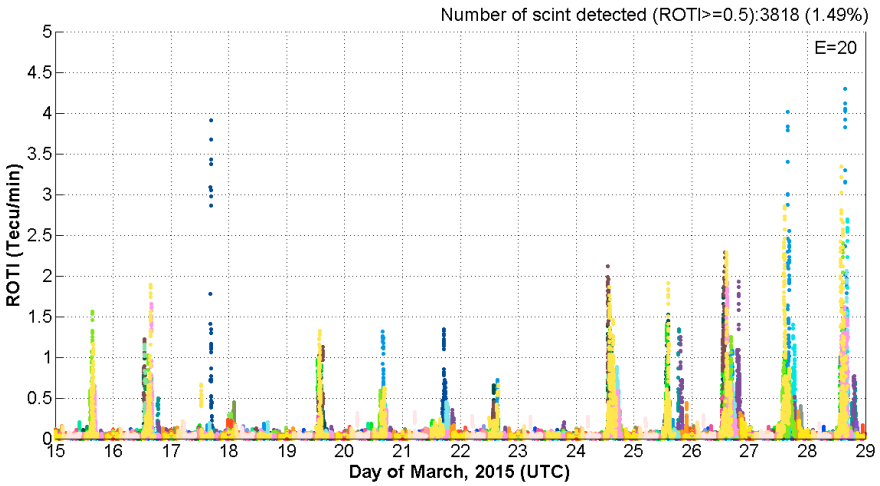

Figure 6.12d. ROTI index at CUSV station during the last two weeks of March 2015

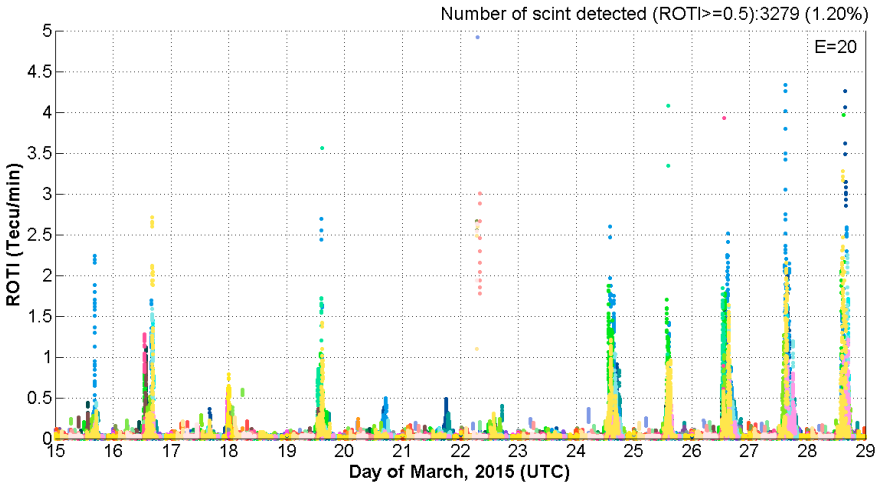

Figure 6.12e. ROTI index at NTUS station during the last two weeks of March 2015

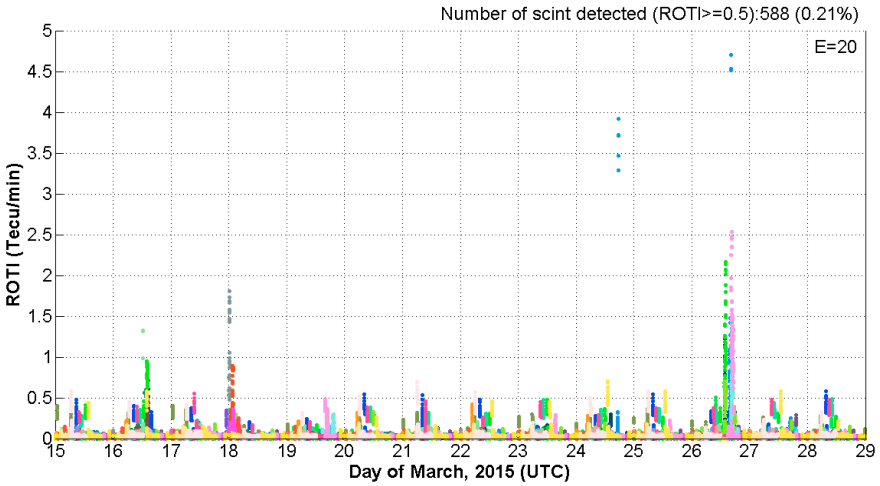

Figure 6.12f. ROTI index at XMIS station during the last two weeks of March 2015

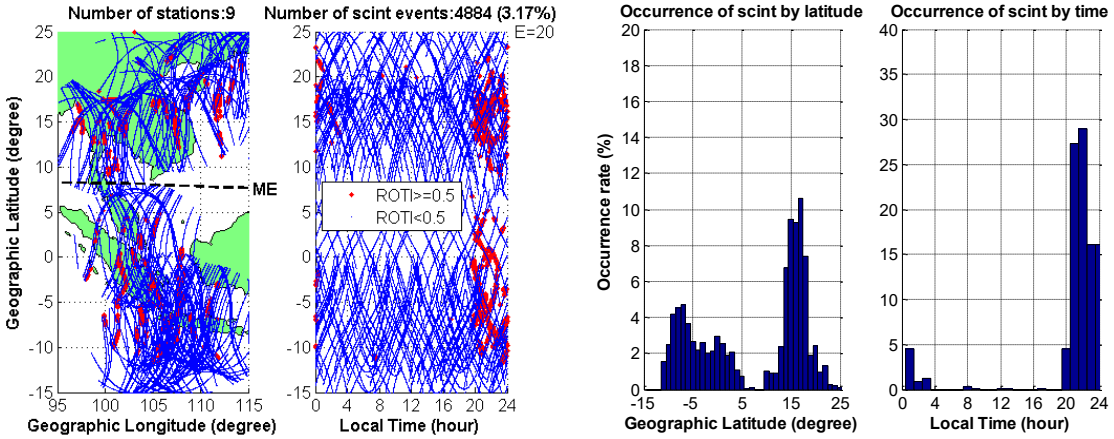

Figure 6.13. Regional ROTI map on March 26th 2015 indicates both temporal and spatial distributions of ionospheric irregularities, which primarily occur during the evening time and appear concentrated around the peak EIA crests and symmetrically over the magnetic equator.

6.3. Characteristics of peak EIA crest in the Southeast Asia area (105° meridian) during SC24

As stated in Section 6.1.4, the monthly mean temporal - latitudinal VTEC maps at 105°E longitude with the latitude from 87.5°S to 87.5°N have been established from 2007 through 2017. In this section, I use these maps to investigate the occurrence characteristics of peak EIA crests including appearance time, position, and its amplitude in the Southeast Asia region during the study period. Research methodology has been introduced in Section 6.1.2. Figures 6.14a-c illustrate the temporal - latitudinal (monthly mean) VTEC maps over the research area during SC24. Each map is averaged for one month and is represented for one day. The purpose of creating mean monthly maps is to determine the characteristics of peak EIA crest for long-term (seasonal and annual variations). TEC bar colour scale (from 0 to 50 TECU) is the same for 11 years of research to facilitate comparison. As mentioned earlier, this map is created from IONEX files and provides information about both temporal and spatial fluctuations of TEC. So from these maps, information about the occurrence time, position and intensity (amplitude) of the anomaly crests can be extracted.

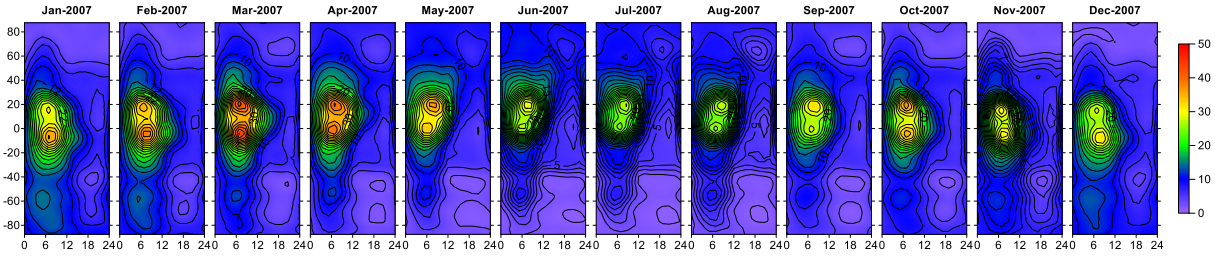

Figure 6.14a. VTEC maps over the Southeast Asia area in 2007 (TECU unit, LT=UTC+7 h)

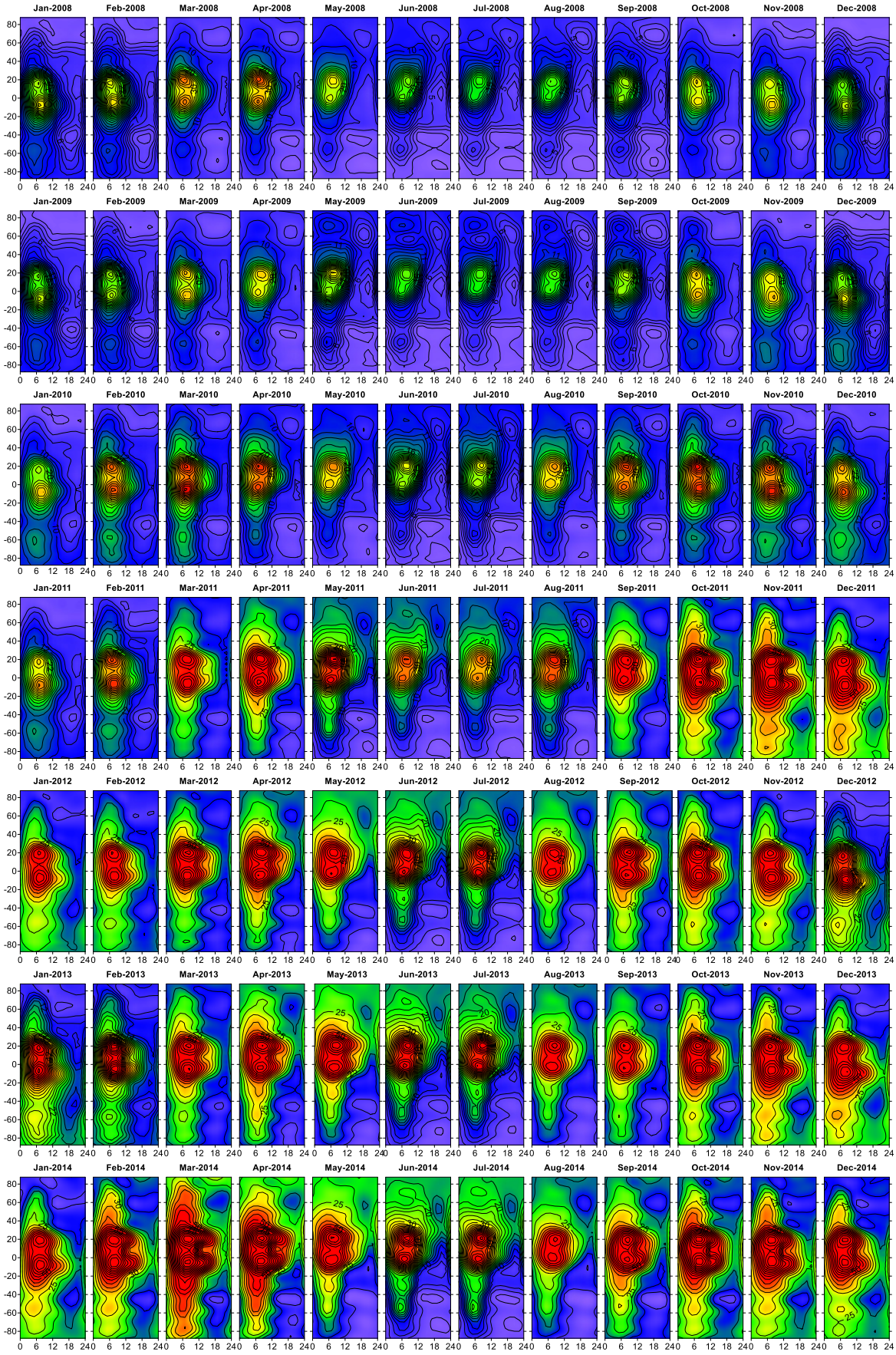

Figure 6.14b. VTEC maps over the Southeast Asia area during the period of 2008 – 2014

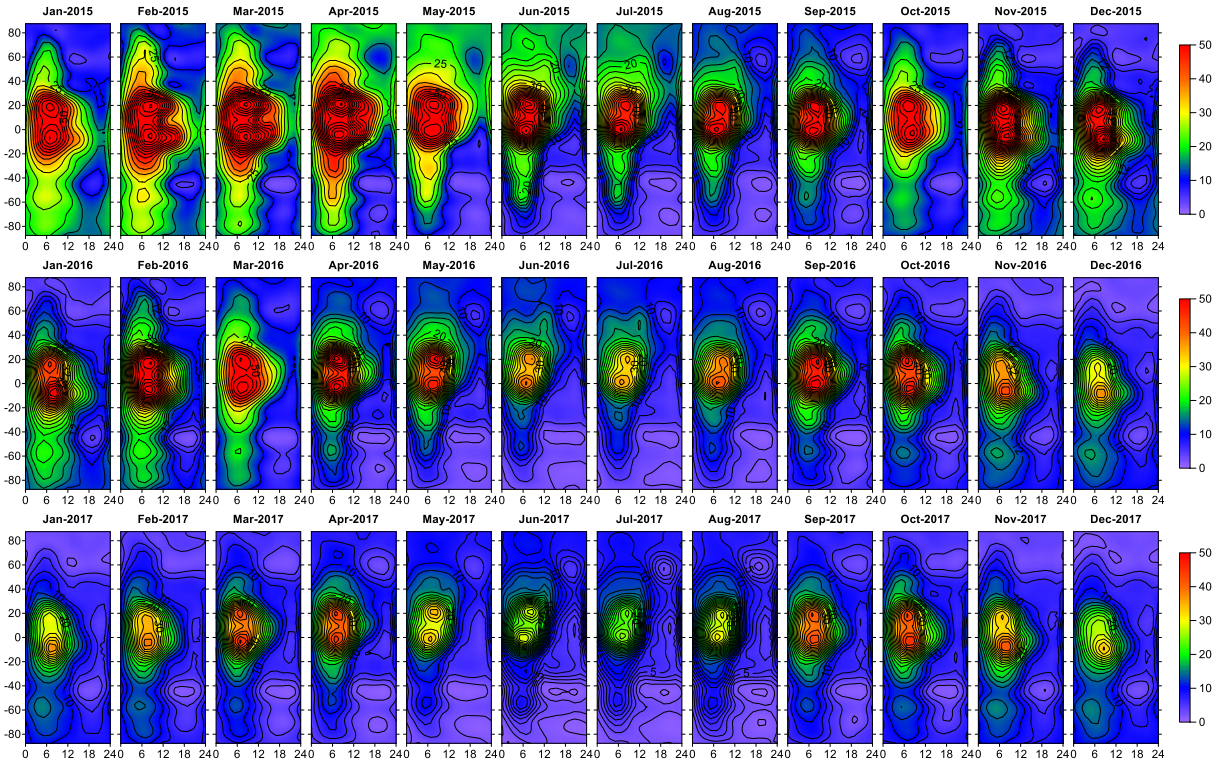

Figure 6.14c. VTEC maps over the Southeast Asia area during the period of 2015 - 2017

6.3.1. Occurrence time of peak EIA crests

Figure 6.15a. Occurrence time of peak EIA crests in each year (LT=UTC+7 h).

This figure clearly shows both crests appear earlier in winter months and later in summer months. Different colours correspond to different years, the bold red line is the average of all 11 years.

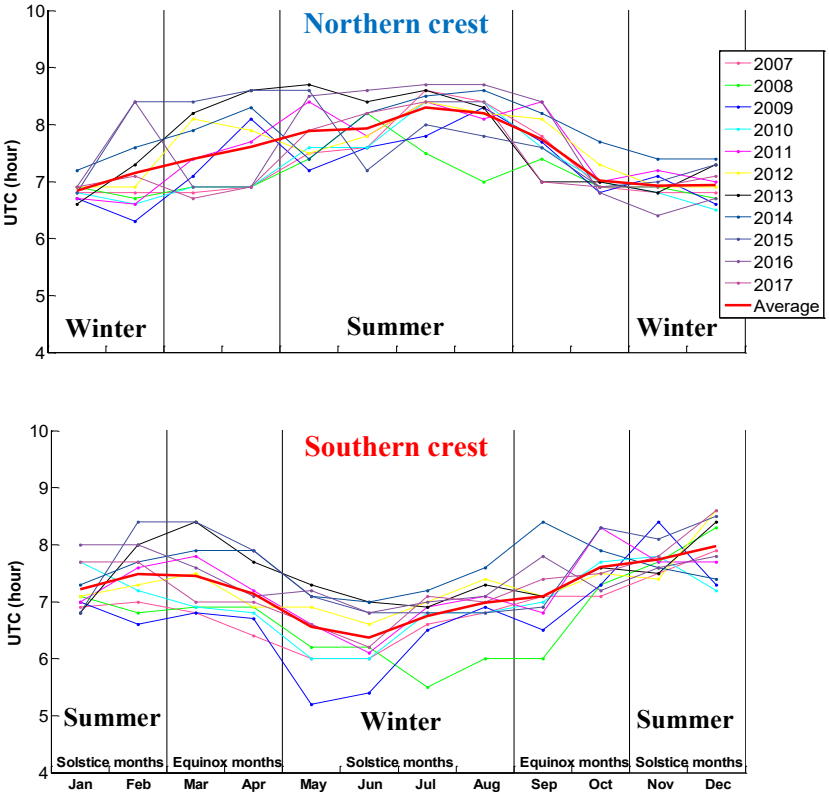

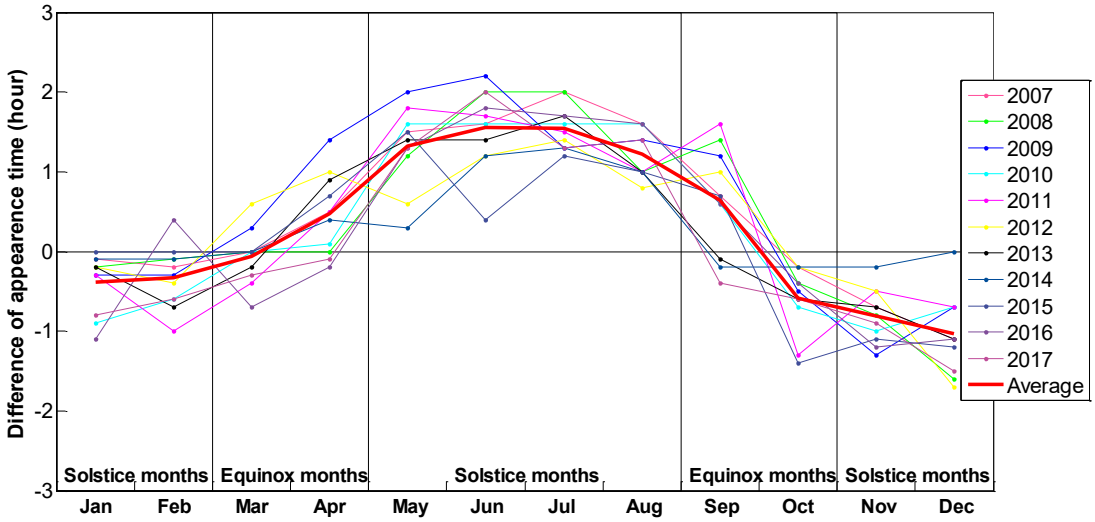

Figure 6.15b. The difference in occurrence time of peak EIA crests in each year. It can be seen that in summer months of northern hemisphere (or winter months of southern hemisphere) $\Delta T>0$, meaning that northern crest occurs later than southern crest; And in winter months of northern hemisphere (or summer months of southern hemisphere) $\Delta T<0$, meaning that northern crest occurs earlier than southern crest.

6.3.2. Occurrence position of peak EIA crests

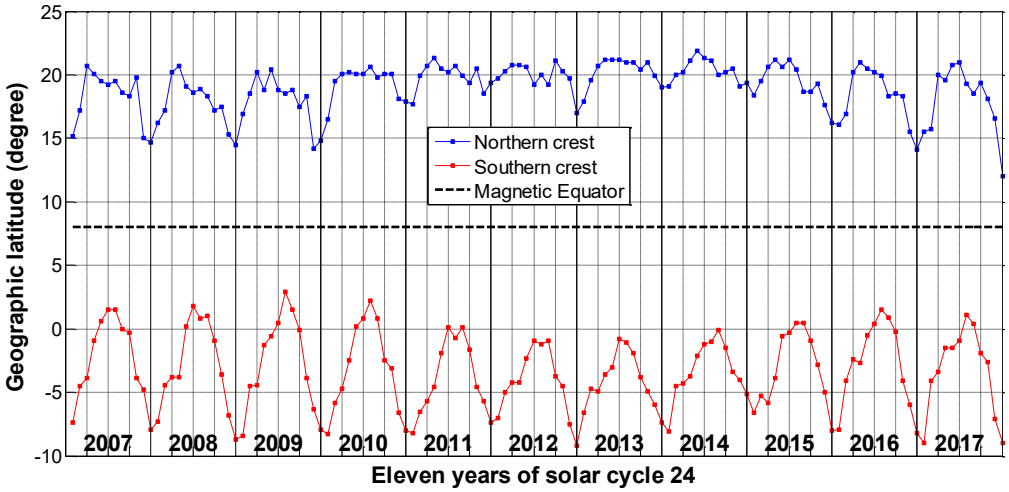

Figure 6.16a. Geographic latitudes of peak EIA crests during 11-year period indicate that two anomaly crests are symmetric over the magnetic equator. The blue line corresponds to northern crest, the red line corresponds to southern crest, and the dashed black line is the magnetic equator.

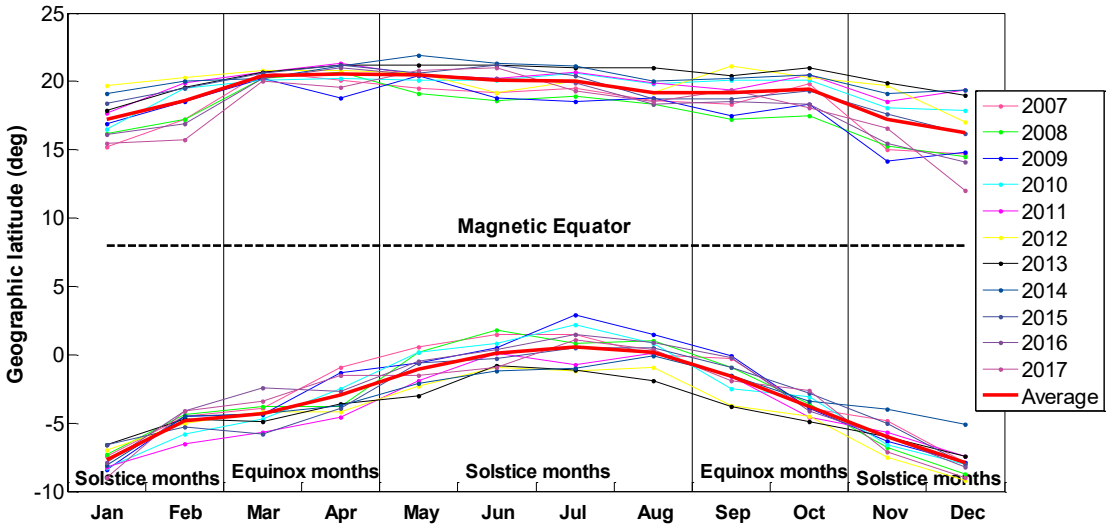

Figure 6.16b. Geographic latitudes of peak EIA crests in each year reveal that both crests tend to move forward to the magnetic equator in the winter season and to move poleward in the summer season. In this case, the trend of the northern crest is somewhat not as clear as that of the southern crest.

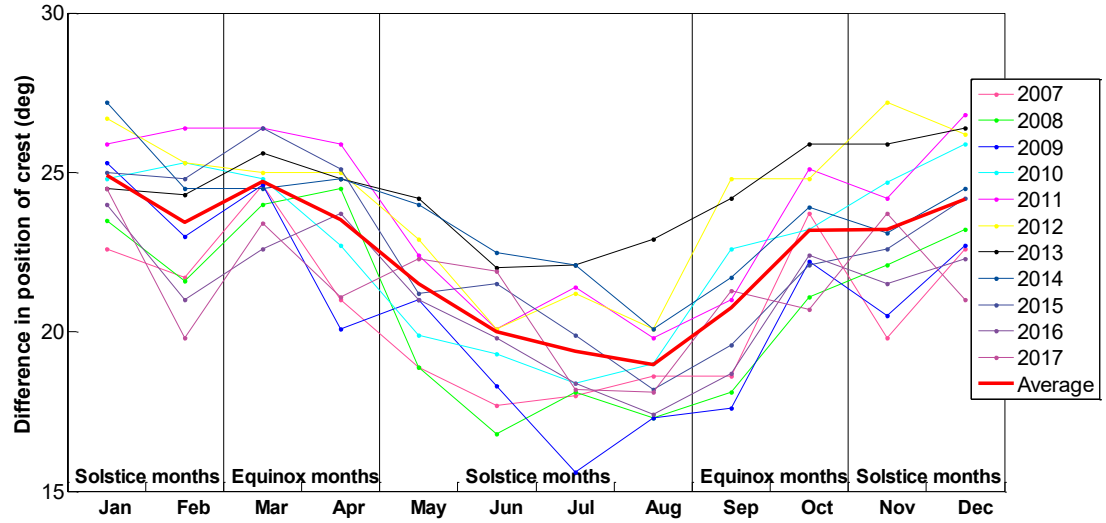

Figure 6.16c. The modification in distance between two peak EIA crests during 2007 - 2017 period. It can be noticed that in summer (of the northern hemisphere), the two anomaly crests are closer to each other and they tend to expand in winter. The specific distance between them will be exposed in Figure 6.18.

6.3.3. Occurrence amplitude of peak EIA crests

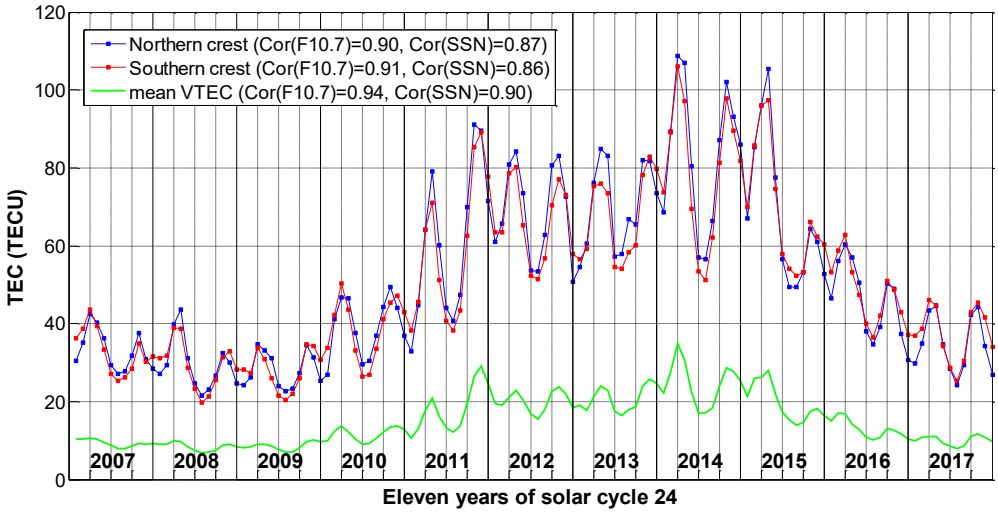

Figure 6.17. Amplitudes of peak EIA crests during 11-year period

Figure 6.17 makes obvious the dependence of the amplitude of peak EIA crests on the phase of solar cycle. That is in the ascending phase, the amplitude of crest in autumnal equinox is larger than that in the vernal equinox, on the contrary, in the descending phase, the crest's amplitude in spring equinox is larger than that in autumnal equinox. Meanwhile, in both solar maximum and minimum years, the differences in amplitudes of the crests in both equinoctial months are negligible. Also in this figure, the monthly average VTEC is determined from IONEX files for the whole area of Southeast Asia and is represented by the green line. Their correlation coefficients with the solar indices (F10.7 index and SSN index) can be found in the legend. It can be seen that monthly mean VTEC has better correlations with solar indices than the amplitude of crests. Once again, the F10.7 index proves to be more suitable with the amplitude of VTEC than the SSN index. In general, the average correlation coefficient of 0.90 shows a high agreement of VTEC with the solar indices during the research period. Refers to Figure 3.15, the annual variations of crests' amplitude and monthly mean VTEC in Figure 6.17 are consistent with the progression of solar cycle.

6.3.4. Annual variations of peak EIA crests

Table 6.4 furnishes with the results of occurrence characteristics of peak EIA crests that are averaged annually over the study period in the Southeast Asia region. Data given in this table including occurrence time (hour in UTC), latitude (degree) and amplitude (TECU) of the two anomaly crests. It is graphed by Figure 6.18a-c. The yearly mean VTEC calculated for the whole region and the yearly average of SSN are also given to study the correlation between them. The correlation coefficients between northern anomaly crest, southern anomaly crest, and yearly mean VTEC with the SSN index are determined to be 0.99, 0.98, and 0.99

respectively. Such high correlation coefficients indicate the almost absolute similarity of VTEC's amplitude with the intensity of Sun's activity during the study period.

Table 6.4. Occurrences of peak EIA crests in the Southeast Asia region during SC24 (LT=UTC+7 h)

Year	Northern crest			Southern crest			mean VTEC (TECU)	Yearly mean SSN (6.4)
	Time (hr)	Latitude (deg)	Amp (TECU)	Time (hr)	Latitude (deg)	Amp (TECU)		
2007	7.3	18.2	33.1	6.8	-2.5	32.9	9.4	12.6
2008	7.1	17.8	29.5	6.7	-3.0	29.3	8.4	4.2
2009	7.3	18.0	28.2	6.7	-2.7	28.0	8.6	4.8
2010	7.3	19.4	39.2	7.0	-3.1	38.9	11.6	24.9
2011	7.6	19.9	61.3	7.2	-3.9	59.0	18.1	80.8
2012	7.6	19.9	68.5	7.3	-4.2	65.8	20.0	84.5
2013	7.7	20.3	70.3	7.5	-4.1	67.4	20.8	94.0
2014	7.9	20.3	83.5	7.6	-3.3	79.4	24.7	113.3
2015	7.7	19.4	68.2	7.6	-3.2	69.2	19.7	69.8
2016	7.7	18.3	45.8	7.4	-2.8	47.8	12.9	39.8
2017	7.4	18.0	34.7	7.3	-3.3	37.4	10.0	21.7
Average	7.5	19.0	51.1	7.2	-3.3	50.5	14.9	50.0

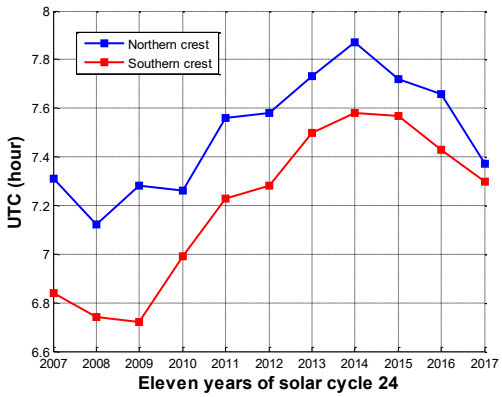

(a) Occurrence time (LT=UTC+7 h)

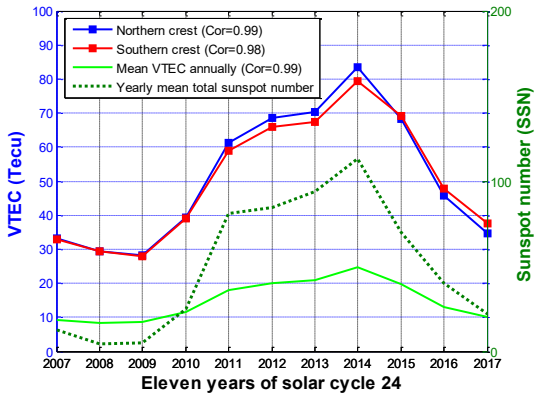

(b) Occurrence amplitude

Figure 6.18. Yearly variations of peak EIA crests. These figures show a high uniformity (correlation coefficients are approximate 1) with the evolution of SC24, of which the quietest year is 2009, and the most disturbed year is 2014. The rising and falling phases of SC24 are clearly displayed in (a) and (b), while (c) shows the symmetry of the two anomaly crests over the magnetic equator.

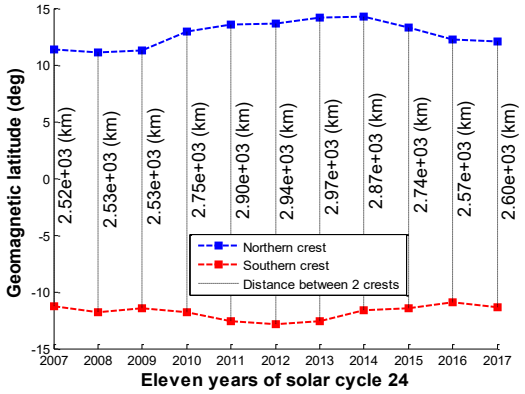

(c) Occurrence position

6.3.5. Remarkable conclusions on the characteristics of peak EIA crest

From Figure 6.14 to Figure 6.18, I conclude the seasonal variations of peak EIA crests over the South East Asia area as follows:

- In each year, the amplitudes of the crests in both hemispheres reach the maximum in equinox months and minimum in solstice months (Figure 6.14 and Figure 6.17).
- In the increasing phase of solar cycle (period of 2009 - 2014), the amplitude of the crest in autumnal equinox is larger than that in the vernal equinox. Conversely, in the decreasing phase of the solar cycle (period of 2007 - 2009 and 2014 - 2017), the crest's amplitude in spring equinox is larger than that in autumnal equinox. For the solar maximum years (period of 2012 - 2014) and solar minimum years (period of 2008 - 2009), the differences in amplitudes between two crests in both equinoctial months are insignificant (Figure 6.17).
- Both anomaly crests are likely to move equatorward, appear earlier in the winter months and to move poleward, occur later in summer months (Figure 6.15a and Figure 6.16b).
- During the period from November to February each year, the northern crest often appears sooner than the southern crest and the distance between them is determined to be the furthest during the year. Meanwhile, in the period between May and August, the southern crest usually occurs earlier than the northern crest and the distance between them is considered to be closer (Figure 6.15b and Figure 6.16c).

For a long-term overview of peak EIA crests, the main conclusions include:

- For SC24, the average geographic latitudes of northern and southern anomaly crests of EIA are about 19.0^{o}N and 3.3^{o}S, respectively. The geographic longitude, of course, is 105^{o}E as for the research area. The average occurrence time of northern anomaly crest is around 14:30 LT, while the southern crest appears about 20 minutes earlier. The mean amplitudes of the two crests are relatively equal with the values of approximately 50-51 TECU.
- Like TEC, the annual variation of the amplitude of anomaly crests has a high agreement with the SSN index with the correlation coefficients between them reach almost 1. The amplitudes of the crests are minimal (around 30 TECU) in the deep solar years and are maximal (around 80 TECU) during the most active years of SC24 (Figure 6.18b).
- In the ascending phase of solar cycle, both crests move further from the magnetic equator, the amplitudes increase and the appearance time is later. On the contrary, in the

descending phase of solar cycle, both crests move closer to the magnetic equator, the amplitudes decrease and the appearance time is sooner (Figure 6.18a-c).

- The two anomaly crests usually appear symmetrically over the magnetic equator, but the distance between them is further (from about 2500 km to nearly 3000 km) following the increasing years of solar cycle since both crests tend to move poleward during this solar phase (Figure 6.18c).

For the explanation of seasonal variations of peak EIA crests, we consider the overall model which is a combination of the theory of neutral wind passing through the equator (trans-equatorial neutral wind), the subsolar point, and the neutral wind blowing from the polar towards equator (auroral equatorward wind) at the time of solstices as indicated in Figure 6.19. According to the model, the central zero shows the geomagnetic equator, other degrees show the geographic equator and tropics where the subsolar points are located. The central and the slant black arrows indicate the directions of the trans-equatorial neutral wind and auroral equatorward wind, respectively. The streamlines show the ionospheric fountain effect. Figure 6.19 shows two cases when the northern hemisphere is in summer (a) and winter (b). The theory of neutral wind blows through the equator can be explained as follows: during the neutral wind blowing from the summer hemisphere to the winter hemisphere, ions are also transported accordingly, thus hindering the development of anomalies in the summer hemisphere and increasing the anomaly crest in the winter hemisphere. In principle, when the neutral wind blows from the polar towards the equator in the winter hemisphere, the electron density at the anomaly crest in this region is maintained and its position tends to be pushed towards the equator. This is the reason why the position of anomaly crest is closer to the equator in the winter.

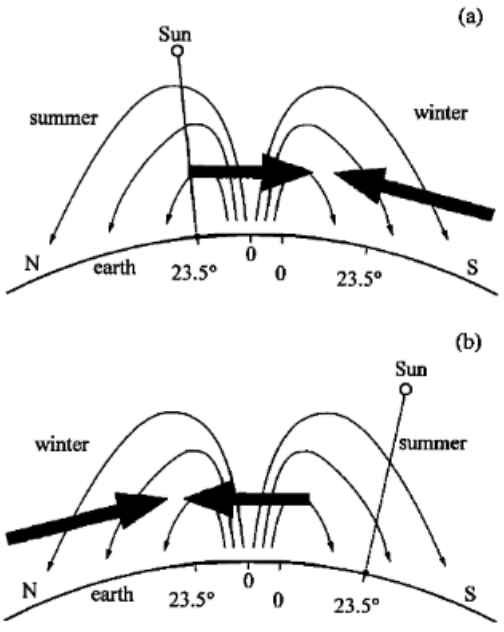

Figure 6.19. The schemes of the combined theory of trans-equatorial neutral wind, subsolar point, and auroral equatorward wind in solstices [Tsai et al., 2001].

[6.4] http://www.sidc.be/silso/datafiles

From Figure 6.19, we see that in northern hemisphere, the subsolar point is closer to the magnetic equator in the summer and it is further away from the magnetic equator in the winter. When the subsolar point is at the average latitude not close to the magnetic equator (winter in the northern hemisphere, Figure 6.19b), then the process of solar ionisation and equatorial plasma transport is predominant and the occurrence time of anomaly crest will be around local noon (12 LT). On the other hand, when the subsolar point is near the magnetic equator (summer in the northern hemisphere, Figure 6.19a), it will significantly reduce the value of TEC in the region due to the increase in the diffusion process leading to an increase in the recombination process of ions and electrons. This process predominates over the process of solar ionisation and the process of equatorial plasma transport in this region, resulting in the late occurrence of the anomaly crest (compared to the winter). This explains why in winter, the occurrence time of anomaly crest is usually earlier and in summer it is later.

6.4. Chapter summary

The main contents of Chapter 6 are summarized as follows:

- Section 6.1 introduces temporal - latitudinal VTEC map and the method to study EIA. Its major contents encompass:
    - Introduces IONEX files and its basic application GIM which provides global VTEC maps with the common time resolution of 1 or 2 hours and the spatial resolution of 5^{o}x2.5^{o} in longitude and latitude respectively (Section 6.1.1).
    - Explains the mechanism of occurrence and existence of EIA and proposes the method of using temporal - latitudinal VTEC map to study the occurrence characteristics of peak EIA crests (Section 6.1.2).
    - Presents the method of establishing the temporal - latitudinal VTEC map from GNSS measurements using RINEX files (Section 6.1.3).
    - Presents the method of establishing the temporal - latitudinal VTEC map from available global VTEC map (GIM) using IONEX files. From there, compares the advantages and disadvantages of the two methods. This section also introduces the types of VTEC maps which have been created in this thesis (Section 6.1.4).

- Section 6.2 studies the case of the most intense geomagnetic storm of SC24 happened on March 17th 2015:
    - Some parameters of the magnetic field, plasma, and solar indices before, during, and after the storm are first exposed aims to indicate the intensity of the storm.
    - TEC variations and the behaviour of the ionosphere are also examined. The results of the study indicate that amplitude of VTEC had a sharp decline (approximately 40-45%) just one day after the storm occurred and it recovered almost the same soon after the next day. The temporal - latitudinal VTEC maps at three different longitudes (90^o, 105^o, and 120^o) have been produced to probe the behaviour of the equatorial anomaly crests during the storm. The results show that one day after the storm took place, the southern anomaly crest completely disappeared, the northern anomaly crest moved about 12^o toward the equator, the amplitude of the common anomaly crest decreased by about 30%, and the occurrence time was about 3.5 hours earlier than usual. However, all of these experiences had only occurred within one day (18th). Since the 19th onwards, the operating status of the anomaly crests recovered almost the same as it was earlier. The cause of such reactions in the ionosphere is attributed to the development of ionospheric disturbance dynamo and the enhancement of the fountain effect due to the interactions between the solar wind and the southward of interplanetary magnetic field during the storm.
    - The correlation coefficients between S_4 and ROTI at HANOI and HUE stations are determined to be 0.92 and 0.86, respectively. These results authenticate the high consistency of these two indices in the study of ionospheric irregularities, especially during strong geomagnetic storms. Investigation results of ionospheric disturbances in the second half of March 2015 (Table 6.3) show that in some days of 16th, 19th and from 24th to 28th, S_4 and ROTI indices fluctuated strongly, while the remaining days were quite quiet, even the day when the storm occurred (17th) and the day the southern anomaly crest disappeared (18th).
    - The main events of the storm can be summarized as in Figure 6.20 with the blue circles represent quiet days, the red circles represent disturbed days (concerning ionospheric irregularities), and bracket indicates the ap index (nT) of the corresponding day of March 2015.

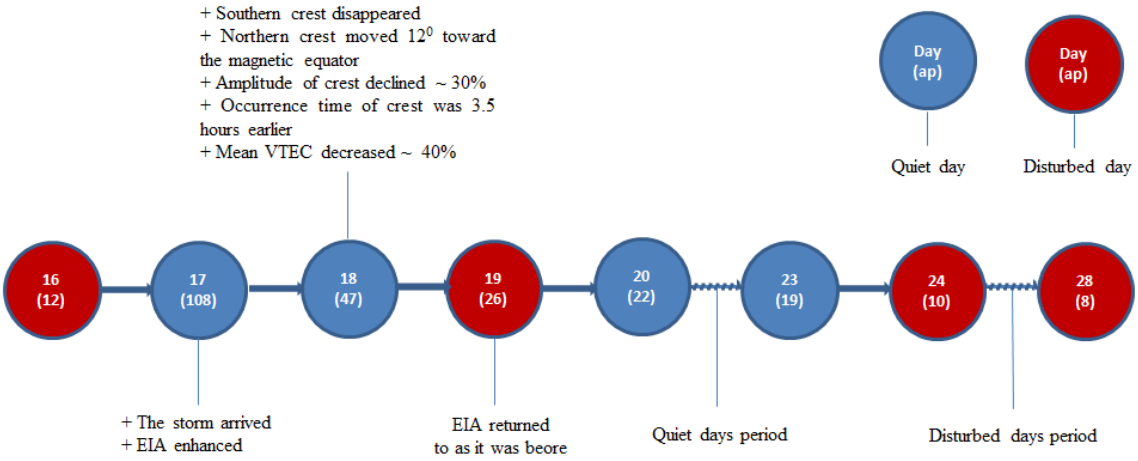

Figure 6.20. Developments of the geomagnetic storm occurred in March 2015

- Section 6.3 presents the temporal - latitudinal (mean monthly) VTEC maps over the Southeast Asia region for the period of 2007 - 2017. From there, the characteristics of seasonal and annual appearance, location and intensity of peak EIA crests are revealed in turn. Some key conclusions about the featured appearance of peak EIA crests have been given in Section 6.3.5. Among them, the most noteworthy results are: very high correlation (approximately 1.0) between VTEC (both mean VTEC and the amplitude of crests) and the SSN index; In one year, the crests tend to move equatorward more significantly in winter than in other seasons. There is a tendency for both crests to appear earlier in winter and later in summer; During the rising phase of solar cycle, both crests tend to move towards the corresponding pole, the amplitude increases, and the occurrence time is later. During the descending phase, both crests shift gradually toward the equator, the amplitude decreases, and the occurrence time is earlier. Explanations on the seasonal variations of peak EIA crests are also given in this section.

7. Summary, conclusions, and outlook

7.1. Summary and conclusions

The first mission of the thesis is to review the basic knowledge of the ionosphere such as its structure and its spatial and temporal variations, with emphasis on the phenomenon of ionospheric scintillation and its risk of interference to the transmission of electromagnetic waves. Other potential sources of disturbance to the ionosphere are also mentioned. In general, signal propagation through the ionosphere is severely affected by solar activity, especially in the areas near the magnetic equator and at high-latitude regions. Due to Earth rotation, there is a correlation between TEC and daily time, that is maximum just after local noon, and minimum during nighttime. Electron density also changes seasonally throughout the year. In spring and autumn in the equatorial regions, the Sun's rays are perpendicular to the Earth's surface, leading to maximum ionization and the maximum electron density. In summer and winter, reduced ionization leads to lower electron density. Besides, the density of the electrons also depends on Earth's magnetic field. According to the geomagnetic reference frame, the Earth is divided into three regions: equatorial, mid-latitude, and polar region. The size and variability of the electron density are largest in the equatorial and polar regions, meanwhile, in the mid-latitude areas, the electron density only fluctuates rapidly in response to extreme levels of ionospheric or geomagnetic storms.

In this thesis, alternative methods have been proposed to detect scintillation error in GNSS measurements. The proposed methods are the method of using high-rate GNSS receivers to directly output S_4 index and the method of using dual-frequency measurements to compute the replacement indices for S_4 including ROTI, VTEC gradient. Each method has its own advantages and disadvantages depending on each specific case to be applied. In principle, the method of using dedicated receivers operating at a high sampling rate to directly output S_4 gives the highest reliability. This is also the best method for studying ionospheric scintillation in areas not too large and when financial ability allows the installation of receivers with a reasonable density (as the case study of Chapter 4 for the Vietnam region). In the absence of scintillation receivers or the need to study scintillation on a large scale, using ROTI index is the recommended solution. The main advantage of this method is the enormous number of standard dual-frequency GNSS receivers on a global scale (along with it, the number of satellites from different GNSS systems is constantly increasing nowadays) compared to the

limited number of scintillation receivers currently available (as the case study of Chapter 5 on a global scale).

One of the contributions from this dissertation work is to develop an ionospheric software tool. This program can handle both standard GNSS measurements and high-rate observations. The outcomes of the program such as VTEC, VTEC gradient, ROT, ROTI, S4, etc. can be used to assess the level of disturbance of the ionosphere.

To detect ionospheric scintillation in case there are no scintillation receivers to provide the indices in-phase and quadrature, another solution can be used by computing VTEC gradient and ROTI index directly from GNSS observations. The results of this study demonstrate that it is possible to use RINEX file to evaluate the presence and intensity of ionospheric irregularities, which are usually characterized by ROTI index. There is a high correlation between VTEC gradient and ROTI in this study and the enhancement of amplitude scintillation (S_4) corresponds quite well with TEC depletions and ROTI fluctuations. Results from Chapter 2 indicate a large scintillation error occurrence at around 11 UT at POTS (in Germany) and BAHR (in Bahrain) stations on October 28th 2003.

As solar flares and solar wind carry charged particles from the Sun, the electron concentration is strongly affected by these factors, and also electromagnetic radiation from the Sun. When these particles reach the Earth, some of them are trapped in the Earth's magnetic field, thus adding to the number of TEC and accompanied by the turbulence in the ionosphere. When the radiation intensity from the Sun increases, it penetrates further into the ionosphere and then increases the electron density and charged particles. Therefore, regions of the ionosphere that are closer to the Sun (F_1 and F_2 layers) typically increase the electron concentrations. As a result, there is a biannually increasing in TEC during the spring and autumnal equinoxes as the Earth is most exposed to the Sun during these seasons. This is one of the basic characteristics of TEC's temporal variations. In Chapter 3, from the results of VTEC calculation in eleven consecutive years at seven IGS stations located in Southeast Asia, conclusions about the variability of TEC have been drawn. In which, new findings and significant results can be listed as follows:

- VTEC has been calculated and investigated in a long-term period (11 years) with different options: maximum monthly, mean monthly, and mean daily. The corresponding correlation coefficients with the solar indices are also attached.

- Presents more detail the development of SC24, especially the abnormal fluctuations during the period of 2012 - 2014.
- Highlights the dependence of seasonal variations of the ionosphere on solar phase.
- Proposes a new method to study spatial variations of TEC.
- Indicates that the F10.7cm index is more appropriate (with the calculated VTEC results) than the SSN index in the research area during the study period.
- For the first time, the mean (monthly) VTEC for an entire large area (Southeast Asia) has been calculated for eleven consecutive years.
- All the phenomena of TEC variations revealed are explained by the physical properties of the ionosphere.

When studying the ionosphere and TEC variations, it would be incomplete if we ignore the effects of ionospheric scintillation. From the data received at three scintillation receivers located in Vietnam in two years 2009 and 2015, the occurrence characteristics of ionospheric scintillation over this region have been revealed. After the process of filtering to detect and eliminate the multipath effect, the temporal and spatial distributions of ionospheric scintillation over Vietnam region are concluded at some points as follows:

- Applying the introduced filtering algorithm can not only separate other errors from the error due to scintillation effect but also a new method to detect and remove the multipath error.
- Diurnal variations: as the F-layer of the ionosphere has an increase in the number of electrons during the evening hours, ionospheric scintillation mainly occurs at pre-midnight hours, that is between 20 and 24h local time, and it rarely appears during the daytime.
- Seasonal variations: ionospheric scintillation occurs more frequently during the equinoctial months and less frequently during the solstitial months. Nonetheless, this pattern of seasonal variations does not apply to South America where the geomagnetic equator deviates sharply from the geographic equator.
- Annual variations: scintillation activity is dependent on solar cycle, it is more intense, and more frequent in the active solar years and weaker, and less common in the low solar years.

- Position and direction: scintillation activity appears primarily surrounding the positions of EIA's crests. It also occurs predominantly in observations with low satellite elevation (less than 40^o) and its positions often direct toward the anomaly crests. Particularly in the Vietnam region, strong ionospheric scintillation occurs more often in the northern area and then to the middle area. The southern area is the least likely to be affected by ionospheric scintillation error.

Using S_4 index to study ionospheric scintillation over Vietnam region has given very clear results, reflecting the exact characteristics and essence of scintillation activity in equatorial regions. Nevertheless, as mentioned above, to study global ionospheric irregularities, the ROTI index is often preferred. Taking advantage of the relatively dense density of IGS stations globally (currently more than 500 stations), the global ionospheric irregularities map using ROTI index has been produced. This map provides both temporal and spatial distributions of worldwide ionospheric scintillation, and clearly shows the distinctive appearance characteristics of different latitude regions of the Earth. That is scintillation often appears in the evening and persists until around midnight with strong intensity in low-latitude areas. In polar regions, it can occur at any time but with lower intensity. Meanwhile, scintillation hardly occurs in mid-latitude areas. This ROTI map also indicates that South America and Southeast Asia are two of the areas most vulnerable to scintillation activity. These two regions, of course, belong to the EIA.

Among different regions of the world, equatorial anomaly region is the region with dense electron density concentrated in the F_2-layer. The ionosphere in this region is most sensitive to electromagnetic waves. In satellite geodesy, this area has potential risks of errors to radio signals. Therefore, understanding the structure of EIA is paying more attention to space geodesists today. The research area (South East Asia) is also located entirely within the EIA. It is well known that EIA is characterized by an electron density trough at the magnetic equator and the two crests of enhanced electron density at approximately ±15° magnetic latitudes. This structure of the equatorial ionosphere is supposed to be caused by during the daytime, the east-west electric field and the north-south geomagnetic field create the lift of plasma in the E-layer by vertical E·B drift. After being transported to higher altitudes (the F-region), the plasma diffuses downward along the geomagnetic field lines into both hemispheres under the influence of gravity and pressure gradients. This fountain effect is the main driver of EIA. Moreover, in the equatorial zone, there are still different physical

processes such as trans-equatorial neutral winds or neutral composition effects leading to the variations in the structure of EIA. The combination of the above effects makes the structure of EIA often in a state of instability and vulnerability. To investigate how EIA's structure had changed during SC24, the temporal - latitudinal VTEC map has been established. Thereby, featured appearance of EIA crests in Southeast Asia is revealed.

The occurrence characteristics of EIA crests in Southeast Asia can be summarized as follows: In winter, anomaly crests often appear early and tend to shift toward the equator. On the contrary, in summer they appear late and tend to move towards the poles. During the solar cycle increasing phase, both crests move further from the equator, the amplitude increases, and the appearance time is later. During the decreasing phase, both crests shift toward the equator, the amplitude decreases, and the appearance time is earlier.

The high consistency between the state of the ionosphere and the activity status of solar cycle is demonstrated by the correlation coefficients between VTEC and the SSN index, recorded at a very high level, approximately 1.0. Meanwhile, the correlation coefficients between S_4 and ROTI at HANOI and HUE stations during the biggest geomagnetic storm of SC24 happened on March 17^{th}, 2015 are determined to be 0.92 and 0.86, respectively. By the way, the behaviour of EIA's structure during an intense geomagnetic storm is exposed. Specifically for this case, one day after the storm arrived, as the ionospheric disturbance dynamo developed and the degeneration of EIA, the northern crest moved equatorward a distance of approximately 12^{o} compared to its previous position, the southern crest completely disappeared, and the average VTEC amplitude for the entire region of Southeast Asia declined about 40% (amplitude of northern and southern crests decreased by 29.2% and 35.4% respectively). Also on this day, the appearance time of the common anomaly crest was about 3.5 hours earlier than usual. Nevertheless, all of these experiences had only occurred within one day (18^{th}), since the 19^{th} onwards the state of the ionosphere was almost returned to as its origin.

7.2. Outlook and further studies

Thus, caused by ionization density irregularities, scintillating signals change phase unexpectedly and vary rapidly in amplitude. Together with phase advance and group delay, scintillations are the major ionospheric effects for microwave signals which limit the performance and availability of satellite geodesy systems. For ionospheric delay, the technique of using multi-frequency measurements has achieved maximum efficiency, but for

scintillation effects, the question now is how to face it and what are the mitigation strategies? A few ideas to solve these problems are as follows:

- Firstly, increasing the number of observed satellites is the key point owing the fact that not all Satellite signals are simultaneously affected during an intense scintillation event. Fortunately, this is possible since Global Navigation Satellite Systems such as GPS, GLONASS, GALILEO, BEIDOU, etc. are growing rapidly, along with the increasing number of satellites (including satellites navigation and LEO).
- Secondly, increase the number of scintillation receivers operating at high-rate of sampling to be able to capture the small-scale irregularities in the ionosphere.
- Thirdly, instead of using normal receivers, try to use receivers that can have a fast re-tracking the satellites after the loss of lock, because this kind of error usually occurs and exists in a very short time.

As discussed in Chapter 2, the most sensible strategy for ionospheric scintillation research is:

- For an area of moderate size, consider setting up scintillation stations with a suitable density. These stations will directly provide S_4 index, which is the most reliable indicator and best reflects the scintillation intensity in satellite signals when they pass through the ionosphere. However, this solution should only be applied in the equatorial regions or high-latitude areas. In mid-latitudes, as scintillation activity is very rare, the installation of scintillation receivers is not truly worth compared to the cost that will have to be spent to build and maintain it. In these areas, the recommendation is to use the next solution.
- The second solution is advisable to be applied to large areas or globally. This solution takes advantage of the vast number of measurements from dual-frequency GNSS receivers being and will be installed with increasing density globally. And as mentioned above, with the growing number of satellites, this method is even easier to implement and can be highly effective. From these data, ROTI index can be derived and used to study the spatial and temporal distributions of ionospheric irregularities.

When forecasting the prospect of ionosphere and scintillation, it would be incomplete without mentioning the solar cycle activity and other extreme phenomena of the ionosphere such as ionospheric storms or geomagnetic storms. The fact shows that the state of the ionosphere during the last years of the previous decade and early 2020 (solar minimum period) is usually maintained at a fairly stable level, without too many strong ionospheric

storms happening. Therefore, the extent of its impact on space geodetic techniques during this period is not too serious. The upcoming solar maximum is predicted to be around 2024 and 2025. Theoretically, it does not affect all regions of the Earth equally but the dense and thick ionosphere arising during this period will slow electromagnetic waves at all latitudes. Meanwhile, storms in the ionosphere (if they occur) present an additional danger to satellite signals when they create irregularities. So, what are the main challenges of scintillation for the three different latitude regions of the Earth in the upcoming solar cycle (SC25)?

- At low-latitudes, the ionosphere will create its own storms, now made more intense by the denser, thicker ionosphere and as usual, this leads to the greatest danger to radio signals in these areas. Ionospheric storms typically form after sunset and last for several hours. As the F-layer in the ionosphere has an increase in the number of electrons during this period and because of the Rayleigh-Taylor instability, scintillation is most intense in the EIA regions during the evening hours.
- At mid-latitudes, the ionosphere will experience storms driven by solar flares and magnetic storms. These storms form irregularities that cause satellite signal to be scintillated. In view of the fact that during the last solar maximum (period of 2013 - 2014) very few resources were applied to understanding scintillation, so what we truly know about the threat of ionospheric scintillation in these areas is very little. These can be considered as the major challenges of ionospheric scintillation at high-latitude areas during SC25.
- At high-latitudes, the threat comes during magnetic storms, in which blobs of the ionosphere from the dayside are swept over the polar cap onto the nightside. These blobs form irregularities that cause satellite signals to scintillate. Besides, individual auroral arcs can cause rapid phase variations or even diffractive scintillation. For the users of space geodetic techniques, the most significant concern in these regions is that the appearance of scintillation does not follow the rule as for the equatorial regions (which often occur only in the evening).

From the issues posed and solved in this thesis, future open research can be outlined as follows:

- Regarding S_4 index calculation technique: it is necessary to study the calculation of S_4 from high-rate scintillation receivers with different samplings. In this thesis, only the 50-Hz scintillation receivers is used to determine S_4. So, the questions are what is the minimum limit of sampling rate that is enough to be able to capture scintillation events and in case of using receivers with higher sampling rate, what will be the pros and cons?
- Regarding ROTI index calculation technique: the time interval over which a value of ROTI is calculated should be paid more attention in subsequent studies. Although there have been studies about the impact of different sampling rates and calculation time intervals on ROTI values, the reality proves that these values are not best fixed for all cases, but they vary flexibly depending on the regions and time of calculation.
- In addition to S_4 and ROTI indices, it is also necessary to invent more indicators and methods to study scintillation and the electron density irregularities in the ionosphere.
- Developing and using scintillation models to predict and warn of ionospheric extremes related to scintillation activity.
- In this thesis, GNSS measurements are mainly used to study ionospheric scintillation. To be eligible for evaluation the reliability as well as to improve the accuracy of the research results, further steps need to be carried out is to use additional space geodetic measurements such as radio occultation observations, VLBI observations, DORIS observations,… The combination of different measurements is always expected to yield better results.
- To study ionospheric scintillation it is best to use specialized receivers which can provide scintillation indices (S_4 index for instance). Therefore, there is a need to consider the installation of additional scintillation stations in EIA areas, especially in the two most affected areas, South America and Southeast Asia. A network of such stations with sufficient density will assist to better control the impacts of scintillation on electromagnetic wave signals.

Bibliography

Aarons, J. (1977). Equatorial scintillations: a review, IEEE Antennas Propag. Mag., 25 (5), 729-736, DOI: 10.1109/TAP.1977.1141649.

Aarons, J. (1982). Global morphology of ionospheric scintillations. Proc IEEE 70:360-378. doi:10.1109/PROC.1982.12314.

Aarons, J. (1993). The Longitudinal Morphology of Equatorial F-Layer Irregularities Relevant to their Occurrence. Space Science Reviews, Vol. 63, pp. 209 - 43, DOI: 10.1007/BF00750769.

Aarons, J. (1995). Fading of GPS Transmissions Due to Ionospheric Irregularities. Center for Space Physics, Boston University, Report to the FAA WAAS Program Office.

Aarons, J., Mendillo, M., and Yantosca, R. (1996). GPS phase fluctuations in the equatorial region during the MISETA 1994 campaign. J. Geophys. Res., 101(A12), 26,851-26,862, doi:10.1029/96JA00981.

Aarons, J. (1997). 50 years of radio-scintillation observations. IEEE Antennas Propagation Magazine, 39, 7-12, DOI: 10.1109/74.646785.

Abadi, P., Saito, S., and Srigutomo, W. (2014). Low-latitude scintillation occurrences around the equatorial anomaly crest over Indonesia. Ann. Geophys., 32, 7-17, doi.org/10.5194/angeo-32-7-2014.

Abdu, M.A. (2001). Outstanding problems in the equatorial ionospherethermosphere electrodynamics relevant to spread F. J.Atmos. Sol. Terr. Phys., 63, 869-884, doi:10.1016/S1364-6826(00)00201-7.

Abdu, M.A., Kherani, E.A., Batista, I.S., and Sobral, H.A. (2009). Equatorial evening prereversal vertical drift and spread F suppression by disturbance penetration electric fields, Geophys. Res. Lett., 36, L19103, doi:10.1029/2009GL039919.

Abhakara, P. (2004). Ionospheric irregularities as observed from the GPS reference station in Singapore. Master of Electrical Engineering Program, Cornell University.

Adewale, A. O., Oyeyemi, E. O., Adeloye, A. B., Mitchell, C. N., Rose, J. A. R., and Cilliers, P. J. (2012). A study of L-band scintillations and total electron content at an equatorial station, Lagos, Nigeria. RADIO SCIENCE, VOL. 47, RS2011, DOI: 10.1029/2011RS004846.

Afraimovich E. L. (2008). First GPS-TEC evidence for the wave structure excited by the solar terminator, Earth, Planets and Space, 60, 895-900.

Alfonsi, L., Spogli, L., Tong, J.R., Franceschi, G.D., Romano, V., Bourdillon, A., Le, H.M., and Mitchell, C.N. (2006). GPS scintillation and TEC gradients at equatorial latitudes in April 2006. Advances in Space Research, Volume 47, Issue 10, Pages 1750-1757, doi.org/10.1016/j.asr.2010.04.020.

Alfonsi, L., Spogli, L., Pezzopane, M., Romano, V., Zuccheretti, E., De Franceschi, G., Cabrera, M.A., Ezquer, R.G. (2013). Comparative analysis of spread-F signature and GPS scintillation occurrences at Tucuma´n, Argentina. J. Geophys. Res. 118, 4483-4502, doi.org/10.1002/jgra.50378.

Alfonsi, L., Wernik, A.W., Materassi, M., Spogli, L. (2017). Modelling ionospheric scintillation under the crest of the equatorial anomaly. Advances in Space Research, Volume 60, Issue 8, Pages 1698-1707, doi.org/10.1016/j.asr.2017.05.021.

Alizadeh, M., Schuh, H., Todorova, S., and Schmidt, M. (2011). Global Ionosphere Maps of VTEC from GNSS, satellite altimetry, and formosat-3/COSMIC data. Journal of Geodesy volume 85, pages975-987(2011), doi.org/10.1007/s00190-011-0449-z.

Alizadeh, M. (2013) Multi-Dimensional modeling of the ionospheric parameters, using space geodetic techniques and formosat-3/COSMIC data. PhD thesis, Vienna University of Technology, Austria.

Alizadeh, M., Wijaya, D., Hobiger, T., Weber, R., and Schuh, H. (2013). Ionospheric effects on on microwave signals. In J. Boehm and H. Schuh, eds., Atmospheric Effects in Space Geodesy, Springer Verlag, ISBN:978-3-642-36931-5.

Anderson, P.C., Straus, P.R. (2005). Magnetic field orientation control of GPS occultation observations of equatorial scintillation. Geophys. Res. Lett. 32 (L21107), 1-4. doi.org/10.1029/2005GL023781.

Anderson, D.N. (2003). Forecasting the occurrence of ionospheric scintillation activity in the equatorial ionosphere on a day-to-day basis. GPS Solutions 7:200-202, DOI 10.1007/s10291-003-0064-4.

Andreeva, E.S., Franke, S.J., Yeh, K.C., and Kunitsyn, V.E. (2000). Some features of the equatorial anomaly revealed by ionospheric tomography. Geophys. Res. Lett., 27(16), 2465-2468, doi:10.1029/1999GL003725.

Amory-Mazaudier, C., Le, H.M., Cohen, Y., Doumbia, V., Bourdillon, A., Fleury, R., Fontaine, B., Duyen, C.H., Kobea, A., Laroche, P., Lassudrie Duchesne, P., Le, V.H., Le, T.T., Truong, H.L.V., Menvielle, M., Nguyen, C.T., Nguyen, X.A., Ouattara, F., Petitdidier, M., Pham, T.H., Pham, T.X., Philippon, N., Tran, T.L., Vu, H.T., and Vila, P. (2006). SunEarth System Interaction studies over Vietnam : an international cooperative project. Annales Geophys., 24, 3313-3327.

Aquino, M., Monico, J.F.G., Dodson, A.H., Marques, H., Franceschi, G.D., Alfonsi, L., Romano, V., and Andreotti, M. (2009). Improving the GNSS positioning stochastic model in the presence of ionospheric scintillation. J Geod 83:953-966, DOI 10.1007/s00190-009-0313-6.

Bagiya, M.S., Joshi, H.P., Iyer, K.N., Aggarwal, M., Ravindran, S., and Pathan, B.M.. (2009). TEC variations during low solar activity period (2005 - 2007) near the Equatorial Ionospheric Anomaly Crest region in India. Ann. Geophys., 27, 1047-1057, doi.org/10.5194/angeo-27-1047-2009.

Bailey, G.J., Su, Y.Z., and Oyama, K.I. (2000). Yearly variations in the low-latitude topside ionosphere. Ann. Geophys., 18, 789-798, doi.org/10.1007/s00585-000-0789-0.

Balan, N., Bailey, G. J. (1995). Equatorial plasma fountain and its effects: Possibility of an additional layer. JGR Space Physics, Volume 100, IssueA11, Pages 21421-21432, doi.org/10.1029/95JA01555.

Balan, N., Liu, L., and Le, H. (2018). A brief review of equatorial ionization anomaly and ionospheric irregularities. Earth and Planetary Physics, 2: 257-275, 2018, doi: 10.26464/epp2018025.

Basu, S., Basu, S., Aarons, J., McClure, J.P., Cousins, M.D. (1978). On the coexistence of kilometer- and meter-scale irregularities in the nighttime equatorial F region. J. Geophys. Res. 83 (A9), 4219-4226.

Basu, S., Basu, S. (1981). Equatorial scintillations. Rev. J. Atmos. Terrestrial Phys. 43, 473-489.

Basu, S., Sa, B. (1985). Equatorial scintillations: advances since ISEA-6. J Atmos Terr Phys 47:753-768. doi:10.1016/0021-9169(85)90052-2.

Basu, S., MacKenzie, E., Sa, B. (1988). Ionospheric constraints on VHF/UHF communications links during solar maximum and minimum periods. Radio Sci 23(3):363-378.

Basu, S., Kudeki, E., Basu, S., Valladares, C.E., Weber, E.J., Zengingonul, H.P., Bhattacharyya, S., Sheehan, R., Meriwether, W., Biondi, M.A., Kuenzler, H., and Espinoza, J. (1996). Scintillations, plasma drifts, and neutral winds in equatorial ionosphere after sunset. J Geophys Res 101:26795-26809. doi:10.1029/96JA00760.

Basu, S., Groves, K., Quinn, J., and Doherty, P. (1999). A comparison of TEC fluctuations and scintillations at Ascension Island. J. Atmos. Sol. Terr. Phys., 61 (16), 1219-1226, DOI: 10.1016/S1364-6826(99)00052-8.

Basu, S., Groves, K.M., Basu S, Sultan, P.J. (2002). Specification and forecasting of scintillations in communication/navigation links: current status and future plans. J Atmos Sol Terr Phys 64:1745-1754. doi:10.1016/S1364-6826(02)00124-4.

Batista, I.S., Abdu, M.A., and Bittencourt, J.A. (1986). Equatorial F region vertical plasma drifts: seasonal and longitudinal asymmetries in the American sector, J. Geophys. Res. [Space Phys.], 91 (A11), 12,055-12,064, DOI: 10.1029/JA091iA11p12055.

Beach, T.L., Kintner, P.M. (1999). Simultaneous Global Position System observations of equatorial scintillations and total electron content fluctuations. J Geophys Res 104(A10): 22553-22556.

Beach, T., and Kintner, P.M. (2001). Development and use of a GPS ionospheric scintillation monitor, IEEE Trans. Geosci. Remote Sens., 39 (5), 918-928, DOI: 10.1109/36.921409.

Beniguel, Y., Adam, J.-P., Jakowski, N., Noack, T., Wilken, V., Valette, J.-J., Cueto, M., Bourdillon, A., Lassudrie-Duchesne, P., and Arbesser-Rastburg, B. (2009). Analysis of scintillation recorded during the PRIS measurement campaign, Radio Science, 44 (1), RS0A30, DOI: 10.1029/2008RS004090.

Beniguel, Y., Romano, V., Alfonsi, L., Aquino, M., Bourdillon, A., Cannon, P., De Franceschi, G., Dubey, S., Forte, B., Gherm, V., Jakowski, N., Materassi, M., Noack, T., Pozoga, M., Rogers, N., Spalla, P., Strangeways, H.J., Warrington, E.M., Wernik, A., Wilken, V., Zernov, N. (2009). Ionospheric scintillation monitoring and modelling. Ann. Geophys. 52, 391-416.

Beniguel, Y. (2011). GISM - Global Ionospheric Scintillation Model. IEEA, GISM technical Manual.

Beniguel, Y., and Hamel, P. (2011). A global ionosphere scintillation propagation model for equatorial regions. J. Space Weather Space Clim. 1 (2011) A04, DOI: 10.1051/swsc/2011004.

Bhattacharyya, A., Beach, T. L., and Basu, S. (2000). Nighttime equatorial ionosphere: GPS scintillations and differential carrier phase fluctuations. Radio Science, vol. 35, pp. 209-224.

Bhattacharyya, A., Kakad, B., Sripathi, S., Jeeva, K., Nair, K.U. (2014). Development of intermediate scale structure near the peak of the F region within an equatorial plasma bubble. J. Geophys. Res. 119, 3066-3076.

Bilitza, D., McKinnell, L.A., Reinisch, B., and Fuller-Rowell, T. (2011). The International Reference Ionosphere today and in the future. J. Geod., 85: 909-920.

Birch, M.J., Hargreaves, J.K., Bailey, G.J. (2002). On the use of an effective ionospheric height in electron content measurement by GPS reception. Radio Sci., 37.

Blanc, M., Richmond, A. (1980). The ionospheric disturbance dynamo. J. Geophys. Res., 85, 1669-1686.

Borries C., Jakowski, N., and Wilken, V. (2009). Storm induced large scale TIDs observed in GPS derived TEC, Ann. Geophys., 27, 1605-1612.

Brunini, C., Camilion, E., Azpilicueta, F. (2011). Simulation study of the influence of the ionospheric layer height in the thin layer ionospheric model. J. Geod., 85, 637-645.

Carrano, C., Groves, K. (2009). Ionospheric data processing and analysis. Workshop on Satellite Navigation Science and Technology for Africa, The Abdus Salam ICTP, Trieste, Italy.

Carrano, C.S., Groves, K.M., McNeil, W.J., and Doherty, P.H. (2010). Scintillation Characteristics across the GPS Frequency Band, in: 25th International Technical Meeting of the Satellite Division of the Institute of Navigation, Nashville TN, September 17-21, pp.1972-1989, https://www2.bc.edu/~carranoc/carrano-ion-2465.pdf.

Carter, B.A., Retterer, J.M., Yizengaw, E., Groves, K., Caton, R., McNamara, L., Bridgwood, C., Francis, M., Terkildsen, M., Norman, R., Zhang, K. (2014). Geomagnetic control of equatorial plasma bubble activity modeled by the TIEGCM with Kp. Geophys. Res. Lett. 41, 5331-5339.

Cesaroni, C., Spogli, L., Alfonsi, L., Franceschi, G.D., Ciraolo, L., Monico, J.F.G., Scotto, C., Romano, V., Aquino, M., and Bougard, B. (2015). L-band scintillations and calibrated total electron content gradients over Brazil during the last solar maximum. J. Space Weather Space Clim., 5, A36 (2015), DOI: 10.1051/swsc/2015038.

Cervera, M.A., Thomas, R.M. (2006). Latitudinal and temporal variation of equatorial ionospheric irregularities determined from GPS scintillation observations. Ann. Geophys. N.24, 3329-3341.

Chakraborty, S.K.,Hajra, R., and DasGupta, A. (2012). Ionospheric scintillation near the anomaly crest in relation to the variability of ambient ionization. RADIO SCIENCE, VOL. 47, RS2006, doi:10.1029/2011RS004942.

Chakraborty, S.K., Chatterjee, S., Jana, D. (2017). A study on multifrequency scintillations near the EIA crest of the Indian zone. Advances in Space Research, Volume 60, Issue 8, Pages 1670-1687, doi.org/10.1016/j.asr.2017.02.020

Chandra, K.R., Srinivas, V.S., and Sarma, A.D. (2009). Investigation of ionospheric gradients for GAGAN application. Earth Planets Space, 61, 633-635.

Chatterjee, S., and Chakraborty, S.K. (2013). Variability of ionospheric scintillation near the equatorial anomaly Discussions crest of the Indian zone. Ann. Geophys., 31, 697-711, 2013, doi:10.5194/angeo-31-697-2013.

Chen, C.H. , Liu, J.Y., Yumoto, K., Lin, C.H., Fang, T.W. (2008). Equatorial ionization anomaly of the total electron content and equatorial electrojet of ground-based geomagnetic field strength. Volume 70, Issue 17, Pages 2172-2183, doi.org/10.1016/j.jastp.2008.09.021.

Cherniak, I., Krankowski, A., Zakharenkova, I. (2014). Observation of the ionospheric irregularities over the Northern Hemisphere: methodology and service. Radio Sci, DOI: 10.1002/2014RS005433.

Cherniak, I., Zakharenkova, I., and Krankowski, A. (2014). Approaches for modeling ionosphere irregularities based on the TEC rate index. Earth Planets Space 66:165.

Cokrlic, M., Galas, R. (2013). TUB software tools for monitoring ionospheric irregularities in a single station mode and first result. 7th European Conference on Antennas and Propagation (EUCAP 2013).

Cokrlic, M., Wezka, K., Galas, R., Jakowski, N. Ionospheric scintillation monitoring in a single station mode, 6th GNSS Vulnerabilities and Solutions Conference.

Conker, R.S., El-Arini, M.B., Hegarty, C.J., and Hsiao, T. (2003). Modeling the effects of ionospheric scintillation on GPS/Satellite-Based Augmentation System availability. RADIO SCIENCE, VOL. 38, NO. 1, 1001, doi:10.1029/2000RS002604.

Dach, R., Hugentobler, U., Fridez, P., and Meindl, M. (2007). Bernese GPS Software,Version 5.0. Astronomical Institute, University of Bern.

Dandekar, B.S., and Groves, K.M. (2004). Using ionospheric scintillation observations for studying the morphology of equatorial ionospheric bubbles. Radio Sci., 39, RS3010, doi:10.1029/2003RS003020.

Dettmering, D., Schmidt, M., Heinkelmann, R., and Seitz, M. (2011). Combination of different space geodetic observations for regional ionosphere modeling. J. Geod., 85: 989-998.

Dettmering, D., Heinkelmann, R., Schmidt, M. (2011). Systematic differences between VTEC obtained by different space-geodetic techniques during CONT08. J Geod (2011) 85:443-451, DOI 10.1007/s00190-011-0473-z.

Dubey, S., Wahi, R., and Gwal, A.K. (2006). Ionospheric effects on GPS positioning. Adv. Space Res., 38(11), 2478-2484, doi:10.1016/j.asr.2005.07.030.

El-naggar, A.M. (2011). Enhancing the accuracy of GPS point positioning by converting the single frequency data to dual frequency data. Alexandria Engineering Journal, Volume 50, Issue 3, Pages 237-243, doi.org/10.1016/j.aej.2011.03.003.

Eyelade, V.A., Adewale, A.O., Akala, A.O., Bolaji, O.S., and Rabiu, A.B. (2017). Studying the variability in the diurnal and seasonal variations in GPS total electron content over Nigeria. Ann. Geophys., 35, 701-710, doi.org/10.5194/angeo-35-701-2017.

Fedorenko, Y.P., Tyrnov, O.F., Fedorenko, V.N., and Dorohov, V.L., Model of traveling ionospheric disturbances. J. Space Weather Space Clim. 3 (2013) A30, DOI: 10.1051/swsc/2013052.

Fejer, B.G., Farley, D.T., Woodman, R.F., and Calderon, C. (1979). Dependence of equatorial F region vertical drifts on season and solar cycle. J. Geophys. Res., 84(A10), 5792-5796, doi:10.1029/JA084iA10p05792.

Fejer, B.G., Scherlies, L., de Paula, E.R. (1999). Effects of the vertical plasma drift velocity on the generation and evolution of equatorial spread F. J. Geophys. Res. 104 (A9), 19859-19869.

Fejer, B.G., Jensen, John W., Su, Shin-Yi. (2008). Quiet time equatorial F region vertical plasma drift model derived from ROCSAT-1 observations. J. Geophys. Res. 113, A05304. doi.org/10.1029/2007JA012801.

Gonzales, C.A., Kelley, M.C., Fejer, B.G., Vickrey, J.F., and Woodman, R.F. (1979). Equatorial electric fields during magnetically disturbed conditions 2. Implications of simultaneous auroral and equatorial measurements, J. Geophys. Res., 84, 5803. doi.org/10.1029/JA084iA10p05803.

Grodent, D., Bonfond, B., Gérard, J., Radioti, A., Gustin, J., Clarke, J.T., Nichols, J., Connerney, J.E.P. (2008). Auroral evidence of a localized magnetic anomaly in Jupiter's northern hemisphere. Journal of Geophysical Research, Space Physics, doi.org/10.1029/2008JA013185.

Groves, K.M., et al. (1997). Equatorial scintillation and systems support. Radio Sci., 32, 2047-2064, doi:10.1029/97RS00836.

GSV GPS Silicon Valley. (2005). GSV4004B GPS Ionospheric Scintillation & TEC Monitor (GISTM). User's manual.

Guo, K., Aquino, M. & Vadakke Veettil, S. (2019). Ionospheric scintillation intensity fading characteristics and GPS receiver tracking performance at low latitudes. GPS Solut 23, 43, doi.org/10.1007/s10291-019-0835-1.

Hatch, R. (1982). Synergism of GPS code and carrier measurements, Proceedings of the Third International Geodetic Symposium on Satellite Doppler Positioning, 2, 1213-1231, New Mexico State University, NM, USA, Feb. 8-12.

Hajra, R., Chakraborty, S.K., Tsurutani, B.T., DasGupta, A., Echer, E., Brum, C.G.M., Gonzalez, W.D., and Sobral, J.H.A. (2016). An empirical model of ionospheric total electron content (TEC) near the crest of the equatorial ionization anomaly (EIA). J. Space Weather Space Clim., 6, A29, DOI: 10.1051/swsc/2016023.

Hanson, W.B., and Moffett, R.J. (1966). Ionization transport effects in the equatorial F region. J. Geophys. Res., 71, 5559.

Hawarey, M., Hobiger, T., and Schuh, H. (2005). Effects of the 2nd order ionospheric terms on VLBI measurements. GEOPHYSICAL RESEARCH LETTERS, VOL. 32, L11304, doi:10.1029/2005GL022729.

Hernández-Pajares, M., Juan, J., Sanz, J., García-Fernández, M. (2005). Towards a More Realistic Ionospheric Mapping Function. XXVIII URSI General Assembly: Delhi, India.

Hernandez-Pajares, M., Juan, J.M., Sanz, J., Orus, R., Garcia-Rigo, A., Feltens, J., Komjathy, A., Schaer, S.C., Krankowski, A. (2009). The IGS VTEC maps: A reliable source of ionospheric information since 1998. J. Geod., 83, 263-275.

Hernández-Pajares, M., Miguel Juan, J., Sanz, J., Aragón-Àngel, A., García-Rigo, A., Salazar, D., and Escudero, M. (2011). The ionosphere: effects, GPS modeling and the benefits for space geodetic techniques. J Geod, DOI 10.1007/s00190-011-0508-5.

Hlubek, N., Berdermann, J., Wilken, V., Gewies, S., Jakowski, N., Wassaie, M., and Damtie, B. (2014). Scintillations of the GPS, GLONASS, and Galileo signals at equatorial latitude. J. Space Weather Space Clim. 4 (2014) A22, DOI: 10.1051/swsc/2014020.

Hobiger, T. (2005). VLBI as tool to probe the ionosphere. PhD thesis, Vienna Univ. of Technology, Austria.

Hofman-Wellenhof, Lichtenegger, H., Collins, J. (2000). GPS Theory and Practice. Fifth revised edition, Springer, New York.

Huang, C.Y., Burke, W.J., Machuzak, J.S., Gentile, L.C., and Sultan, P.J. (2001). DMSP Observations of equatorial plasma bubbles in the topside ionosphere near solar maximum. J. Geophys. Res., 106(A5), 8131-8142, doi:10.1029/2000JA000319.

Huang, L., Wang, J., Jiang, Y., Chen, Z., Zhao, K. (2014). A study of GPS ionospheric scintillations observed at Shenzhen. Adv. Space Res. 54, 2208-2217.

Humphreys, T.E. (2008) Modeling ionospheric scintillation and its effects on GPS carrier tracking loops and two other applications of modeling and estimation. Degree of Doctor of Philosophy, Cornell University.

Jacobsen, K.S., and Schäfer, S. (2012). Observed effects of a geomagnetic storm on an RTK positioning network at high latitudes. J. Space Weather Space Clim., 2, A13, 2012, DOI: 10.1051/swsc/2012013.

Jacobsen, K.S. (2014). The impact of different sampling rates and calculation time intervals on ROTI values. J. Space Weather Space Clim., 4, A33, DOI: 10.1051/swsc/2014031.

Jacobsen, K.S., Daehnn, M. (2014). Statistics of ionospheric disturbances and their correlation with GNSS positioning errors at high latitudes. J. Space Weather Space Clim. 4, A27, DOI: 10.1051/swsc/2014024.

Jakowski, N., Mayer, C., Hoque, M.M., and Wilken, V. (2011). Total electron content models and their use in ionosphere monitoring. RADIO SCIENCE, VOL. 46, RS0D18, doi:10.1029/2010RS004620.

Jakowski, N., Borries, C., Wilken, V. (2012). Introducing a disturbance ionosphere index. RADIO SCIENCE, VOL. 47, RS0L14, doi:10.1029/2011RS004939, 2012.

Jiao, Y. (2013). High latitude ionospheric scintillation characterization. Master of Science, Department of Electrical & Computer Engineering, Miami University, Oxford, Ohio.

Jiyun, L., Pullen, S., Datta-Barua, S., and Enge, P. (2006). Assessment of Nomial Ionosphere Spatial Decorrelation for LASS. IEEE/ION PLANS 2006, pp. 506-514.

Kakinami, Y., Liu, J.Y., Tsai, L.-C., and Oyama, K.-I. (2010). Ionospheric electron content anomalies detected by a FORMOSAT-3/COSMIC empirical model before and after the Wenchuan earthquake. International Journal of Remote Sensing, Vol. 31, 13, 3571-3578.

Kelley, M.C., Makela, J.J., Chau, J.L., and Nicolls, M.J. (2003). Penetration of the solar wind electric field into the magnetosphere/ionosphere system. Geophys. Res. Lett., 30(4), 1158, doi:10.1029/2002GL016321.

Kikuchi, T., Lühr, H., Schlegel, K., Tachihara, H., Shinohara, M., and Kitamura, T.I. (2000). Penetration of auroral electric fields to the equator during a substorm. J. Geophys. Res., 105, 23251-23261.

Kintner, P.M., Ledvina, B.M., and Paula, E.R. (2007). GPS and ionospheric scintillations. SPACE WEATHER, VOL. 5, S09003, doi:10.1029/2006SW000260.

Kintner, P.M., Humphreys, T., and Hinks, J. (2009). GNSS and ionospheric scintillation, How to Survive the Next Solar Maximum. Cornell University and The University of Texas at Austin.

Klobuchar, J.A. (1996). Ionospheric effects on GPS, in Global Positioning System: Theory and Application. Volume I. American Institute of Aeronautics and Astronautics, Washington DC.

Komjathy, A. (1997). Global Ionospheric Total Electron Content Mapping Using the Global Positioning System. Ph.D dissertation, Department of Geodesy and Geomatics Engineering Technical Report No.188, University of New Brunswick, Fredericton, New Brunswick, Canada, 248 pp.

Koval, A., Cesra. (2019). Researchers simulate focusing effect of traveling ionospheric disturbances on solar dynamic spectra. https://phys.org/news/2019-01-simulate-focusing-effect-ionospheric-disturbances.html.

Lachapelle, G., Hagglund, J., Falkenberg, W., Bellemare, P., Casey, M., and Eaton, M. (1986). GPS land kinematic positioning experiments, Proceedings of the 4th International Geodetic Symposium on Satellite Positioning, 2, 1327-1344, Austin, TX, USA, Apr. 28-May 2.

Lanyi, G.E., Roth, T. (1988). A comparison of mapped and measured total ionospheric electron content using global positioning system and beacon satellite observations. Radio Sci. 1988, 23, 483-492.

Le, H.M., Amory-Mazaudier, C., Fleury, R., Bourdillon, A., Duchesne, P.L., Tran, T.L., Nguyen, C.T., Nguyen, H.T., and Vila, P. (2014). Time variations of the total electron content in the Southeast Asian equatorial ionization anomaly for the period 2006-2011. Advances in Space Research, 54, 355-368, doi.org/10.1016/j.asr.2013.08.003.

Le, H.M., Tran, T.L., Fleury, R., Le, T.T., Nguyen, C.T., Nguyen, H.T. (2016). TEC variations and ionospheric disturbances during the magnetic storm in March 2015 observed from continuous GPS data in the Southeast Asia region. Vietnam Journal of Earth Sciences Vol 38 (3) 287-305.

Le, H.M., Tran, T.L., Amory-Mazaudier, C., Fleury, R., Bourdillon, A., Hu, J., Vu, T.H., Nguyen, C.T., Le, T.T., and Nguyen, H.T. (2016). Continuous GPS network in Vietnam and results of study on the total electron content in the South East Asian region. Vietnam Journal of Earth Sciences Vol 38 (2) 153-165.

Li, G., Ning, B., and Yuan, H. (2007). Analysis of ionospheric scintillation spectra and TEC in the Chinese low latitude region. Earth Planets Space, 59, 279-285.

Li, G., Ning, B., Zhao, B., Liu, L., Liu, J.Y., Yumoto, K. (2008). Effects of geomagnetic storm on GPS ionospheric scintillations at Sanya. J. Atmos. Sol.-Terrestrial Phys. 70, 1034-1045.

Li, G., Ning, B., Liu, L., Wan, W., Liu, J.Y. (2009). Effect of magnetic activity on plasma bubbles over equatorial and low-latitude regions in East Asia. Ann. Geophys. 27, 303-312.

Lin, C.H., Richmond, A.D., Liu, J.Y., Yeh, H.C., Paxton, L.J., Lu, G., Tsai, H.F., Su, S.Y. (2005). Large - scale variations of the low - latitude ionosphere during the October - November 2003 superstorm: Observational results. J. Geophys. Res., 110, A09S28, doi:10.1029/2004JA010900.

Liu, J.Y., Tsai, H.F., and Jung, T.K. (1996). Total electron content obtained by using the global positioning system. Terr. Atmos. Oceanic Sci., 7, 107-117.

Liu, J.Y., Tsai, H.F., Wu, C.-C., Tseng, C. L., Tsai, L.-C., Tsai, W.H., Liou, K., and Chao, J.K. (1999). The effect of geomagnetic storm on ionospheric total electron content at the equatorial anomaly region. Adv. Space Res., 24(11), 1491-1494.

Liu, Z. Z., and Gao, Y. (2001). Ionospheric tomography using GPS measurements, Proceedings of the International Symposium on Kinematic Systems in Geodesy, Geomatics and Navigation, 111-120, Banff, Alberta, Canada, Jun. 5-8.

Liu, Z. Z. (2004). Ionosphere tomographic modeling and applications using Global Positioning System (GPS) measurements, Ph.D thesis, 304 pp., Department of Geomatics Engineering, The University of Calgary, Calgary, Alberta, Canada.

Liu, Z., Gao, Y., and Skone, S. (2005). A study of smoothed TEC precision inferred from GPS measurements. Earth Planets Space, 57, 999–1007.

Liu, L., Wan, W., Ning, B., Pirog, I.M., and Kurkin, V.I. (2006). Solar activity variations of the ionospheric peak electron density. J. Geophys. Res., 110, A08304, doi.org/10.1029/2006JA011598.

Liu, L., and Chen, Y. (2009). Statistical analysis of solar activity variations of total electron content derived at Jet Propulsion Laboratory from GPS observation. J. Geophys. Res., 114, A10311, doi.org/10.1029/2009JA014533.

Liu, Y.-H., Liu, C.-H., and Su, S.-Y. (2010). Global and Seasonal Scintillation Morphology in the Equatorial Region Derived from ROCSAT-1 In-situ Data, Terr. Atmos. Ocean. Sci., 23, 95-106, DOI: 10.3319/TAO.2011.06.30.01(AA).

Liu, K., Li, G., Ning, B., Hu, L., Li, H. (2015). Statistical characteristics of low-latitude ionospheric scintillation over China. Adv. Space Res. 55, 1356-1365.

Luo, X., Gu, S., Lou, Y. et al. (2020). Amplitude scintillation index derived from C/N0 measurements released by common geodetic GNSS receivers operating at 1 Hz. J Geod 94, 27, doi.org/10.1007/s00190-020-01359-7.

Maruyama, T. (2002). Ionospheric irregularities. J. Commun. Res. Lab. 49 (3), 163-178.

Meng, X., Mannucci, A.J., Verkhoglyadova, O.P., and Tsurutani, B.T. (2016). On forecasting ionospheric total electron content responses to high-speed solar wind streams. J. Space Weather Space Clim., 6, A19 (2016), DOI: 10.1051/swsc/2016014.

Moral, A.C., Eyiguler, E.C.K., and Kaymaz, Z. (2013). Sudden Ionospheric Disturbances and their detection over Istanbul. 6th International Conference on Recent Advances in Space Technologies (RAST), Istanbul, pp. 765-768, doi: 10.1109/RAST.2013.6581313.

Nguyen, T.C., Le, T.N., Alizadeh, M., Schuh, H. (2017). Alternative approach for detecting ionospheric scintillation using GNSS measurements. Geo-Spatial Technologies and Earth Resources, ISBN:978-604-913-618-4, pp. 261-271.

Ngwira, C.M., Klenzing, J., Olwendo, J., D'ujanga, F.M., Stoneback, R., and Baki, P. (2013). A study of intense ionospheric scintillation observed during a quiet day in the East African low-latitude region. RADIO SCIENCE, VOL. 48, 396-405, doi:10.1002/rds.20045.

Olatunji, E.O. (1967). The total columnar electron content of the equatorial ionosphere. J. Atmos. Terr. Phys., 29, 277-285.

Oluwadare, T.S., Nguyen, T.C., Akala, A.O., Heise, S., Alizadeh, M., and Schuh, H. (2019). Characterization of GPS-TEC over African equatorial ionization anomaly (EIA) region during 2009 - 2016. Advances in Space Research, 63 (1), pp. 282-301, doi.org/10.1016/j.asr.2018.08.044.

Otsuka, Y., Ogawa, T., Saito A., Tsugawa T., Fukao S., and Miyazaki, S. (2002). A new technique for mapping of total electron content using GPS network in Japan. Earth planets space, 54, 63-70.

Paznukhov, V.V., Carrano, C.S., Doherty, P.H., Groves, K.M., Caton, R.G. (2010). Equatorial plasma bubbles and L-band scintillations in Africa during solar minimum, Ann. Geophys., 30 (4), 675-682, http://www.ann-geophys.net/30/675/2012/.

Pi, X., Mannucci, A.J., Lindqwister, U.J., and Ho, C.M. (1997). Monitoring of global ionospheric irregularities using the worldwide GPS networks. Geophys. Res. Lett., 24 (18), 2283-2286, DOI: 10.1029/97GL02273.

Polekh, N., Zolotukhina, N., Kurkin, V., Zherebtsov, G., Shi, J., Wang, G., and Wang, Z. (2017). Dynamics of ionospheric disturbances during the 17-19 March 2015 geomagnetic storm over East Asia. Advances in Space Research, DOI: 10.1016/j.asr.2017.09.030.

Rao, R., Krishna, G., Niranjan, K., and Prasad, D. (2006). Temporal and spatial variations in TEC using simultaneous measurements from the Indian GPS network of receivers during the low solar activity period of 2004 - 2005. Ann. Geophys., 24, 3279-3292, doi.org/10.5194/angeo-24-3279-2006.

Rao, R., Krishna, G., Niranjan, S., and Prasad, D. (2006). Study of spatial and temporal characteristics of L-band scintillation over the Indian low latitude region and their possible effects on GPS navigation. Ann. Geophys., 24, 1567-1580.

Richmond, A.D., Peymirat, C., and Roble, R.G. (2003). Longlasting disturbances in the equatorial ionospheric electric field simulated with a coupled magnetosphere-ionospherethermosphere model.

J. Geophys. Res., 108(A3), 1118, Doi:10.1029/2002JA009758Rishbeth, H. (1972). Thermospheric winds and the F region: A review. J. Atmos. Terr. Phys., 34, 1.

Rishbeth, H. (2000). The equatorial F-layer: progress and puzzles. Annales Geophysicae, European Geosciences Union, 18 (7), pp.730-739. ffhal-00316693f.

Rodríguez-Bouza,M., Paparini, C., Otero, X., Herraiz, M., Radicella, S.M., Abe, O.E., Rodríguez-Caderot, G. (2017). Southern European ionospheric TEC maps based on Kriging technique to monitor ionosphere behavior. Advances in Space Research, Volume 60, Issue 8, Pages 1606-1616, doi.org/10.1016/j.asr.2017.05.008.

Romano, V., Spogli, L., Aquino, M., Dodson, A., Hancock, C., Forte, B. (2013). GNSS station characterisation for ionospheric scintillation applications. Adv. Space Res. 52, 1237-1246.

Rovira-Garcia, A., Ibáñez-Segura, D., Orús-Perez, R. et al. (2020). Assessing the quality of ionospheric models through GNSS positioning error: methodology and results. GPS Solut 24, 4, doi.org/10.1007/s10291-019-0918-z.

Saito, S., Maruyama, T., Ishii, M., Kubota, M., Ma, G., Chen, Y., Li, J., Duyen, C.H., Truong, T.L. (2008). Observation of small to large scale ionospheric irregularities associated with plasma bubbles with a transequatorial HF propagation experiment and spaced GPS receivers. J. Geophys. Res. 113 (A12313), 1-10.

SBAS Ionospheric Working Group (2010). Effect of Ionospheric Scintillations on GNSS - A White Paper.

Schaer, S. (1996). Proposal Concerning VTEC Data Format. GPS-IONO mail.

Schaer, S. (1999). Mapping and predicting the Earth's ionosphere using the Global Positioning System. PhD thesis, Bern University, Switzerland.

Shanmugam, S., Jones, J., MacAulay, A., and Dierendonck, A.V. (2012). Evolution to Modernized GNSS Ionospheric Scintillation and TEC Monitoring, in: Proceedings of IEEE/ION PLANS, Myrtle Beach, South Carolina, April 2012, pp. 265-273, DOI: 10.1109/PLANS.2012.6236891.

Scherliess, L., and Fejer, B.G. (1999). Radar and satellite global equatorial F-region vertical drift model. J. Geophys. Res., 104, 6829-6842.

Seeber, G. (2003). Satellite geodesy. 2nd completely revised and extended edition, Walter de Gruyter - Berlin - New York.

Shim, J.S., Scherliess, L., Schunk, R.W., and Thompson, D.C. (2008). Spatial correlations of day-to-day ionospheric total electron content variability obtained from ground-based GPS. JOURNAL OF GEOPHYSICAL RESEARCH, VOL. 113, A09309, doi:10.1029/2007JA012635.

Siefring, C.L., Bernhardt, P.A., Koch, D.E., and Galysh, I.J. (2011). Using TEC and radio scintillation data from the CITRIS radio beacon receiver to study low and mid-latitude ionospheric irregularities. Radio Sci., 46, RS0D19, doi:10.1029/2010RS004585.

Skone, S. (1998). Wide area ionosphere grid modeling in the auroral region, Ph.D thesis, Department of Geomatics Engineering, The University of Calgary, Calgary, Alberta, Canada.

Solomon, S.C., Roble, R.G. (2015). Encyclopedia of Atmospheric Sciences (Second Edition) – Thermosphere. Pages 402-408, doi.org/10.1016/B978-0-12-382225-3.00408-4.

Spiro, R.W., Wolf, R.A., and Fejer, B.G. (1988). Penetration of high-latitude-electric-field effects to low latitudes during SUNDIAL 1984. Ann. Geophys., 6, 39-50.

Spogli, L., Alfonsi, L., De Franceschi, G., Romano, V., Aquino, M.H.O., Dodson, A. (2009). Climatology of GPS ionospheric scintillations over high and mid-latitude European regions. Ann. Geophys. 27, 3429-3437.

Sreeja, V., Aquino, M., Elmas, Z.G., and Forte, B. (2012). Correlation analysis between ionospheric scintillation levels and receiver tracking performance, Space Weather, 10 (6), 1-2, S06005, DOI: 10.1029/2012SW000769.

Sreeja, V., Aquino, M., Forte, B., Elmas, Z., Hancock, C, et al. (2011). Tackling ionospheric scintillation threat to GNSS in Latin America, J. Space Weather Space Clim., 1 (1), A05, DOI: 10.1051/swsc/2011005.

Sripathi, S., Kakad, B., and Bhattacharyya, A. (2011). Study of equinoctial asymmetry in the Equatorial Spread F (ESF) irregularities over Indian region using multi-instrument observations in the descending phase of solar cycle 23. J. Geophys. Res. [Space Phys.], 116 (A11), DOI: 10.1029/2011JA016625.

Sultan, P.J. (1996). Linear theory and modeling of the Rayleigh-Taylor instability leading to the occurrence of equatorial spread F. J. Geophys. Res., 101(A12), 26,875-26,891, doi:10.1029/96JA00682.

Suvorova, A.V., Tsai, L.-C., Dmitriev, A.V. (2011). On relation between mid-latitude ionospheric ionization and quasi-trapped energetic electrons during 15 December 2006 magnetic storm. Planetary and Space Science, doi:10.1016/j.pss.2011.11.001.

Taoufiq, J., Mourad, B., Rachid, A., Amory-Mazaudier, C. (2018). Study of Ionospheric Variability Using GNSS Observations. Scientific Research, Vol.9 No.4.

Titheridge, J. E. (1995). Winds in the ionosphere. A review, J. Atmos. Terr. Phys., in press.

Todorova, S., Schuh, H., and Hobiger, T. (2007). Using the global navigation satellite systems and satellite altimetry for combined global ionosphere maps. Adv. Space Res, 42: 727-736.

Todorova, S. (2008). Combination of space geodetic techniques for global mapping of the ionosphere. PhD thesis, Vienna University of Technology, Austria.

Tran, T.L., Le, H.M., Amory-Mazaudier, C., Fleury, R. (2017). Climatology of ionospheric scintillation over the Vietnam low-latitude region for the period 2006-2014. Advances in Space Research 60 (2017) 1657-1669, doi.org/10.1016/j.asr.2017.05.005.

Tsai, H.F., Liu, J.Y., Tsai, W.H., and Liu, C.H. (2001). Seasonal variations of the ionospheric total electron content in Asian equatorial anomaly regions. J. Geophys. Res., 106, No. A12, 30, 363-369.

Tsai, L.-C., Liu, C.H., and Hsiao, T.Y. (2009). Profiling of ionospheric electron density based on the FormoSat-3/COSMIC data: results from the intense observation period experiment. Terr. Atmos. Ocean. Sci., 20, 181-191, doi: 10.3319/TAO.2007.12.19.01(F3C).

Tsai, L.-C., Liu, C.H., Hsiao, T.Y., and Chang, C.C. (2009). Maps of the ionospheric F2-layer characteristics derived from GPS radio occultation observations. Terrestial, Atmospheric and Oceanic Sciences (SCI Journal), doi:10.3319/TAO.2008.07.07.02(AA).

Tsai, L.-C., Liu, C.H., Hsiao, T.Y., and Huang, J.Y. (2009). A near real-time phenomenological model of ionospheric electron density based on GPS radio occultation data. Radio Science, 44, doi:10.1029/2009RS004154.

Tsai, L.-C., Chang, K.K., and Liu, C.H. (2011). GPS radio occultation measurements on ionospheric electron density from low Earth orbit. Journal of Geodesy (SCI Journal), doi:10.1007/s0019001104769.

Tsai, L.-C., Su, S.-Y., Liu, C.H., and Ram, S.T. (2015). Ionospheric electron density profiling and modeling of COSMIC follow-on simulations. Journal of Geodesy (SCI Journal), doi:10.1007/s00190-015-0861x.

Tsai, L.-C., Su, S.-Y., and Liu, C.-H. (2016). Global morphology of ionospheric F-layer scintillations using FS3/COSMIC GPS radio occultation observations. GPS Solutions (SCI Journal), 21: 1037-1048, doi:10.1007/s10291-016-0591-4.

Tsagouri, I., and Belehaki, A. (2015). Ionospheric forecasts for the European region for space weather applications. J. Space Weather Space Clim., 5, A9, DOI: 10.1051/swsc/2015010.

Tsunoda, R.T. (1980). Backscatter measurements of 11 cm equatorial spread F irregularities. Geophys. Res. Lett. 7, 848-850.

Tsunoda, R.T. (1985). Control of the seasonal and latitudinal occurrence of equatorial scintillation by the longitudinal gradient of integrated E region Pedersen conductivity. J. Geophys. Res., 90(A1), 447-456, doi:10.1029/JA090iA01p00447.

Tsurutani, B.T., Verkhoglyadova, O.P., Mannucci, A.J., Lakhina, G.S., Li, G., and Zank, G.P. (2009). A brief review of ‘‘solar flare effects’’ on the ionosphere. RADIO SCIENCE, VOL. 44, RS0A17, doi:10.1029/2008RS004029.

Tulasi Ram, S., Sunil, P.S., Ravi Kumar, M., Su, S.-Y., Tsai, L.C., and Liu, C.H. (2017). Coseismic travelling ionospheric disturbances during the Mw 7.8 Gorkha, Nepal, Earthquake on 25 April 2015 from ground and spaceborne observations. Journal of Geophysical Research: Space Physics, 122. doi.org/10.1002/2017JA023860.

Valladares, C.E., Villalobos, J., Sheehan, R., Hagan, M.P. (2004). Latitudinal extension of low latitude scintillations measured with a network of GPS receivers. Ann. Geophys. 22, 3155-3175.

Walker G.O., Ma, J.H.K., and Golton, E. (1994). The equatorial ionospheric anomaly in electron content from solar minimum to solar maximum for South East Asia, Ann. Geophys., 12, 195-209.

Wang, C., Rosen, I.G., Tsurutani, B.T., Verkhoglyadova, O.P., Meng, X., and Mannucci, A.J. (2015). Statistical characterization of ionosphere anomalies and their relationship to space weather events. J. Space Weather Space Clim., 6, A5 (2016), DOI: 10.1051/swsc/2015046.

Wang, X.L., Wan, Q.T., Ma, G.Y., Li, J.H., Fan, J.T. (2016). The influence of ionospheric thin shell height on TEC retrieval from GPS observation. Res. Astron. Astrophys., 16, 116.

Wells, D.E. (1974). Doppler satellite control. Technical Report 29, UNB, Fredricton.

Wienia, R.J. (2008). Use of Global Ionospheric Maps for Precise Point Positioning. MSc scriptie.

Wilson, B.D., Mannucci, A.J,. Edwards, C.D., and Roth, T. (1992). Global ionospheric maps using a global network of GPS receiver. International Beacom Satellite Symposium, Cambridge.

Wu, C.C., Fryb, C.D., Liu, J.Y., Lioud, K., and Tseng, C.L. (2004). Annual TEC variation in the equatorial anomaly region during the solar minimum: September 1996 - August 1997. J. Atmos. Sol.-Terr. Phys., 66, 199-207.

Wu, C. C., Liou, K., Shan, S.J., and Tseng, C.L. (2008). Variation of ionospheric total electron content in Taiwan region of the equatorial anomaly from 1994-2003, Adv. Space Res., 41, 611-616.

Xiang, Y., Gao, Y. (2019). An Enhanced Mapping Function with Ionospheric Varying Height. Remote sensing, doi.org/10.3390/rs11121497, 2019.

Xiong, B., Wan, W.-X., Ning, B.-Q., Yuan, H., and Li, G.-Z. (2007). A Comparison and analysis of the S4 index, C/N and Roti over Sanya. Chinese J. Geophys., 50 (6), 1414-1424, DOI: 10.1002/cjg2.1161.

Xu, J.-S., Zhu, J., and Chen, G.-H. (2006). GPS observations of ionospheric effects of the major storm of Nov. 7-10, 2004. Chinese J. Geophys., 49 (4), 848-855, DOI: 10.1002/cjg2.904.

Xu, G. (2007). GPS, Theory, Algorithms and Applications. 2nd Edition, Springer.

Xu, J.S., Zhu, J., Li, L. (2007). Effects of a major storm on GPS amplitude scintillations and phase fluctuations at Wuhan in China. Adv. Space Res. N.39, 1318-1324.

Yang, Z., Liu, Z. (2015). Correlation between ROTI and Ionospheric Scintillation Indices using Hong Kong low-latitude GPS data. GPS Solut (2016) 20:815-824, DOI 10.1007/s10291-015-0492-y.

Yeh, K.C., Liu, Chao-Han. (1982). Radio wave scintillation in the ionosphere. Proc. IEEE 70 (4), 324-358.

Yeh, K.C., Franke, S.J., Andreeva, E.S., Kunitsyn, V.E. (2001). An Investigation of Motions of the Equatorial Anomaly Crest. GEOPHYSICAL RESEARCH LETTERS, VOL. 28, NO. 24, PAGES 4517-4520.

Zhang, J., Schmidt, M., Dettmering, D., Meng, L., Zhu, Y., and Wang, Y. (2013). Enhanced TEC Maps Based on Different Space Geodetic Observations. Springer.

Zhao, B., Wan, W., Liu, L., Ren, Z. (2009). Characteristices of the ionospheric total electron content of the equatorial ionization anomaly in the Asian-Australian region during 1996-2004, Ann. Geophys., 27, 3861-3873.

Zhong, J., Lei, J., Dou, X., Yue, X. (2016). Assessment of vertical TEC mapping functions for space-based GNSS observations. GPS Solutions, DOI: 10.1007/s10291-015-0444-6.

Zou, Y., and Wang, D. (2009). A study of GPS ionospheric scintillations observed at Guilin. J. Atmos. Sol. Terr. Phys., 71, 1948-1958, doi:10.1016/j.jastp.2009.08.005.

ISSN 2190-7110